NASA CR-159667

ACOUSTIC TEST AND ANALYSIS OF THREE ADVANCED TURBOPROP MODELS

Bennett M. Brooks and F. B. Metzger

Hamilton Standard
United Technologies Corporation
Windsor Locks, Connecticut 06096

Contract NAS3-20614
January 1980

NASA

National Aeronautics and Space Administration
Lewis Research Center
Cleveland, Ohio 44135

FOREWORD

All of the testing reported here was conducted in the Acoustic Research Tunnel at United Technologies Research Center.

The authors wish to express their thanks for the support provided by the personnel of the United Technologies Research Center. R.W. Paterson, W.P. Patrick, and R.H. Schlinker were the UTRC personnel in charge of various portions of the acoustic testing. R.K. Amiet provided the computerized analysis to correct for sound transmission through the shear layer in the Acoustic Research Tunnel. J.C. Bennett was responsible for hot wire anemometry measurements of the prop-fan model wakes. R.J. Haas was responsible for acquiring the shadowgraphs showing bow and trailing waves near the prop-fan blades.

TABLE OF CONTENTS

TABLE OF CONTENTS (Cont.)

SUMMARY

Hamilton Standard under contract to NASA Lewis has completed an acoustic evaluation of three 62.2 cm (24.5 inch) diameter models of the prop-fan, an advanced propeller concept appropriate for energy efficient transport aircraft designed to cruise at 0.7 to 0.8 Mach number. Tests were conducted on the SR-2 model with unswept blades, the SR-1 model with a small amount of sweep at the blade tips, and the SR-3 model with a larger amount of sweep at the tip, The SR-2 model served as a reference for the other blades as it has unswept blades like conventional propellers. The SR-3 model was acoustically designed to produce lower noise than the SR-1 or SR-2 designs. This reduction was expected 1) as a result of the phase cancellation of noise produced by various spanwise locations on the blade resulting from sweep and 2) as a result of suppression of non-linear noise sources which become important as the effective Mach number of the air flow over the blade airfoil approaches 1.0 (sweep reduces the effective Mach number of a blade).

The objective of the program was to obtain the test data necessary to show the acoustic benefits of blade sweep in the near field at cruise conditions and in the far field at takeoff and landing conditions. In the near field this was accomplished by establishing the correlation between model test results and the frequency domain noise prediction methodology developed by Hamilton Standard and then predicting the full scale cruise levels. In obtaining test data for cruise noise evaluation, measurements were made at a 0.8 prop-fan diameters tip clearance, similar to the location expected for the fuselage of a prop-fan aircraft. However, the flight velocity was limited to 0.32 Mach number due to facility fan capacity. Therefore, the model was oversped to achieve an operating condition with a tip helical Mach number similar to the full scale cruise condition. Also the propeller drive rig was limited in power so tests were conducted primarily with two and four blade configurations rather than eight blades as in the full scale design. At cruise the full scale prop-fan operates at 10,667m (35,000 ft) altitude so the ambient conditions differ from the sea level conditions of the test.

In order to evaluate the far field noise at takeoff and landing conditions, tests were conducted at 0.2 Mach number flight speed and measurements were made at 4.9 diameters from the prop-fan axis of rotation.

Test results in both the near and far field show a gradually increasing noise level as tip helical Mach number and/or loading (horsepower) per blade is increased. The near and far field levels of the acoustically designed SR-3 are approximately 10 dB less than those of the earlier SR-1 and SR-2 designs, at loading conditions and tip relative Mach numbers approaching those of the prop-fan at cruise. Except for subsonic blade operating conditions, the slightly swept SR-1 and unswept SR-2 designs produce essentially the same noise level. Subsonically, in the near field at lightly loaded conditions, some noise reduction is seen in the SR-1 design relative to the SR-2 design. The benefits of the

SR-3 design are most apparent at highly loaded conditions typical of the projected prop-fan operating condition. At lightly loaded conditions more like conventional propellers in cruise the noise reduction benefits of SR-3 are about 5 dB in both the near and far field.

Correlation of test with predicted noise levels shows good agreement at the peak directivity point. Some lack of agreement was found aft of the plane of rotation which is believed due to be a discrepancy in predicted tip loading at the low through flow velocities characteristic of this test program. The comparison of measured and predicted acoustic pressure pulses generated by the blades shows good general agreement. The benefits of blade sweep can be seen in these comparisons. The SR-3 shows a reduction in integrated areas within the pressure pulse which causes a reduction in low frequency noise and a reduction in sharp leading edge spikes which is beneficial for reducing high frequency noise. The trailing edge spike which exists in both predicted and measured pulses is believed due to lack of sufficient sweep at the trailing edge of the blade. The predicted length of the acoustic pulses is less than measured. This discrepancy can cause a difference in predictions of the high frequency portions of the noise.

Shadowgraph evaluations confirm the above pulse correlation results. The location of the aft wave generated by the blades appears well predicted. Bow waves are predicted to occur close to the leading edge of the blade. However, none were observed close to the blade.

Hot wire anemometry measurements downstream of the blades established the feasibility of using such measurements as a diagnostic tool to evaluate the performance of airfoils at various spanwise locations on a prop-fan blade during actual test. The resolution of the measurements was sufficient to define the peak and width of the very narrow wake defect created by a thin prop-fan model blade operating at very high rotational Mach number.

Predicted full scale prop-fan levels adjusted on the basis of correlations of measured and predicted model levels showed the SR-3 should produce 146 dB at blade passage frequency at the high power loading, high tip speed, 0.8 Mach number cruise condition. The overall near field level is estimated to be 3 dB above the blade passage frequency level on the basis of model test data. At takeoff, the level for a large four engine aircraft is estimated to be 91.5 EPNdB at a point 640 m (2 100 ft) to the side of the aircraft. This estimate is based on scaling blade passage frequency levels from test data and adding the broadband noise predicted for full scale propellers.

SYMBOLS AND ABBREVIATIONS

AF	Activity Factor/Blade $= \frac{100,000}{16} \int_{r/R = \frac{HUB}{TIP}}^{r/R = 1.0} b/D\ (r/R)^3\ d\ (r/R)$
b	Blade Chord
C	Speed of Sound $= 20.05 \sqrt{T_S}$
C_{L_D}	Design Lift Coefficient (Camber)
C_{L_i}	Integrated Design Lift Coefficient $= 4 \int_{r/R = \frac{HUB}{TIP}}^{r/R = 1.0} C_{L_D}\ (r/R)^3\ d\ (r/R)$
D	Prop-fan Diameter
dB	Decibel $= 20 \log p/p_{REF}$
kW/m^2	Kilowatts per Square Meter
M_t	Blade Tip Rotational Mach Number
M_{TH}	Blade Tip Helical Mach Number $= (M_t{}^2 + M_X{}^2)^{1/2}$
M_X	Flight Mach Number
p_{REF}	Reference Acoustic Pressure = 20 μPa
Pa	Pascals
P_A	Atmospheric Pressure
P_S	Static Pressure
P_T	Total Pressure
P.D.R.	Propeller Drive Rig

SYMBOLS AND ABBREVIATIONS (Continued)

r	Blade Radial Station
R	D/2
RPM	Rotations Per Minute
SHP	Shaft Horsepower
SHP/D^2	Shaft Horsepower Per Diameter (in Feet) Squared
SPL	Sound Pressure Level (Decibels)
T_S	Absolute Static Temperature = $T_T/(1 + 0.2\ M_X^2)$
T_T	Absolute Total Temperature
V_t	Blade Tip Rotational Velocity = $\frac{RPM}{60} \cdot D \cdot \pi$
X_c	Corrected (For Tunnel Shear Layer Effects) Axial Microphone Position
X_m	Measured (Actual) Axial Microphone Position
X, Y, Z	Axial, Horizontal and Vertical Position Relative to Propeller Spinner Tip
Λ	Blade Tip Sweep Angle = Angle Between Relative Velocity and Normal to 50% Swept Chord Line at Tip
1P	Frequency = One per Propeller Revolution
8P	Frequency = Eight Per Propeller Revolution

SI Units of measurement used throughout (U.S. Customary Units may be included in parentheses to enhance communication).

INTRODUCTION

The occurrence of fuel shortages and increased fuel cost and the threat of future worsening conditions for air transportation caused NASA to sponsor studies of new aircraft and propulsion systems. One of the promising concepts established by these studies is the advanced high speed turboprop (prop-fan). This propulsion system differs from existing turboprops. The prop-fan has greater solidity than a turboprop, achieved by more blades of larger chord. The turboprop has straight blades with relatively thick airfoil sections; the prop-fan has swept back blades with thin airfoil sections to enhance performance and reduce noise. The turboprop cruises at no more than 0.65 Mach number; the prop-fan is designed to cruise at 0.7 to 0.8 Mach number. The diameter of the prop-fan is about 40 to 50% smaller than that of the turboprop. For maximum performance the prop-fan makes use of advanced core engines of the kind being used in modern turbofan engines. Performance is also enhanced by use of a spinner and nacelle aerodynamically contoured to reduce compressibility losses by retarding the high velocity flow through the root sections of the prop-fan blades.

Utilizing predicted aerodynamic performance data, weight estimates, and noise projections; several NASA sponsored studies by both engine and airframe manufacturers have concluded that a fuel savings of approximately 20 to 40% depending on operating Mach number should be achieved by a prop-fan aircraft, as compared with a high bypass ratio turbofan aircraft. With these encouraging results, a research technology effort has been instituted to establish the design criteria for this new propulsion system.

The objective of the work has been the development of prop-fan configurations with high efficiency and low noise. Propellers in the past that operated at the transonic helical tip speeds of the prop-fan at cruise showed performance losses and high noise levels. High performance is required to reduce fuel consumption. Low noise is required to minimize the weight of the fuselage wall treatment used to reduce cabin noise to levels consistent with those found in turbofan aircraft. Also, low noise is required for a prop fan aircraft to meet the noise certification levels established to control noise around airports during takeoff and landing.

In this report the results of the acoustic tests of the first three prop-fan model designs are summarized. Measurements were obtained in an acoustically treated wind tunnel at conditions simulating high speed cruise as well as takeoff and landing conditions. Acoustic measurements were obtained in the near field as well as the far field at sufficient fore and aft locations necessary to define the directivity of the noise. This report summarizes the measurements and their correlation with predicted levels. Also the full scale levels of a prop-fan in the near field at cruise and in the far field at takeoff and landing are presented. In addition to noise measurements, shadowgraphs showing the location of bow and trailing waves and hot wire anemometry measurements of blade wakes were obtained at some conditions.

SECTION 2
TEST PROGRAM

Model Description

Three prop-fan model blades, SR-1, SR-2 and SR-3 (Figure 2-1) were used for acoustic testing. The SR-2 and SR-3 models were used for shadowgraph testing. The SR-2 model was used for the hot wire feasibility study.

The SR-1 model incorporates the thin airfoils and blade sweep inherent in the prop-fan concept. The SR-2 (straight blade) model was included in the program as a reference for evaluating the effect of sweep in the tip sections. Except for the tip sweep and a blade root modification to accommodate an area-ruled spinner, the SR-2 is essentially the same as SR-1. The SR-3 model blade was more highly swept with reduced tip chord to improve efficiency and reduce near field noise as compared to the earlier designs.

All three blade models were designed to operate at 0.8 flight Mach number, 10.667 km (35 000 ft) altitude, 243 m/s (800 ft/sec) tip speed and a cruise power loading of 302 kW/m^2 (37.5 SHP/D^2 where D is diameter in feet). The overall characteristics of these models are listed below:

	SR-1	SR-2	SR-3
Blades	8	8	8
Activity Factor/Blade (AF)	203	203	235
Integrated Design Lift Coefficient (C_{L_i})	0.081	0.081	0.214
Blade Sweep (Λ)	23°	0°	34°
NACA Airfoils	16 & 65	16 & 65/ Circular Arc	16 & 65/ Circular Arc

The blade sweep is measured on the helix formed by the advancing blade. The aerodynamic design philosophy and test results are described in detail in Reference 2-1 for the SR-1 model. The aerodynamic test results for SR-1, SR-2 and SR-3 are discussed in Reference 2-2. The aeroacoustic design of SR-3 is described in Reference 2-3.

Test Model Geometry

The small scale models used for this test have a nominal diameter of 0.62 m (24.5 in.). However, it should be noted that the diameter of the current variable pitch prop-fan models with swept blades changes as the blade angle is varied. For example,

the diameter of the SR-3 model varies with blade angle as shown in Figure 2-2. The static or zero RPM curve shows that the diameter varies from 62.2 cm (24.5 in.) at approximately the feather angle to a maximum of 64.8 cm (25.5 in.) at nearly flat pitch. As shown in the plot, the diameter of the model SR-3 blades is further increased with tip speed as a result of centrifugal loads. The diameter of the SR-1 and SR-2 models do not increase significantly at test conditions.

The mechanism by which the diameter of the SR-3 model varies is shown schematically in Figure 2-3. The height, Y, of the tip airfoil center of gravity (CG) above a plane passing through the propeller axis of rotation and perpendicular to the pitch change axis is 31.12 cm (12.25 in.). This height is shown in both the side and front views. The top view looking from tip to hub shows the distance, Z, from the pitch change axis to the tip airfoil CG. The tip airfoil offset, Δ, is the perpendicular distance from the projected tip chord line to the pitch change axis. This offset occurs because the SR-3 model was swept along the advance angle line rather than the extended chord line. These dimensions are constant for a given geometry. Finally, X is the projected distance from the section CG to the axis of rotation and varies with blade angle as a function of Δ and Z. Thus, the tip radius at any blade angle is given by $R_{TIP} = (Y^2 + X^2)$. For the SR-3 model Δ and Z are 0.64 cm (0.25 in.) and 8.76 cm (3.45 in.), respectively. These values result in the static diameter variation with blade angle shown in Figure 2-2. The static diameter variation of the SR-1 blade model can be calculated in a similar manner.

At the blade angles and rotational speeds used in the acoustic test program, the diameters of the models do not vary significantly. The actual model diameters, as used for analysis of test data are as follows:

Model	Actual Model Diameter
SR-1	0.631 m (24.84 inches)
SR-2	0.622 m (24.5 inches)
SR-3	0.648 m (25.5 inches)

The nominal diameter 0.622 m (24.5 in.) was used as a normalizing reference for all set-up in the test program, such as microphone tip clearance and axial position, i.e. tip clearances for the near field microphones were 0.6 nominal diameter, 0.8 nominal diameter and 1.6 nominal diameter.

Model Test Configurations

The current prop-fan model is designed to operate in an eight-blade configuration. The eight-blade 10 667 m (35 000 ft) altitude cruise design power loading is 302 kW/m^2 (37.5 SHP/D^2 where D is diameter in feet), or 354 kW (475 SHP) for the 62.2 cm

(24.5 in.) diameter model when operated at sea-level density. It was determined that simulation of the prop-fan cruise condition in the UTRC tunnel required 22 to 45 kW (30 to 60 SHP) per blade depending on tip helical Mach number. The UTRC Propeller Drive Rig (PDR) has an available power input of 112 kW (150 SHP) at 12 000 RPM, which is not enough to simulate the eight-blade full scale loading. Thus, all three models (SR-1, SR-2, SR-3) were run in a two-blade configuration which required a maximum of 90 kW (120 SHP) to simulate full scale loading. Testing of all the models in an eight-blade configuration at lower blade loadings was performed for comparison in order to confirm the validity of using two-blade configurations for simulating eight-blade operation. In addition, the SR-3 model was run in a four-blade configuration.

The SR-1 model hub was used for SR-1 model blade testing. The SR-2 model hub was used for a portion of the SR-2 model blade testing. The SR-2 model hub with some modifications was used for the remaining SR-2 model and all of the SR-3 model blade testing. These modifications included the addition of a light-weight spinner and backing plate each with holes available for attachment of balance weights. Use of these two planes of balance holes aided the high speed dynamic balancing procedure. Also, multiple blade angle locking pins similar to those used by NASA in aerodynamic testing were used for high rotational speed (RPM) SR-2 and SR-3 model acoustic testing.

Structural Design Analysis

A structural design analysis of the SR-1, SR-2 and SR-3 model hardware was performed in order to define the safe operating regime. This included a finite element analysis of blade stress, detailed analysis of barrel lip and bolt steady stresses and calculations of the blade dynamic characteristics. It was found that the SR-1 model could be safely operated in both two and eight-blade configurations to 335 m/s (1100 FPS) tip speed (10 290 RPM). The SR-2 could be safely operated in two and eight-blade configurations to 391 m/s (1283 FPS) tip speed (12 000 RPM). The safe operating regime of the SR-3 model in two, four and eight-blade configurations is bounded by the 12 000 RPM speed limit, a steady blade stress limit, and zero power (windmill) limit. The minimum static blade angle allowed at 12 000 RPM is 27.5° (at the 3/4 radius), linearly decreasing to 22.0° at 11 300 RPM. Thus, the power and RPM conditions used for acoustic testing of SR-3 (see Test Procedure section) could be run safely.

Calculations of the blade dynamic characteristics for all models show no blade critical speeds within the test speed range for the more important 1P and 2P excitation orders. The higher order excitations were calculated to be small and to pose no stress problems. Vibratory strain monitoring during test verified this analysis.

Facility Description

All acoustic and shadowgraph testing was conducted in the Acoustic Research Tunnel (ART) at the United Technologies Research Center (UTRC) in East Hartford, Connecticut. A detailed description of this facility is given in Reference 2-4. The tunnel, shown schematically in Figure 2-4 is an open-circuit open jet design (Eiffel configuration). The inlet is provided with a high length-to-diameter ratio honeycomb section and a series of turbulence suppression screens. Inlet nozzles of 1.067 m (42 in.) diameter and 1.168 m (46 in.) diameter were used for this test program.

The open jet test section is surrounded by a sealed anechoic chamber 4.9 m (16 ft) high, 5.5 m (18 ft) long (axial direction), and 6.7 m (22 ft) wide. The interior walls of the chamber, shown in Figure 2-5 are lined with fiberglass wedges with a depth of 0.3 m (1 ft). The chamber has been found to be anechoic (Reference 2-4) for broadband noise over a 200 Hz to 20 kHz range of calibration frequencies. That is, the sound pressure followed a 6 dB decay curve per doubling of source-observer separation distance within approximately 1/2 dB over this frequency range.

The test section airflow enters the diffuser by way of an acoustically treated collector ring which can be seen at the right of Figure 2-5. Initial facility tests (Reference 2-4) identified an acoustic coupling between the inlet nozzle and the collector lip resulting in low frequency pulsations at high tunnel speeds. To suppress this noise triangular tabs, which can be seen on the nozzle at the left of Figure 2-5, were distributed around the nozzle periphery to disturb the azimuthal symmetry of the shear layer and prevent the generation of pulsations. Although the shear layer thickness is increased by the tabs, acoustic propagation through the shear layer is well predicted. This is discussed further in a later section.

The diffuser operates unstalled and is thus not a major source of background noise. To prevent tunnel fan noise from propagating upstream into the anechoic chamber a z-shaped muffling section with two right angle bends and parallel treated baffles is located between the diffuser and the fan. This muffler section can be seen in the middle figure in Figure 2-4. The 1120 kW (1500 HP) centrifugal fan, which drives the tunnel, exhausts to the atmosphere through an exhaust tower.

Flow Capability

The 1.067 m (42 in.) diameter tunnel inlet nozzle allows a maximum tunnel flow velocity of about 0.34 Mach number. The 1.168 m (46 in.) diameter nozzle allows a maximum flow velocity of about 0.29 Mach number. Tunnel speed is determined from total pressure measurements at the inlet contraction upstream of the anechoic test section and static pressure measurements within the anechoic chamber. Since losses are confined to the boundary layer, total pressure upstream and downstream of the contraction are predicted as well as measured to be equal. The test section velocity

has been shown to be temporally steady. Due to the inlet honeycomb and turbulence screens the test section velocity is spatially uniform to within 0.3% with a controlled turbulence level of less than 0.15%.

The open jet nature of the tunnel gives rise to a shear layer between the jet potential core and the surrounding quiescent air in the anechoic test section. The shear layer increases in thickness with increasing axial distance from the nozzle. For this test program the prop-fan was located totally within the potential flow so that there would be no interaction between the shear layer and the blade tips due to inward shear layer growth. The plane of rotation was located as far downstream of the nozzle as possible to allow the greatest angle of measurement forward of the prop-fan. This is illustrated in Figure 2-6. The optimum PDR location was defined as having the maximum axial separation between the tunnel nozzle exit and the plane of rotation while the blade tips remain free of shear layer turbulence ingestion.

Hot Wire Anemometry Study of Tunnel Shear Layer

A hot wire flow study was made to determine the extent of penetration of the open jet turbulent shear layer into the potential core of the tunnel test section and to thus find the optimum Propeller Drive Rig (PDR) location. Three rig axial locations were investigated: 0.46, 0.61 and 0.91 m (1.5, 2 and 3 ft) distance between the nozzle exit and the prop-fan plane of rotation. For each location hot wire traverses were made in a radial direction both 76 mm (3 in.) upstream and downstream of the plane of rotation. During these traverses the tunnel was operated at 0.2 Mach number. The SR-2 model prop-fan was operated in an eight-blade configuration at 0.934 blade tip helical Mach number with a power loading of 94 kW (126 SHP). This high power point at low tunnel test speed was selected as the worst case from the standpoint of streamline contraction and possible shear layer ingestion.

A 5.1 micron (0.0002 in.) diameter tungsten hot wire with a measured frequency response of 17 kHz was employed for the measurements. Both mean velocity and axial turbulence component data were obtained. A linearizer was used in the anemometer system to provide accurate measurement of turbulence intensities at the high levels encountered in shear layers. The radial extent of each traverse was 38.1 cm (15 in.). For measurements upstream of the prop-fan the traverse covered a range of 5.1 to 43.2 cm (2 to 17 in.) from the prop-fan tip. For measurements downstream, the corresponding range was 0 to 38.1 cm (0 to 15 in.).

Figure 2-7 shows a typical plot of mean velocity versus prop-fan tip clearance. The traverse was conducted 7.6 cm (3 in.) upstream of the prop-fan plane with the rig at the 0.46 m (1.5 ft) axial position. The mean velocity falls to 99% of its potential core value at a radial distance of 7.9 cm (3.1 in.) from the blade tip. This distance can be considered one measure of the clearance between the blade tip and the tunnel shear layer.

A second and more sensitive measure of the shear layer-potential core interface is the onset of intermittency. Intermittency is defined as the occurrence of alternating periods of laminar and turbulent flow in the instantaneous velocity signal at a fixed location. It is caused by large eddies at the interface of turbulent and nonturbulent regions. Intermittency is readily detected by observing the oscilloscope trace of a hot wire. Using this technique, intermittency was found to occur at a radial distance of 6.1 cm (2.4 in.) from the blade tip at the traverse position described above. Although the mean velocity criterion indicated a shear layer-tip clearance of 7.9 cm (3.1 in.), the intermittency criterion indicated a clearance of 6.1 cm (2.4 in.).

A third measure of shear layer position is the change in rms percent turbulence level as a probe is traversed from within the potential core into the shear layer. Figure 2-8 shows the results of a typical traverse conducted 7.6 cm (3 in.) upstream of the prop-fan plane with the PDR at 0.46 m (1.5 ft) axial position. Turbulence level increased from 0.8% within the potential core (5.1 cm (2 in.) tip clearance) to 1.3% at a clearance of 9.1 cm (3.6 in.). The high level (0.8%) in the freestream is due to acoustic excitation by the prop-fan. Applying the criterion that an increase of 0.5% in turbulence intensity defines the shear layer boundary, the tip clearance for the 0.46 m (1.5 ft) PDR position would be estimated to be 9.1 cm (3.6 in.).

Figure 2-9 summarizes the results of the shear layer location study. Circles indicate positions at which intermittency was observed. Squares denote positions at which the rms percent turbulence level increased 0.5% from potential core values. This criterion could only be applied for traverses conducted 7.6 cm (3 in.) upstream of the 0.46 and 0.61 m (1.5 and 2.0 ft) PDR positions. At the 0.91 m (3 ft) position the measurement at the upstream minimum clearance position of 5.1 cm (2 in.) was outside the potential core as indicated by the intermittency in the hot wire signal. For traverses conducted downstream of the prop, the turbulence signal was contaminated by a periodic signal arising from the blade tip vortex.

Based on the data shown in Figure 2-9 it was concluded that the PDR could be located at the 0.91 cm (3 ft) position without encountering shear layer interaction effects. At this position, tip clearance to the intermittency boundary was 2.5 cm (1 in.). Location of the PDR further downstream was considered unacceptable.

Acoustic data were also acquired at the three PDR axial locations. Good agreement among 90° (in the plane of rotation) near-field microphone spectra for the three locations confirmed the conclusion that the 0.91 m (3 ft) rig position was acceptable since previous studies have shown that when the prop-fan tip interacts with the shear layer there is a marked change in the spectral character of the signal.

Propeller Drive Rig

The Propeller Drive Rig (PDR) is powered by a constant torque, water cooled, variable frequency A.C. motor rated at 112 kW (150 SHP) at 12 000 RPM. The drive is shown in Figure 2-10, drawn to scale with a 0.61 m (2 ft) diameter rotor installed. The rig includes a low-noise slip ring assembly for transmission of blade dynamic strain and torquemeter signals with good signal-to-noise ratio. A once-per-revolution signal generator (1P pipper) and a sixty-per-revolution signal generator (60P pipper) were used to provide a rotational speed reference as well as trigger signals for some portions of the test.

Instrumentation

Acoustic Data Acquisition

The UTRC acoustic data acquisition system is shown schematically in Figure 2-11. For clarity only one of thirteen microphone channels is displayed. Numbers shown on Figure 2-11 correspond to item numbers in Table 2-I where additional equipment information such as manufacturer and model number are tabulated. Seven 6 mm (1 4 in.) diameter microphone systems (Items 1A, 2A) were used for all far field testing. Six 3 mm (1 8 in.) systems (Items 1B, 2B) were used for all near field testing. The microphone test set-up is described in another section. The microphone signal from the anechoic chamber was amplified or attenuated in 6 dB steps by use of the amplifier attenuator (Item 8), to provide maximum allowable signal level (1.4 volts peak-to-peak) to the tape recorder (Item 13). Amplifier attenuator output for each channel was monitored on the oscilloscope (Item 11) prior to each tape record to ensure that the tape recorder input voltage limit was not exceeded. A real time narrow bandwidth spectrum analyzer (Item 14) was used for on-line data reduction of one microphone channel as an independent check on tape recorded data. Analyzed spectra were displayed on an oscilloscope (Item 16) and X-Y plotter (Item 15). For each test run, an on-line spectrum was made of the signal from the near field microphone in the prop-fan plane of rotation.

Prior to the start of program testing, the gain attenuation settings of the amplifier attenuator were calibrated for each of sixteen channels at all gain attenuation switch positions and for the frequency range of 300 Hz to 20 kHz. This was accomplished by introducing white noise (using Item 10) into the amplifier attenuator and spectrum analyzing the output for the various switch positions. A similar technique was used to calibrate the gain attenuation settings of the spectrum analyzer (Item 14). The uncertainty in each of these calibrations was ± 0.5 dB. The cable response of the microphone channels was determined over the frequency range from 300 Hz to 20 kHz. This was accomplished by introducing sine waves from the signal generator (Item 9) to the

microphone preamplifier (Item 3) via a preamplifier input adapter (Item 6). Comparison of rms voltage at the preamplifier (using Item 7) with the voltage at the tape recorder input (using Item 12) yielded the required cable corrections. The uncertainty in the cable calibration was ± 0.25 dB.

Prior to the start of program testing all the microphones were calibrated using a variable frequency, electrostatic actuator to obtain open circuit sensitivity and frequency response. The microphones provided essentially flat response (± 0.2 dB) between 300 Hz and 20 kHz. A sample calibration is shown in Figure 2-12. A pistonphone (Item 5) was calibrated with an accuracy of ± 0.2 dB. Regularly throughout the test, each microphone channel was calibrated by recording the pistonphone signal. In addition, before and after each test series, the pistonphone signal was monitored for rms level and signal purity. The repeatability of the pistonphone calibration was ± 0.25 dB.

The tape recorder was set up for FM intermediate bandwidth recording under the IRIG-B standard. Recording speed was 152.4 cm/sec (60 IPS) giving 0-20 kHz frequency response. Very near field (within several chord lengths) data for the SR-2 model was recorded at 304.8 cm sec (120 IPS) to give 0-40 kHz frequency response. The fourteen tape channels were allocated as follows: ten data channels, two 1P pippers for prop-fan speed reference, time code and voice. Thus, the thirteen microphone channels were recorded in two twenty second record passes for each test condition. The seven near field microphones were recorded twice and the six far field microphones were recorded three at a time. A 500 mV 250 Hz sine wave signal was recorded on all data channels at the start of each tape as a reference level. White noise was recorded to establish a frequency calibration. The uncertainty in this calibration was within ± 0.5 dB.

If all of the above levels of uncertainty are combined as suggested in Reference 2-5, the uncertainty in the sound pressure level (at an arbitrary frequency between 300 Hz and 20 kHz) obtained from a spectrum plotted by the spectrum analyzer (Item 14) is ± 1.1 dB.

Shadowgraph Data Acquisition

The shadowgraph data acquisition system is shown in Figure 2-13. Two distinct light systems were used in this test. A high voltage spark gap point light source (Item 17) was used to project an image of the prop-fan blade and its associated wave patterns on a screen (Item 18) which was photographed using a remotely-controlled camera (Item 19). The light source consisted of an air gap spark placed in a casing directly behind a 1 mm (0.040 in.) pinhole to approximate a point source of light. The flash of light projected through the pin hole produced a shadowgraph with high resolution and a light intensity strong enough for the light-to-screen distance required for this test.

A 16 kV electric discharge of very short duration (1/2 μsec) was remotely triggered into the spark gap from the control room. This was done using a variable time delay trigger unit (Item 20). To provide a range of precise viewing angles of the blade this unit was synchronized to the prop-fan rotor using a once-per-revolution (1P) and sixty-per-revolution (60P) photoelectric pulse generator (Item 21) (pipper). The pipper provided the reference input pulse to the trigger delay unit (Item 20) and the 60P pipper pulse was used to digitally delay the output trigger pulse in increments of 6° of prop rotation. The output pulse was also independently continuously variable within the 6° increments and could be adjusted for a single trigger pulse or a repeated once-per-revolution trigger pulse.

The blade position was calibrated statically using 6° increment position markings on the hub and PDR. These positions could be monitored during test operation using the trigger delay unit (in the repeated 1P trigger mode) and a xenon strobe light (Item 22). The strobe emitted a short duration (12 μsec) flash with the prop-fan at some azimuthal position relative to the 1P pipper firing and appeared to "freeze" the pattern of position markings on the hub. The trigger delay was adjusted until the hub markings indicating the desired shadowgraph test position could be seen in the viewing scope at the window. Once the initial trigger position was set, a series of test positions at 6° increments could be easily set using the digital delay to fire the shadowgraph spark light source when the desired azimuth position was obtained.

The reflective screen material (Item 18) was attached to a heavy board which was rigidly fixed in the test chamber. The screen is highly reflective over a relative small acceptance angle ($< 5°$) and was thus oriented as close to normal as possible to the spark line-of-sight across the blade. Due to the small reflection acceptance angle and also to avoid parallax errors, the camera line-of-sight was coincident with that of the point light source within a few degrees.

The camera used for this test was a 35 mm Single Lens Reflex with remote-controlled shutter and motorized film advance drive (Item 19). A 55 mm f/1. 2 lens focused on the screen (at a distance of about 2.2 m) and ASA 400 film (TRI-X) were used. Test procedure for each shadowgraph was as follows. The desired trigger delay was set. The camera shutter was opened in the darkened test chamber. Then the point light source was triggered for a single flash producing a shadowgraph image of the moving blade on the screen which was captured on film. The camera shutter was then closed and the film advanced to obtain additional shadowgraphs.

Measurement of Operating Condition

Tunnel Speed Measurement - Figure 2-14 shows the arrangement for measuring the Acoustic Research Tunnel speed. Test section total pressure (P_T) was obtained from a Pitot probe (Item 23) located outside the wall boundary layer in the tunnel inlet downstream of the last inlet screen. The pressure was read on a water manometer open to atmospheric pressure (Item 25) which was located in the Acoustic Research Tunnel control room. With

scale divisions of 2.5 mm (0.1 in.), the measurement uncertainty was less than ± 2.5 mm (± 0.1 in.) water. Test section static pressure (P_S) was obtained from static pressure probes (Item 27) located inside the sealed anechoic chamber in a region of negligible room recirculation velocity. Static pressure was obtained from a differential pressure gage (Item 26) in which one port was connected to the total pressure probe (Item 23) and one port connected to a static pressure probe (Item 27). Prior to the start of testing the gage was calibrated by a dead weight tester. The gage uncertainty is 2.5 mm (± 0.1 in.) water. An independent measurement of test section pressure was obtained from a second static pressure probe connected to a water manometer with 0.1 in. scale divisions. Atmospheric pressure (P_A) was obtained from a barometer (Item 29) with scale divisions of 0.1 mm Mercury. From measurement of P_A, P_A-P_T and P_T-P_S, tunnel pressure ratio (P_T/P_S) was obtained. Tunnel Mach number follows from isentropic flow equations. Applying the uncertainties of 2.5 mm (± 0.1 in.) water for P_A-P_T, 2.5 mm (± 0.1 in.) water for P_T-P_S and ± 0.2 mm Mercury for P_A, and using equation (?.?) of Reference 2-5, the uncertainty in tunnel Mach number was 0.6% or less depending on tunnel speed.

Total Temperature - Test section total temperature (T_T) was obtained from a thermocouple (Item 24) located in the tunnel inlet. Temperature was read on a thermocouple readout (Item 30) in the control room. The temperature system was calibrated using a Fisher Model 15-043A thermometer with 1/10°C scale divisions.

Rotor RPM - Rotor RPM was obtained from a once-per-revolution shaft signal generated by a photo cell on the PDR (1P pipper) (Item 21) and a frequency counter (Item 31). Prior to the start of testing the counter was calibrated. With a counter resolution to 0.1 Hz, the uncertainty in rotor RPM was ± 6 RPM.

Rotor Horsepower - Rotor horsepower was obtained from a measurement of shaft torque and rotor RPM. The strain gage system mounted on the rig shaft was calibrated prior to start of testing using a weight of 222.4 N (50 lbs) and a lever arm of .305 m (1 ft). The estimated accuracy of this static torque calibration is 2%.

Blade Vibratory Strain - Strain gages for the measurement of the blade bending at two locations, and blade torsion at one location were bonded to one SR-1, SR-2 and SR-3 model blade as shown in Figures 2-15, 2-16 and 2-17, respectively. The strain gages were wired into four-arm wheatstone bridges at a hub-mounted terminal board. From there, wires passed through the rig drive and motor shafts to an aft-mounted slip ring assembly which provided the rotating/stationary electrical interface.

Strain gage excitation, signal conditioning and signal amplification were provided by a UTRC electronic system. The amplified strain signals were displayed on a four-beam oscilloscope in the rig control room. A once-per-revolution pulse signal was simultaneously displayed on the oscilloscope as an aid in determining blade mode shapes. The "as-installed" gage factor of the strain gages was estimated to be accurate to within 1-1/2%.

Rotor Balancing - In addition to measuring required test parameters, measurements of rotor dynamic unbalance were made. Accelerometers (Item 32) were fixed on the rig housing above two of the rotor shaft bearings. The peak vibration amplitude and phase relative to the 1P pipper for both locations was read on a digital phase meter (Item 33). This information, for the initial test run of a model configuration and for runs with trial weights of known size and location in each of the two balance planes, was used in a two-plane dynamic balance procedure. This procedure was stored in a programmable calculator (Item 34) for on-site determination of the resultant balance weights needed for high rotational speed (RPM) operation.

Test Procedure

Acoustic Test Configurations and Conditions

Near Field and Far Field Tests - The acoustic test configuration is shown in Figure 2-18. Acoustic data were obtained at locations along lines parallel to the axis of the tunnel (also the axis of prop-fan rotation) at four distances. A moveable line array of seven near field microphones was placed parallel to the prop-fan axis of rotation at a tip clearance of 0.8 and 1.6 prop-fan diameters (nominally 62.2 cm (24.5 in.)) for SR-1 model testing. The near field microphones were at 0.6 and 0.8 diameter (D) tip clearance for SR-2 and SR-3 model testing. The microphones were placed axially in the plane of rotation and symmetrically fore and aft of the plane of rotation at + 0.25 D, + 0.5 D and ± 1.0 D (see also Figure 2-5). Fixed far field microphones remained at 70, 80, 90, 100, 110 and 120° relative to the axis of rotation and 3.05 m (10 ft) from the tunnel centerline for SR-1 model testing. This corresponds to a 4.4 D tip clearance. The far field microphones were in the 60, 70, 80, 90, 100 and 110° positions for SR-2 and SR-3 model testing. By convention, the 0° position is assumed to be on the axis of rotation upstream of the prop-fan and the 90° position is in the prop-fan plane of rotation.

To meet test objectives acoustic measurements were made for a variety of test conditions. A test condition is defined as one (1) blade angle (measured at the reference station), one (1) near field microphone array location, one (1) tunnel Mach number and one (1) model test configuration. The acoustic test conditions were allocated between the three blade models, SR-1, SR-2 and SR-3 in both two-blade and eight-blade configurations. The SR-3 model was also tested in a four-blade configuration. All the models were tested at both 0.20 and 0.32 tunnel Mach number. Limited testing was performed at 0.1 tunnel Mach number. The test conditions for all the models form a distribution of tip speeds and blade power loadings which simulate takeoff, landing and cruise operation. Test conditions for which acoustic measurements were made at the 0.8 D (nominal) tip clearance near field microphone array location were generally repeated for the complimentary microphone array location (1.6 D for SR-1, and 0.6 D for SR-2, SR-3). The power loading per blade vs. blade tip helical Mach number for

test conditions with two-blade and four-blade configurations and 0.8 D tip clearance are shown in Figure 2-19. Blade loading conditions ranged from 1.5 to 46.6 kW (2 to 62.5 SHP) per blade at blade tip helical Mach numbers ranging from 0.591 to 1.235. Test conditions with eight-blade configurations and 0.8 D tip clearance are shown in Figure 2-20. Blade loading conditions ranged from 3.6 to 14.9 kW (4.9 to 20.0 SHP) per blade at 0.592 to 1.150 tip helical Mach number. Shown next to the symbols indicating blade model type are test run numbers. These are useful for cross reference of operating conditions in data analysis.

Background Noise - An investigation of the background noise in the tunnel was conducted with the tunnel, the PDR and all instrumentation in operation. A dummy hub without blades was installed for this test. Measurements were obtained at the 0.6 D and 0.8 D (nominal) tip clearance near field microphone locations and at the far field microphone locations. Two tunnel speeds, 0.20 and 0.32 Mach number, and three rig rotational speeds, 8, 10 and 12 krpm were tested. Measurements at a complete range of attenuator/amplifier settings were obtained as well.

Boundary Layer Trip - Acoustic measurements at 0.8 D near field and far field locations were made with a 51 mm (0.002 in.) diameter boundary layer trip wire attached to the camber side of the unstrain-gaged blade of the SR-2 model in a two-blade configuration. The wire was at the 5% chord position to cause transition of the normally laminar boundary layer. The wire size was chosen using the Braslow Method (Reference 2-6) for determining the critical trip height for boundary layer transition. The wire as installed on the blade and the conditions tested are shown on Figure 2-21. Immediately after the boundary layer trip test, the trip wire was removed and acoustic testing with clean blades was conducted. Atmospheric conditions were the same and thus a valid comparison between the tripped and untripped conditions could be made.

Very Near Field Microphone Traverse - Detailed very near field acoustic measurements were made for the SR-2 model in a two-blade configuration. The PDR was located such that the prop-fan plane of rotation was 46 cm (18 in.) downstream of the nozzle exit to maximize the clearance between the blade tips and the inner boundary of shear layer turbulence. Measurements at three operating conditions were obtained at transonic tip speeds and at low to high loading as shown in Figure 2-19. A 3 mm (1/8 in.) diameter microphone was mounted on a traverse mechanism which allowed movement normal to the prop-fan axis in the plane of rotation as shown in Figure 2-22. Measurements at ten radial positions were obtained, with distances between the blade tip and the microphone diaphragm as listed below.

1.9 cm (0.75 in.)	12.7 cm (5.0 in.)
2.5 cm (1.0 in.)	20.3 cm (8.0 in.)
3.8 cm (1.5 in.)	27.9 cm (11.0 in.)
5.1 cm (2.0 in.)	37.3 cm (14.7 in., 0.6 D)
7.6 cm (3.0 in.)	49.8 cm (19.6 in., 0.8 D)

On-line oscilloscope photographs of the acoustic pressure pulse traces were taken in addition to tape recorded measurements made at the above discrete microphone locations. At the highest tip speed and loading condition, a continuous traverse of the microphone from the 1.9 cm (0.75 in.) position to the 37.3 cm (14.7 in., 0.6 D) position was done at a uniform traverse rate of 20.3 cm/min (8.0 in./min). A tape record of this traverse was made.

Within-Flow Microphones for SR-3 Model Testing - Limited acoustic measurements of the SR-3 model in a four-blade configuration were made at three fixed microphone locations within the tunnel stream potential core, as shown in Figure 2-23. The 1.168 m (46 in.) diameter nozzle was used for this test with the PDR mounted 3.8 cm (1.5 in.) off center and 46 cm (18 in.) downstream of the nozzle exit. The prop-fan and microphones were located within the inner boundary of shear layer turbulence as defined by the intermittency criterion. The three 3 mm (1/8 in.) diameter microphones were mounted such that they did not mutually interact in the flow. Their common radial location was 5.1 cm (2.0 in.) outboard of the blade tips and they were axially located in the prop-fan plane of rotation at the prop-fan tip, 0.5 D (nominal 62.2 cm) upstream and 0.5 D downstream, respectively. Also, measurements were made in the plane of rotation at 1.6 D clearance. Data was taken for three transonic operating conditions at moderate to high blade loading as shown in Figure 2-19.

Shadowgraph Test Configurations and Conditions

The general shadowgraph test configuration is shown in Figure 2-24. Looking upstream while on the axis of rotation of the prop, the camera and point light source are on the left and the screen is on the right, and the prop-fan rotates counterclockwise. Thus, because of blade twist, the blade planform shadow is viewed by directing the line of sight under the hub. The edge is viewed from this viewing position by directing the line of sight over the hub. The camera line of sight and light source line of sight across the blade were coincident within a few degrees. The position of the point light source relative to the spinner tip and screen are given in Figure 2-24 for the three configurations tested. They were the SR-2 two-blade and SR-3 four-blade planform tests and the SR-3 four-blade edgewise test.

Four views of the test set up are shown in Figure 2-25. Figure 2-25A shows a close-up of the point light source and camera. Figure 2-25B displays the set-up for plan-view shadowgraphs and the edgeview testing set-up is seen in Figure 2-25C. A simulation showing how planform and edgewise views are obtained is shown in Figure 2-25D. The operating conditions for the test are shown in Figure 2-19.

The shadowgraph system was triggered by a dual pipper system. The prop-fan azimuth zero reference was an arbitrary position at which the 1P pipper fired. There

was also a 60P pipper input which allowed the choice of discrete 6° intervals in azimuth. Prop-fan azimuth positions are numbered in these 6° intervals relative to the 1P zero reference. Table 2-II gives a list of measurements from the point light source to the blade leading and trailing edges at the reference station for the prop-fan azimuth positions photographed. The absolute location of the photographed blade in the zero position for the two models is also given.

Since the blade is twisted, there is only one radial location at which the blade chord is normal to the line of sight for a given azimuth position. For another azimuth position the blade chord will be normal to the line of sight at a different radial location. In order to avoid parallax errors in reducing the data, it is necessary to know the radial location on the blade at which the blade chord is normal to the line of sight for each azimuth position tested. Using the measurements given in Table II and knowledge of the blade twist distribution, the radial location at which the blade chord is normal to the line of sight can be calculated for each azimuth position. For the SR-3 model blade, this radial location was measured for four azimuth positions. The location on the blade which was normal to the line of sight is given as radial distance from the trailing edge of the most inboard station of the blade as follows:

Azimuth Position		Blade Normal
0	0°	2.2 cm (0.85 inches)
6	36°	2.3 cm (0.90 inches)
10	60°	6.2 cm (2.45 inches)
15	90°	15.7 cm (6.2 inches) (Reference Station)

For the SR-2 model blade, the blade chord was normal to the line of sight at the reference station with the model in the Number 10, or 60° azimuth position.

Data Reduction

Acoustic Test Data

The acoustic data were reduced in three forms, narrow band spectral plots, one-third octave band spectral plots, and oscilloscope trace photographs of acoustic pressure pulse waveforms. The spectra were produced using the set-up diagrammed in Figure 2-26. This five part system consists of the following equipment with associated accuracies:

1. 1" FM tape playback system
   - Amplitude: ± 0.5 dB
   - Frequency: ± 0.2%

2. Amplifier (System corrector)

   - Amplitude: ± 0.1% of full scale

   - Frequency: Essentially flat response

3. 1/3 octave band analyzer (with self-contained plotter)

   - Amplitude linearity: + 1 db

   - Filter center frequency: ± 2%

4. Narrowband (60 Hz bandwidth) analyzer

   - Amplitude linearity: ± 0.25% of full scale

     or: ± 0.5 dB whichever is greater

   - Frequency linearity: ± 0.2% of full scale

5. X-Y plotter

   - X, Y linearity: ± 0.2% of full scale

The system for 1/3 octave band data reduction includes items 1, 2, and 3 above. It has a total uncertainty of ± 1.1 dB amplitude and ± 2% center frequency. The system for narrowband data reduction includes items 1, 2, 4 and 5. It has a total uncertainty of ± 1 dB amplitude and ± 1% frequency. When these playback accuracies are combined with the record accuracy of ± 1.1 dB, it is seen that the total uncertainty for data acquisition and reduction is ± 1.5 dB on a root-sum-squared basis.

In conjunction with the calibration of the data acquisition system, a test tape was made at the test facility and played back at the data reduction facility. A known pure tone signal input was applied at the amplifier/attenuator for each data channel and evaluated over a frequency range of 250 Hz to 20 kHz. Upon playback the signal level was measured. The variation in level between the recorded signal and that played back was within ± 0.7 dB across the entire frequency range. The uncertainty of each component (amplifier, tape record and tape playback) is ± 0.5 dB. The test tape uncertainty is ± 0.9 dB as calculated on a root-sum-squared basis. Thus, uncertainty in actual practice is less than that calculated.

Acoustic pressure pulse waveforms were made by photographing several oscilloscope sweeps of the data signal obtained during tape playback through items 1 and 2 above. Additionally, signal enhanced pressure pulse waveforms were made of the SR-2 model data obtained during the boundary layer trip test. These were processed through a Saicor SAI-43A in the signal enhance mode to derive 400 line waveforms of the coherent portion of the acoustic pressure pulse.

All of the data obtained during the program were reduced on a narrowband basis. The frequency range covered was 0 to 20 kHz on a linear frequency scale for most of the data. This frequency range gives an effective filter bandwidth (half power) of 60 Hz. A limited number of SR-1 model test runs obtained in an earlier test series were analyzed for a frequency range of 0 to 10 kHz on a linear scale giving an effective filter bandwidth (half power) of 30 Hz. The very near field SR-2 model test runs were recorded at 305 cm/sec (120 IPS) tape speed. When played back at 152 cm/sec (60 IPS) tape speed and spectrum analyzed from 0 to 20 kHz the actual range of analysis for this data became 0 to 40 kHz with an effective filter bandwidth of 120 kHz.

One-third octave band plots were made for all far field data taken on test runs for which the near field microphone was located at 0.8 D (nominal) tip clearance. The range of analysis included all standard bands with center frequencies from 25 Hz to 20 kHz. Also, A-weighted and linear overall levels were obtained.

Oscilloscope trace photographs of the acoustic pressure pulse waveforms were made for selected test runs. In these traces, time moves from left to right and positive acoustic pressure is toward the top of the photograph. The total time covered by each trace is equal to one period of revolution of the model prop-fan, and thus changes with test condition.

Shadowgraph Test Data

Data reduction of the shadowgraph pictures was straight forward. The view is normal to the blade chord at one radial position on the blade. The locations of the bow and trailing waves can be accurately located relative to the blade leading and trailing edges by scaling distances in the photographs and normalizing by the local blade chord.

Table 2-I. Instrumentation data

Item Number	Item	Manufacturer	Manufacturers Designation	Location
1A	Microphone Cartridge (6mm)	Bruel and Kjaer	4136	A.C.
1B	Microphone Cartridge (3 mm)	Bruel and Kjaer	4138	A.C.
2A	Adaptor	Bruel and Kjaer	UA0035	A.C.
2B	Adaptor	Bruel and Kjaer	UA0036	A.C.
3	Microphone Preamplifier	Bruel and Kjaer	2619	A.C.
4	Power Supply	Bruel and Kjaer	2801	A.C.
5	Pistonphone	Bruel and Kjaer	4220	A.C.
6	Adaptor	Bruel and Kjaer	JJ2615	A.C.
7	RMS Meter	Hewlett Packard	400D	A.C.
8	Amplifier/Attenuator	UTRC	--	C.R.
9	Signal Generator	Hewlett Packard	3311A	C.R.
10	White Noise Source	Scott	811-A	C.R.
11	Oscilloscope	Tektronix	RM31A	C.R.
12	RMS Meter	Bruel and Kjaer	2113	C.R.
13	Tape Recorder	Honeywell	Model 96	C.R.
14	Spectrum Analyzer	Spectral Dynamics	SD301C/302C	C.R.
15	X-Y Plotter	Hewlett Packard	7035B	C.R.
16	Oscilloscope	Tektronix	545A	C.R.
17	Spark Gap Point Light Source	EG&G	Microflash	A.C.
18	Projection Screen	3M	Scotchlite	A.C.
19	Camera W/Motor Film Drive	Nikon	F2	A.C.
20	Variable Time Delay Trigger Unit	UTRC	--	C.R.
21	1P and 60P Pipper	UTRC	--	A.C.
22	Xenon Strobe Light	General Radio	1540 Strobolume	A.C.
23	Pitot Probe	UTRC	--	Tunnel Inlet
24	Thermocouple	Project Inc.	Ch-A1	Tunnel Inlet
25	Manometer	UTRC	--	C.R.
26	Differential Pressure Gage	Wallace Tiernan	62B-4C-0120	C.R.
27	Static Pressure Probes	UTRC	--	A.C.

Table 2-I. (Continued)

Item Number	Item	Manufacturer	Manufacturers Designation	Location
28	Thermocouple	Project Inc.	Ch-A1	C.R.
29	Barometer	Sargent Walch	1215	C.R.
30	Thermocouple Read-out	ERC	T/C Type K	C.R.
31	Frequency Counter	Systron Donner	6202	C.R.
32	Accelerometer	Columbia	902	A.C.
	W/Amplifier	Endevco	Dial-a-Gain	A.C.
33	Phase Meter	Spectral Dynamics	SF-119B	C.R.
34	Programmable Calculator	Hewlett Packard	HP-97	C.R.

A.C. denotes Anechoic Chamber
C.R. denotes Control Room

Table 2-II. Shadowgraph planform tests. Distance from point light source to blade edge @ reference station

SR-2 Model						SR-3 Model					
Prop Azimuth Position		Leading Edge		Trailing Edge		Prop Azimuth Position		Leading Edge		Trailing Edge	
		cm	(in)	cm	(in)			cm	(in)	cm	(in)
Zero	0°					Zero	0°	109.9	43 1/4	107.6	42 3/8
1	6°	112.6	44 5/16	110.5	43 1/2	1	6°	111.3	43 13/16	108.6	42 3/4
2	12°	114.3	45	111.9	44 1/16	2	12°	113.2	44 9/16	111.0	43 11/16
3	18°	115.6	45 1/2	113.3	44 5/8	3	18°	114.6	45 1/8	111.4	43 7/8
4	24°	117.2	46 1/8	114.9	45 1/4	4	24°	116.4	45 13/16	113.5	44 11/16
5	30°	118.3	46 9/16	116.5	45 7/8	5	30°	118.1	46 1/2	114.9	45 1/4
6	36°	119.4	47	118.0	46 7/16	6	36°	120.0	47 1/4	117.0	46 1/16
7	42°	120.5	47 7/16	119.4	47	7	42°	121.8	47 15/16	119.1	46 7/8
8	48°	122.2	48 1/8	121.0	47 5/8	8	48°	123.5	48 5/8	120.7	47 1/2
9	54°	122.6	48 1/4	121.9	48	9	54°	124.8	49 1/8	122.2	48 1/8
10	60°	123.2	48 1/2	123.2	48 1/2	10	60°	126.4	49 3/4	124.0	48 13/16
11	66°	123.8	48 3/4	124.1	48 7/8	11	66°	127.6	50 1/4	125.7	49 1/2
12	72°	124.3	48 15/16	124.6	49 1/16	12	72°	128 7	50 11/16	127.3	50 1/8
13	78	124.6	49 1/16	125.3	49 5/16	13	78°	129.7	51 1/16	128.7	50 11/16
14	84°	124.6	49 1/16	125.9	49 9/16	14	84°	130.5	51 3/8	130.0	51 3/16
15	90	124.6	49 1/16	127.0	50	15	90°	131.3	51 11/16	131.3	51 11/16
16	96°	124.5	49	127.2	50 1/16						
17	102°	124.1	48 7/8	127.3	50 1/8						
18	108°	123.7	48 11/16	127.0	50						
19	114°	123.0	48 7/16	126.8	49 15/16						
20	120	121.9	48	126.5	49 13/16						
21	126°	121.3	47 3/4	126.0	49 5/8						

SR-2 Blade 2 past downward vertical in direction of rotation for zero position.

SR-3 Blade 4 past downward vertical in direction of rotation for zero position.

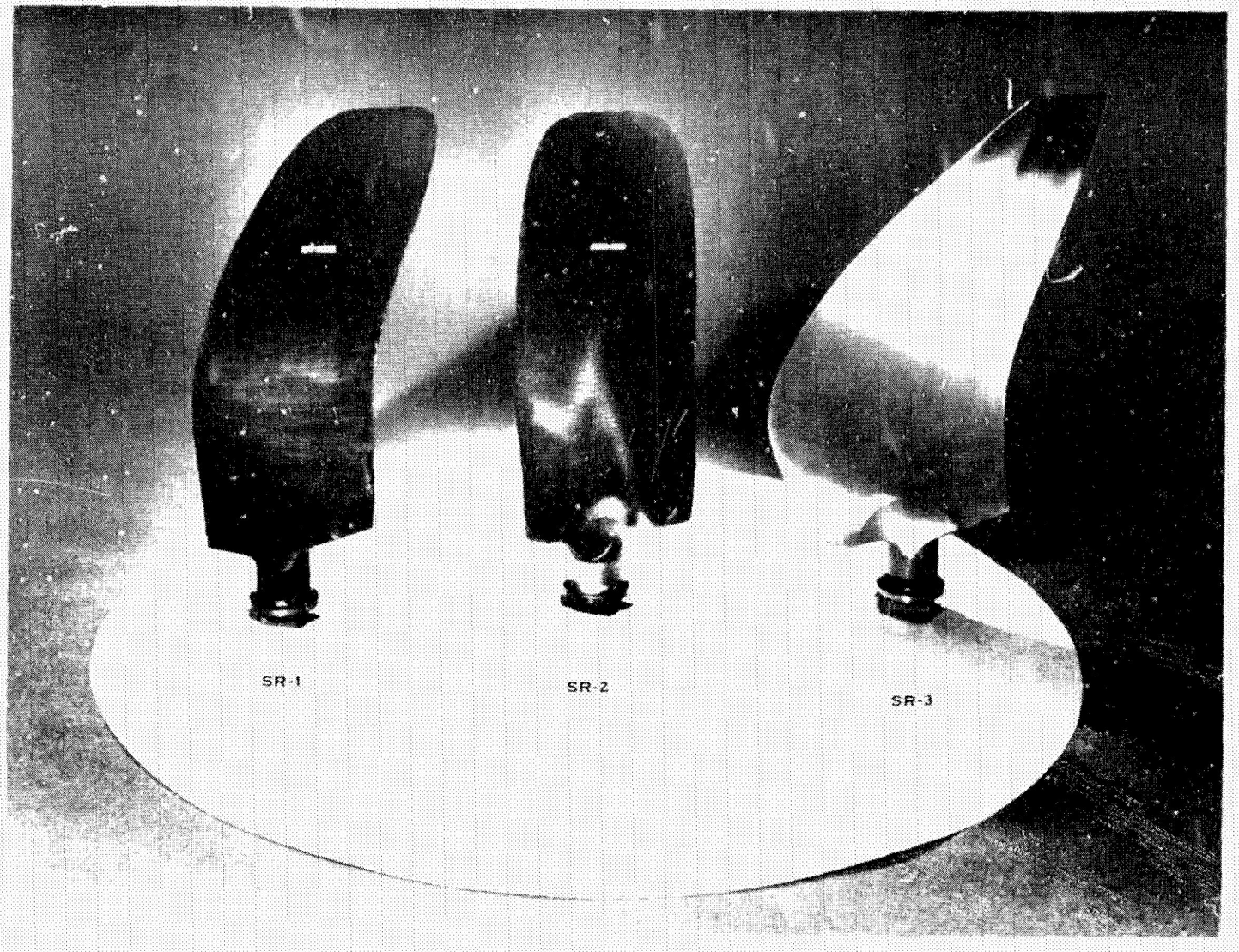

FIGURE 2-1. PROP-FAN MODEL BLADE CONFIGURATIONS

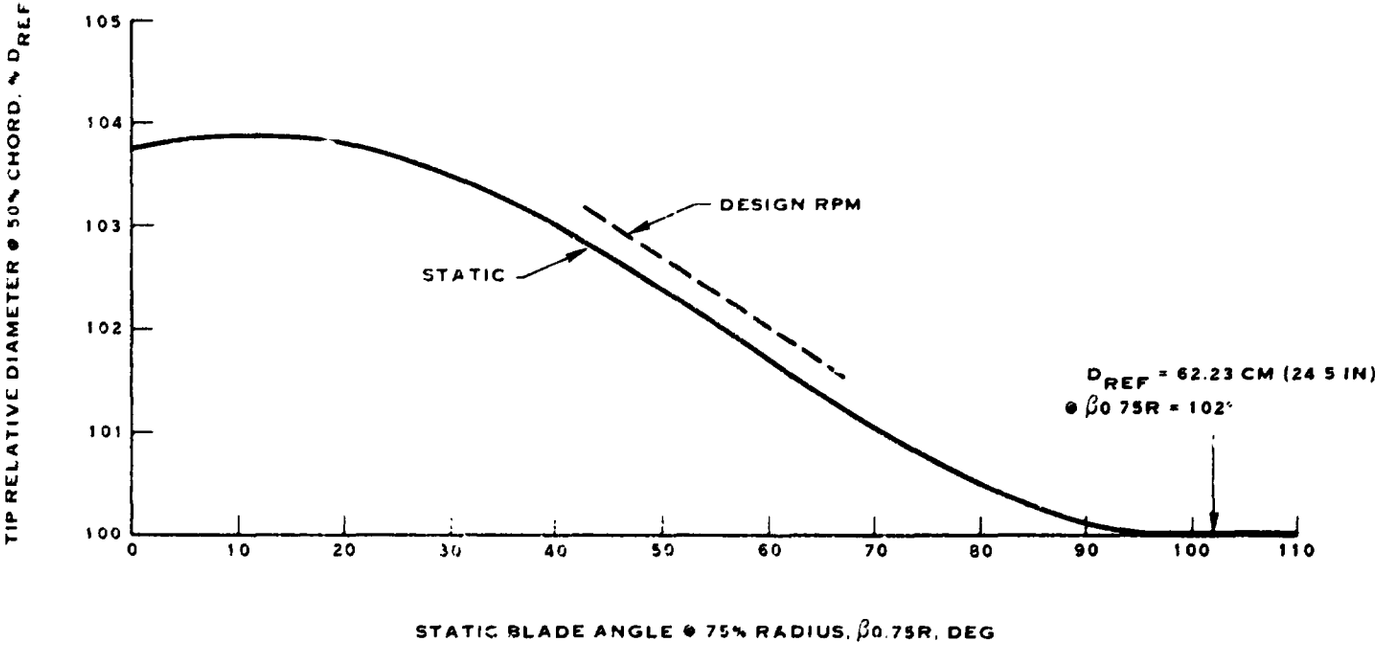

FIGURE 2-2. VARIATION OF TIP RELATIVE DIAMETER WITH BLADE ANGLE FOR SR-3 MODEL

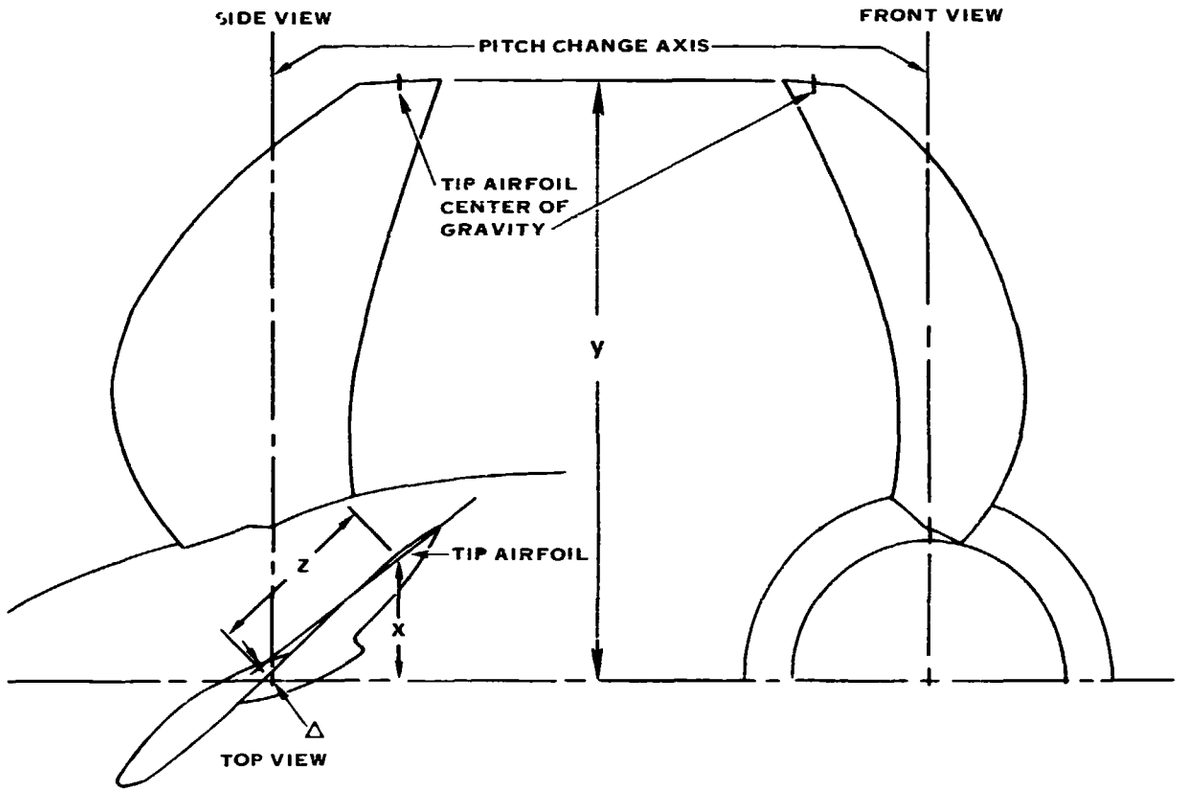

FIGURE 2-3. THREE VIEW SKETCH OF SR-3 SHOWING RELATIVE LOCATION OF TIP AIRFOIL AND PITCH CHANGE AXIS

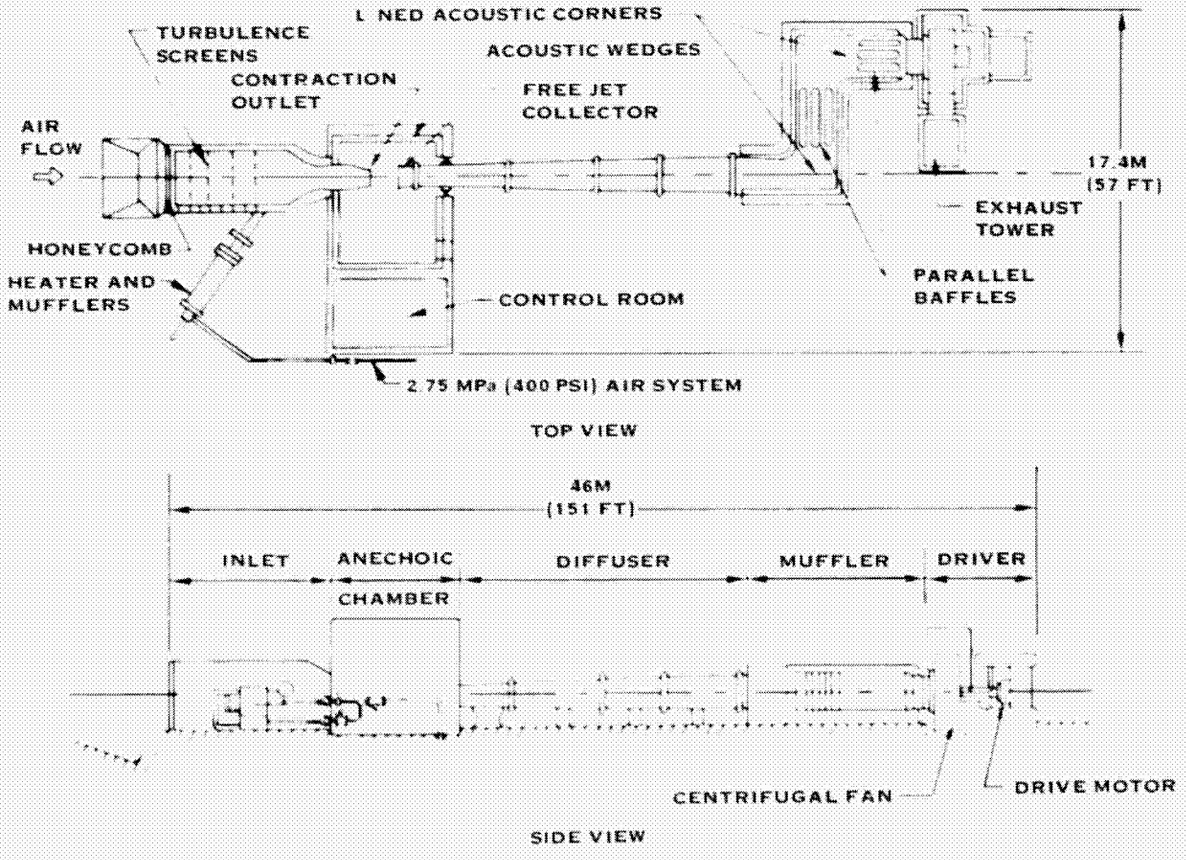

FIGURE 2-4. UTRC ACCOUSTIC RESEARCH TUNNEL

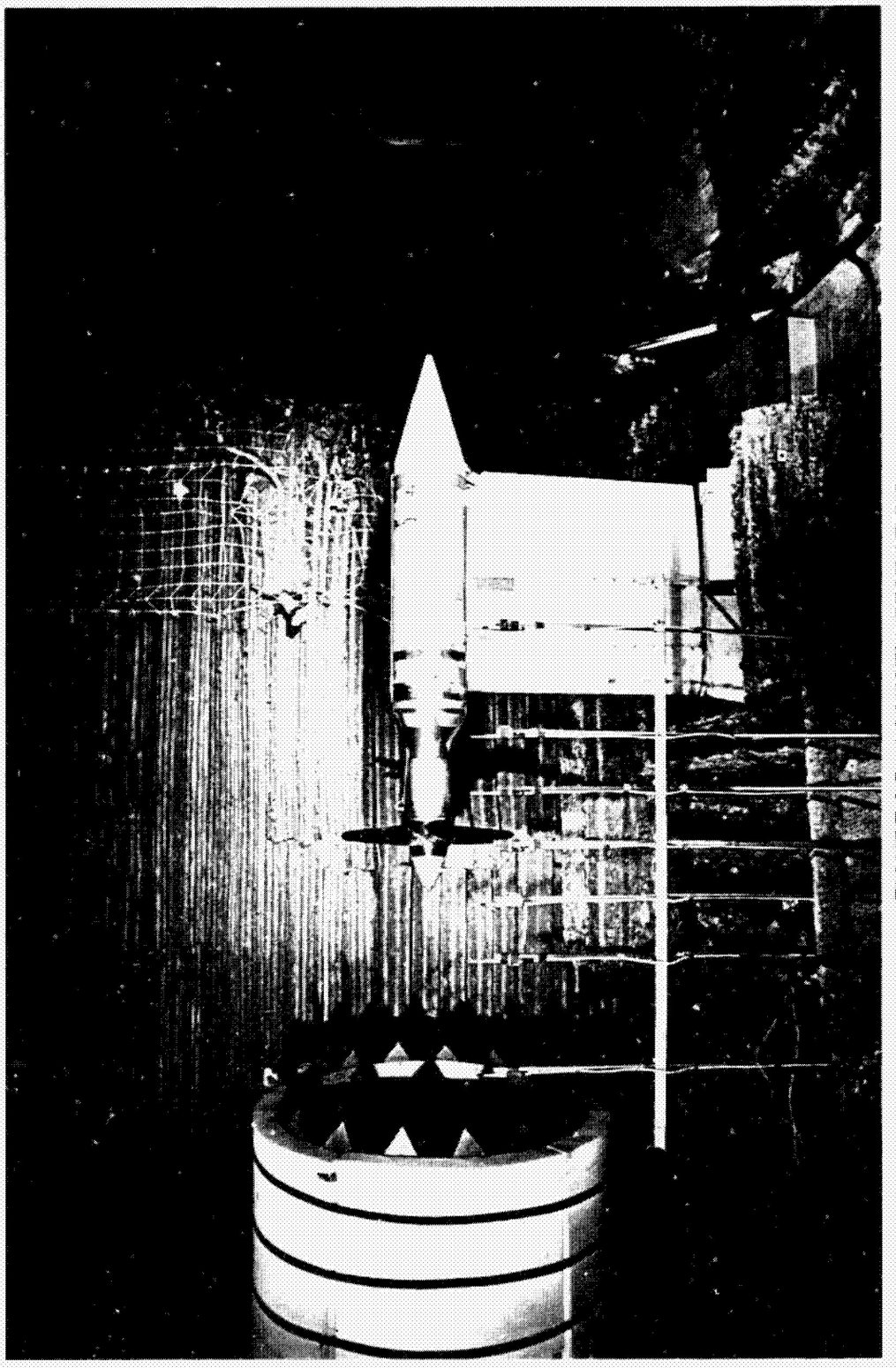

FIGURE 2-5. ACOUSTIC TEST SETUP

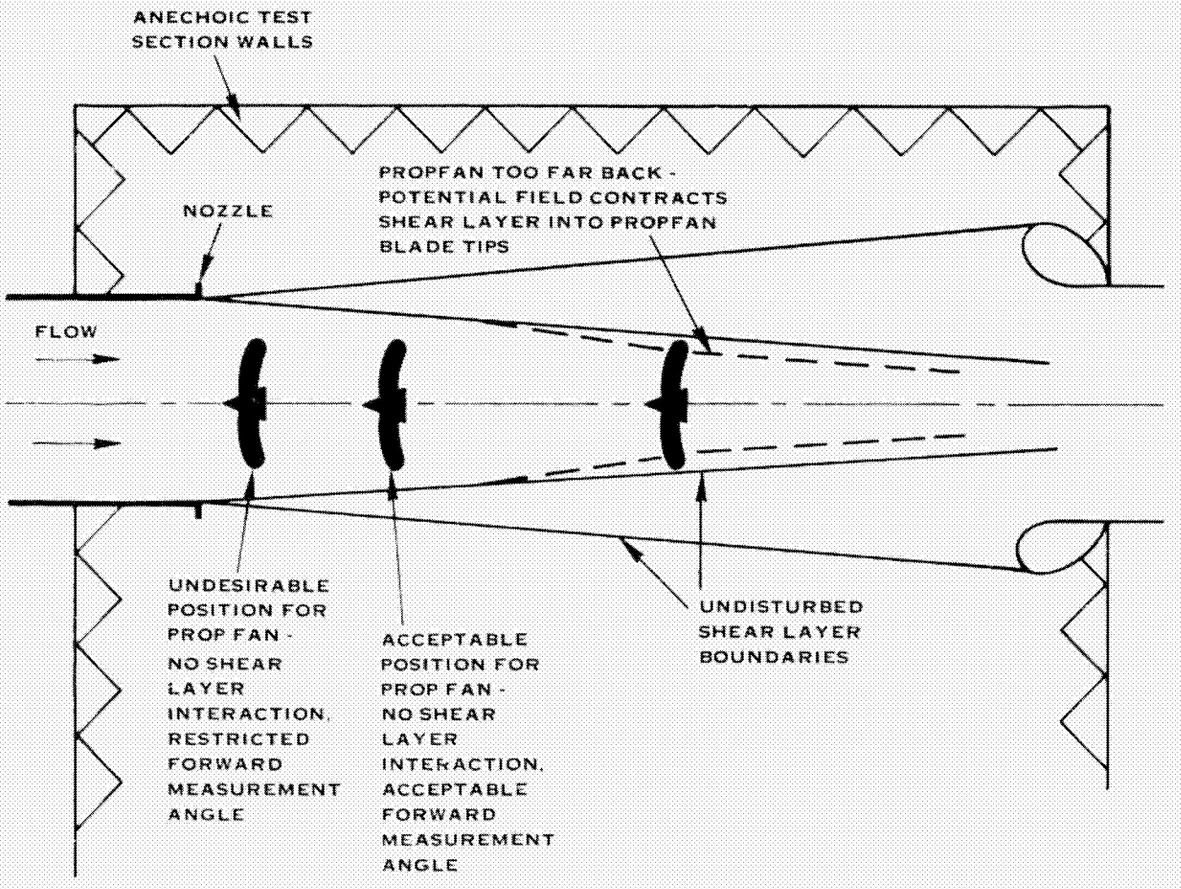

FIGURE 2-6. PROP-FAN BLADE TIP/SHEAR LAYER INTERACTION

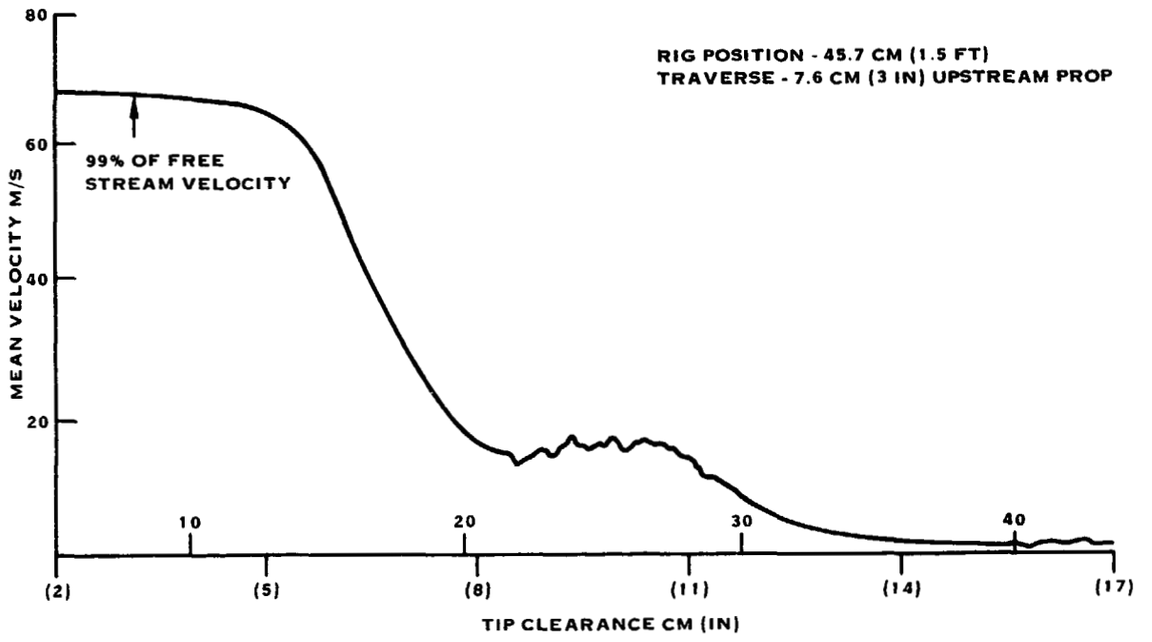

FIGURE 2-7. MEAN VELOCITY TRAVERSE

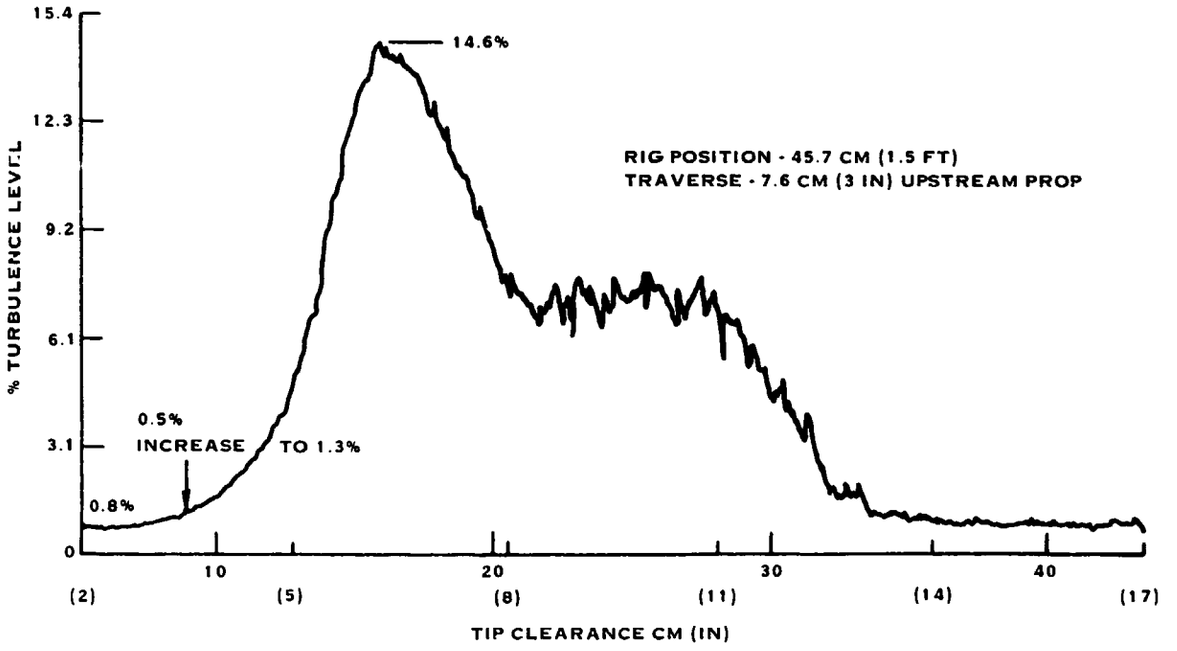

FIGURE 2-8. AXIAL TURBULENCE COMPONENT TRAVERSE

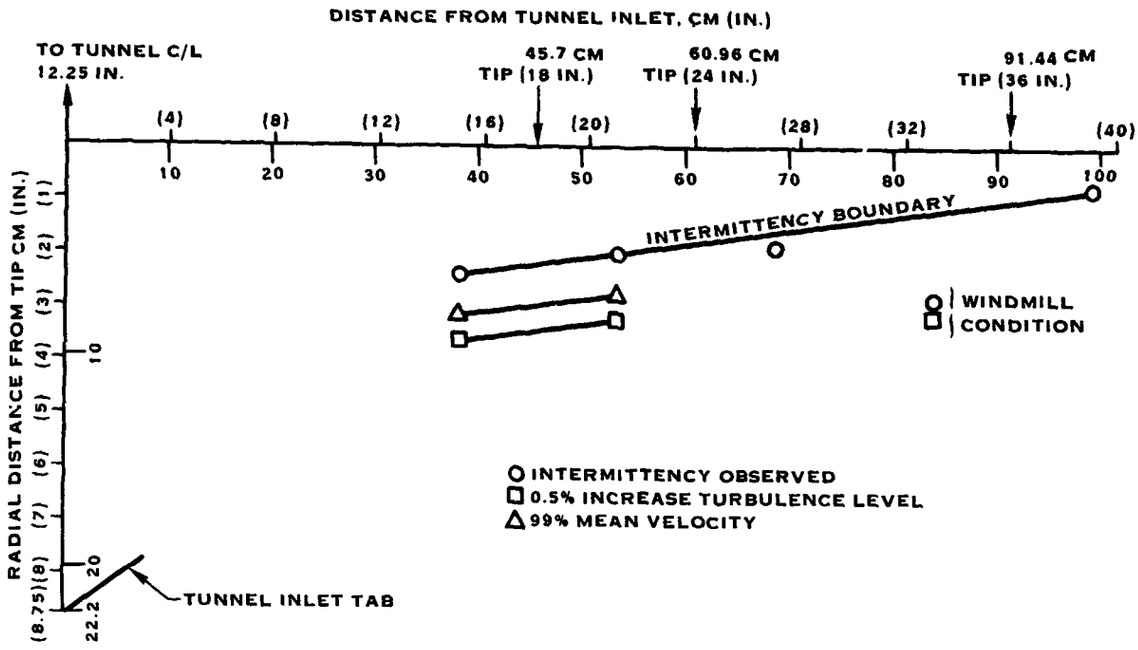

FIGURE 2-9. SHEAR LAYER STUDY SUMMARY

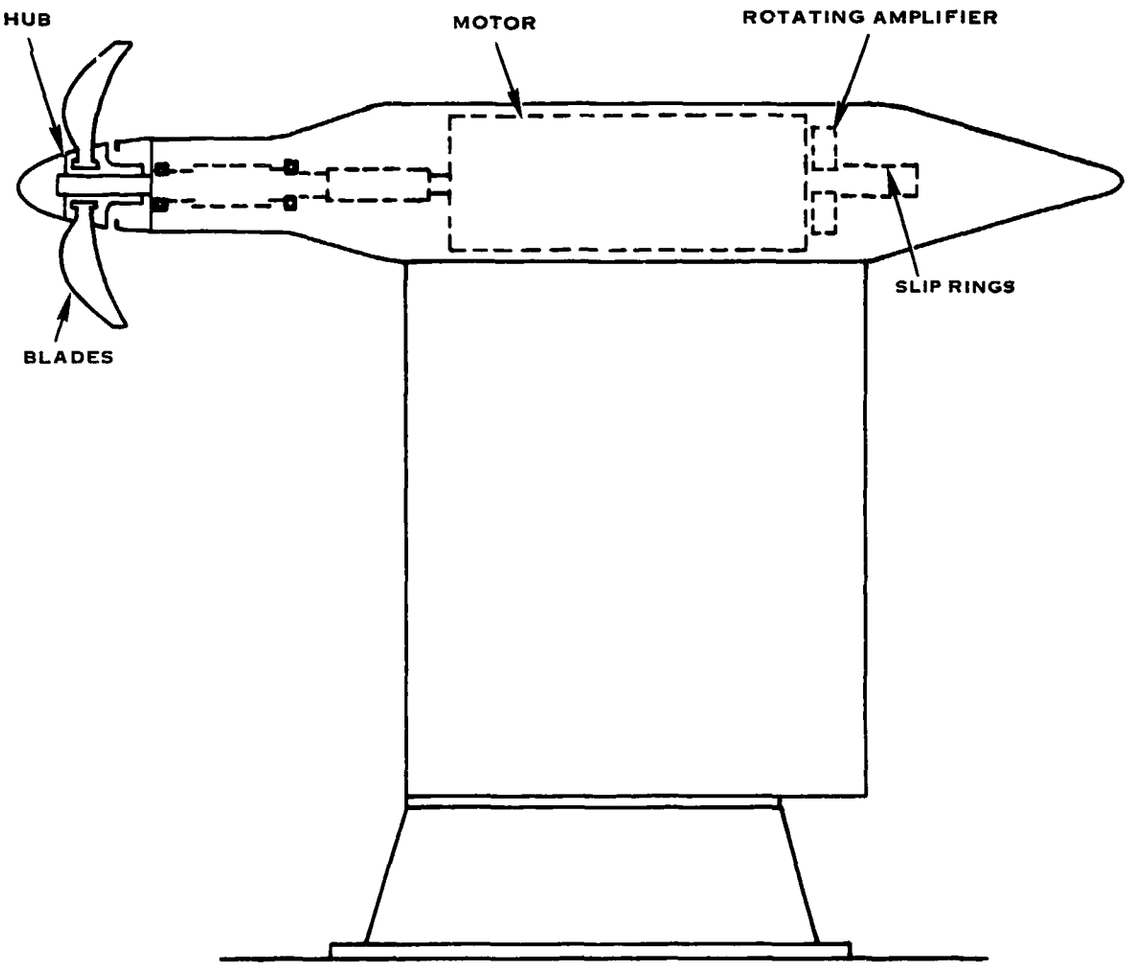

FIGURE 2-10. UTRC 112 KW (150 HP) DRIVE

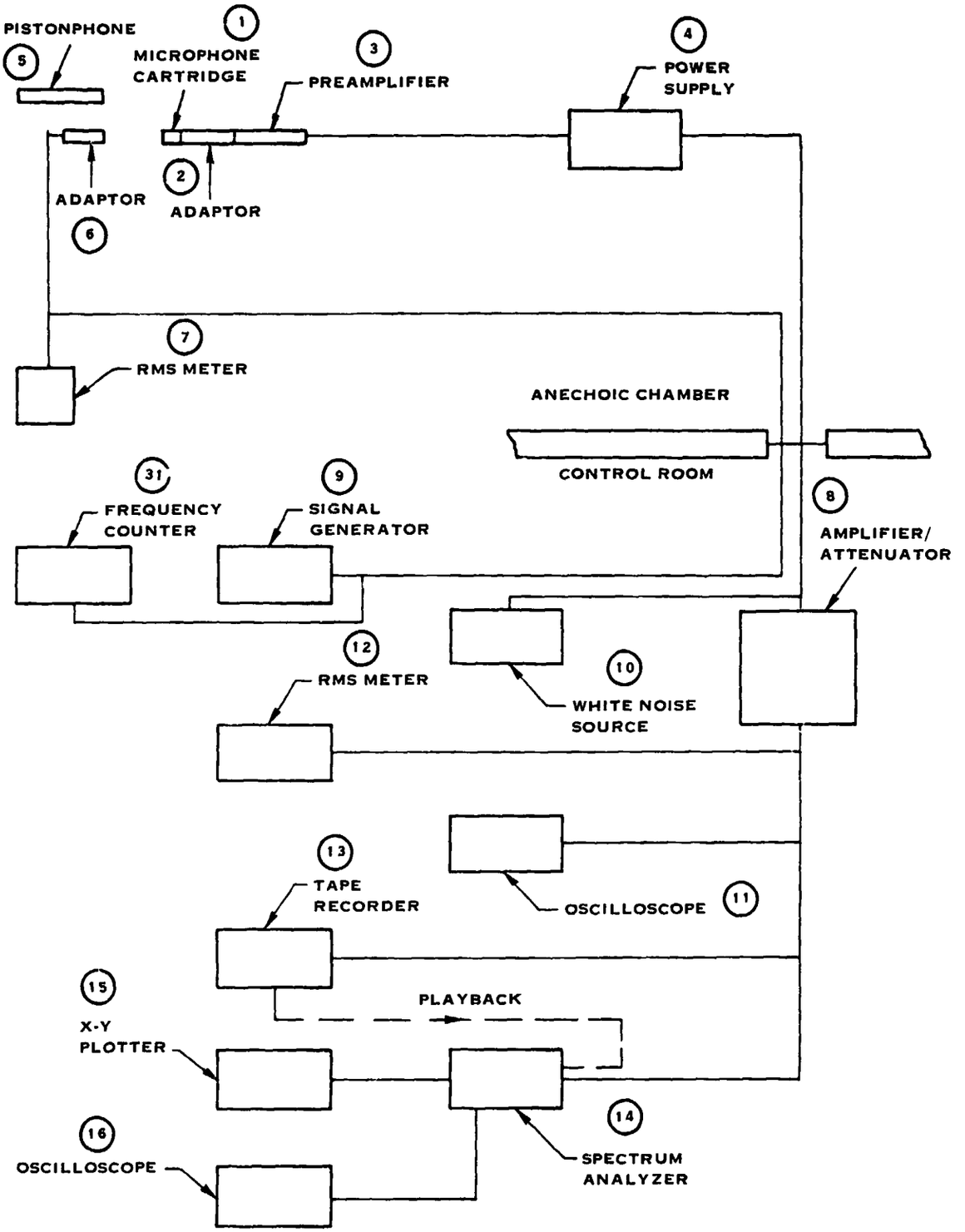

FIGURE 2-11. ACOUSTIC DATA ACQUISITION SYSTEM

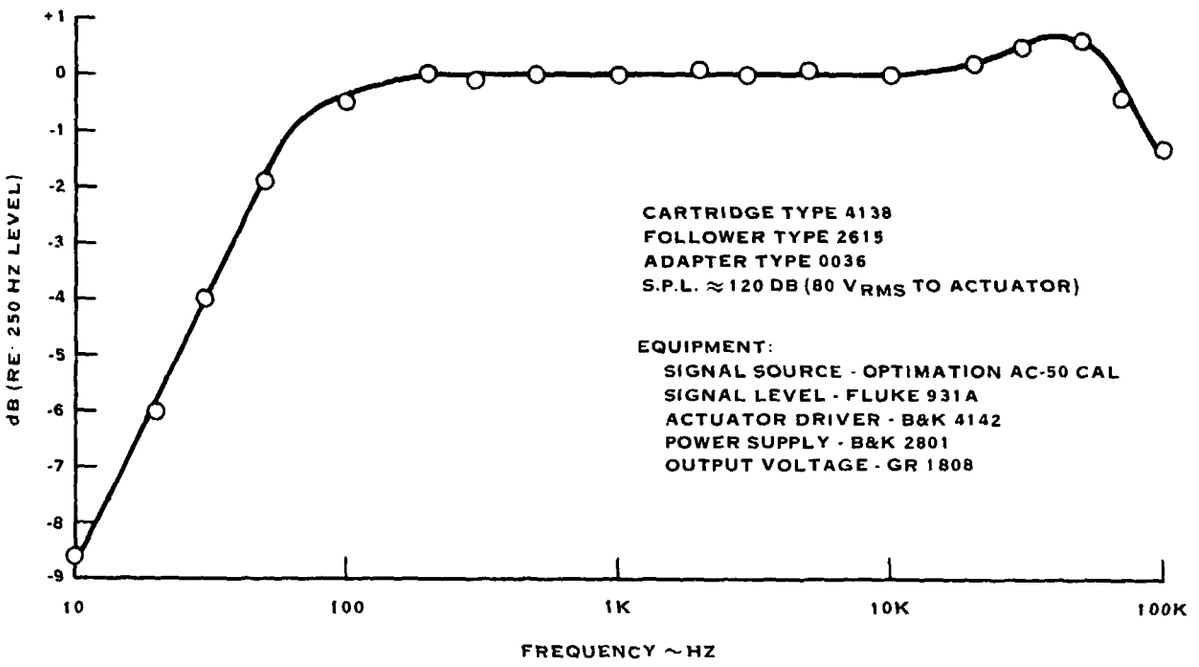

FIGURE 2-12. MICROPHONE FREQUENCY RESPONSE BY ELECTROSTATIC ACTUATOR METHOD

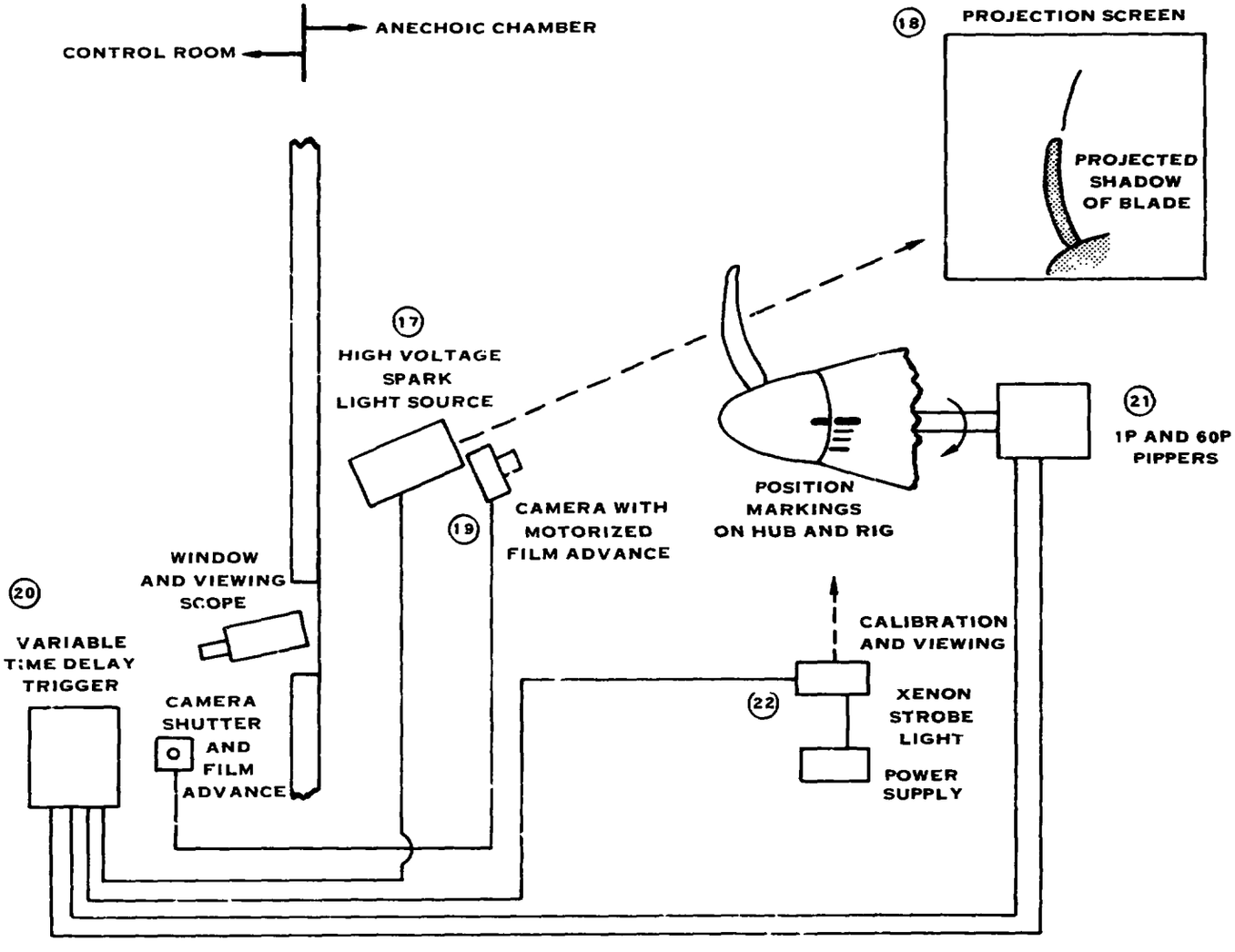

FIGURE 2-13. SHADOWGRAPH INSTRUMENTATION

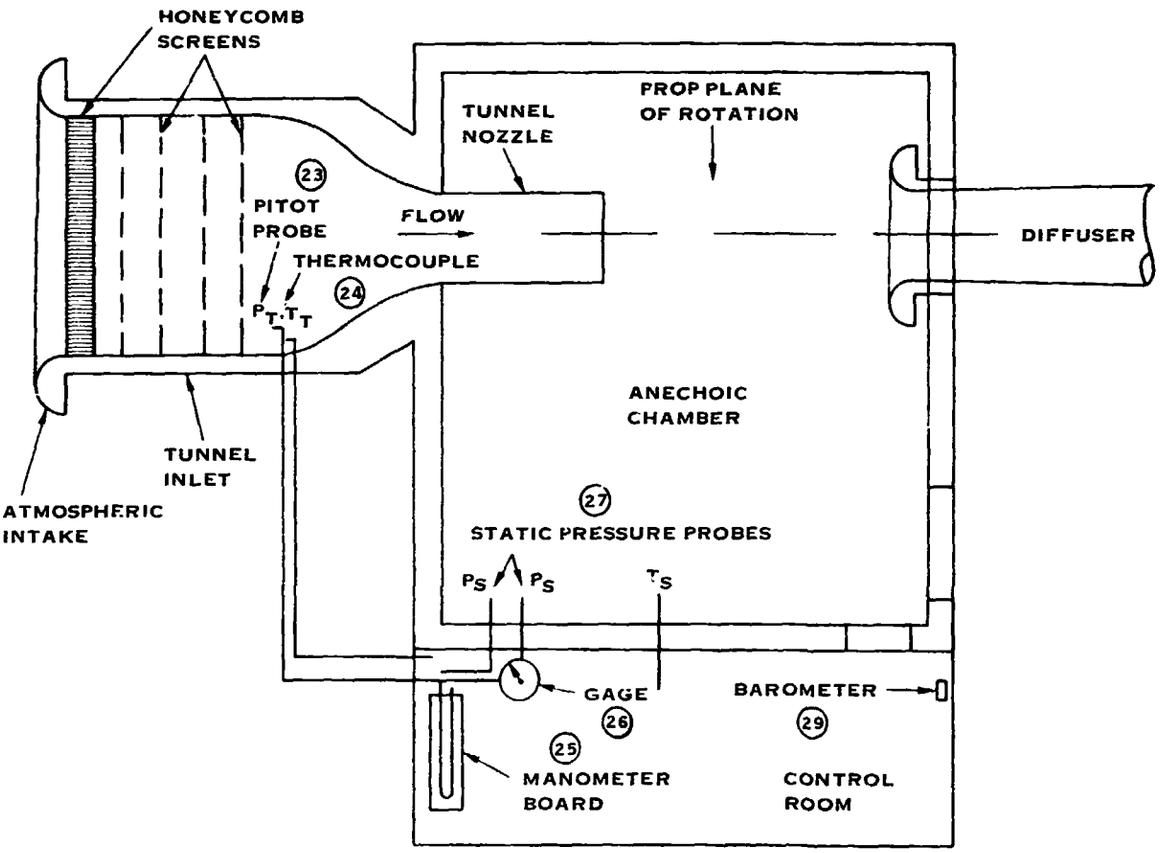

FIGURE 2-14. UTRC ACOUSTIC RESEARCH TUNNEL SPEED MEASUREMENT SYSTEM

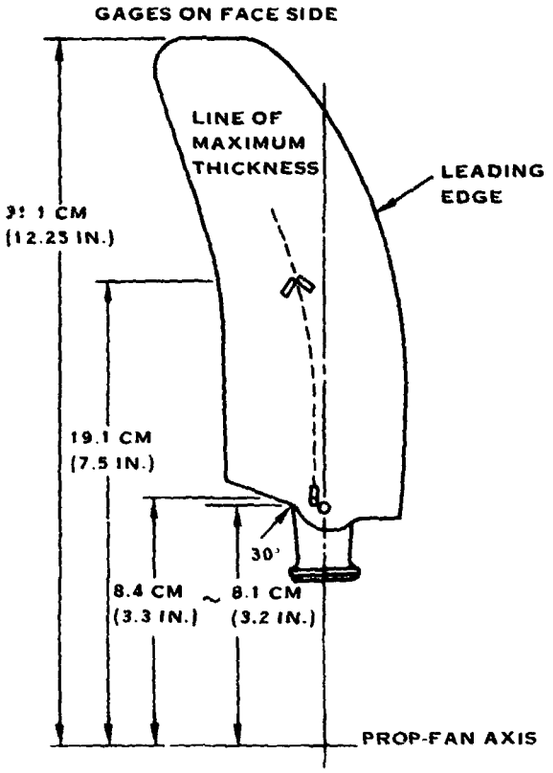

FIGURE 2-15. SR-1 BLADE STRAIN GAGE LOCATIONS

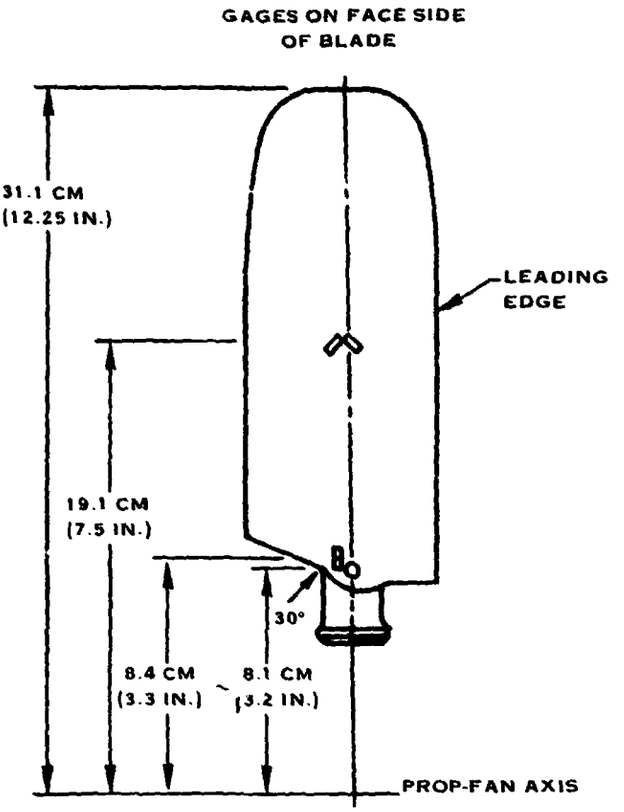

FIGURE 2-16. SR-2 BLADE STRAIN GAGE LOCATIONS

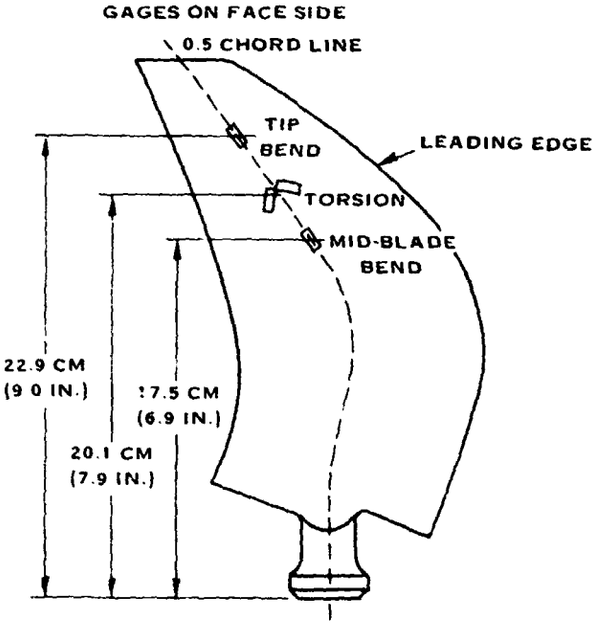

FIGURE 2-17. SR-3 BLADE STRAIN GAGE LOCATIONS

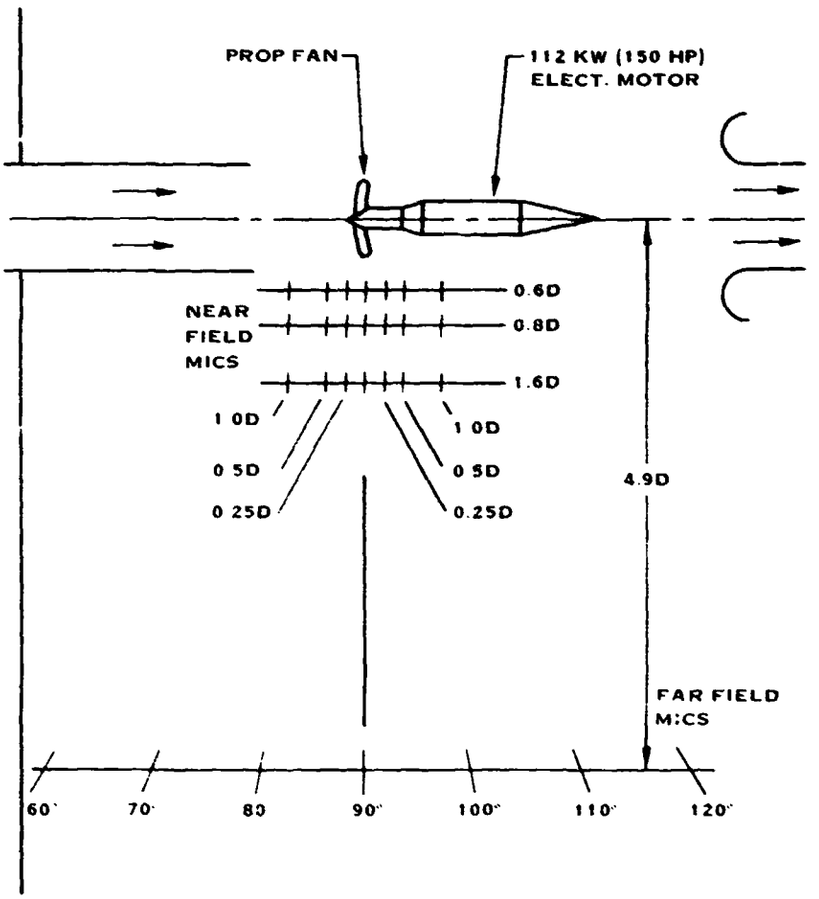

FIGURE 2-18. PROP-FAN ACOUSTIC TEST MICROPHONE LOCATIONS PLAN VIEW

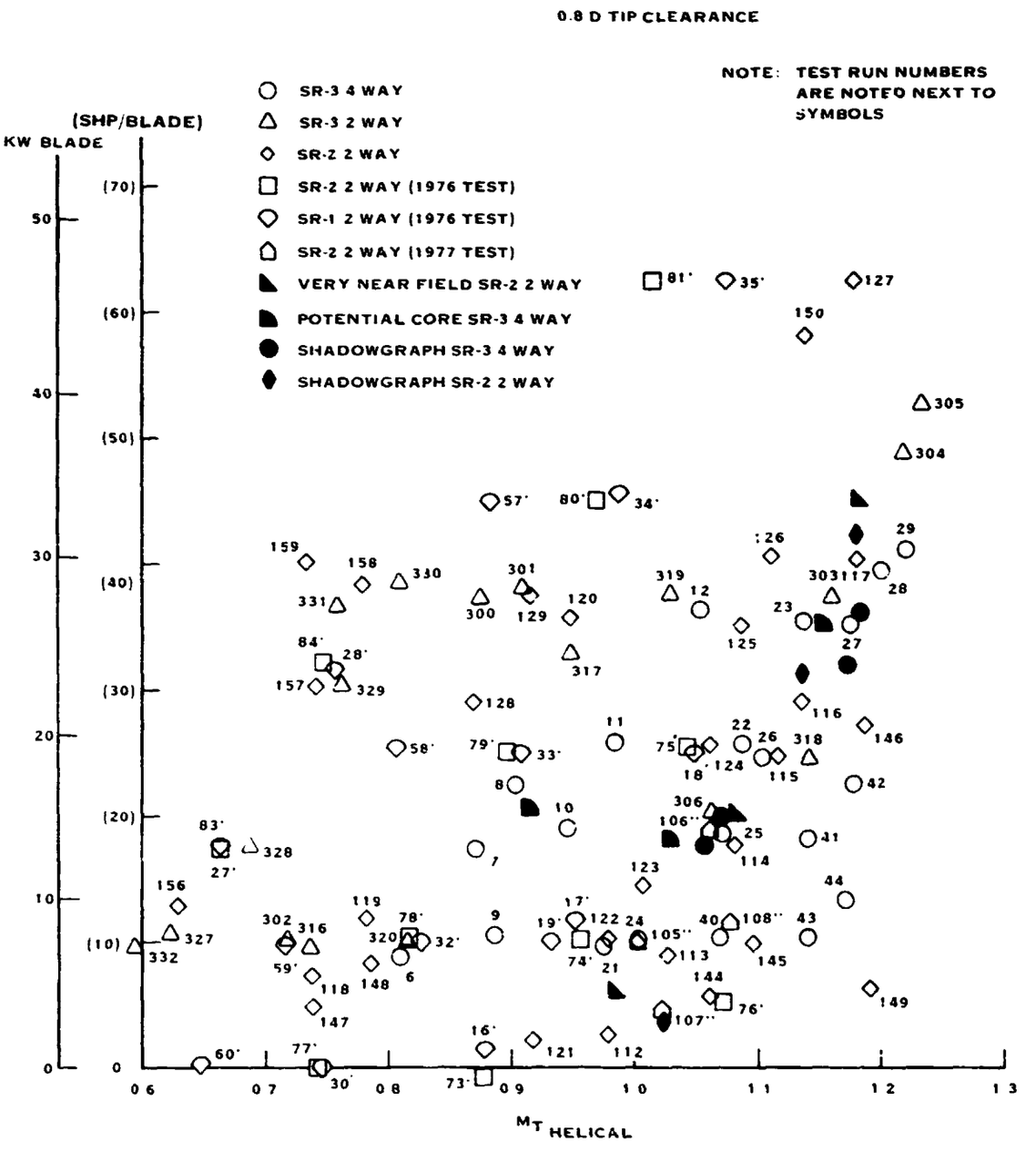

FIGURE 2-19. PROP-FAN ACOUSTIC TEST CONDITIONS WITH TWO OR FOUR BLADES INSTALLED

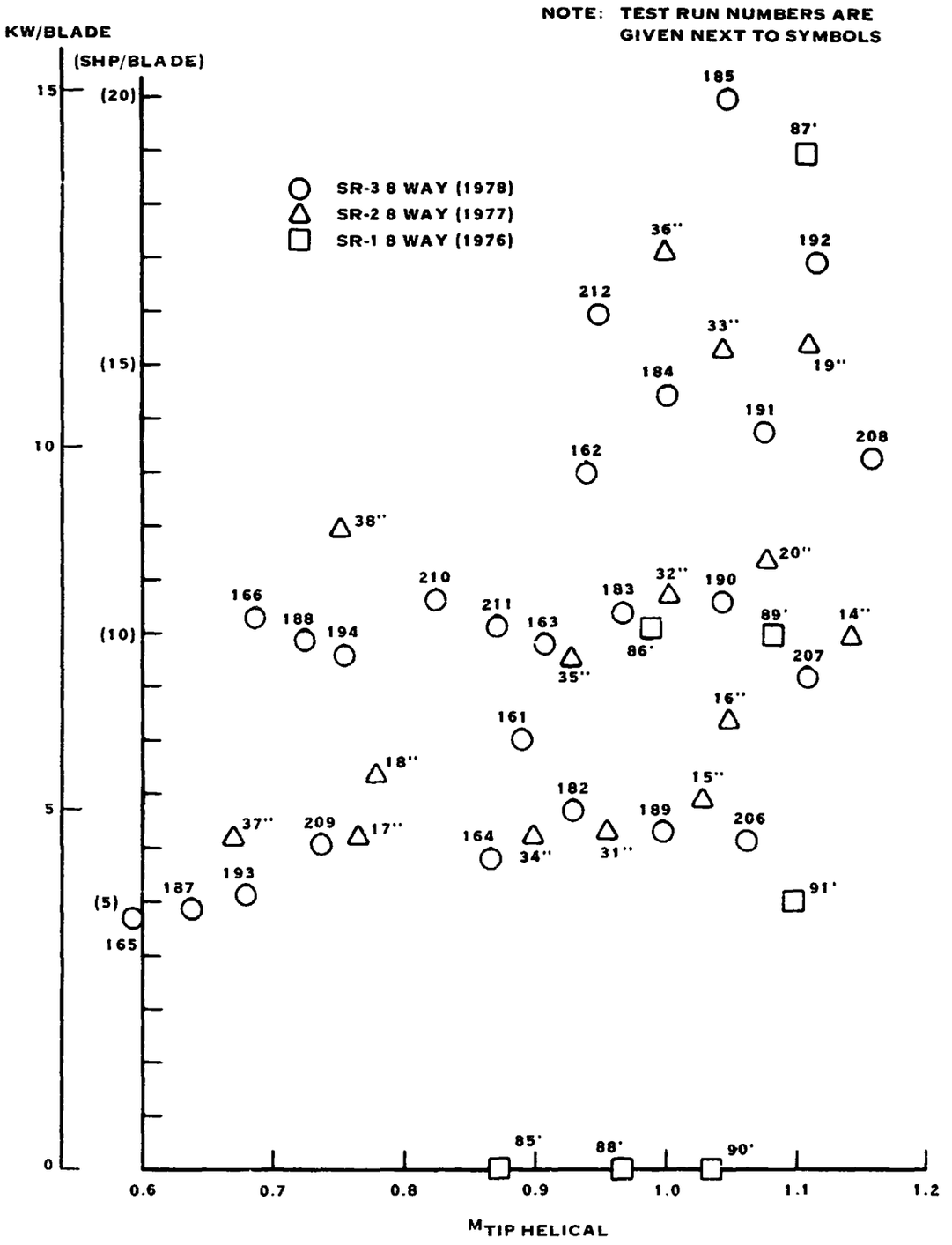

FIGURE 2-20. PROP-FAN ACOUSTIC TEST CONDITIONS WITH EIGHT BLADES INSTALLED

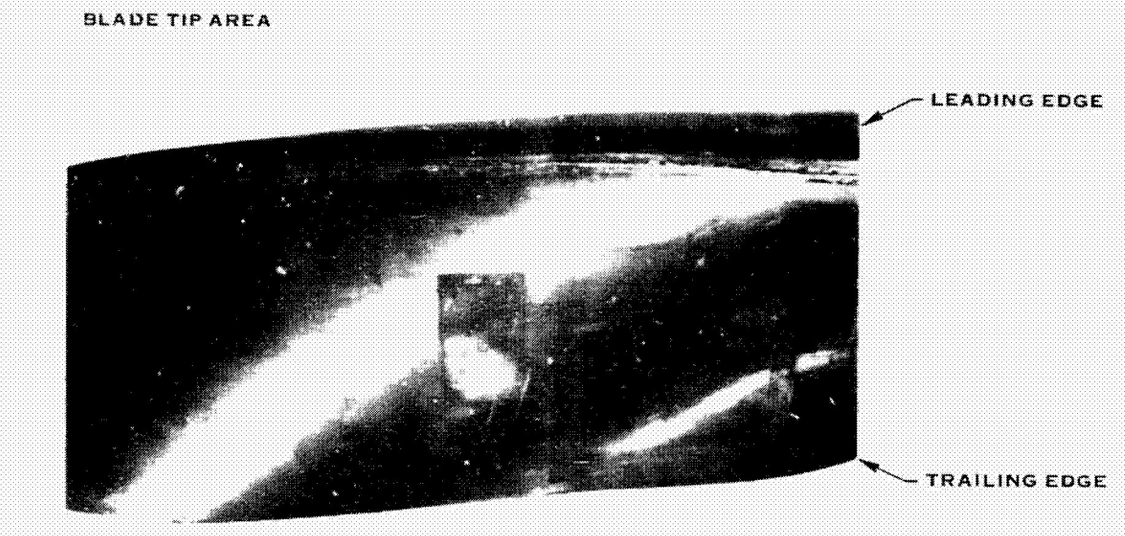

A) BOUNDARY LAYER TRIPWIRE INSTALLED ON SR-2 MODEL BLADE

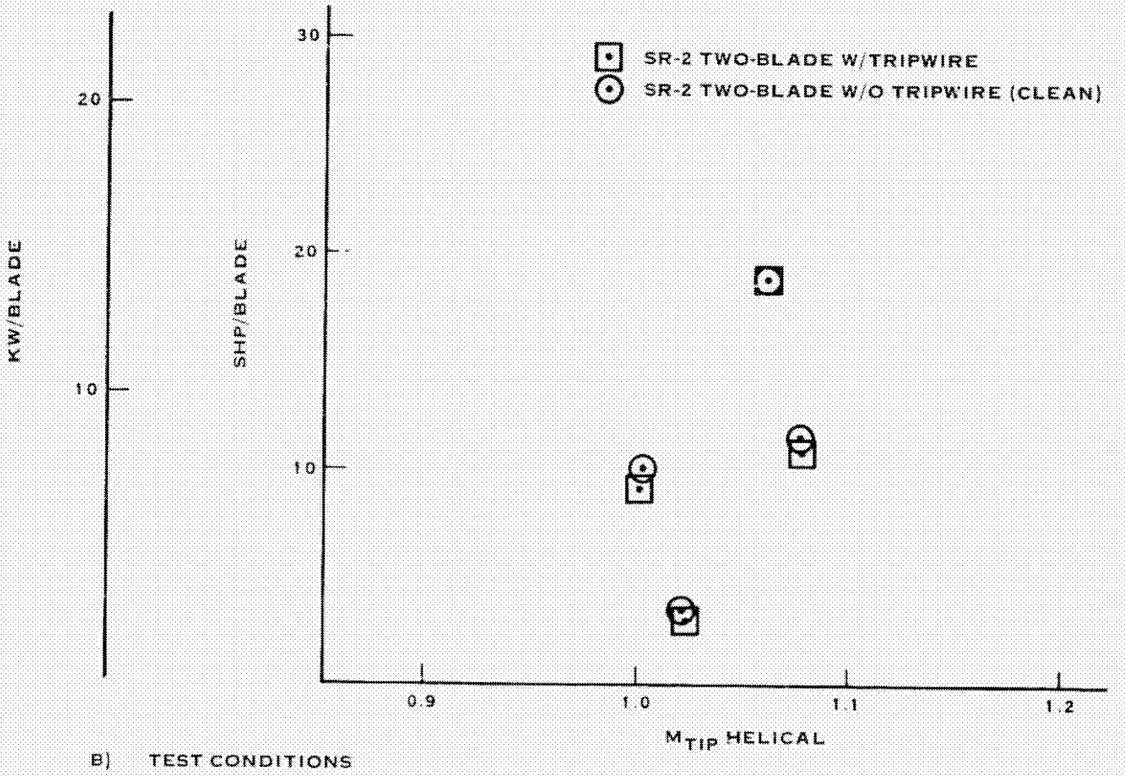

B) TEST CONDITIONS

FIGURE 2-21. BOUNDARY LAYER TRIP ACOUSTIC TEST

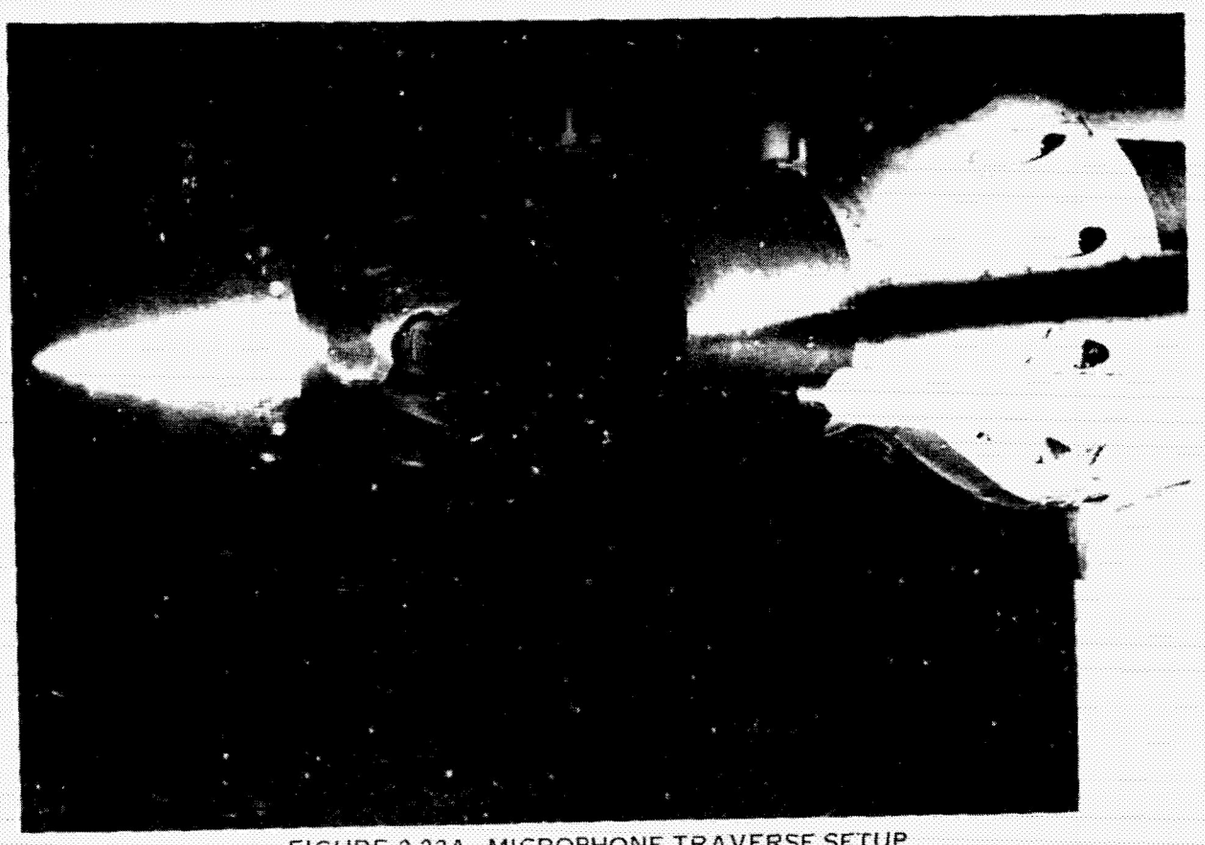

FIGURE 2-22A. MICROPHONE TRAVERSE SETUP

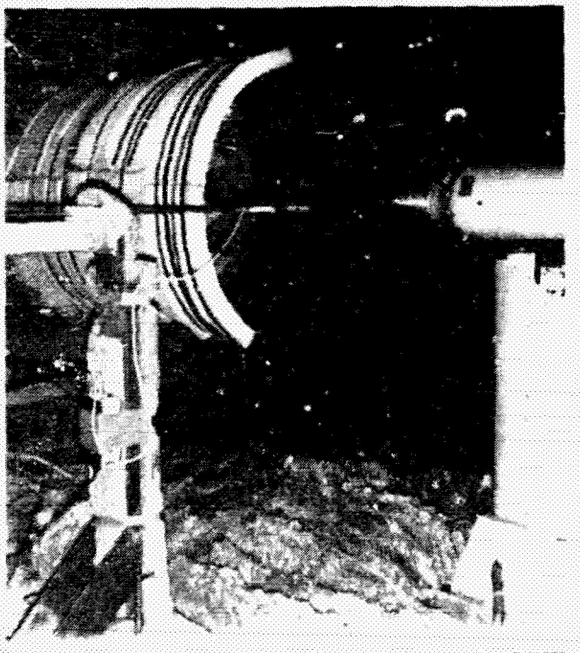

FIGURE 2-22B. MICROPHONE TRAVERSE SETUP

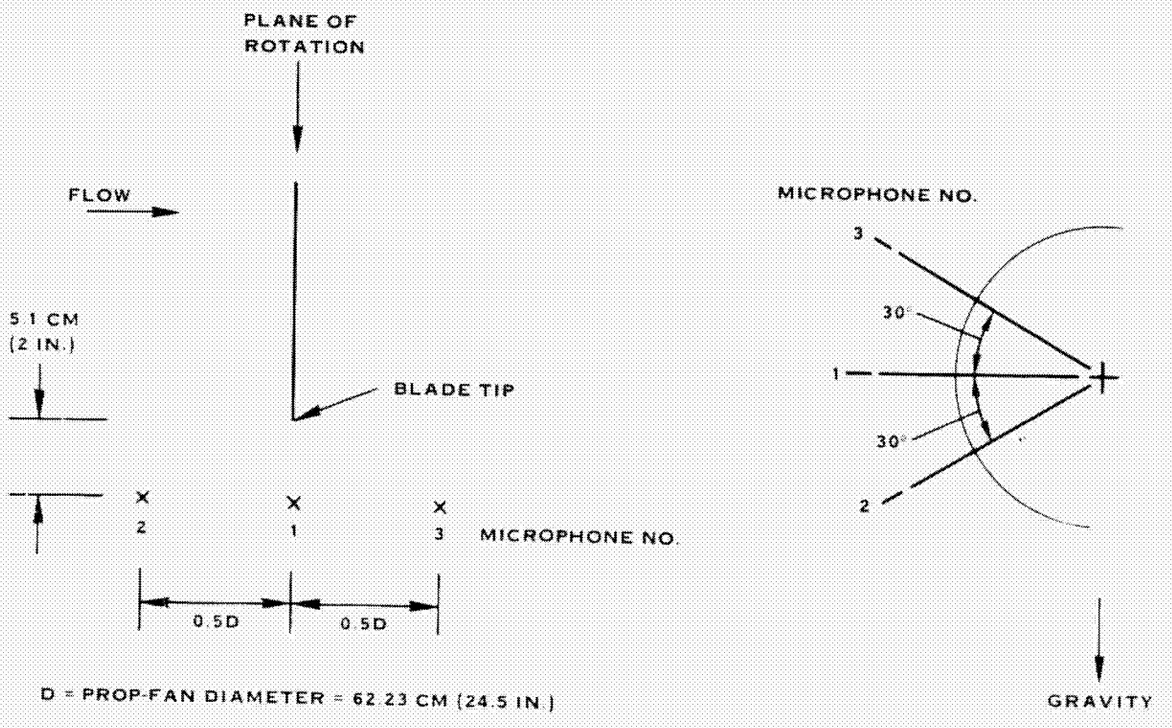

FIGURE 2-23A. NEAR FIELD MICROPHONE LOCATIONS (INSIDE POTENTIAL CORE)

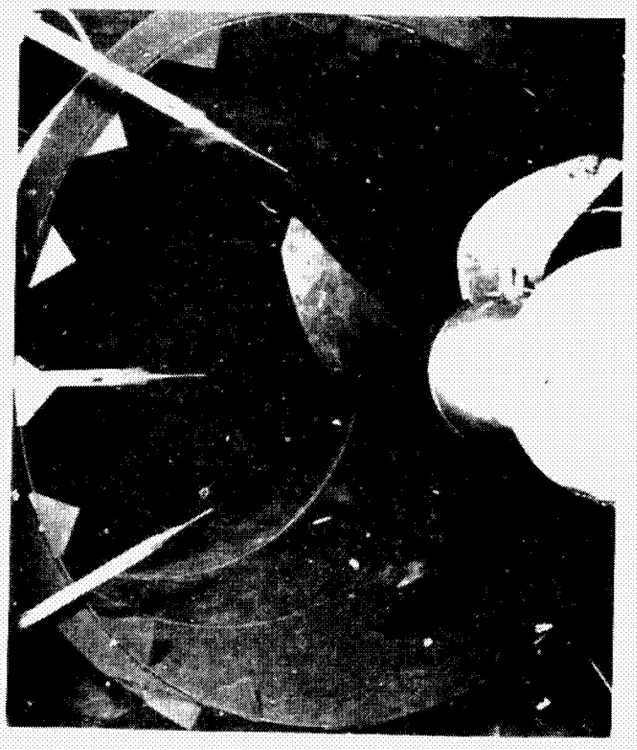

FIGURE 2-23B. NEAR FIELD (INSIDE POTENTIAL CORE) MICROPHONE TEST SET-UP

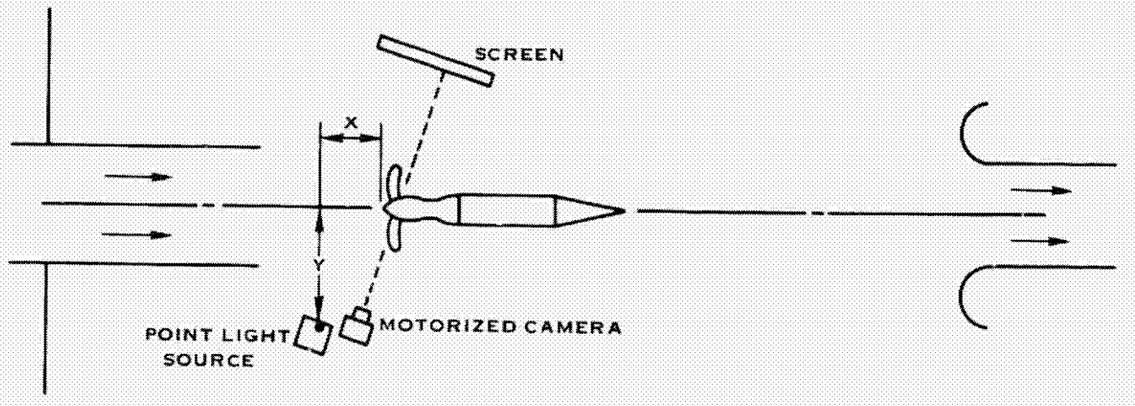

PLAN VIEW

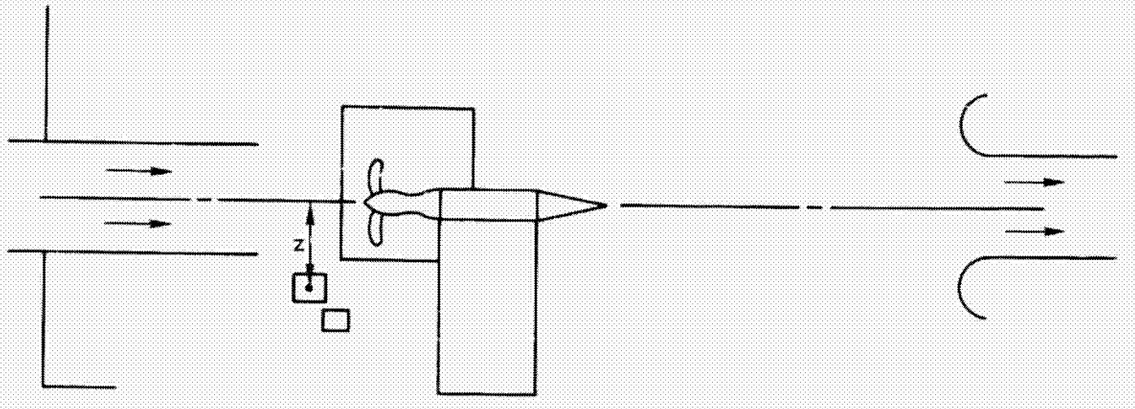

SIDE VIEW

DISTANCES TO POINT LIGHT SOURCE CM (IN)

	X	Y	Z	DISTANCE TO SCREEN
SR-2 PLANFORM	65.6 (26-1/4)	67.7 (26-5/8)	11.7 (4-5/8)	223.5 (88)
SR-3 PLANFORM	63.1 (24-13/16)	67.9 (26-3/4)	44.5 (17-1/2)	228.0 (89-3/4)
SR-3 EDGEWISE	12.7 (5)	86.7 (34-1/8)	-25.4 (-10)	212.7 (83-3/4)

Z POSITIVE BELOW PROP FAN AXIS

FIGURE 2-24. SHADOWGRAPH TEST SET-UP

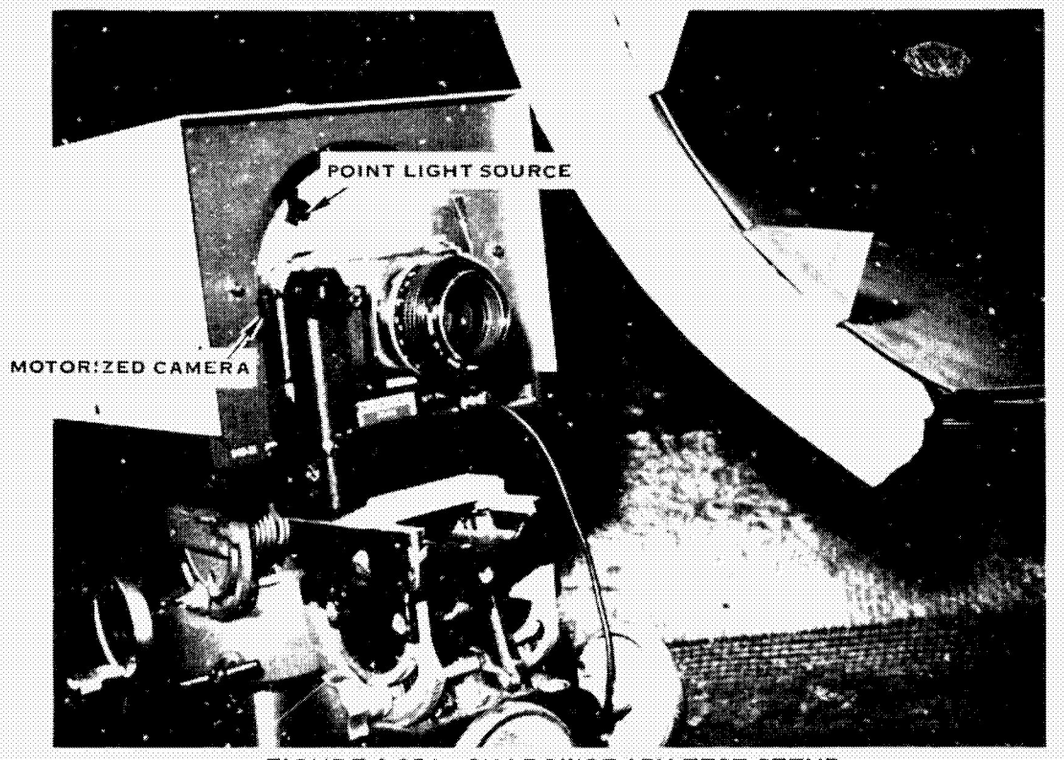

FIGURE 2-25A. SHADOWGRAPH TEST SETUP

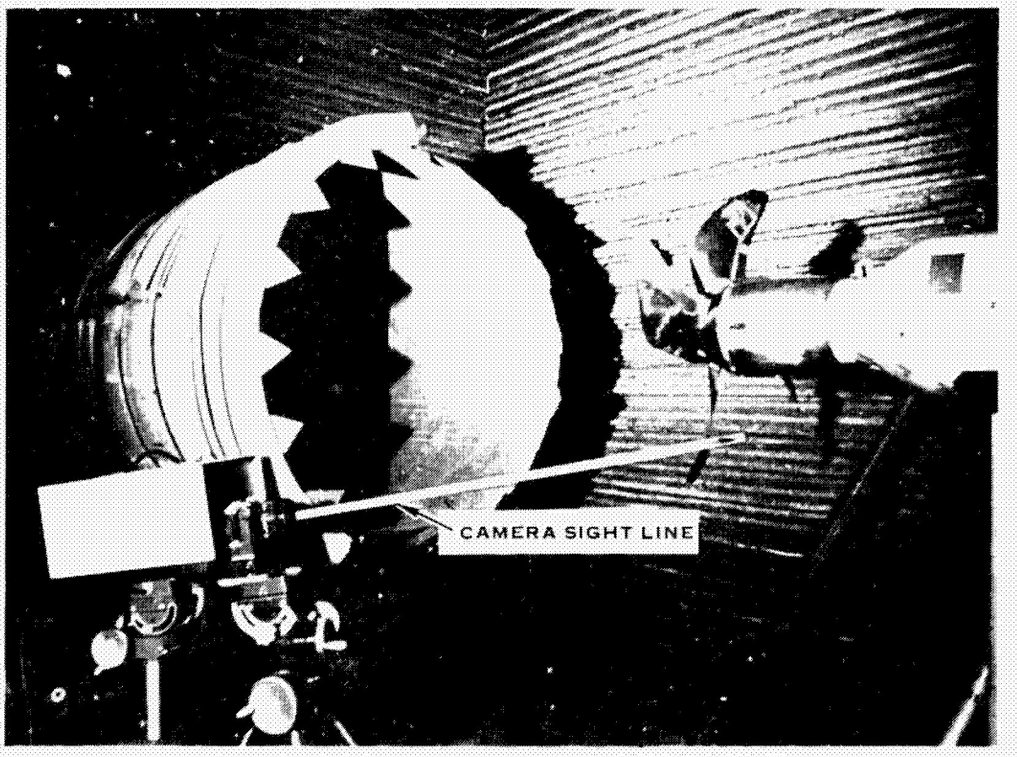

FIGURE 2-25B. SHADOWGRAPH TEST SETUP

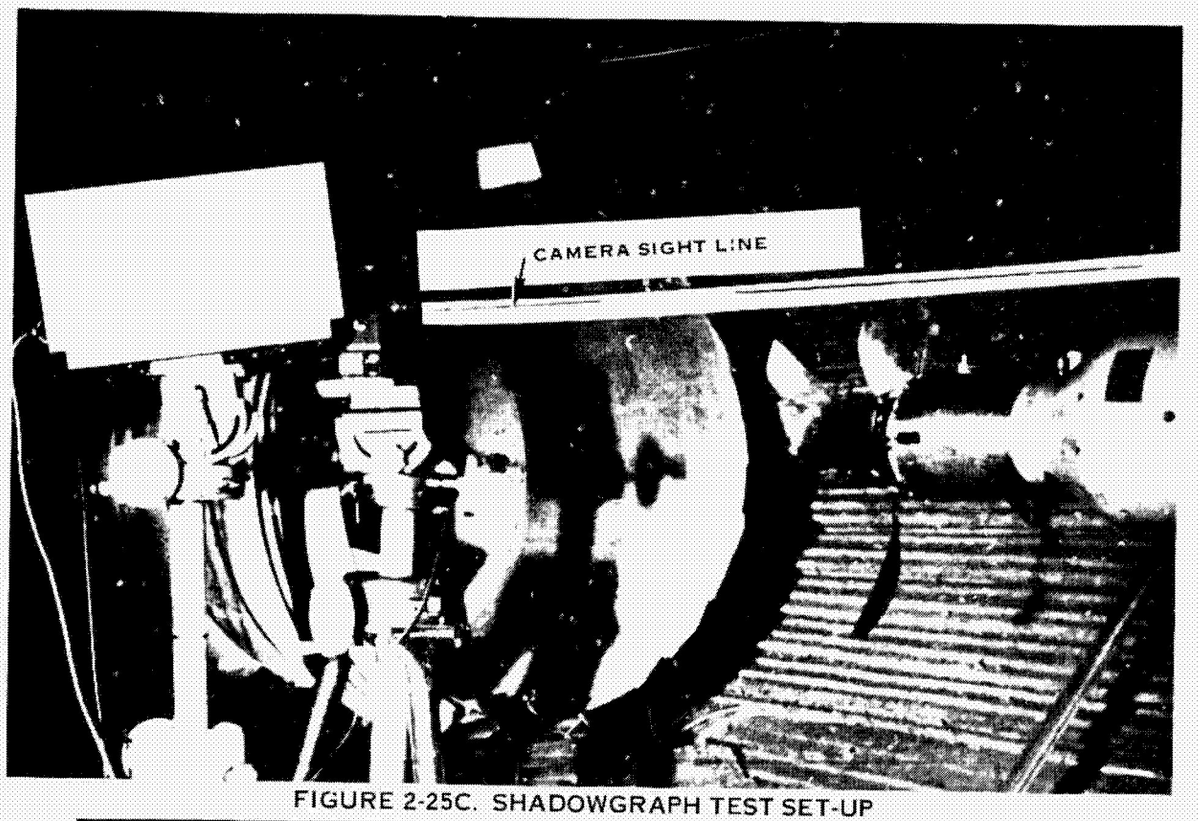

FIGURE 2-25C. SHADOWGRAPH TEST SET-UP

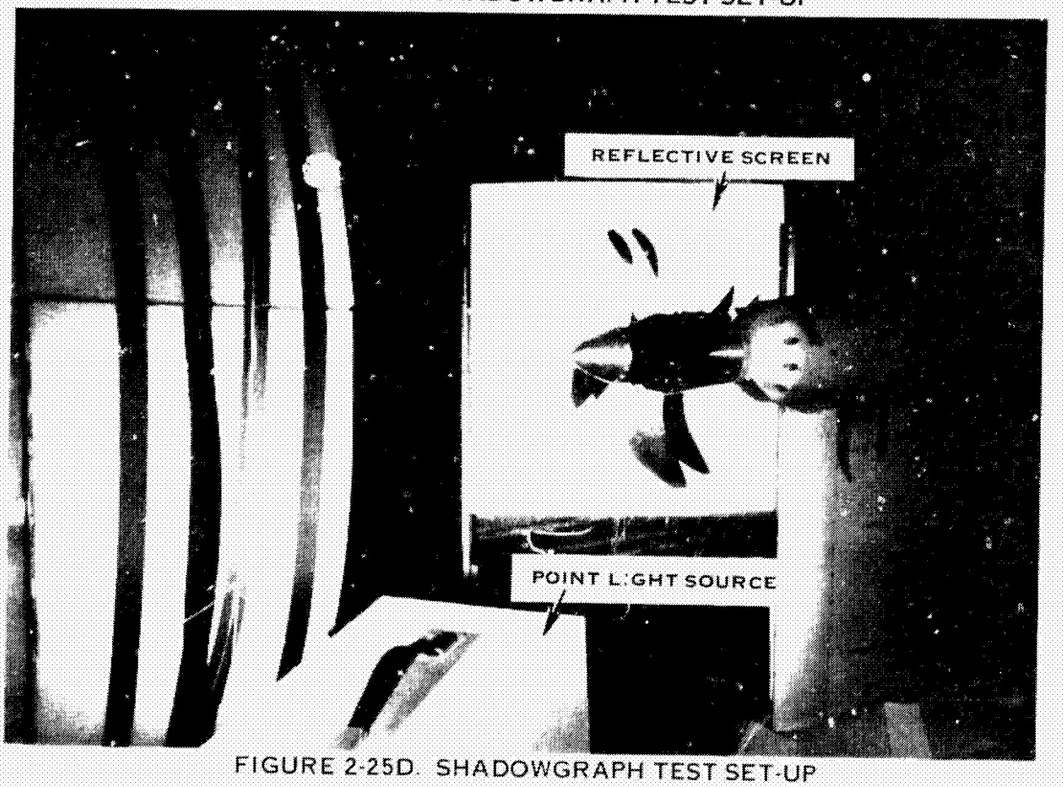

FIGURE 2-25D. SHADOWGRAPH TEST SET-UP

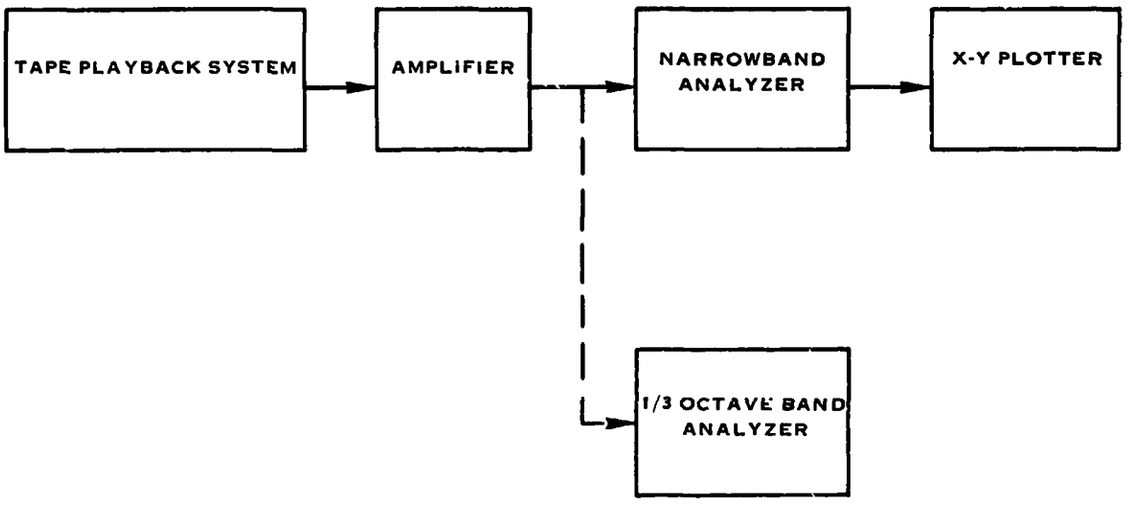

ITEM	MANUFACTURER	MANUFACTURER'S DESIGNATION
TAPE PLAYBACK	AMPEX	FR1900
AMPLIFIER	HSD	–
NARROWBAND ANALYZER	SPECTRAL DYNAMICS	SD301D
1/3 OCTAVE BAND ANALYZER	GENERAL RADIO	1921
X-Y PLOTTER	MOSELY	7030 AR

FIGURE 2-26. DATA REDUCTION SYSTEM

SECTION 3
RESULTS AND DISCUSSION

Analysis of Test Data

Background Noise

The background noise in the Acoustic Research Tunnel was measured during operation of the tunnel, all instrumentation and the PDR using a dummy hub without blades. Typical narrow band background noise sound pressure level spectra are shown in Figure 3-1. The top spectrum represents data taken at a microphone location corresponding to the prop-fan plane of rotation at 0.8 D (nominal) tip clearance during model acoustic testing. Note that the low frequency flow noise drops below 100 dB (re: 20μPa) at frequencies greater than 200 Hz. In the frequency range of the first few blade passage harmonics of a two-blade model (<2000 Hz) the ambient noise level is on the order of 90 dB. At higher frequencies it drops even lower. The level of background noise is sufficiently below harmonic tone and broadband levels that it does not influence analysis of the prop-fan model acoustic data. A sound pressure level spectrum of background noise at the far field position in the plane of rotation is shown in Figure 3-1B.

Shear Layer Effects

Calculation of Corrections for Shear Layer Refraction - The test facility which was used for this investigation is an open jet wind tunnel. Thus, there is a shear layer which appears between the tunnel jet freestream and the quiescent air in the anechoic chamber. An acoustic wave propagating from the moving stream to the still air will be refracted to a degree that depends upon both the speed of the tunnel jet and the location of the source. This will alter the sound levels and directivities measured in the chamber from those that would be measured in the absence of a shear layer. Thus, there is a need to correct the measured data for shear layer effects. A theoretical methodology which calculates the change in acoustic propagation direction and sound level due to shear layer refraction was developed and experimentally verified by Schlinker and Amiet (Reference 3-1).

The methodology has the capability for analyzing propagation from an acoustic point source located arbitrarily within a cylindrical thin shear layer. The geometry of shear layer refraction, exaggerated for clarity, is shown in Figure 3-2. The correction method calculates the acoustic ray path and provides the correction to the sound pressure level at the microphone position. The corrected level is derived from the ratio of path lengths of the actual refracted ray and the calculated ray which would occur were there no shear layer, for listeners at constant sideline distance. The sound level is then corrected by 6 dB per doubling of distance. The corrected position of the microphone as though there were no propagation through the shear layer is also calculated.

The corrections are independent of source frequency. Since reflections are insignificant it is assumed that all of the acoustic energy incident on the shear layer is transmitted. Since the prop-fan is not a point source of sound, the shear layer correction method was used to evaluate the effect of source location on the corrected level and corrected position. The diameter of the thin cylindrical shear layer was assumed equal to the nozzle diameter in the exit plane, 1.067 m (42 in.). This was shown to be valid in Reference 3-1. The results of this study are shown in Figures 3-3 to 3-7.

Figure 3-3 shows the correction to measured sound pressure levels required to account for shear layer effects as a function of axial listener position X, normalized by the nominal prop-fan diameter 62.2 cm (24.5 in.), for the near field microphone locations at 0.8 diameter blade tip clearance. This is shown for point sources located in several positions within the shear layer. These include a point source on the tunnel axis in the prop-fan plane of rotation and sources in locations corresponding to the blade tip location at various aximuth positions as defined in Figure 3-2. The tunnel flow speed is 0.32 Mach number. The level correction required for a microphone near the plane of rotation is small regardless of source position. At the microphone location furthest up or downstream, the level correction varies significantly with source position. The level correction for a source on the tunnel axis lies between the extremes posed by blade tip sources at the 0 and 180° azimuth positions. The on-axis correction is also nearly equal to that for a blade tip source at 90° azimuth. Thus, the level correction for a source on-axis can be considered a good approximation to the mean given an arbitrary source. Similar behavior with somewhat less variation at the extremes can be seen for far field listener positions (4.4 D tip clearance) in Figure 3-4, also for 0.32 Mach number flow.

The corrected listener position at constant sideline distance, versus the measured (microphone) position is shown in Figure 3-5 for the near field microphone locations, 0.32 Mach number flow and a variety of source positions. The corrected position is the position of the microphone as though there were no shear layer refraction. The corresponding relation for far field listener positions is shown in Figure 3-6. Note first that the corrected microphone position is always downstream of the actual position. Thus, the directivity pattern measured must be shifted downstream. As before, the position correction for a source on-axis is a good mean to the corrections for extreme source locations. However, unlike the corrections for sound level, the position correction is relatively insensitive to source location, particularly in the far field.

Since the distribution of acoustic sources within the prop disk is not known, a representative source location must be chosen to establish the shear layer corrections to measured level and position to be used for data analysis. The corrections for the on-axis source were shown to be good mean approximations to corrections for an arbitrary source on the prop-fan disk. Thus, these will be used for this study. The corrections for microphone locations are listed in Table 3-I. The level correction in

dB is directly added to the measured level to arrive at the corrected level at the actual microphone location. The corrected microphone axial position at constant sideline distance is given normalized by prop-fan diameter. The corrections are given for 0.32 and 0.20 Mach number flow. Note that less correction is required at lower Mach number. It can be shown (Reference 3-1) that below 0.1 Mach number, corrections for shear layer effects become insignificant.

The use of a single correction factor for sound from a distributed source like the prop-fan introduces the possibility of some error in data reduction. As shown before in Figures 3-3 and 3-4, the level and position corrections vary most widely at the furthest fore and aft microphone locations. The variation in level correction with microphone location is shown in Figure 3-7 as an uncertainty band for data reduced using the correction for an on-axis source. This shows that the shear layer level correction for the far field microphones is generally accurate within ± 1 dB. Greater variation is possible for the near field microphones in the extreme positions. For all microphones near the plane of rotation the uncertainty is small. The variation in microphone position correction with source location is shown in Figures 3-5 and 3-6. It is insignificant except at the most extreme microphone positions, where the uncertainty in ray path direction is still less than 10°, and is neglected here.

Effect of Propagation Through Shear Layer on Acoustic Signals - The character of the acoustic signal of the prop-fan, as defined by waveform shape and spectrum shape, is unaffected by propagation through the tunnel shear layer. Any differences between signals obtained inside and outside of the shear layer for a particular test condition can be shown to be attributable to distance alone. Sound pressure level spectra of acoustic signals measured inside and outside the shear layer are compared in Figures 3-8, 3-9 and 3-10. The linear frequency range is 0 to 40 kHz. Data are shown for SR-2 two-blade model testing at 1) subsonic tip speed with low blade power loading, 2) transonic tip speed with moderate power, and 3) high tip speed at high power, respectively. The measurements were made in the plane of rotation at 5.1 cm (2 in.) and 49.8 cm (19.6 in.) (0.8 D) tip clearances. The spectrum peaks represent harmonics of the blade passage tone with frequencies given by:

$$\frac{\text{RPM} \times \text{Number of Blades}}{60} \times \text{harmonic number.}$$

It is important to note that, although the level drops from the inner to the outer measurement location due primarily to distance decay, the basic shape of the harmonic envelope is retained. The spectra at the outer location have envelope humps that are more rounded than spiked at the highest frequencies because the measurements in this region are influenced by the tunnel noise floor. The spectra at the high speed condition have differing envelope valleys due to different phase combinations of the distributed acoustic sources within the prop-fan disk, which is also a distance effect. This will be discussed further in a later section.

Consider the fourth harmonic of blade passage frequency in the spectra from the two-blade model described above. This corresponds to the blade passage tone of an eight-blade model, also known as the 8P harmonic, since it has a frequency of eight per revolution. The 8P harmonic levels measured in the plane of rotation at radial stations ranging from 1.9 cm (0.75 in.) to 49.8 cm (19.6 in.) for the high speed and loading condition are shown in Figure 3-11. The decrease in level with increasing tip clearance is evident. Also indicated on this curve is the radial extent of shear layer turbulence (1% higher intensity level than free stream) and the location of the thin shear layer which was assumed for calculation of refraction corrections. The data points outboard of the assumed shear layer were corrected using this calculation. The measured levels are compared with levels predicted using the theoretical methodology. The theoretical methodology predicts levels at the corrected listener position, that is the location of the microphone as though there were no shear layer. Thus, this comparison is a test of both the refraction corrections to the data and the theoretical methodology. Predicted levels compare well with measured levels inside and outboard of the shear layer. This indicates the validity of the hypothesis that the acoustic signal is relatively undisturbed by the shear layer, particularly at low frequencies where the dominant noise of the prop-fan occurs.

The acoustic pulse waveform itself is shown for several of the measurement locations. The linear amplitude for each pulse is given in Pascals and time moves left to right. The sharpness of the peak is not diminished as the pulse moves through the shear layer. However, the amplitude drops primarily because of increased distance. Further evidence that the waveform is undisturbed by the shear layer is presented in Figure 3-12. Here, pulse waveforms of the SR-2 and SR-3 models at similar operating conditions are compared inside and outboard of the shear layer. In each case the sharpness of the waveform peak is preserved.

8P Harmonic Trends

8P Harmonic vs Overall Levels - The blade passage tone of a symmetrical eight-bladed prop-fan is known as the 8P harmonic since it has a frequency of eight per revolution. This tone is also known as the first or fundamental blade passage harmonic of an eight blade prop-fan. The 8P harmonic generally dominates all others and provides the major contribution to the overall noise level.

Consider the sound pressure level spectra obtained at high speed, high loading conditions for the SR-1, SR-2 and SR-3 models shown in Figures 3-13, 3-14 and 3-15, respectively. These spectra were measured at microphone position 3, the corrected location which is nearest the rotational plane (see Table 3-I) in the near field at 0.8 D tip clearance. The models were tested as two-blade configurations. Thus, the fourth blade passage harmonic is the 8P harmonic. This tone would be the fundamental harmonic if the model was an eight-blade configuration and is used for such comparison.

If the levels of the n8P harmonics, where n = 1, 2, 3, ..., for a two-blade model are summed on a logarithmic basis, the overall level corresponding to an eight-blade configuration can be calculated. Direct comparison requires adjusting the level based on the ratio of the numbers of blades and is discussed later in this section. The levels of the significant harmonics corrected for shear layer effects are given for the three model test conditions in Table 3-II.

The level of the 8P harmonic is within about 3 dB of the overall level for these test conditions. High tip speed and loading conditions were chosen as the worst case because of the greater high frequency content of the acoustic signal. Yet, it is the 8P harmonic which provides the major part of the acoustic energy that is measured. Consequently, trends in 8P harmonic level with such test parameters as blade model, tip helical Mach number and blade power loading, give a valid indication of the variation in overall sound pressure level. Emphasis in the trend analysis in the remaining sections will therefore be on the dominant 8P harmonic.

Effect of Blade Tip Speed and Loading - The effect on maximum sideline 8P harmonic level of varying blade tip speed with constant blade loading is shown in Figures 3-16 through 3-18. The data shown are from either two-blade or four-bladetest configurations. The four-blade data were corrected to two-blade levels by subtracting 6 dB to account for the ratio of the number of blades. This correction is discussed in a later section. The trend lines are derived from a least-squares linear fit of the data.

The maximum sideline 8P harmonic level in the near field at 0.8 D tip clearance as a function of blade tip helical Mach number for SR-2 and SR-3 model testing at constant loading of about 27.6 kW/blade (37 SHP/B) is shown at the top of Figure 3-16. At high tip speeds this test loading approaches the level and spanwise distribution of lift coefficient on the blades for a prop-fan at the cruise condition. Therefore, these data are considered an indication of the noise reduction potential of the SR-3 design. The SR-3 model is about 10 dB lower in level than the SR-2 model at high tip speed and 9 dB less at low tip speed. The noise reduction benefits of the SR-3 design are seen in test points up to 1.21 tip helical Mach number.

The same test conditions are compared in the far field (4.4 diameters tip clearance) at the bottom of Figure 3-16. The SR-3 model is lower in level than the SR-2 model by about 9 dB at high tip speed and 5 dB at low tip speed. The reduction of 5 dB at 0.7 to 0.8 tip helical Mach number for the swept SR-3 blade relative to the unswept SR-2 blade is considered particularly important, as this is the operating regime during take-off and landing where Federal regulations must be satisfied for aircraft noise certification (Reference 3-2). These results confirm that prop-fan configurations designed to reduce near field noise in cruise are also beneficial in reducing far field noise at take-off and landing conditions.

The maximum sideline 8P harmonic level in the near field at 0.8 D tip clearance as a function of blade tip helical Mach number for SR-1, SR-2 and SR-3 at a constant loading of 18.7 kW/blade (25 SHP/B) is shown at the top of Figure 3-17. The differences between the SR-1 and SR-2 models are small, indicating that the sweep of the SR-1 design was not sufficient to achieve measurable level reductions at these test conditions. The SR-3 model is about 3 dB lower in level than the SR-1 and SR-2 models, nearly constant with tip speed. Far field data (4.4 D tip clearance) are shown at the bottom of Figure 3-17. Again, there is little difference between the SR-1 and SR-2 models. The SR-3 model is lower in level than the earlier designs by about 6 dB at low tip speed and 5 dB at high tip speed.

The effect of blade loading can be seen by comparing the high loading and moderate loading trend curves. If the absolute levels for moderate loading in Figure 3-17 are compared with those for higher loading in Figure 3-16 it can be seen that raising the loading of SR-2 causes a substantially greater increase in level than raising the loading of SR-3. It appears that the SR-3 design is capable of absorbing higher power without large increases in noise.

The advantage of the SR-3 model over the earlier designs is summarized in Figure 3-18. The sound level reduction in the near field is shown at top, with the far field trends below. These curves indicate that the noise reduction advantage due to the blade sweep of the SR-3 model is greater at higher loading, particularly for high tip speeds in the near field. This indicates the success of the design process for SR-3 since the noise reduction effort was focused on this operating regime.

Sideline Directivity

The measured directivity of sound around the prop-fan is useful for the comparison of different models at varying test operating conditions. It is also a powerful tool for assessing predictions made using the theoretical methodology, as will be described in a later section. The directivity was measured using an array of axial locations at constant sideline distance from the prop-fan axis of rotation. The directivities of test data presented here were obtained in the near field at 0.8D tip clearance and in the far field at 4.4D tip clearance. The microphone positions used in the present analysis are shown in scale in Figure 3-19. The origin is on the axis of rotation, in the plane of rotation. The microphone positions have been corrected to account for shear layer refraction with a tunnel speed of 0.32 Mach number. These positions are for microphones which move with an identical flight velocity to the prop-fan. By use of Figure 3-19 the reader can compare the directivities in the near and far field. For example, the second and third microphones in the near field correspond to the first and second far field microphones ahead of the plane of rotation.

8P Harmonic Sideline Directivity - The 8P harmonic was shown earlier to dominate the overall sound pressure level and thus is a good indicator of acoustic behavior for the prop-fan. Consider the near field and far field sideline directivities of 8P harmonic sound pressure level for SR-1, SR-2 and SR-3 testing at similar subsonic tip speeds and blade loadings shown in Figure 3-20. Four-blade model data were corrected to two-blade levels by subtracting 6 dB to account for the ratio of the number of blades. The near field directivity, shown at the top, is a function of corrected axial distance relative to the plane of rotation and normalized by the prop-fan nominal diameter. As was also indicated by the trends discussed in the previous section, the difference between the directivities of the SR-1 and SR-2 models is small. The SR-3 model, however, shows differences both in level and in directivity shape. The SR-3 has a dip near the plane of rotation which is not evident in the humped directivity of the SR-2 model. As will be demonstrated in a later section by use of the theoretical methodology, this difference is caused by the dominance of different types of acoustic sources. The SR-2 model directivity is dominated by thickness noise, represented in the acoustic analogy by a monopole source which peaks near the plane of rotation, thus the hump. The sweep of the SR-3 model is designed to suppress thickness noise. As the thickness noise level drops, loading noise, represented by an acoustic dipole source which peaks at two locations forward and aft of the plane of rotation, becomes more important. This is evident in the directivity curve.

This behavior is also seen in the far field directivity at the bottom of Figure 3-20. The SR-1 and SR-2 model directivities peak near the plane of rotation (0 corrected axial position) while the SR-3 model directivity dips. The SR-1 and SR-2 model data for these cases were acquired during a different test sequence than that for the SR-3 model data. That is why different arrays of far field microphones are seen for these models. Note also the difference in peak levels between the SR-1 and SR-2 models and the SR-3 model. (The most forward SR-3 microphone probably indicates the peak in the far field as it corresponds to the microphone at 0.27 X_c/D (mic 2) in the near field which was a local peak.) As indicated in the trend discussion earlier, at moderate loading this difference is greater in the far field than the near field.

A directivity comparison of the SR-1, SR-2 and SR-3 models at higher tip speed and moderate loading is shown in Figure 3-21. The match in tip speed and loading is not perfect but the comparisons are considered instructive. The near field directivity is seen at top. The SR-1 and SR-2 show similar results. The SR-3 directivity is markedly different. The peak level is ahead rather than behind the plane of rotation as for SR-1 and SR-2. The SR-3 level drops where the SR-1 and SR-2 levels peak, indicating further suppression of thickness noise relative to loading noise. As would be expected, thickness noise suppression is more effective at higher tip speeds where this noise mechanism becomes more important. This result is also observed in the far field as shown at the bottom of Figure 3-21.

Consider the directivity comparison of the SR-2 and SR-3 models at high tip speed and similar moderate loading in Figure 3-22. The SR-3 model is quieter than the SR-2 model across the entire near field sideline. The far field directivity is shown below. The SR-2 model directivity has the characteristic thickness noise hump. The SR-3 model has a dip in the plane of rotation characteristic of loading noise. That was not as evident in the near field. The reason for this is that the complex phases of the sound waves, from the distributed acoustic sources on the blades combine differently at different distances from the prop-fan. The distribution of the sources themselves changes with operating condition and this effect can be employed to maximize the noise suppression inherent in a blade model operating at the cruise design point, as is demonstrated next.

Consider the directivity comparison in Figure 3-23 for the SR-2 and SR-3 models operating at high tip speed and high loading. At this tip speed and blade loading, the level and spanwise distribution of lift coefficient on the blades approaches that for a prop-fan at the cruise condition. Thus, these data indicate the noise reduction potential of the SR-3 design. The near field directivity is shown at top. The SR-3 model level is lower than the SR-2 level by more than 10 dB in the plane of rotation. Again it is thickness noise suppression due to the SR-3 blade sweep that is indicated by the central dip. This thickness noise suppression is carried into the far field as seen in the lower curves of the figure.

A directivity comparison of the SR-1, SR-2 and SR-3 blade models operated at low tip speed and high blade loading is shown in Figure 3-24. The conditions shown approximate the operating regime during take-off and landing. The near field results are shown at top. The SR-1 and SR-3 models both have peak levels lower than the SR-2 model indicating that the SR-1 model sweep is effective in reducing near field noise at this low speed. This effect does not carry over to the far field for SR-1 as shown at the bottom. The far field is where takeoff and landing noise is most important. The SR-1 and SR-2 have comparable levels in the far field. The SR-3 model is consistently lower in both the near and far fields.

The effect of tip speed on directivity for the SR-3 blade model operated with moderate blade loading is shown in Figure 3-25. The near field directivity is shown at top. The lower tip speed case shows more of a dip near the plane of rotation than the high speed case. This follows naturally since the thickness noise component will tend to become more important than the loading noise component as tip speed rises. Ahead of the plane of rotation a peak occurs which may be due to negative tip loading caused by operation at low blade angles. Such a peak would probably not occur in normal prop-fan operation. This behavior is also observed in the far field, shown below.

Thus, 8P harmonic sideline directivity measurements reveal differences in the acoustic behavior of the SR-1, SR-2 and SR-3 models. The sweep of the SR-1 model blade is effective in reducing noise only in the near field at low tip speeds. At higher tip speeds the SR-1 and SR-2 have similar directivity patterns. The sweep of the SR-3 model blade is effective in reducing noise below SR-1 and SR-2 model levels at all tip speeds. The SR-3 is most effective in reducing noise at the high tip speed and loading condition that simulates the cruise operating condition for which the prop-fan was designed. The SR-3 configuration also reduces noise at conditions approximating take-off and landing.

8P Harmonic vs Overall Sideline Directivity - Sideline directivities of 8P harmonic level and the overall level for SR-1, SR-2 and SR-3 model testing are shown in Figures 3-26, 3-27 and 3-28, respectively. The peak sideline levels for these cases were discussed in a previous section. The overall level was found by logarithmically summing the levels of all the multiples of the 8P harmonic, including the fundamental. High tip speed and very high loading conditions are shown with the highest tip speed attained for SR-3 model testing. Note in these curves that the 8P harmonic level is everywhere within the overall level by a few dB. Further, the shape of the overall level sideline directivity pattern is mirrored by the directivity pattern of the 8P harmonic. Thus, the 8P harmonic is a good indicator of acoustic behavior along the entire sideline as well as the peak location.

Sideline Directivity of Harmonic Order Spectra - Harmonic order spectra of prop-fan acoustic data are useful for understanding the noise reduction mechanism of the SR-3 model. Near field sound pressure levels of the first twelve 8P harmonic orders for the SR-2 and SR-3 models operating at high tip speed and loading are shown in Figure 3-29. These data were measured near the plane of rotation at microphone 3 and behind the plane of rotation at microphone 5 (see Figure 3-19). The test operating condition simulates the prop-fan cruise condition. The significant difference between the spectra of the SR-2 and SR-3 models is at the lowest harmonics. The levels of both the 8P and 16P harmonics for SR-3 are more than 10 dB lower than the levels of the corresponding harmonics for the SR-2 model near the plane of rotation. Behind the plane of rotation, the 8P harmonic level for SR-3 is about 10 dB lower than that for the SR-2 model. The higher harmonics for the SR-2 and SR-3 models have comparable levels at the two listener positions. Thus, the near field noise reduction inherent in the SR-3 model at these test operating conditions is due mainly to suppression of the lowest harmonic orders.

A comparison of harmonic order spectra obtained in the far field is shown in Figure 3-30. The measurement positions correspond to those that are along ray paths similar to those for the near field positions discussed above. They are microphones B and D of Figure 3-19. Note that both the 8P and 16P harmonic levels for the SR-3 model are significantly lower than those for SR-2 both near and behind the plane of rotation. The level fluctuations in the higher harmonics for SR-2 are due to the extremely "humped" character of the spectrum envelope. The SR-3 model has, by

contrast, smoother spectra beneath the SR-2 peaks and will thus provide less noise contribution at the high frequencies. Thus, in the far field, the SR-3 appears effective in reducing harmonic levels at high as well as low frequencies. The spectra for each model change as the listener moves from the near field to the far field because the phases of the acoustic waves, from the distribution of acoustic sources on the prop-fan blades, combine to form a different resultant sum at different listener distances.

It should be noted that the higher harmonics roll-off with frequency more quickly behind the plane of rotation than near the plane of rotation. This effect is indicative of the directivity pattern of thickness noise since it is known (Reference 3-3) that loading noise harmonics roll-off more rapidly.

Sideline Directivity of Narrow Band Spectra - Spectra of SR-2 and SR-3 model data measured at the far field sideline are shown in Figures 3-31, 3-32 and 3-33 for a range of tip speeds at high loading. Data measured at microphones A through D are shown. These positions covered the region of peak level near the plane of rotation (see Figure 3-19).

Spectra for the SR-2 and SR-3 models operating in the two-blade configuration at low tip speed are compared in Figure 3-31. At this low tip speed loading noise dominates the noise spectrum as indicated by the rapid decay with frequency of the blade passage harmonics. The spectral tones which appear in these data correspond to the first few 8P harmonic orders. The levels of these tones for the SR-3 model are markedly lower than those for SR-2.

A spectra comparison for SR-2 and SR-3 models operating at high subsonic tip speed is shown in Figure 3-32. The difference in the shape of the harmonic envelopes of the SR-2 and SR-3 spectra is immediately evident. Also evident is the greater high frequency content of the SR-2 spectra. Since these frequency domain spectra are the Fourier transforms of the acoustic pressure pulse waveforms in the time domain, changes in spectrum shape indicate changes in the acoustic waveform. The SR-2 and SR-3 blade models are physically much different and so naturally produce different acoustic waveforms. Note that for both models, high harmonics are more prevalent near the plane of rotation than away from it, again indicating the directivity pattern of thickness noise.

The difference between SR-2 and SR-3 model far field spectra is most evident for the high tip speed simulated cruise condition shown in Figure 3-33. The SR-2 harmonic levels are higher than for SR-3 and the spectra of the respective models have a much different shape. The envelope of SR-3 harmonics decays smoothly, while the SR-2 envelope shows a pronounced humped shape, characteristic of a signal with sharp peaks.

Acoustic Pressure Pulse Waveforms

Near field sideline acoustic pressure pulse waveforms (0.8 D tip clearance) are shown in Figures 3-34 to 3-37. Waveforms are a useful diagnostic tool for analyzing the relationship between a blade shape and the acoustic signal it produces at different operating conditions. Examples of acoustic waveforms for the SR-1, SR-2 and SR-3 models operating at subsonic tip speed and moderate loading are seen in Figure 3-34. The blade models are arranged with blade sweep increasing down the page. Measurements at all near field directivity points are shown. The ordinate of each curve is acoustic pressure in Pascals with positive pressure toward the top. The abscissa of each curve is in time units increasing left to right. The pulses are obtained from oscilloscope photographs where the full horizontal scale is one prop-fan revolution. Since the prop-fan rotational speed (RPM) for the three cases is nearly the same, the time scales in the figure are also nearly the same. The pressure scales of some of the curves vary because different attenuator settings were used for those data channels during testing. To assist the reader in interpreting the relative amplitude of the pressures, the figures include dashed lines which represent acoustic pressures of ± 100 Pascals. Recalling the corrected listener positions of the near field directivity points shown in Figure 3-19, microphone 3 is just forward of the rotational plane, while microphone 4 is behind it.

A feature of these curves to be noted is the similarity of the waveforms for the SR-2 and SR-1 models. The waveforms show a similar progression of shape from the forward to the aft sideline positions, beginning as a simple negative pressure pulse and transforming to one with a nearly equal positive pressure leading edge hump. This follows since the progression is toward the direction of thrust. The negative hump is primarily thickness noise related. The passing of the blade increases the local instantaneous particle velocity causing the pressure to drop relative to the static level. The hump is partially loading related since forward of the rotational plane the flow is drawn toward the prop.

Note that the peak pressure levels of the SR-1 and SR-2 models are quite similar, showing that the limited sweep of SR-1 is not effective in altering the acoustic signal at these conditions. Contrary to the SR-1 and SR-2 model data the SR-3 model waveforms develop a positive peak only at the aftmost locations. The pressure level is also significantly reduced. Thus, the greater sweep and reduced chord at the tip of the SR-3 model effectively reduces noise. This is indicated by the near field 8P harmonic sideline directivity for these cases shown in Figure 3-20.

Acoustic waveforms for the SR-1, SR-2 and SR-3 models operating at supersonic tip speeds with moderate blade loading are shown in Figure 3-35. The dashed lines represent constant acoustic pressure of ± 300 Pascals. At supersonic tip speed the behavior

of the SR-1 and SR-2 models begins to diverge. The leading edge spike which developed on the SR-2 waveform is absent in the SR-1 data. This pressure spike is related to a bow wave. The sweep of SR-1 effectively eliminates this leading edge peak. As seen at lower tip speeds, the positive component of the pressure pulse increases in the downstream direction. The width, or time duration of the SR-1 pulse is equal to that for the SR-2 pulse.

The SR-3 model waveforms again differ from the SR-1 and SR-2 data. The leading edge spike and the positive pressure hump downstream of the rotational plane are absent due to the effect of blade sweep. Also, there is an important reduction of the pulse width, or time duration. Thus, even though the negative and trailing edge peaks have greater sharpness and intensity, there is a decrease in noise level. The acoustic energy of each pulse is a function of the area associated with the absolute value of the pressure pulse. Thus, it follows that the narrower SR-3 pulse will produce less noise. This is evident in the near field 8P harmonic sideline directivity for similar cases shown in Figure 3-21.

Acoustic waveforms for the SR-2 and SR-3 models operating at high tip speeds and moderate loading are shown in Figure 3-36. The dashed lines represent constant acoustic pressure of ± 1000 Pascals. At these operating conditions the pressure signature is more dominated by thickness effects, particularly in the plane of rotation and forward, than at lower tip speeds. The SR-2 model waveforms measured near the plane of rotation (microphone locations 2, 3 and 4) have the shape of classical thickness pulses (Reference 3-4, 3-5 and 3-6). Only at the aftmost locations is there any hint of loading influence. The SR-3 waveforms again display the advantages of blade sweep and reduced tip chord. The leading edge spike is absent and the pulse is narrow. These effects combine such that the SR-3 waveform contains less acoustic energy than the SR-2 pulse and thus produces less noise.

The advantage of the SR-3 design is seen in the acoustic waveforms for the SR-2 and SR-3 models operating at several high tip speed and high loading conditions which approximate the cruise condition. These are shown in Figure 3-37. The data were measured just upstream of the rotational plane at microphone position 3. The dashed lines represent acoustic pressure of ± 1000 Pascals. All the traces have common amplitude and time scale to assist in comparison. The shaded regions are the areas associated with the absolute value of the pressure pulses, of which the acoustic energy is a function. Note that the peak values of the SR-2 pulses are larger than those for the corresponding SR-3 waveforms. Additionally, the areas subtended by the SR-2 pulses are greater than those for SR-3, showing that the SR-2 pulses contain greater acoustic energy. This occurs partially because the SR-2 pulses have greater time duration than the SR-3 pulses. The SR-3 waveforms are narrower by about 30 percent due largely to the absence of the leading edge spike. Thus, the advantages of blade sweep and reduced tip chord result in less noise for the SR-3 model. The acoustic mechanisms which cause this noise reduction are discussed in the sections on comparison of test and theory.

Boundary Layer Trip

The effect of attaching a boundary layer tripwire to the SR-2 model blade was examined. Comparisons of acoustic data were made for normal (untripped) operation and for operation with a 51 μm (0.002 in.) tripwire attached at 5% chord to the camber side of one blade of a two blade model. The rotor RPM and the atmospheric conditions for each set of test cases were identical. Calculations show that the laminar boundary layer is tripped to turbulent at 5% chord with the wire. Normal laminar to turbulent transition occurs near 30% chord.

Signal enhanced acoustic pressure waveforms for untripped and tripped testing at very low power loading and about 1.02 tip helical Mach number are shown in Figure 3-38. The curves are plots of acoustic pressure in Pascals versus time, as measured in the near field (0.8 D tip clearance) just aft of the rotational plane. Note that duration of the pulse is unchanged by the addition of the tripwire to the blade. The only change is a slight modification of the pulse shape in the negative pressure region near the leading edge. Since this is a very low power case at high tip speed, the acoustic pulse is attributed mainly to thickness noise. The difference in pressure at the leading edge can thus be related to the difference in thickness profile. The pressure change due to the tripwire is about 7% of the peak to peak value. The diameter of the tripwire is about 4% of the blade thickness in the tip region, which contributes the most to thickness noise. Thus the change in the acoustic signal is due to the additional solid boundary on the blade and not to changes in the boundary layer.

The change in the acoustic pressure waveform is reflected in the corresponding sound pressure level spectra shown in Figure 3-39 for the untripped and tripped cases. The increased pressure amplitude due to the trip generally raises the harmonic level about 1 dB. The humps in the spectrum envelope do not repeat as rapidly with frequency for the tripped case as they do for the untripped case. This is due to change in waveform shape. The differences seen in both the waveforms and spectra are small compared to the overall character of the acoustic signal. There was also a small change in the power absorbed by the rotor. The model with the tripped blade absorbed about 12% less power indicating less drag. This is consistent with well known results (Reference 3-7, pg 898) stating that the pressure drag in transonic flow is less for flow with a turbulent boundary layer than for flow with a laminar boundary layer.

Acoustic pressure waveforms for untripped and tripped boundary layers at a higher tip speed and loading condition are shown in Figure 3-40. The pulse durations are about the same as for the low power cases and the pressure amplitude is about 50% higher, due to the addition of a loading noise contribution. Since thickness is not the sole contributor to the acoustic signal the change caused by the tripwire is less than for the lower power case. The amplitude change at the leading edge is only about 4% of the peak to peak value. Little change is also seen in the corresponding spectra shown in Figure 3-41.

Thus, it is concluded that the addition of the tripwire causes only minor changes to the thickness noise contribution of the model. These changes are due only to a difference in the blade solid boundary and not due to differences in the boundary layer of the flow over the blade.

Linear Superposition of Two, Four and Eight Way Data

The validity of superposition of acoustic data from prop-fan models in two, four and eight blade configurations was examined. Data from test conditions with similar tip helical Mach number and loading were compared. The principle of superposition states that for linear sources, the total acoustic field may be derived by summing the acoustic fields of all the individual sources. This principle applies for prop-fan acoustic measurements despite the existence of nonlinear sources because the regions of the nonlinear sources from each blade do not overlap. Thus, the acoustic field of an eight blade prop-fan can be found from the two blade test data by choosing multiples of the 8P harmonic and multiplying the acoustic pressure at each of these frequencies by four, the ratio of the number of blades. In terms of sound pressure level this is equivalent to adding 12 dB to each of the multiples of the 8P harmonic from two blade test data.

Sound pressure level spectra from two blade and four blade SR-3 model testing at similar high tip speed and loading conditions are shown in Figures 3-42 and 3-43. Data measured in the near field (0.8 D tip clearance) near the plane of rotation are shown in Figure 3-42. Data measured in the far field (4.4 D tip clearance) aft of the rotation plane are shown in Figure 3-43. In both figures, the spectrum curve represents data from 4 blade testing. The small circles represent two blade SPL harmonic peaks which have been adjusted by adding 6 dB to the 4P harmonic and its multiples. Note the close agreement between these data at all but the highest harmonics. The 8P harmonic, the blade passing harmonic of an eight blade rotor, shows particularly close agreement. Near field acoustic pressure pulses corresponding to the SPL spectra for two and four blade testing are shown at the top and bottom of Figure 3-44, respectively. The similarity between the individual pulses indicates that the pulse from one blade is independent of the pulse from the next.

Near and far field sound pressure level spectra from two, four and eight blade SR-3 model testing at moderate tip speed and loading are shown in Figures 3-45 and 3-46, respectively. Both sets of data were measured near the rotational plane. The spectrum curve in each figure represents data from eight blade testing. The circles represent two blade harmonic peaks adjusted by adding 12 dB to the 8P harmonic and its multiples. The squares represent four blade harmonic peaks adjusted by adding 6 dE to the 8P harmonic and its multiples. The good agreement between the data indicates the validity of the linear superposition method.

Hot Wire Anemometry Measurements of Blade Wakes

An exploratory experimental study was conducted to determine the feasibility of using hot-wire anemometry to measure three velocity components in the blade wakes immediately downstream of a model prop-fan. Such measurements are of potential use in assessing the aerodynamic and acoustic performance of present and future model prop-fan designs. The study was conducted using a very high frequency response hot-wire anemometer system (450 kHz) capable of high spatial resolution. Measurements were obtained with prop-fan model SR-2 in a two-bladed configuration. Tests were conducted at free-stream Mach number RPM combinations of $M_X = 0.20$, 7500 RPM and $M_X = 0.32$, 10 900 RPM. The study which is presented in Reference 3-8 indicates that detailed wake velocity data can be obtained using the technique described in this report and that measurements at the test facility operating limit of 12 000 RPM would be feasible.

Analysis of Theoretical Predictions

Prediction Methodology

Figure 3-47 shows the chronological development of the prop-fan Acoustic Method. It can be seen in Figure 3-47 that the SR-1 and SR-2 models were designed with empirical methodology. This was necessary because the existing theoretical propeller noise prediction methodology was not capable of evaluating the supersonic helical tip speed operation of the prop-fan at cruise or the effects of blade sweep. In the SR-1 design, the features included to minimize noise were a reduction in airfoil thickness over existing turboprops and propellers and a moderate amount of sweep. The reduction in thickness was expected to reduce the near field noise in cruise since propeller noise theory showed that thickness related (monopole) noise was a dominant part of the noise of existing propellers operating at high tip speed. The moderate amount of sweep incorporated was expected to lower the effective Mach number at which the blade airfoils operate and, therefore, reduce the excess noise which had been observed in conventional propellers when they operate at helical tip Mach numbers exceeding the critical Mach number of the blade airfoils (the operating Mach number of an airfoil at which local flow over the surface reaches sonic velocity). Unfortunately, in 1975, when SR-1 and SR-2 were designed, the effect of these features could not be accurately analyzed without an appropriate theory.

The SR-2 design is exactly like the SR-1 except the SR-2 has no blade sweep. This model was built as a reference design to establish the benefits of advanced swept blades relative to a conventional unswept blade planform. SR-2 did, however, include thin airfoil sections and had eight blades; so it was expected to perform better than a conventional four-blade propeller. Also, the thin blades were expected to provide some noise reduction relative to conventional propellers.

The SR-1M has the same moderately swept planform of the SR-1. However, it has different twist and camber distributions which were established as a result of analysis of the wind tunnel performance data from SR-1. The SR-1M was not tested in the current program.

In 1976, a theory was developed by Hanson (Reference 3-6) which allowed prediction of near field noise of propellers operating at high subsonic speed. This work was based on the Ffowcs Williams-Hawkings "acoustic analogy" (Reference 3-9) in which all equations of fluid motion are cast into a wave equation for acoustic pressure. In the formulation of this theory, Hanson assumed that the prop-fan blades travel along helical surfaces defined by the forward flight speed of the aircraft and the angular velocity of the prop-fan. Two components of noise are calculated in this theory: 1) monopole (thickness) noise, which is determined by the blade airfoil section thickness distribution; and 2) dipole (loading) noise, which is determined by the pressure distribution on the surface of the blade. A third (second order) term in the Ffowcs Williams-Hawkings equation, the quadrupole source term, was ignored in this early theoretical development because it was believed to be small relative to the monopole thickness term. Of course, the lack of the quadrupole source should not be surprising as none of the propeller and rotor noise prediction procedures which existed in 1976 had ever included this source. This method is a time domain method, i.e., the acoustic pressure wave form generated by a blade is calculated and then the frequency spectrum of the noise is obtained by Fourier analysis.

The inputs to the computer program based on Hanson's Time Domain theory include chordwise and spanwise blade differential pressure distributions as well as chordwise and spanwise blade thickness distributions. For prop-fan loading noise predictions, the chordwise variation in pressure is based on the chordwise loading distribution of airfoils of the type used in the prop-fan design. For thickness noise calculations the actual blade thickness distribution is the input to the program.

The basic output of the program is the acoustic pressure waveform at a specified point in space assumed to be moving forward at the same speed as the prop-fan. The harmonic components of noise obtained from a Fourier analysis of this waveform are also an output. Thus, it is possible to calculate the noise at the location of a fuselage near a prop-fan as the aircraft is flying at cruise speed. For the SR-3 the primary noise reduction feature of the design was the blade sweep which was optimized using the theory described above. This sweep optimization utilized the concept of destructive interference of noise from different spanwise stations of the prop-fan blade. This concept is based on the fundamental assumption of linear acoustics that the acoustic pressure at any observer position can be calculated as the sum of contributions from each element of the source volume and surface area. To be done correctly, the summation (or integration) process must account for the amplitude and phase of the elemental contributions. If source dimensions of the blades are greater than about 1/2 the wavelength of interest (i.e., if the source is "acoustically non-compact"), then at some observer positions, elemental signals from different portions of the source will arrive out of phase. The net noise will then be reduced by self-interference below the level which would be obtained if the source dimension were very small ("acoustically compact"). Although the term,

"acoustically non-compact," is relatively new, the principle has been known for many years. For example, in Gutin's original theory for propeller noise (Reference 3-10), the appearance of Bessel functions and the polar directivity pattern result from phase variation around the propeller circumference. For most conventional propellers, chordwise and spanwise phase variations can be neglected at blade passing frequency (number of blades times rotation speed). However, for the prop-fan, the combination of high Mach number, many blades, and large chord require that chordwise and spanwise phase variations be included.

The phase interference concept is most clearly illustrated with reference to the effect of sweeping a blade planform as suggested by Figure 3-48. At blade passing frequency, the noise from any strip of the blade is a sinusoidal wave with an amplitude and phase angle. The noise from one propeller blade is simply the vector sum of the contributions from each strip and the noise of the total propeller is the product of the vector sum and the number of blades. The effect of a sweep of the tip is to cause the signal from the tip to lag (increased phase angle) the signal from the mid-blade region, thus causing partial interference and a reduction in net noise.

For the SR-3 design a short form version of the Time Domain Method was developed in 1976 which included a graphical version of the concept discussed above. In this graphical procedure the strip noise contributions are treated as vectors in the complex plane having amplitude and phase angle. Then, the summation of the contributions from the strips is performed by adding the vectors head-to-tail, as shown at the top of Figure 3-48. It can be seen that a lack of variation in phase angle in the individual contributions from several spanwise locations on the blade would vectorially add up to a value no different from the total length of the vectors (analogous to the resultant noise). This is the general result for unswept and slightly swept prop-fan blades. However, by varying the amplitude and phase of the noise produced by the various spanwise stations on the blade, substantial reduction in the resultant amplitude can be achieved, as shown in the phase plot at the right of Figure 3-48. This is the result for a prop-fan blade with substantial blade sweep.

In 1977, a Frequency Domain Method was developed for predicting prop-fan noise (Reference 3-3). This Frequency Domain Method offered several advantages over the Time Domain Method. First, in order to calculate the noise of a swept blade at supersonic tip speed, the computation time of the Time Domain Method is high because the acoustic pressure waveform must be accurately defined. Unless the span of the blade is divided into very small strips near the point where the flow over the blade reaches Mach 1, substantial numerical noise is generated in the numerical differentiation procedure. This results in an unacceptable error in the acoustic pressure waveform generated by the program.

Second, in the Time Domain Method the acoustic pressure waveform of the blade must be calculated precisely if accurate levels of blade passage frequency harmonics are to be generated by Fourier analysis of the waveform. While this means of obtaining harmonic levels would be quite desirable if many harmonics were required, prop-fan model test data has shown that the blade passage harmonic substantially dominates the higher harmonics in a prop-fan. Therefore, the Frequency Domain Method offers cost advantages over the Time Domain Method for most prop-fan studies.

Late in 1977 Hanson developed a quadrupole prediction theory (Reference 3-11) and was able to show at the end of 1977, by use of a simplified nonlifting aerodynamic model, that the quadrupole noise is an important noise source in prop-fans with unswept or slightly swept blades operating at transonic tip speeds.

Throughout 1978 the major prop-fan Methodology development consisted of establishing a working procedure for including the quadrupole component in the prop-fan Acoustic Design Procedure. Figure 3-49 shows a block diagram of the current method. The transonic airfoil design program at the upper left of Figure 3-49 is used to generate the data set which consists of the chordwise thickness distribution of an airfoil, the pressure distribution on the surface of an airfoil and the quadrupole distribution in the air surrounding an airfoil. A Fourier Transform Program is used to generate the Data Sets needed for noise calculations by the Frequency Domain Noise Prediction Program shown at the lower right of Figure 3-49. In addition, the Fourier Transform Program can be used to generate plots of frequency domain loading and thickness noise functions which are required for optimizing airfoil shape to noise. The application of this part of the method is discussed in Reference 3-3.

The prop-fan Performance Analysis Program at the upper right of Figure 3-49 is used to define the lift coefficient distribution for the prop-fan configuration and operating condition being considered. Either the Propeller Performance Prediction Method (used primarily for propellers operating at moderate forward speeds) or the Compressible Induction Method (developed for prop-fan performance calculations) can be used as the Performance Analysis Program. This information is used by the Frequency Domain Noise Prediction Program to predict the cases for the Acoustic Data Sets which are a function of thickness, camber, operating lift coefficient, and operating Mach number of the airfoils making up the prop-fan blade. The Frequency Domain Noise Prediction Program calculates monopole, dipole, quadrupole and total noise. To generate a frequency spectrum any number of harmonics of blade passage frequency may be calculated. Also the harmonics may be calculated for several observer locations to define the directivity of the prop-fan. In order to ensure that the input to the program is correct, the program plots the planform of the blade being evaluated. Phase plots for each harmonic and each location calculated are diagnostic output which is particularly important in optimizing the sweep distribution of a prop-fan blade during the design process.

Waveforms for the acoustic pressure pulse generated by a blade are also an output of the program. These are important diagnostic aids which can be compared with measured acoustic pressure pulses to establish areas of deficiency of the methodology.

For the correlations presented in this report the directivities of the blade passage frequency (8P) were calculated by use of the Frequency Domain Method. The majority of the acoustic pressure pulses were predicted by use of the Frequency Domain Method. However, some of the SR-2 cases were predicted by use of the Time Domain Method in order to minimize computer running time. Prediction of bow and trailing wave locations for the shadowgraph analysis was also done using the Time Domain Method. For the acoustic pressure pulse predictions and the shadowgraph predictions the quadrupole term was not included because of the high computer running time. Although inclusion of the quadrupole term would make some quantitative changes in the predictions the qualitative character of the predictions should not differ. Thus the predictions in this report are considered fully satisfactory for analysis purposes.

Comparison of Predicted and Measured Directivities

Comparisons between predictions and measurements were made for twenty-two test points selected from the points where noise data was obtained in the test program. The points selected are shown in Figure 3-50. It can be seen that most of the points are at approximately 18.7 kW (25 Shaft Horsepower (SHP) per blade). This allowed comparisons of SR-1, SR-2 and SR-3 at similar conditions. Additional points at 26-30 kW (35-40 SHP) were also evaluated at supersonic tip helical Mach number as the blade loading for these points simulates that of the prop-fan at 0.8 Mach number cruise. Most correlations were done for SR-3 as this model was the only one of the three tested which was designed for noise reduction by use of acoustic methodology. A substantial number of points were selected at various levels of loading (SHP) at tip helical Mach numbers between 1.15 and 1.21 in order to evaluate the influence of loading on the correlation between prediction and measurement. The points at 0.66 to 0.76 Tip Helical Mach number were evaluated because they are similar to the conditions for a prop-fan aircraft during takeoff and landing. In fact the 0.2 through flow Mach number in the Acoustic Research Tunnel which was used in acquiring these data is similar to the flight Mach number for a prop-fan aircraft during takeoff and landing. The complete set of correlations is presented in Appendix A. In each case the measured 8P harmonic level at 0.8 tip clearance is shown compared to the predicted levels. Predictions and measurements are shown for the seven microphone locations used during test. The fore and aft visual positions for these microphones used in the figures include corrections for the shear layer which is described elsewhere in this report. The measured levels also include a shear layer correction.

While the latest performance methodology is considered the best available for performance and noise predictions at cruise conditions, the performance predictions made with the latest method for the low through flow velocities encountered in the Acoustic Research Tunnel were found to be inadequate in defining tip loading. Therefore, predictions were made using the performance prediction methodology used during the design of SR-3.

The difference between SR-1, SR-2, and SR-3 noise characteristics can be seen in Figure 3-51 where data from runs 79', 33' and 8 (at a loading of approximately 19 kW/blade (25 SHP/blade) and at tip helical Mach number of 0.9) are compared. It can be seen that the peak level is slightly underpredicted in each case. Aft of the plane of rotation the underprediction is greatest. It can be seen that this is the area of the directivity plot that is influenced primarily by the dipole (loading) noise and to a lesser extent the quadrupole noise. An increase in predicted tip loading by the prop-fan performance analysis program would correct this deficiency. Note that both the measured and predicted levels for SR-3 are slightly less than the SR-1 or SR-2 but the measured levels show a greater reduction for SR-3.

At supersonic tip helical Mach number Figure 3-52 shows a comparison of data from runs 18', 75' and 26 (at a loading of approximately 18.7 kW/blade (25 SHP/blade)) and a range of tip helical Mach number of 1.04 to 1.10. It can be seen that the peak sideline directivity is well predicted for the SR-2 and SR-3 with some underprediction of SR-1. As in Figure 3-51 the deficiency in predicted levels aft of the plane of rotation in SR-1 and SR-2 could be corrected by an increase in dipole noise. The greatest difference between SR-2, SR-1 and SR-3 in Figure 3-52 is the reduction in quadrupole noise which is caused by increased sweep. The sweep causes spanwise phase cancellation and reduces the effective helical Mach number at the tip of the blade. These both influence quadrupole noise. The increase in monopole (thickness) noise for SR-3 in Figure 3-52 is due to its higher tip helical Mach number relative to SR-1 and SR-2. If the SR-3 tip helical Mach number had been equal to that of SR-1 and SR-2 the monopole noise would be lower.

Figure 3-53 shows a comparison of SR-2 (run 146) and SR-3 (run 42) at approximately 18.7 kW/blade (25 SHP/blade) and approximately 1.18 tip helical Mach number. The SR-2 prediction is quite good with only a slight deficiency aft of the plane of rotation. The SR-3 prediction is very good in and aft of the plane of rotation but deficient ahead of the plane of rotation. The reduction in both measured and predicted levels for SR-3 relative to SR-2 demonstrate the benefits of sweep. Note that due to lack of blade sweep the quadrupole contribution in SR-2 is quite large compared to that in SR-3.

The influence of loading on SR-2 at supersonic tip helical Mach number is shown in Figure 3-54 for run 146 (20.2 kW/blade (27 SHP/blade) and 1.189 tip helical Mach number), run 117 (30.1 kW/blade (40 SHP/blade) and 1.181 tip helical Mach number) and run 127 (46.6 kW/blade (62.5 SHP/blade) and 1.180 tip helical Mach number). For the two lower loading cases the agreement in peak level between prediction and measurement is seen to be quite good. However, the higher loading case is seen to be underpredicted. Fore and aft of the plane of rotation it appears that the underprediction is due to a deficiency in dipole (loading) noise which would be corrected by an increase in tip loading on the blade. The contribution of quadrupole noise in these predictions is shown to be particularly important. It contributes significantly to the peak levels at the two lower loading conditions and is the dominant source for the highest loading condition.

The influence of loading on SR-3 at supersonic tip helical Mach number is shown in Figure 3-55 for run 42 (16.7 kW/blade (22.4 SHP/blade) and 1.171 tip helical Mach number), run 27 (26.2 kW/blade (35.2 SHP/blade) and 1.169 tip helical Mach number), and run 304 (36.4 kW/blade (48.8 SHP/blade) and 1.211 tip helical Mach number). It can be seen that increasing the loading on the SR-3 model does not significantly affect the peak sideline noise. In each case the noise is dominated by monopole (thickness) noise with the dipole (loading) and quadrupole noise fairly low in level. Predictions match the measurements in peak sideline noise fairly well for the two highest loadings. The peak in measured level ahead of the plane of rotation for the lowest loading condition is not predicted. As in the previous case discussed where measured noise has an unusual peak ahead of the plane of rotation, this discrepancy may be associated with an abnormal tip loading condition.

Figure 3-56 shows a comparison of data from SR-1, SR-2 and SR-3 at subsonic tip helical Mach number simulating that encountered during takeoff and landing. The data for this figure were obtained at a 0.2 tunnel through flow Mach number similar to the flight speed of a prop-fan aircraft during takeoff and landing. It can be seen that the measured levels are substantially underpredicted. This is probably due to the same underprediction of loading encountered at higher tip helical Mach number. However, for the low tip helical Mach number of Figure 3-56 the monopole noise is much lower so the dipole noise is probably dominant. It should be noted, however, that the SR-3 measured noise is lower in level than SR-2 or SR-1. It appears that the sweep included in SR-3 to reduce noise at cruise is also beneficial in reducing noise at takeoff conditions.

The agreement between peak sideline predictions and measurements is summarized in Figure 3-57. It can be seen in the lower curve that the latest methodology is a substantial improvement over the earlier methodology in the upper curve. The deficiency of the earlier methodology is due primarily to the lack of the quadrupole source.

Comparison of Predicted and Measured Acoustic Pressure Pulses

Comparisons between predicted and measured acoustic pressure pulses were made for the same twenty-two test points used in the previous section on 8P harmonic directivity. The complete set of pulse comparisons is presented in Appendix A. The acoustic pressure pulse is the disturbance measured by a microphone which is associated with the passage of a single blade on a prop-fan. If there are four blades on the prop-fan there will be four pulses per revolution. If there are eight blades there will be eight pulses per revolution. Fourier analysis of these pulses produces the harmonic noise spectrum typical of propeller noise.

In order to control computation costs, the predictions were made using the methodology without the quadrupole term included. This does not detract from the value of the comparisons as addition of the quadrupole term alters the amplitude but not the general characteristics of the pulse waveforms. The waveform shape is of great interest for evaluating the accuracy and establishing deficiencies in the methodology.

The difference between SR-1, SR-2 and SR-3 pulse characteristics can be seen in Figure 3-58 where data from runs 79', 33' and 8 (at a loading of approximately 18.7 kW/blade (25 SHP/blade) and a tip helical Mach number of 0.9) are compared. Note that the scales for each of the three comparisons are different. It can be seen that the SR-2 and SR-1 pulses are quite similar and that the prediction matches the measured pulse quite well. The SR-3 predicted pulse differs from the SR-2 and SR-1 pulses in that the positive portion of the leading edge of the pulse is not as sharp, because of the influence of sweep at the leading edge of the SR-3 blade. This lack of sharpness would reduce the high frequency noise.

Figure 3-59 shows comparison of SR-2 (run 75'), SR-1 (run 18), and SR-3 (run 26) at a supersonic tip helical Mach number (1.04 - 1.10) and a loading of approximately 18.7 kW/blade (25 SHP/blade). The most distinctive feature of these pulses is the reduction of the leading positive part of the pulse which appears to be influenced by increasing sweep (note that SR-2 with no sweep has a sharp predicted and measured pulse; the SR-1 with some sweep shows a reduction of this peak and the SR-3 shows further reduction of the peak). The amplitude of the negative part of the pulse both measured and predicted, is similar for SR-2 and SR-1. For SR-3 the predicted negative pulse amplitude is less than measured. Note also that the short rise time characteristic of a shock at the end of the negative portion of the pulse is well predicted by the theory.

Figures 3-60 and 3-61 show how the predictions match test data at supersonic tip helical Mach number (1.18 - 1.19) and moderate loading of 16.7 to 20.2 kW/blade (22 - 27 SHP/blade). The positive sharp spikes at the leading and trailing edges of the pulse are shown to be well predicted for SR-2 in Figure 3-60. In fact, larger spikes are predicted

than are measured. For the SR-3, Figure 3-61 shows that the leading edge spike, visible in Figure 3-60 for SR-2, is predicted to be suppressed. Also, the duration of the SR-3 pulse is predicted to be shorter than that of SR-2. This shorter pulse is an indication of the reduction in acoustic energy achieved by use of blade sweep in the SR-3 design.

Figure 3-62 shows the influence of an increase in loading on SR-2 at a relatively constant supersonic helical Mach number (1.18 - 1.19). Little difference is seen in the general character of the measured pulses.

Figure 3-63 shows the influence of an increase in loading on SR-3 at a relatively constant supersonic tip helical Mach number (1.17 - 1.21). The negative portion of the pulses are shown to be well predicted. Also, the width of the pulse is well predicted in each case. The positive spike near the end of the pulse is not well predicted. For both runs 42 and 27 the amplitude of the spike is overpredicted. This overprediction would lead to an overprediction in high frequency noise. Although the positive spike at the end of the pulse in run 304 is somewhat overpredicted, this overprediction is not as bad as that in runs 42 and 27. Further improvements in methodology are needed to correct this overprediction.

Figure 3-64 shows a comparison of SR-1, SR-2 and SR-3 at subsonic tip helical Mach number simulating that encountered during takeoff and landing. Very little difference in predicted and measured pulse characteristics is seen and it is clear that the noise spectrum derived from such a pulse waveform would be dominated by low frequency harmonics of blade passage frequency. Also, it can be seen that the amplitude of the predicted pulses is less than that of the measured pulses. Since these cases are dominated by loading noise components, it appears that an increase in predicted blade loading is required to improve the correlation between test and prediction.

In summary, the agreement between predicted and measured acoustic pressure pulses has been found, in general, to be good. The prediction procedure appears capable of reproducing all of the features of the measured pulses including the sharp rise times characteristic of shocks. Overprediction of the magnitude of the positive peaks has been seen in these comparisons. This is expected to have a negligible effect on prediction accuracy of the more important lower harmonics.

Shadowgraph Evaluation

In this section the analysis of selected shadowgraph pictures obtained during the test program is presented. This includes comparisons of wave patterns seen in the pictures with those predicted by use of the Time-Domain prop-fan noise prediction methodology.

The shadowgraph pictures of the SR-2 and SR-3 models which were analyzed are presented in Appendix B. The effect of operating condition on the location of shock wave formations relative to the blade was determined for the two models.

It is known from the examination of the planform and edgewise shadowgraph views of the SR-3, the SR-2 planform views (see Appendix B) and Hilton's photographs (Reference 3-12) that the wave formations associated with the blade are sets of complex three-dimensional surfaces. These surfaces rotate in a pattern which is fixed relative to the rotor. Thus, for analysis purposes it is best to choose a coordinate system which is fixed to the blade to describe the pattern. The blade helicoidal coordinates are the natural choice. These coordinates are defined relative to the helicoidal surface which is described by the blade pitch change axis as the blade both rotates and translates forward. An example of this surface for one blade is shown in Figure 3-65. In this analysis, the lines of intersection between the helicoidal surface and the wave surfaces are of primary interest. These are the positions of the waves directly forward or aft of the blade in the blade's path. For analysis of test data, the helicoid can be approximated near the blade by the extended chord line. While this is not exact, it is sufficiently accurate for purposes of locating wave formations near the blade (within a chord).

The methods of locating the wave formations of the SR-2 model and the SR-3 model are similar in principle. The assumption critical to both methods is that wave formations are very nearly symmetrical about the chord line. This assumption allows the gap between the blade and the three-dimensional wave surface to be determined from the two-dimensional projection of the shadowgraph. The gap along the extended chord line is properly determined only when the line of sight is perpendicular to the chord line as shown in Figure 3-66. Maximum refraction of light from the point source will occur in the region of greatest second order density gradient. In the prop-fan tests this region is the portion of the wave formation which is tangent to the line of sight. In the example of Figure 3-66 the line of sight perpendicular to the chord line is tangent to the trailing wave, also at the chord line, so that the desired gap is projected to the shadowgraph screen. Any other line of sight gives a false indication of the gap size. Thus it is necessary to know the position on the blade for which the chord is perpendicular to the line of sight.

The prop-fan blades have twist and the shadowgraph light source is fixed in space. Therefore, the blade radial station for which the chord is normal to the line of sight is a function of rotor azimuth. Measurements were made of the distance between the point light source and both the leading and trailing edges of the blade at the reference radius for the SR-2 and SR-3 models in all tested aximuth positions. Using these values and the known blade chord, the angle between the line of sight and the chord line at mid-chord can be calculated for each azimuth position. Then using the known blade twist distribution, the radial station at which the chord is normal to the line of sight can be found. Figure 3-67 shows the blade twist distributions for the SR-2 and SR-3 models relative to the blade angle at the reference station. The distribution is plotted such that the angle given

at each radial station is added to the calculated angle between the line of sight and the chord line at the reference station. For example, if the angle to the line of sight is 95° at the SR-2 reference station, -5° must be added for normality. Thus the chord is normal at the 19.4 cm (7.65 in.) radial station.

Once the radial station for which the chord is normal to the line of sight at each azimuth position is known, its location in the shadowgraph must be found. Using the known source location, the source to screen distance and rotor geometry, the distance between the blade tip and the radial station of interest as projected on the screen can be calculated. Finally, using reference photographs, the relation between distances on the shadowgraph screen and those measured on the actual photographic enlargement is determined.

Wave formations associated with the SR-2 blade were measured for two test conditions. Measured wave locations and those predicted by the prop-fan noise prediction methodology are shown in Figures 3-68 and 3-69. The model was in a two-blade configuration, tunnel Mach number was 0.323 and the blade angle at the reference station was 23.2 degrees for both tests. The results of measurements for testing at 1.181 tip helical Mach number and blade loading of 31.4 kW (42.1 SHP) per blade are shown in Figure 3-68. The blade is shown in developed planform, that is, the planform if the blade were flattened by removing twist. The trailing wave is well defined in the shadowgraphs. It has an apparent attachment to the blade at the 26.2 cm (10.3 in.) radial station (84% radius). At this station a 1.01 section Mach number is calculated. The attachment point is well predicted.

The wave locations outboard of the blade tip are calculated by the same method as these inboard except that the blade pitch change axis and twist are extrapolated from inboard values. Since the waves do not surround a physical blade, as they do inboard of the tip, the assumption of symmetry about the extended chord line is not as well supported. Within a chord length of the tip, however, the assumption is considered reasonable.

Outboard of the tip, wave formations further upstream near the pitch change axis are visible, in addition to the trailing wave. These formations are believed to be evidence of recompressions due to interactions with the blade turbulent boundary layer rather than bow waves. This can be deduced since the structure of the formations varies considerably in shadowgraphs for neighboring azimuth positions, while the shape of the trailing wave does not. Also, a faintly visible bow wave formation is seen in some of the shadowgraph views about a chord upstream of the leading edge. The prediction for the bow wave is in the neighborhood of the fluctuating recompressions rather than the observed upstream position. Further study of the aerodynamics of the prop-fan blade is necessary to clarify the nature of the bow wave and the downstream recompressions.

The results of shadowgraph measurements for the SR-2 model, operating at 1.138 tip helical Mach number with a loading of 23.2 kW (31.2 SHP) per blade, are shown in Figure 3-69. Note that the trailing wave attaches to the blade further outboard than it does for the higher tip speed case shown above. The section Mach number is about 1.02 at the attachment point. The attachment point is well predicted. Note also that there are fewer upstream wave formations. The bow wave is predicted to be in the area of recompression although a faint bow wave was observed further upstream in some shadowgraph views.

Wave formations associated with the SR-3 model blade were measured for the two test conditions shown in Figures 3-70 and 3-71. The measurements are shown with respect to the developed planform projected onto the helicoid as defined by the noise prediction computer program. The model was in a four-blade configuration, with 25.2 degrees reference blade angle and 0.320 tunnel Mach number for both tests.

The results of measurements for 1.185 tip helical Mach number testing at a loading of 26.7 kW (36 SHP) per blade are shown in Figure 3-70. The trailing wave is well defined in the shadowgraphs and is well predicted. It attaches to the blade at about the 90% radius. The section Mach number is about 1.08 at this point. Note that this is further outboard (due to blade sweep) than in the SR-2 case operating at a similar tip helical Mach number. A bow wave is not predicted for this case although it is faintly visible in some views. Results for the SR-3 operating at 1.071 tip helical Mach number at a loading of 15.1 kW (20 SHP) per blade are shown in Figure 3-71. The trailing wave attaches at about the 95% radius where the section Mach number is 1.04 and is well predicted. A bow wave is predicted for this case but not observed in the shadowgraphs. Note that outboard of the 90% radius, the leading edge of SR-3 is swept behind the predicted bow wave. The leading edge of the unswept SR-2 model (Figures 3-68 and 3-69) is not. At the trailing edge, however, the wave and edge line up to concentrate the recompression and thus produce the strong positive peaks seen in the acoustic pressure pulse waveforms in Figures 3-35 and 3-63.

In summary, it has been shown that the trailing wave shapes and attachment points to the blades established by the shadowgraph technique are well predicted by the prop-fan noise methodology. The shadowgraphs do not clearly show the location of the bow waves for either the unswept or swept blades although the location of a bow wave is predicted by the methodology. Further work is required to establish the reason for the lack of a well defined bow wave in the shadowgraphs.

Evidence of Non-Linear Flow Effects

In this section the experimental and theoretical evidence described above is used to study the extent to which linear acoustic theory represents the noise generation process. In the earlier section where experimental and theoretical pulse shapes were compared,

it was shown that the qualitative features of the pulses were well predicted: the shapes were generally correct as were the trends with directivity, Mach number, and loading. In a quantitative sense, however, there were some consistent discrepancies: the amplitude of the negative part of the pressure pulse and the pulse duration were both underpredicted. Agreement was generally better for swept blades than for straight blades. The amplitude discrepancy is believed to be caused primarily by transonic non-linearity effects. These can be accounted for approximately with the quadrupole source term in the Acoustic Analogy as described by Hanson and Fink (Reference 3-11).

The pulse duration discrepancy, in principal, should also be calculable with the quadrupole term. In fact, Ffowcs Williams (Reference 3-13) showed for the supersonic wedge problem that a primary role for the quadrupoles is to relocate wavefronts. Ffowcs Williams' analysis was possible because the exact flow field for the wedge is known from aerodynamic theory. Since the answer must be known in advance for this kind of analysis, it is not useful in noise prediction methods. However, the experimental evidence for prop-fans reported above gives new insight on the pulse duration discrepancy and will now be discussed.

Theoretical Comparisons - Figures 3-58 through 3-64 show the extent to which pulse duration is underpredicted by the linear theory. The predictions for straight blades at high loading are least accurate, with durations being underpredicted by as much as 50%. This kind of discrepancy was noted by Hawkings and Lowson (Reference 3-4) who claimed this was the result of non-linear propagation from source to far field observer. However, the very near field waveform data (to be discussed below) shows that the discrepancy appears as close as 1.9 cm (3/4 inch) from the blade tip.

The shadowgraph results in Figures 3-68 to 3-71 show that the linear theory predicts the trailing wave attachment point reasonably accurately. The error then must be in the bow wave location. This is reasonable since it is well known that bow shocks are detached from blunt bodies at low supersonic speeds as shown in Figure 3-72. Unfortunately, the bow waves could not be located accurately in the prop-fan shadowgraphs although Hilton's shadowgraphs for a different propeller (Reference 3-12) clearly show the bow shock detached about 1/2 chord from the leading edge as shown in Figure 3-73. The presence of the bow wave is evident, however, in the oscilloscope pulse photographs taken of the SR-2 acoustic waveform during very near field testing (see Figure 3-11). The arrival time of these pulses was measured from the photographs and was plotted versus microphone distance in Figure 3-74 along with predictions from the linear theory. Since the absolute location of the blade at the firing of the sync signal (pipper) was known only within $\pm 5^{c}$ of shaft rotation, the experimental pattern was shifted in the time direction to match trailing waves with the shadowgraph results shown in Figures 3-68. The 5° uncertainty does not cause significant error in the shadowgraph interpretation discussed in the preceding section.

Figure 3-74 thus demonstrates important differences between test results and linear theory. First, the bow wave does appear to be detached, causing the test pulse to be longer than predictions at the blade tip. Second, the pulse discrepancy increases with distances out to about 12.7 cm (5 in.) from the tip where the propagation rate appears to match linear predictions. Note the theoretical propagation rate, as given by the slopes of the curves in Figure 3-74, is greater than the ambient sound speed because of geometric near field effects.

Conclusions on Pulse Duration Discrepancy - The underprediction of the pulse widths for the straight blades is explainable as a combination of bow shock detachment and non-linear propagation within 2 chords of the blade tip. The conclusion of Hawkings and Lowson (Reference 3-4) that the discrepancy develops in propagation to a far field observer does not seem to apply to this prop-fan data.

As seen in the measured acoustic pressure pulse waves (see Figure 3-37), the SR-3 blades do not exhibit a prominent bow shock. This is because they are swept behind the Mach waves (i.e., predicted bow waves). The linear theory is thus more successful for swept blades than for unswept blades and, with minor amplitude adjustments from quadrupole estimates, should be accurate enough for design of swept blades.

Full Scale Noise Projections

The near field 8P harmonic noise level at cruise and the far field Effective Perceived Noise Level during takeoff have been estimated based on the results of the test program and the prop-fan noise prediction methodology.

The near field 8P harmonic noise at the cruise condition of 302 kW/m^2 (37.5 SHP/D^2) at 10,667 m (35,000 ft) altitude and a tip clearance of 0.8 D was predicted using the prop-fan Frequency Domain Noise Prediction Method. The theoretical prediction was adjusted upward by 2 dB based on studies of the correlation between measurements in the Acoustic Research Tunnel and theoretical predictions. This prediction is shown in Figure 3-75. The free field peak level of 146 dB is seen to occur aft of the plane of rotation with level falling off rapidly fore and aft of this location. The monopole (thickness) noise is seen to be the dominant source at the peak directivity point. The dipole (loading) noise contributes fore and aft of the plane of rotation with the quadrupole noise lower in level.

Sideline takeoff noise at a loading of 564 kW/m^2 (70 SHP/D^2), 244 m/s (800 ft/sec) tip speed, 25°C (77°F) and 70% relative humidity was estimated at 640 m (2100 ft) based on test data. The far field Effective Perceived Noise Level was derived from 1/3 octave band Acoustic Research Tunnel measurements of a two blade version of the SR-3. Measurements of tone noise components of prop-fan noise used for the predictions were

obtained at a tunnel through flow Mach number of 0.2 so no forward speed adjustments were required to make the full scale estimates at a 0.2 Mach number takeoff speed. Test data was interpolated to match the 564 kW/m^2 (70 SHP/D^2) and 244 m/s (800 ft/sec) tip speed requirements. Directivity data for the Effective Perceived Noise calculation was derived from the directivity data from the test with far forward and aft directivity based on past propeller prediction experience. Broadband noise used in the prediction is based on past experience with conventional propellers. A 3.84 m (12.6 ft) diameter was assumed to be the full scale size of the prop-fan for the estimate. A correction of +4.5 dB was used to correct for sideline prediction of a four engine aircraft. Figure 3-76 shows the resulting full scale estimate of the 1/3 octave band noise at the maximum sideline location. The Effective Perceived noise level based on this analysis is 91.5 EPNdB.

Table 3-I. Correction to Acoustic Data for Tunnel Shear Layer Effects

Sideline Tip Clearance (Prop Diameters)	Microphone Position	Measured Microphone Location	0.32 Mn		0.20 Mn	
			Level Correction	Corrected Location	Level Correction	Corrected Location
		X_{MEAS}/D	ΔdB	X_{CORR}/D	ΔdB	X_{CORR}/D
0.8 D (Near Field)	1	1.0	+3.3	0.57	+1.6	0.77
	2	0.5	+1.8	0.27	+0.9	0.37
	3	0.25	+1.2	0.07	+0.6	0.15
	4	0.0	+0.6	-0.15	+0.2	-0.09
	5	-0.25	+0.1	-0.39	-0.1	-0.34
	6	-0.5	-0.5	-0.65	-0.4	-0.60
	7	-1.0	-1.1	-1.21	-0.8	-1.15
4.4 D (Far Field)	60°	2.83	+3.0	0.83	+1.8	1.58
	70°	1.78	+2.0	0.20	+1.2	0.79
	80°	0.86	+1.1	-0.52	+0.6	0.0
	90°	0.0	+0.3	-1.29	+0.1	-0.81
	100°	-0.86	-0.6	-2.18	-0.4	-1.70
	110°	-1.78	-1.5	-3.27	-1.0	-2.73
	120°	-2.83	-2.5	-4.76	-1.6	-4.06

- Listener axial location relative to prop-fan plane of rotation.

-- Source location on-axis in plane of rotation.

Table 3-II. 8P Harmonic Vs. Overall Level (dB Re: 20 μPa)
Two-Blade Models

Harmonic	SR-1 1.073 M_{TH} 46.6 kW/Blade (62.5 SHP/B)	SR-2 1.180 M_{TH} 46.6 kW/Blade (62.5 SHP/B)	SR-3 1.225 M_{TH} 39.4 kW/Blade (52.8 SHP/B)
8P	137.1	143.6	133.0
16P	134.8	134.7	131.5
24P	127.4	133.9	125.9
32P	121.5	117.7	126.3
40P	116.9	126.6	121.2
48P	116.3	118.3	118.3
56P	118.3	120.3	117.3
64P	120.3	118.9	114.9
72P	121.2	107.4	111.9
80P	120.8	115.3	112.1
Sum	139.7	144.6	136.6
Sum 8P + 16P	139.1	144.1	135.3

Near Field Microphone 3 at 0.8 D Tip Clearance

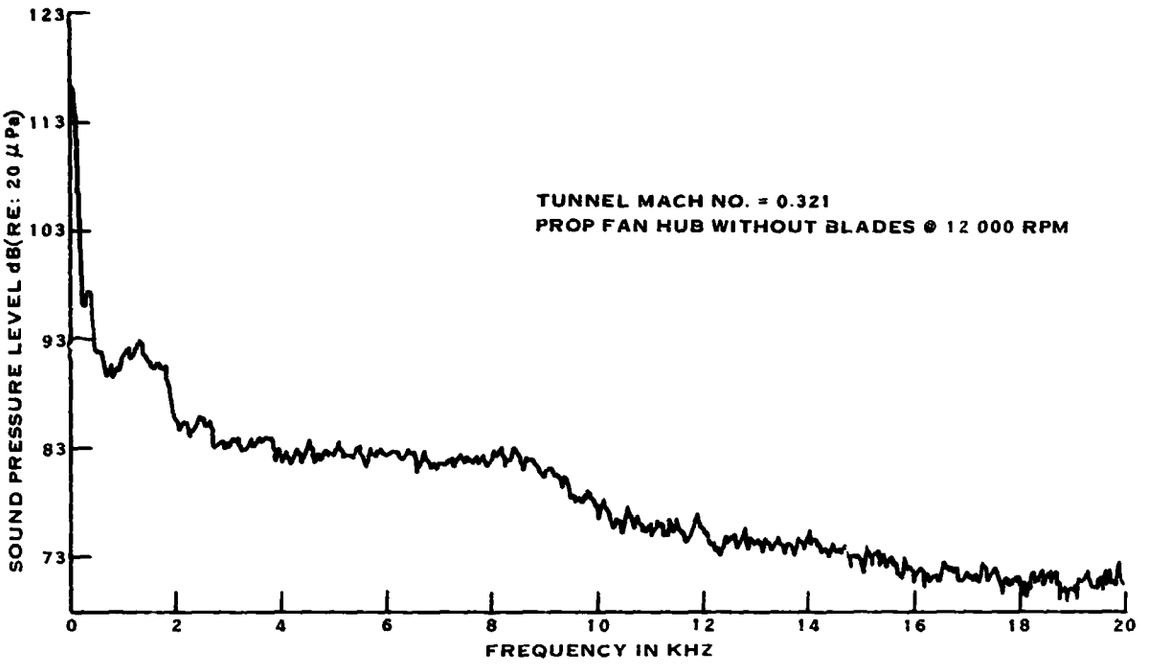

FIGURE 3-1A. BACKGROUND NOISE - NEAR FIELD

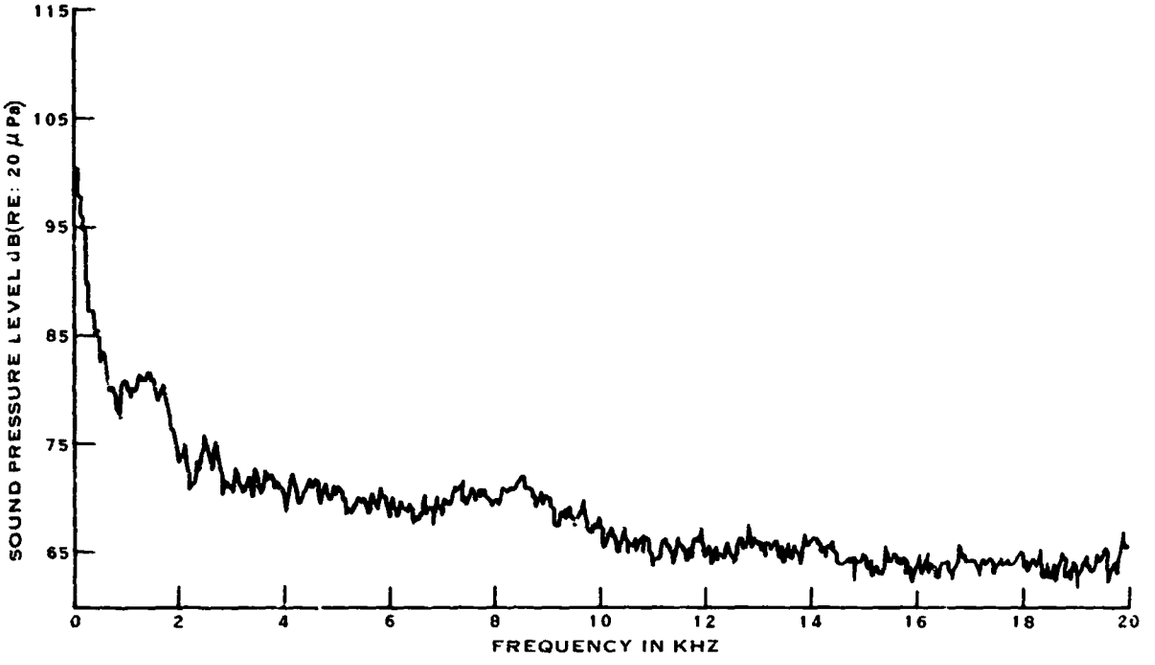

FIGURE 3-1B. BACKGROUND NOISE - FAR FIELD

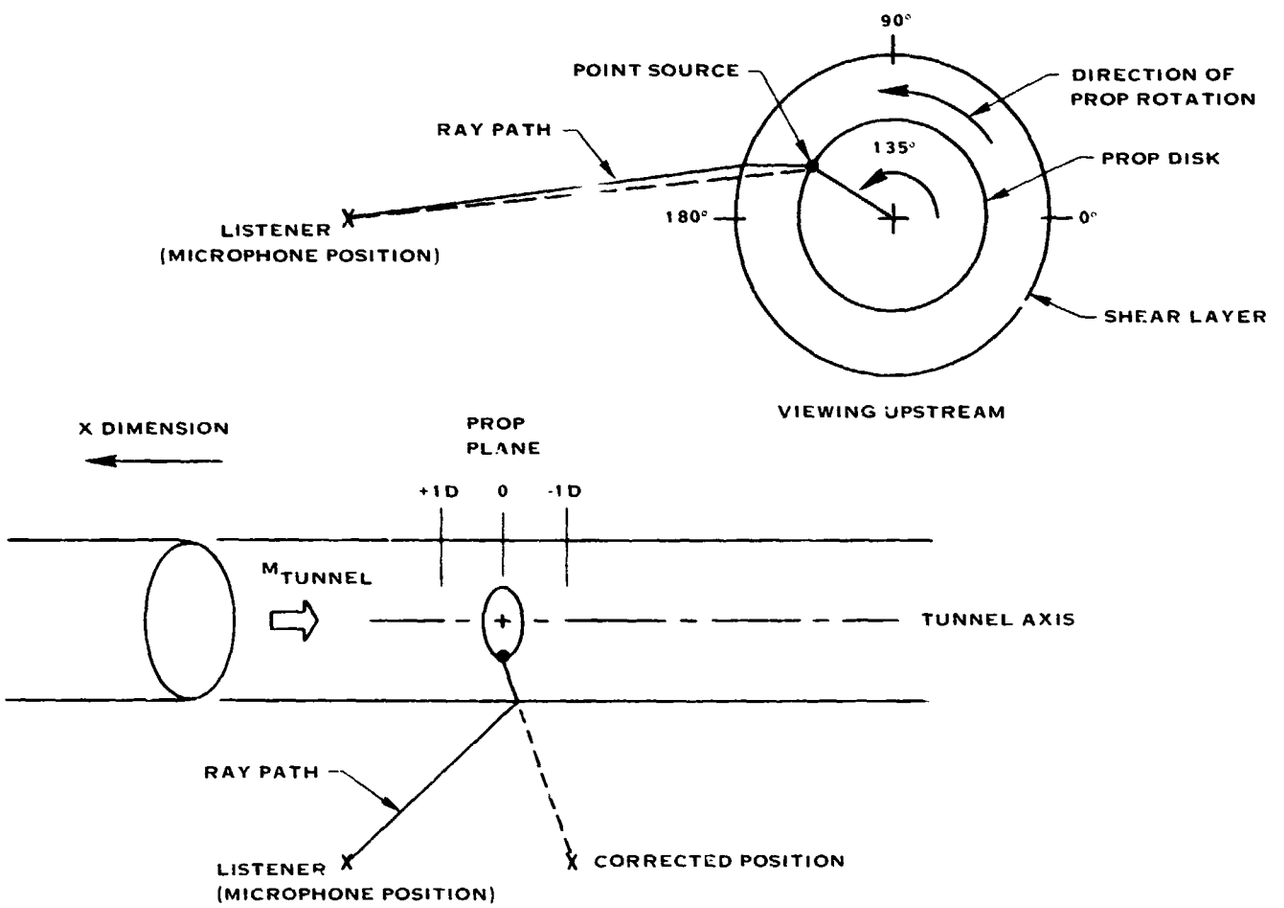

FIGURE 3-2. GEOMETRY FOR SHEAR LAYER CORRECTION

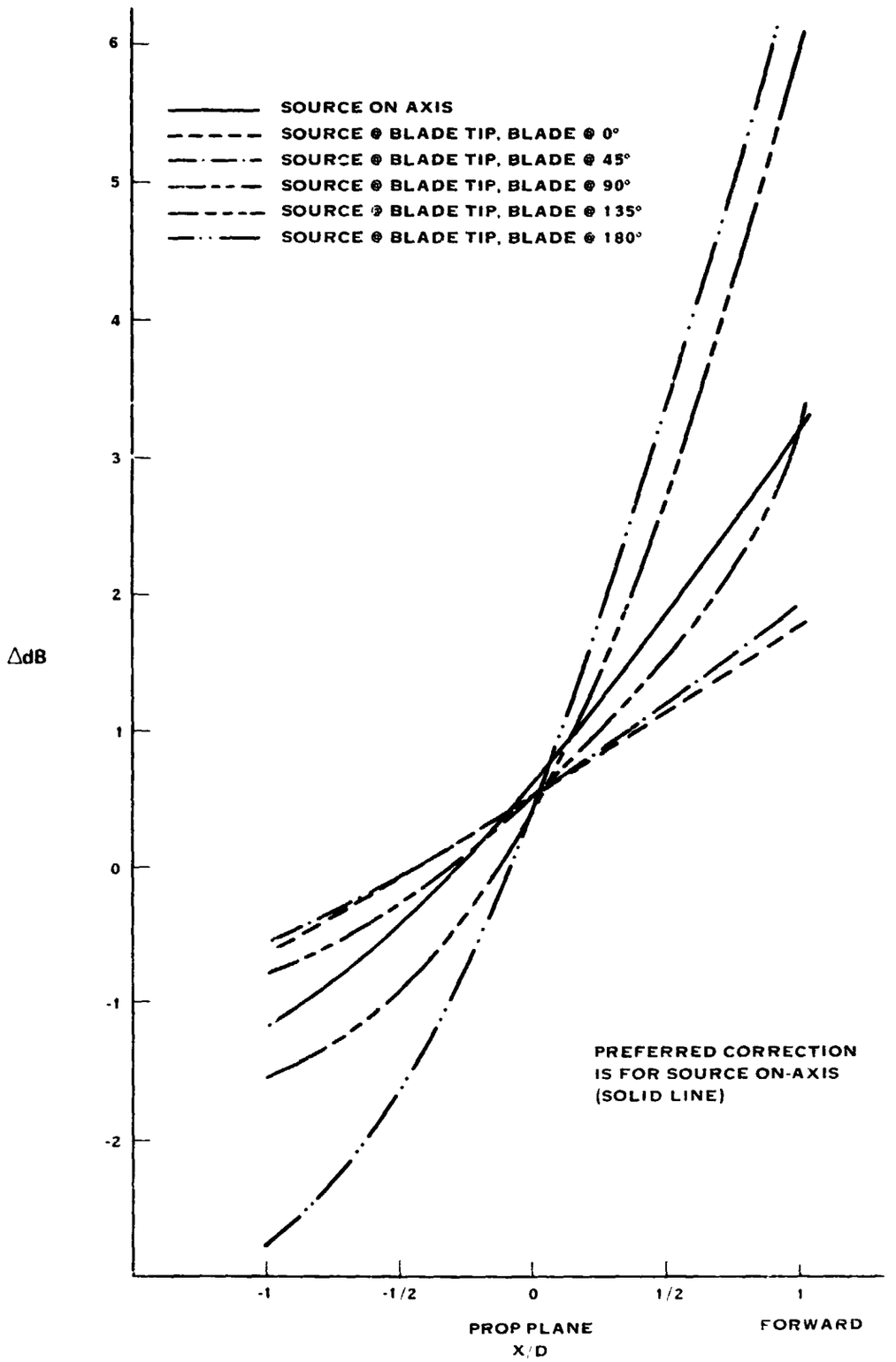

FIGURE 3-3. TUNNEL SHEAR LAYER AMPLITUDE CORRECTION
0.8D TIP CLEARANCE 0.32 TUNNEL MACH NUMBER

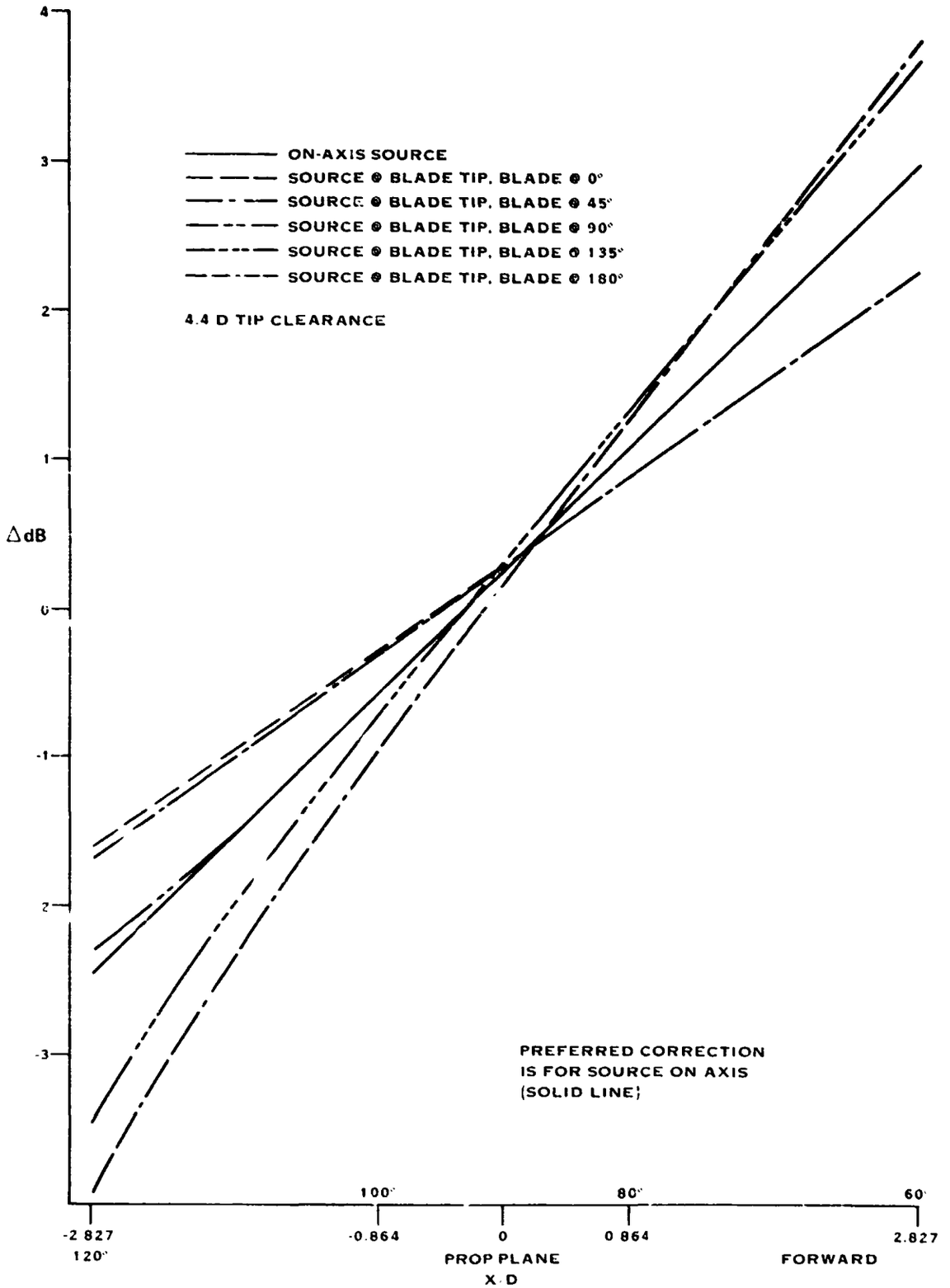

FIGURE 3-4 TUNNEL SHEAR LAYER AMPLITUDE CORRECTION
FAR FIELD 0.32 TUNNEL MACH NUMBER

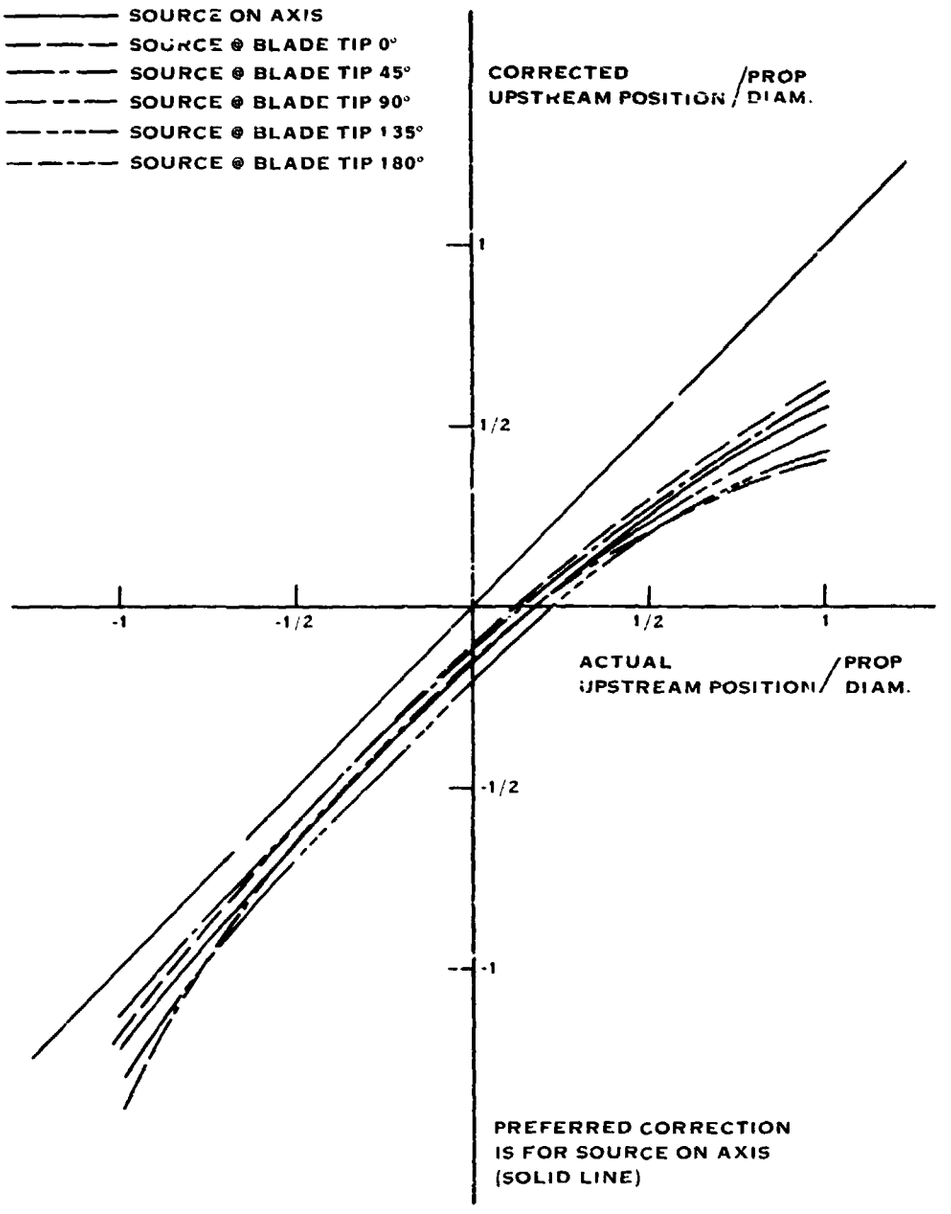

FIGURE 3-5. TUNNEL SHEAR LAYER AXIAL LOCATION CORRECTION
0.8D TIP CLEARANCE 0.32 TUNNEL MACH NUMBER

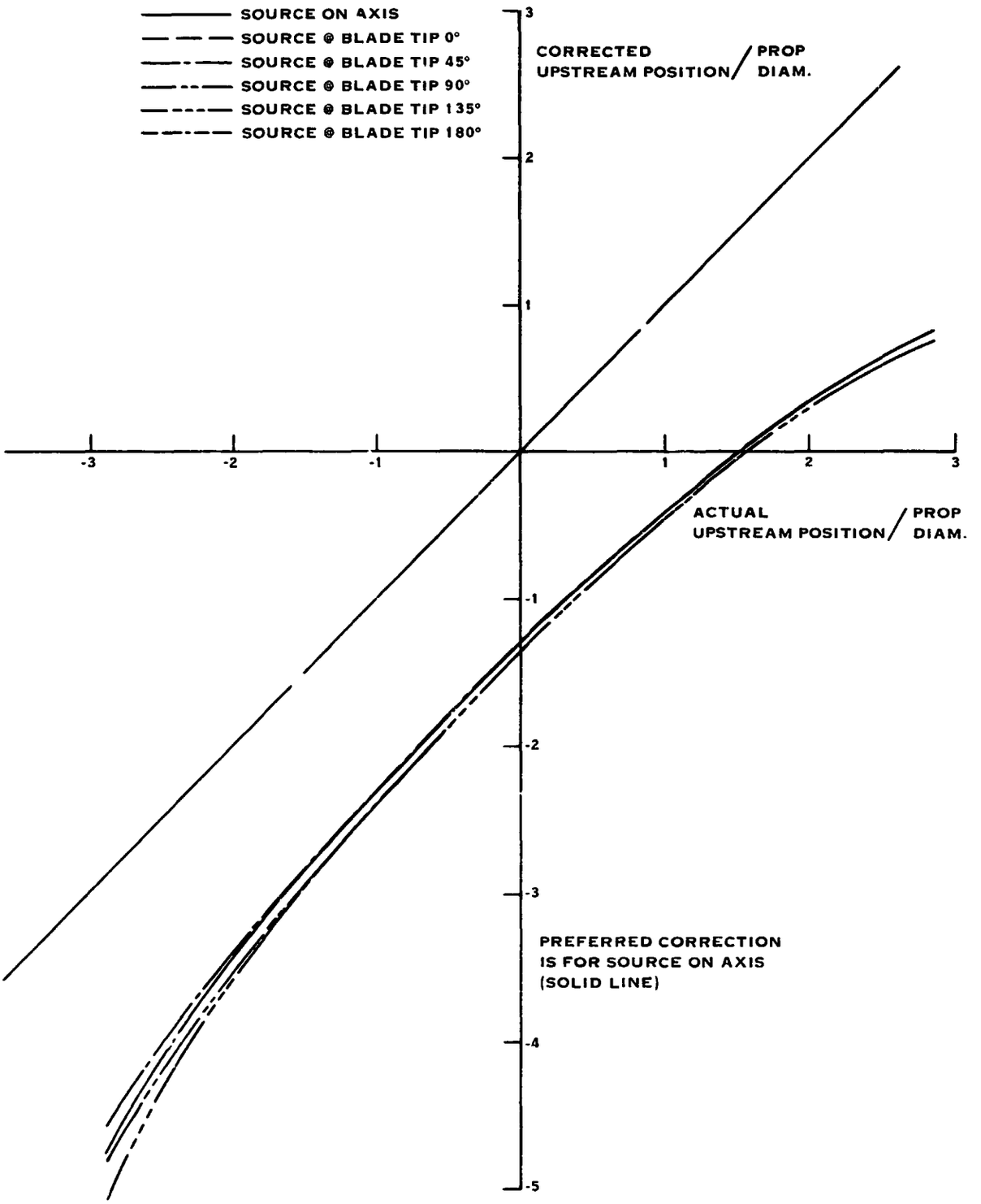

FIGURE 3-6. TUNNEL SHEAR LAYER AXIAL LOCATION CORRECTION FAR FIELD 0.32 TUNNEL MACH NUMBER

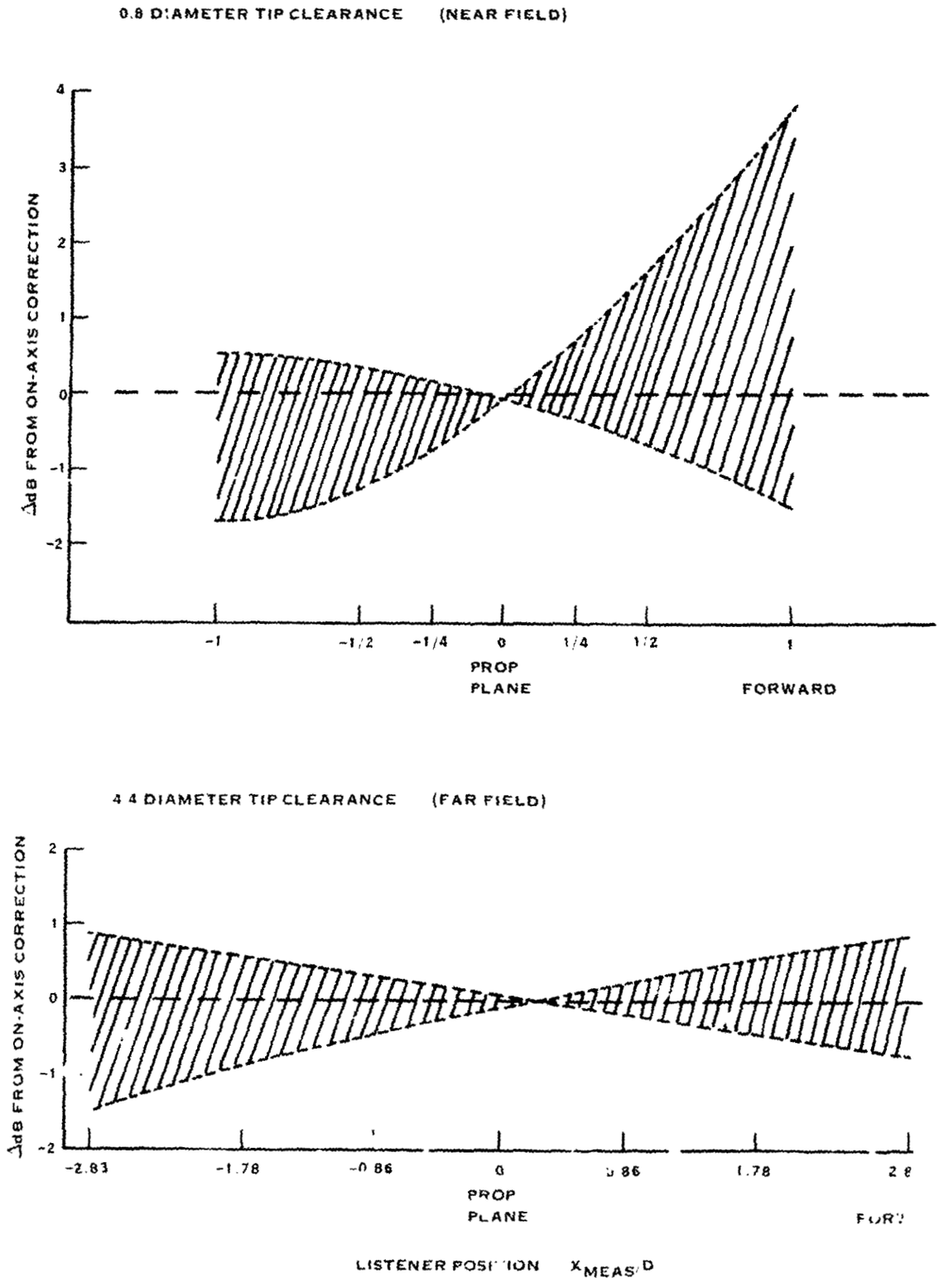

FIGURE 3-7. UNCERTAINTY IN SHEAF AYER CORRECTION

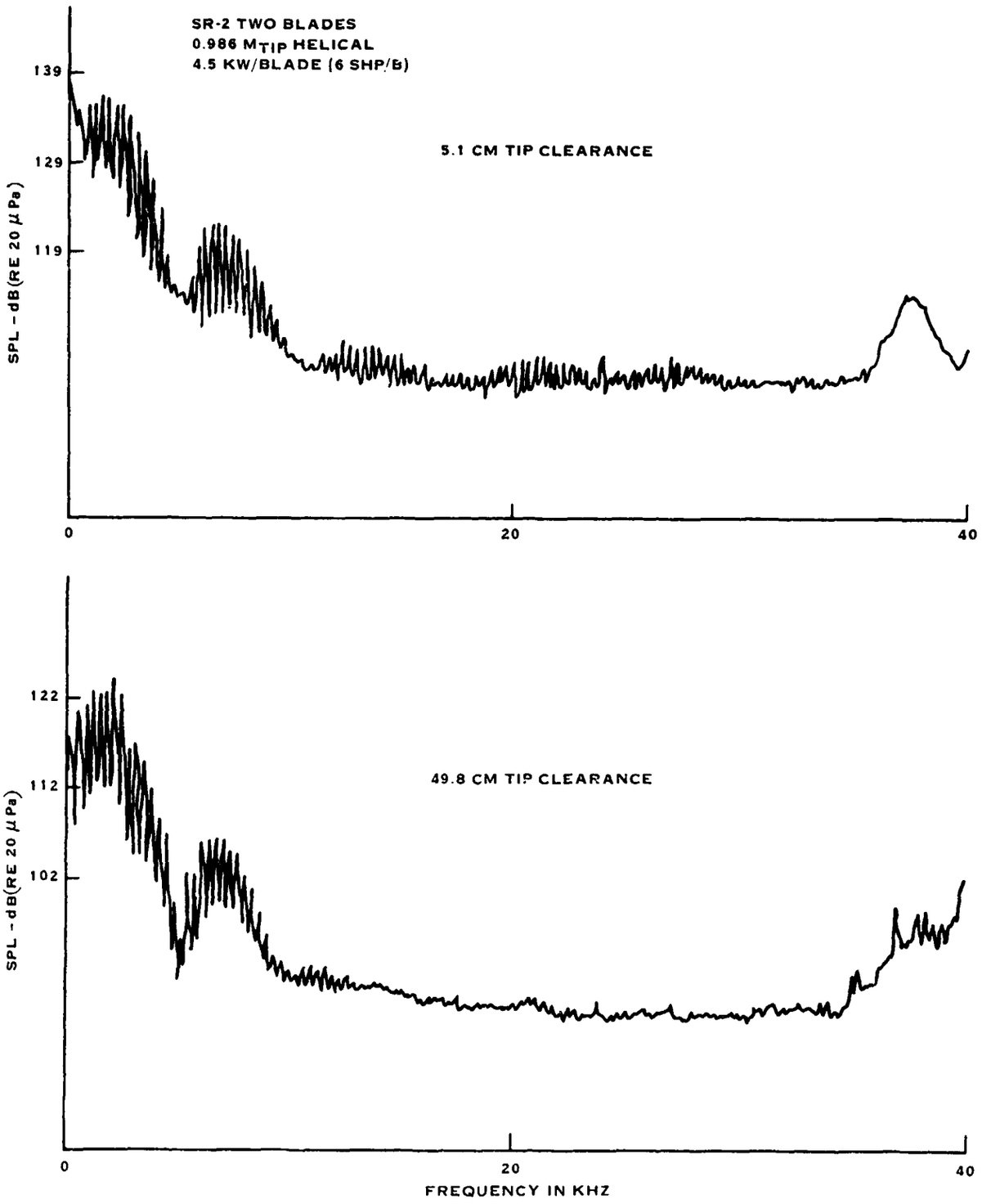

FIGURE 3-8. COMPARISON OF SPECTRA MEASURED INSIDE AND OUTSIDE THE SHEAR LAYER

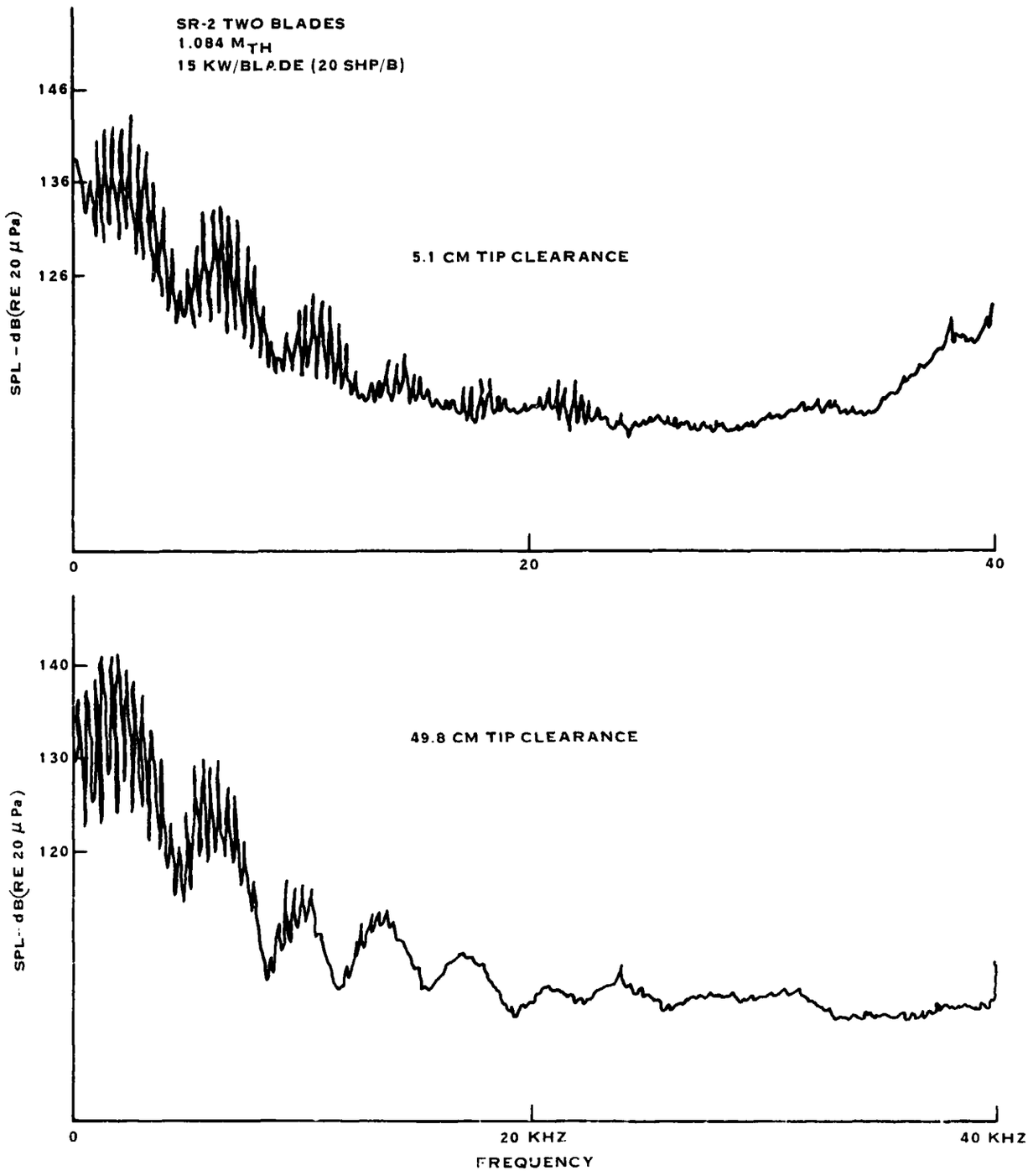

FIGURE 3-9. COMPARISON OF SPECTRA MEASURED INSIDE AND OUTSIDE OF SHEAR LAYER

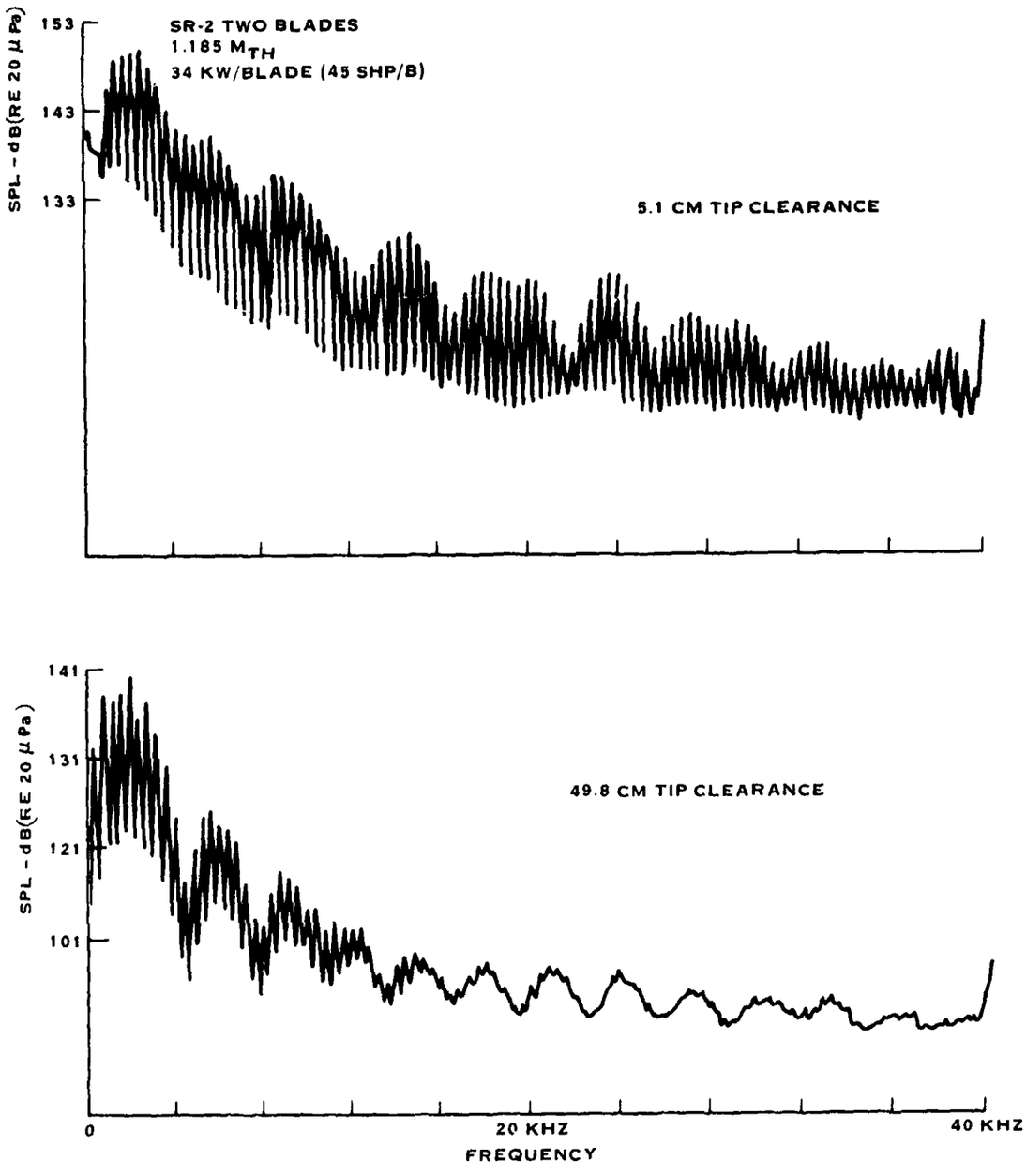

FIGURE 3-10. COMPARISON OF SPECTRA MEASURED INSIDE AND OUTSIDE OF SHEAR LAYER

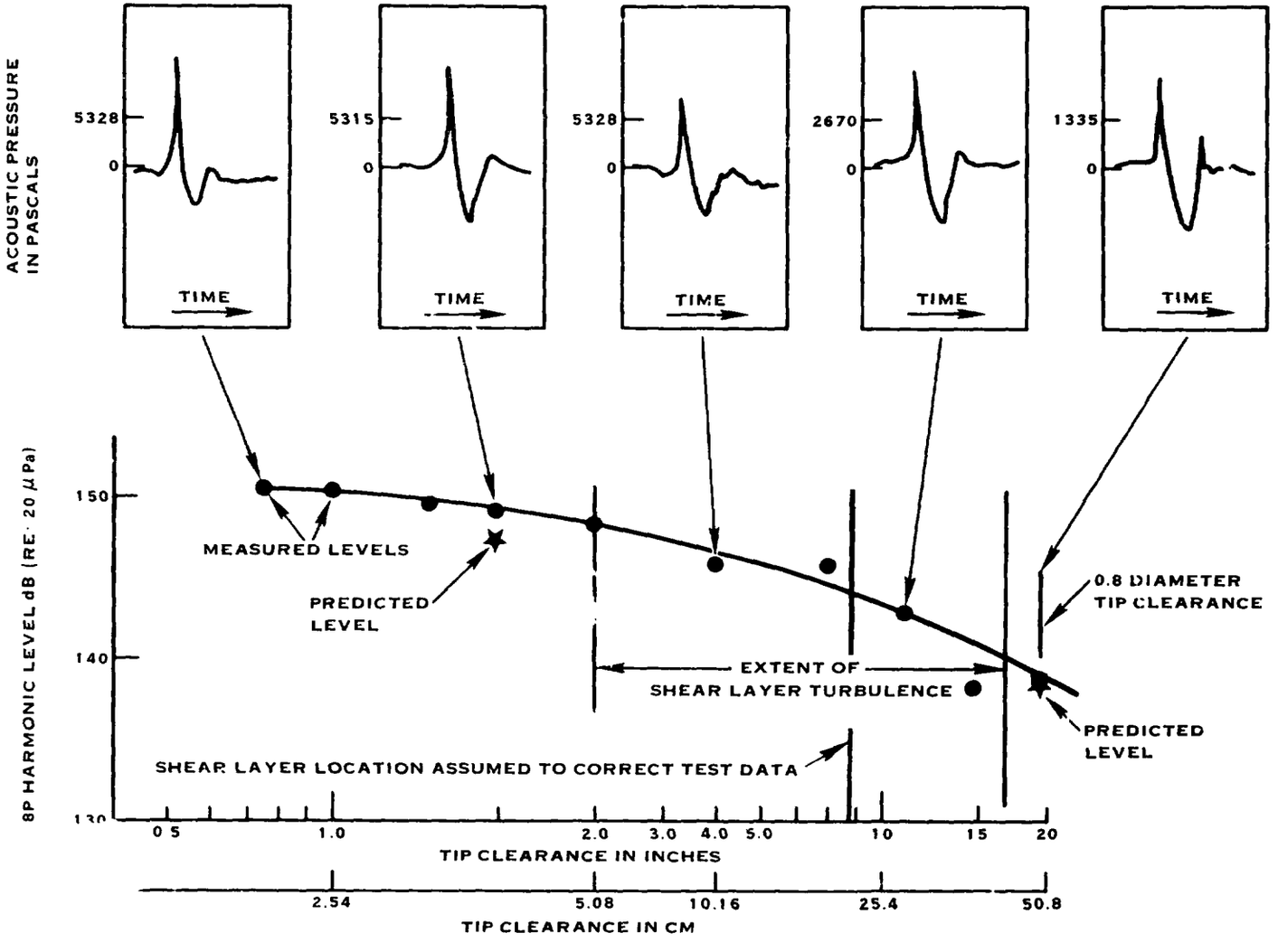

FIGURE 3-11. INFLUENCE OF SHEAR LAYER ON ACOUSTIC PRESSURE PULSE AND 8P HARMONIC LEVEL OF SR-2 AT 1.185 TIP HELICAL MACH NUMBER (2 BLADE 33.6 KW (45 SHP) PER BLADE)

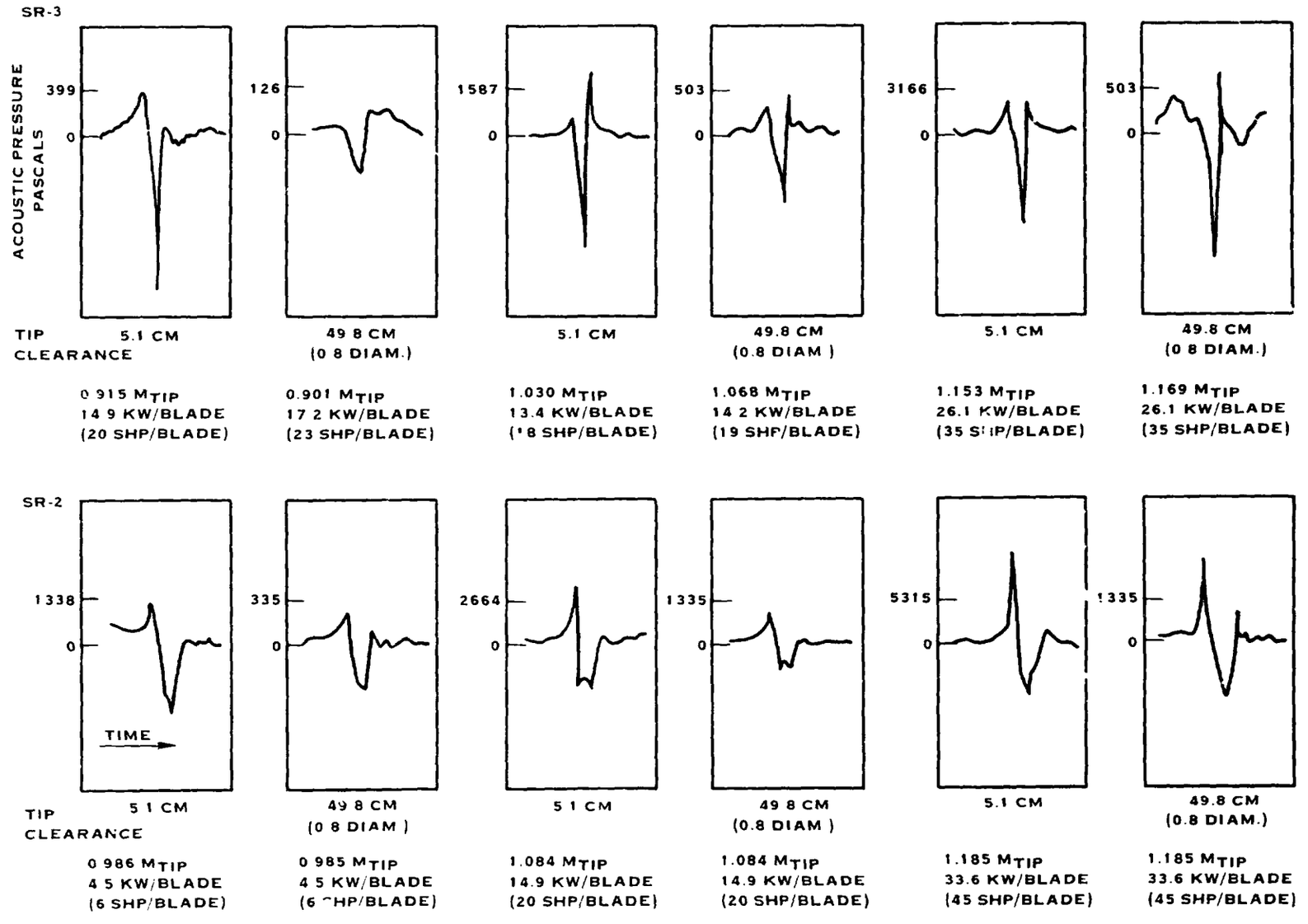

FIGURE 3-12. ACOUSTIC PULSE - INSIDE AND OUTSIDE SHEAR LAYER

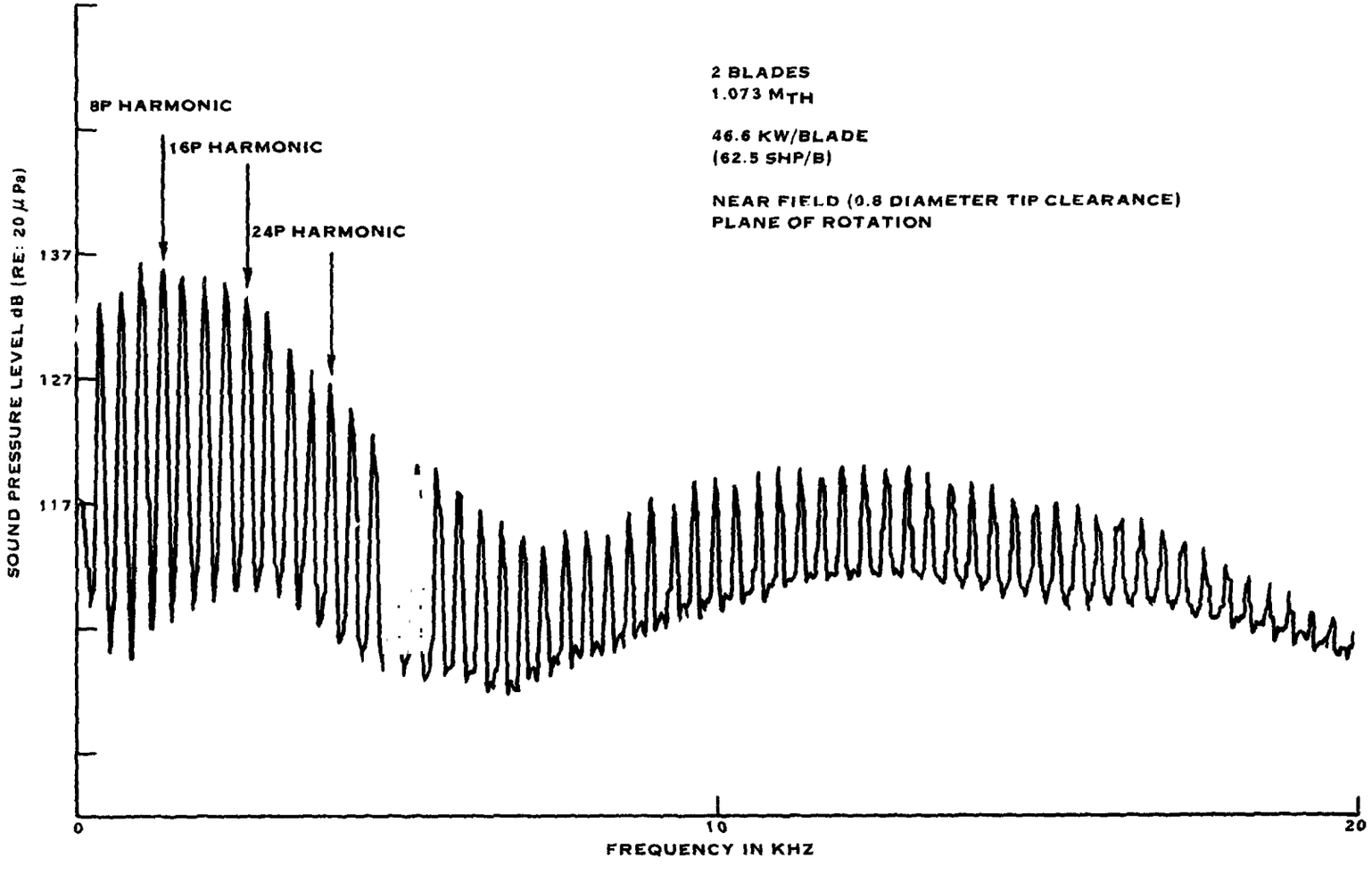

FIGURE 3-13. SR-1 SOUND PRESSURE LEVEI SPECTRUM

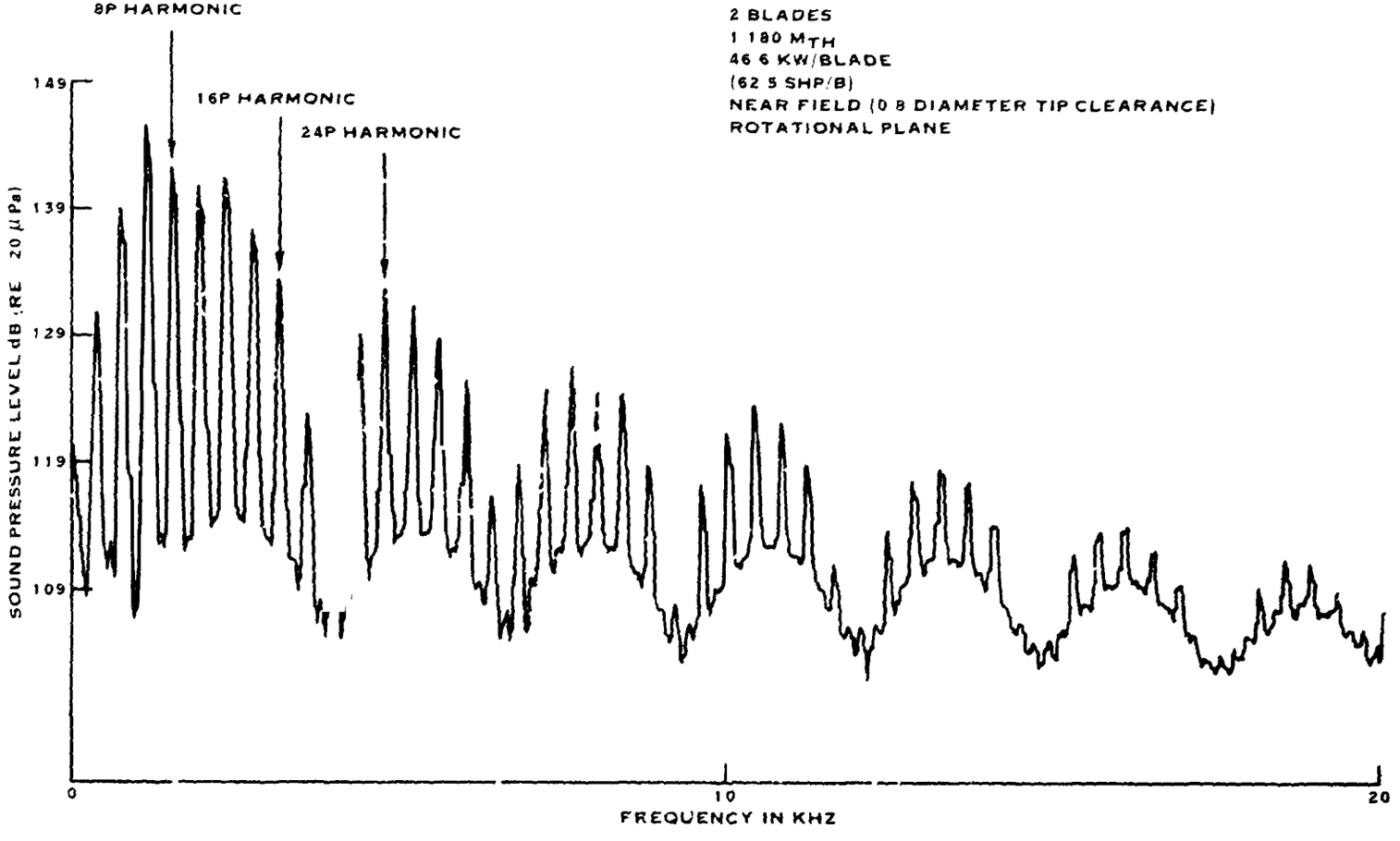

FIGURE 3-14. SR-2 SOUND PRESSURE LEVEL SPECTRUM

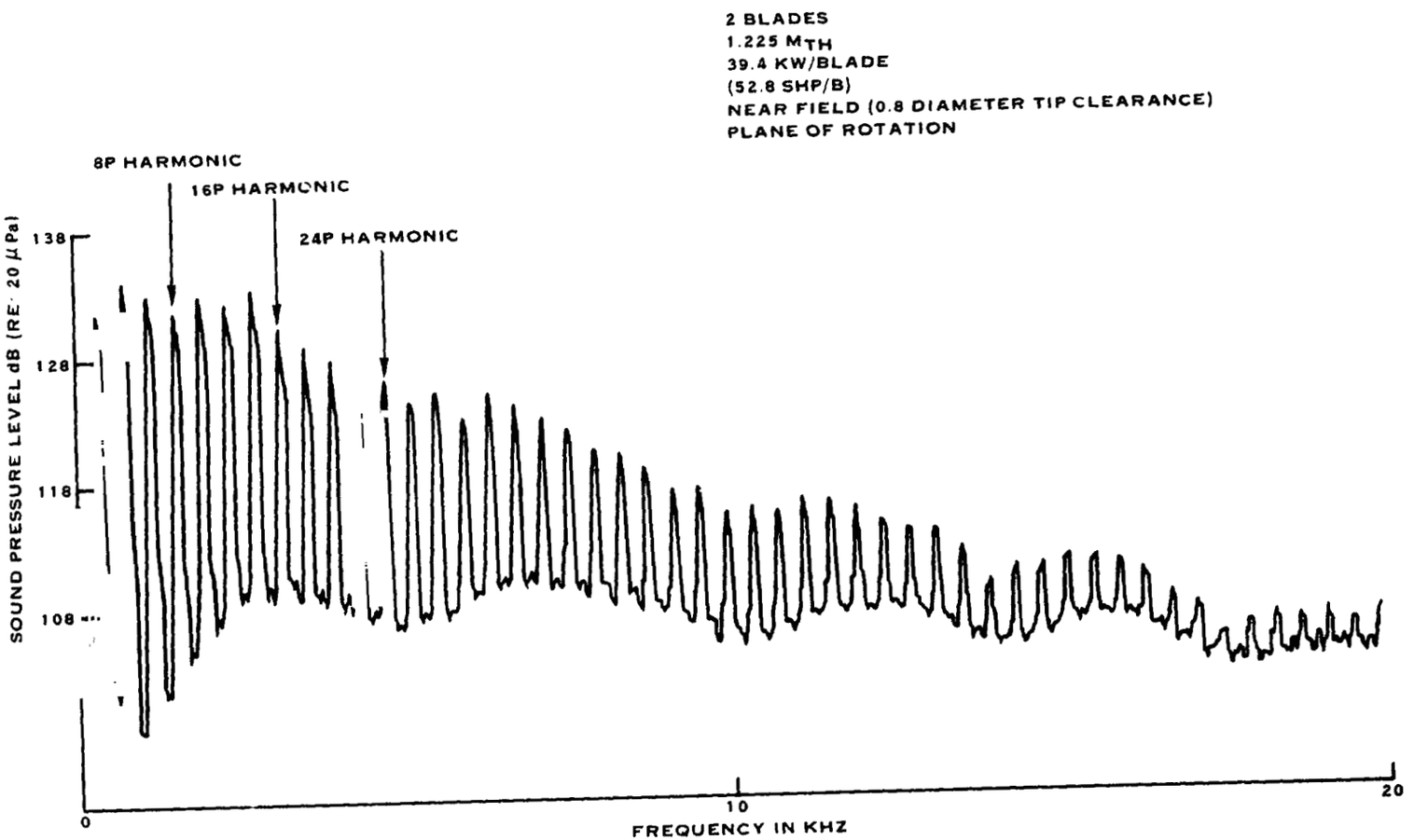

FIGURE 3-15. SR-3 SOUND PRESSURE LEVEL SPECTRUM

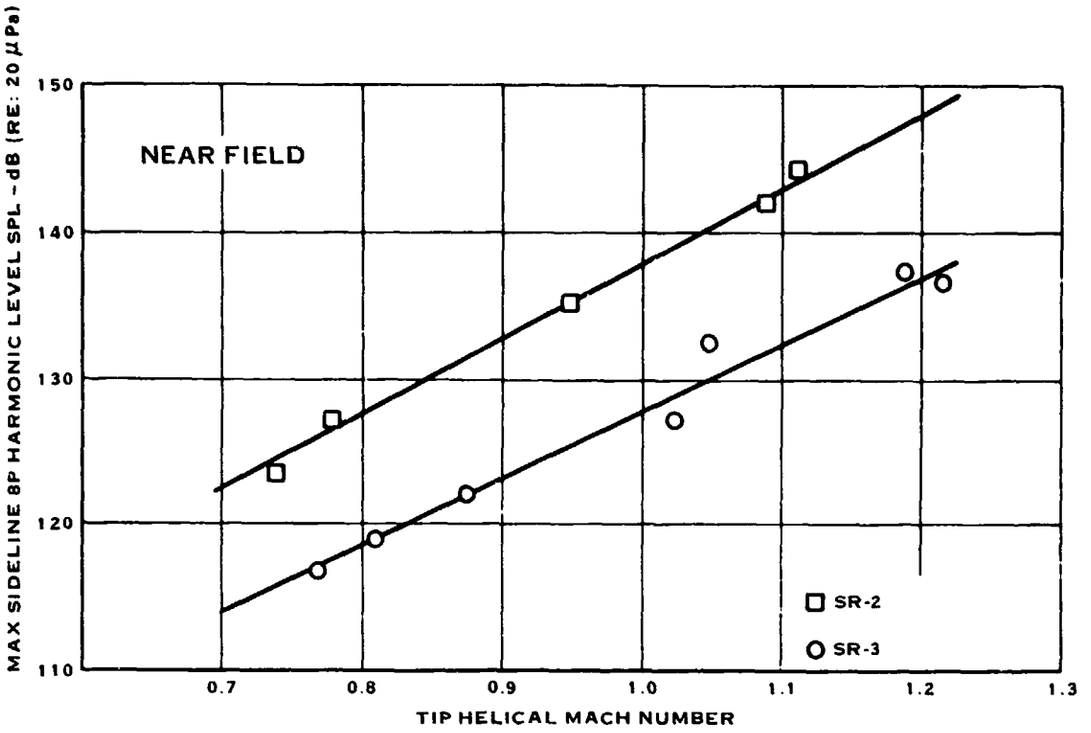

FIGURE 3-16A. MAXIMUM SIDELINE 8P HARMONIC FOR A TWO BLADE CONFIGURATION
HIGH LOADING ~ 28 KW (37 SHP) PER BLADE
0.8D TIP CLEARANCE

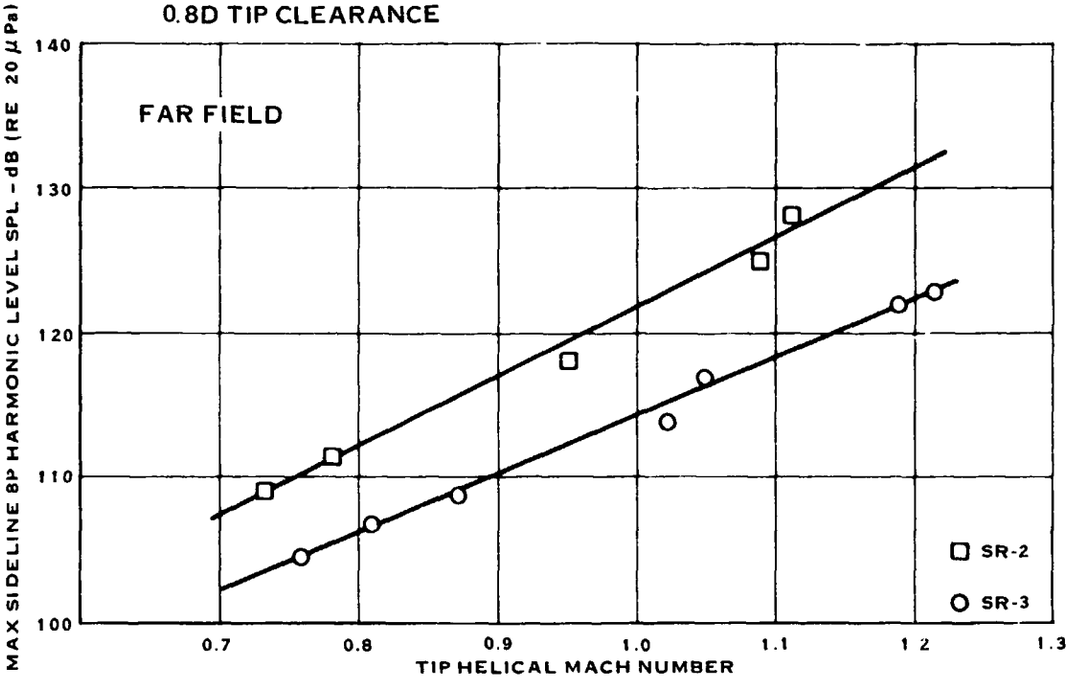

FIGURE 3-16B. MAXIMUM SIDELINE 8P HARMONIC FOR A TWO BLADE CONFIGURATION
HIGH LOADING ~ 28 KW (37 SHP) PER BLADE
4.4D TIP CLEARANCE

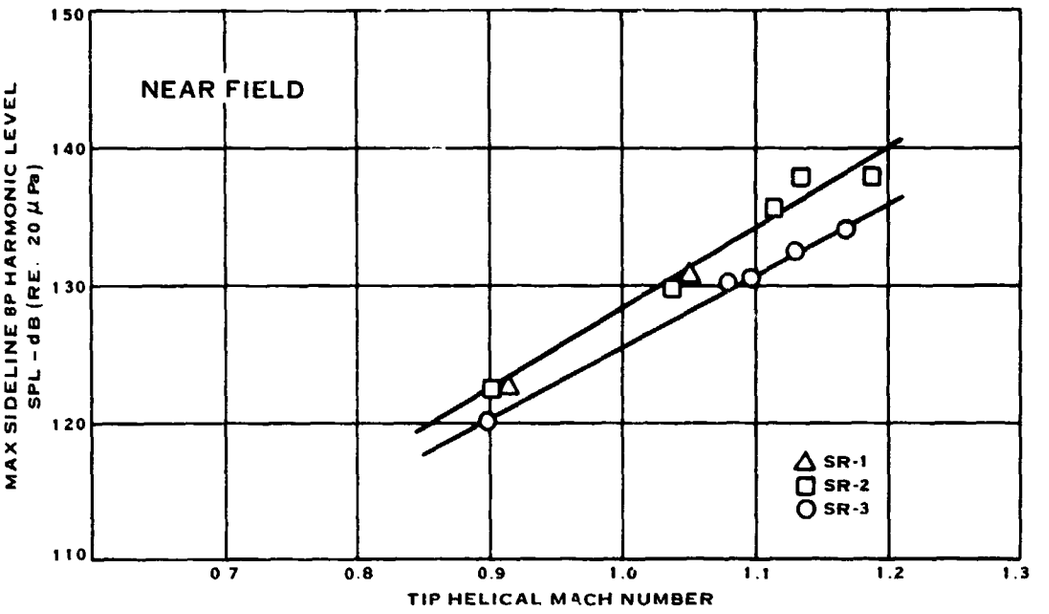

FIGURE 3-17A. MAXIMUM SIDELINE 8P HARMONIC FOR A TWO BLADE CONFIGURATION
MODERATE LOADING ~ 19 KW (25 SHP) PER BLADE
0.8D TIP CLEARANCE

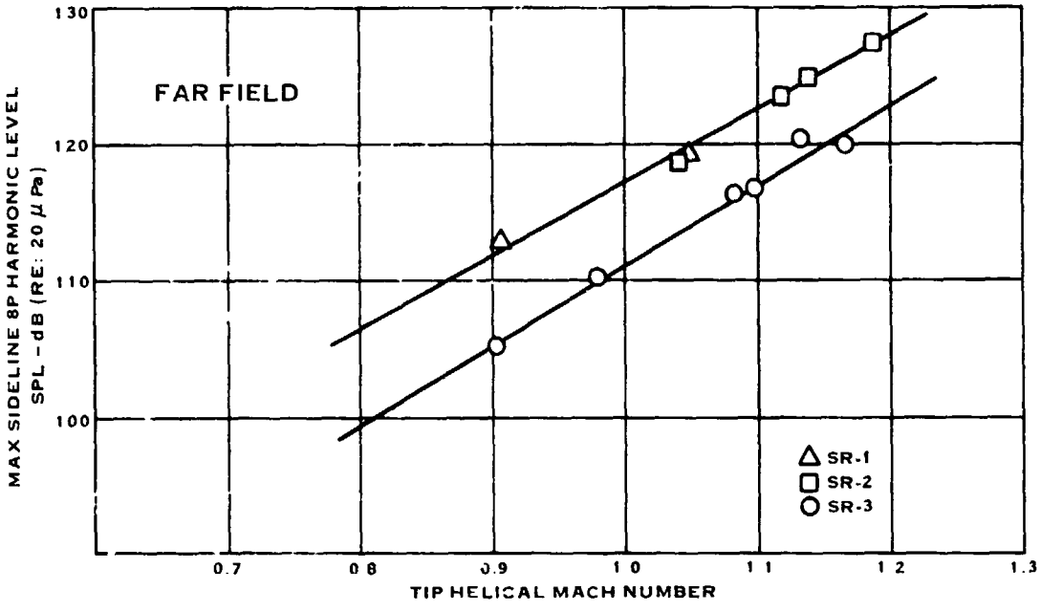

FIGURE 3-17B. MAXIMUM SIDELINE 8P HARMONIC FOR A TWO BLADE CONFIGURATION
MODERATE LOADING ~ 19 KW (25 SHP) PER BLADE
4.4D TIP CLEARANCE

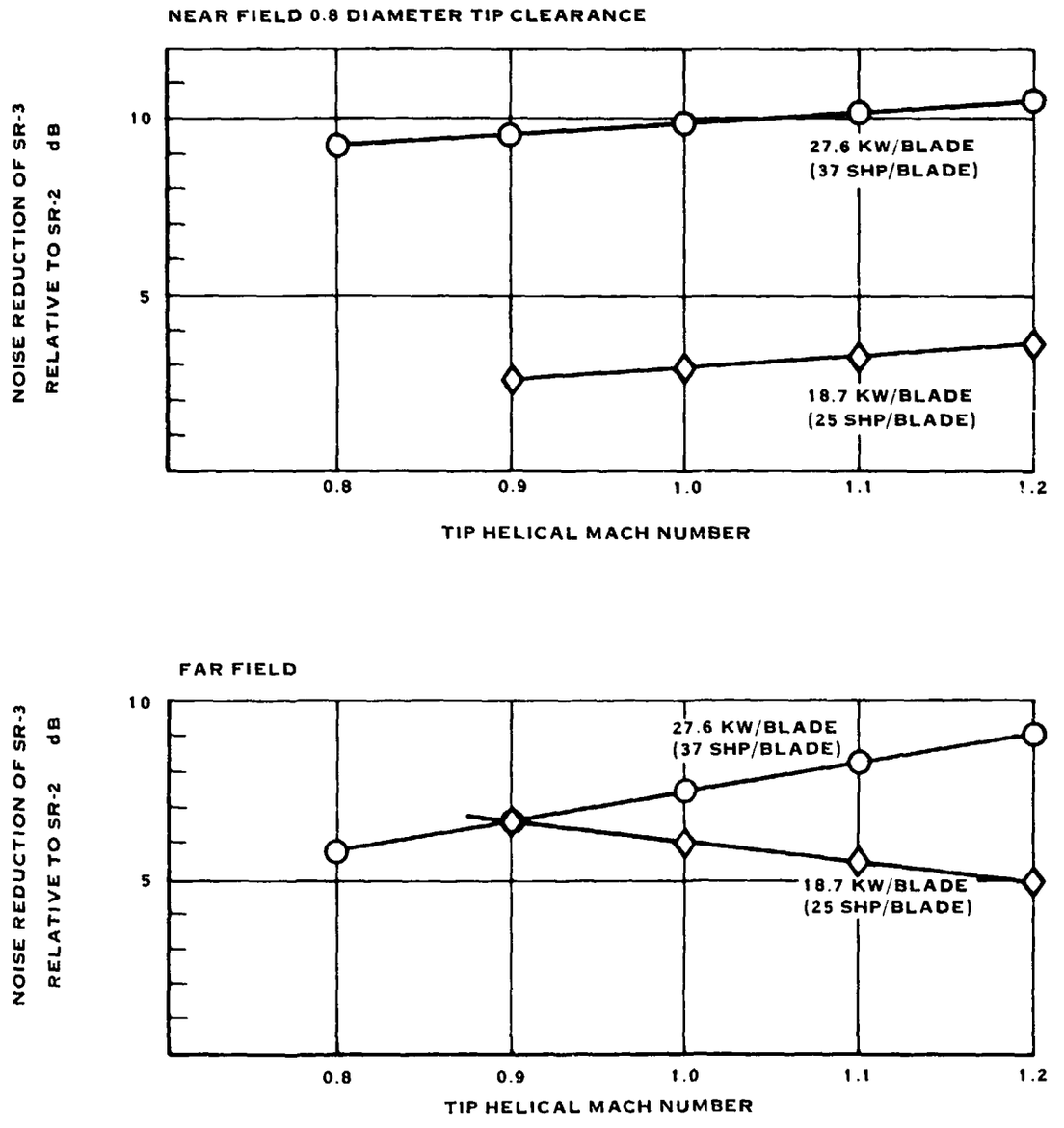

FIGURE 3-18. 8P HARMONIC NOISE REDUCTION OF SR-3 RELATIVE TO SR-2

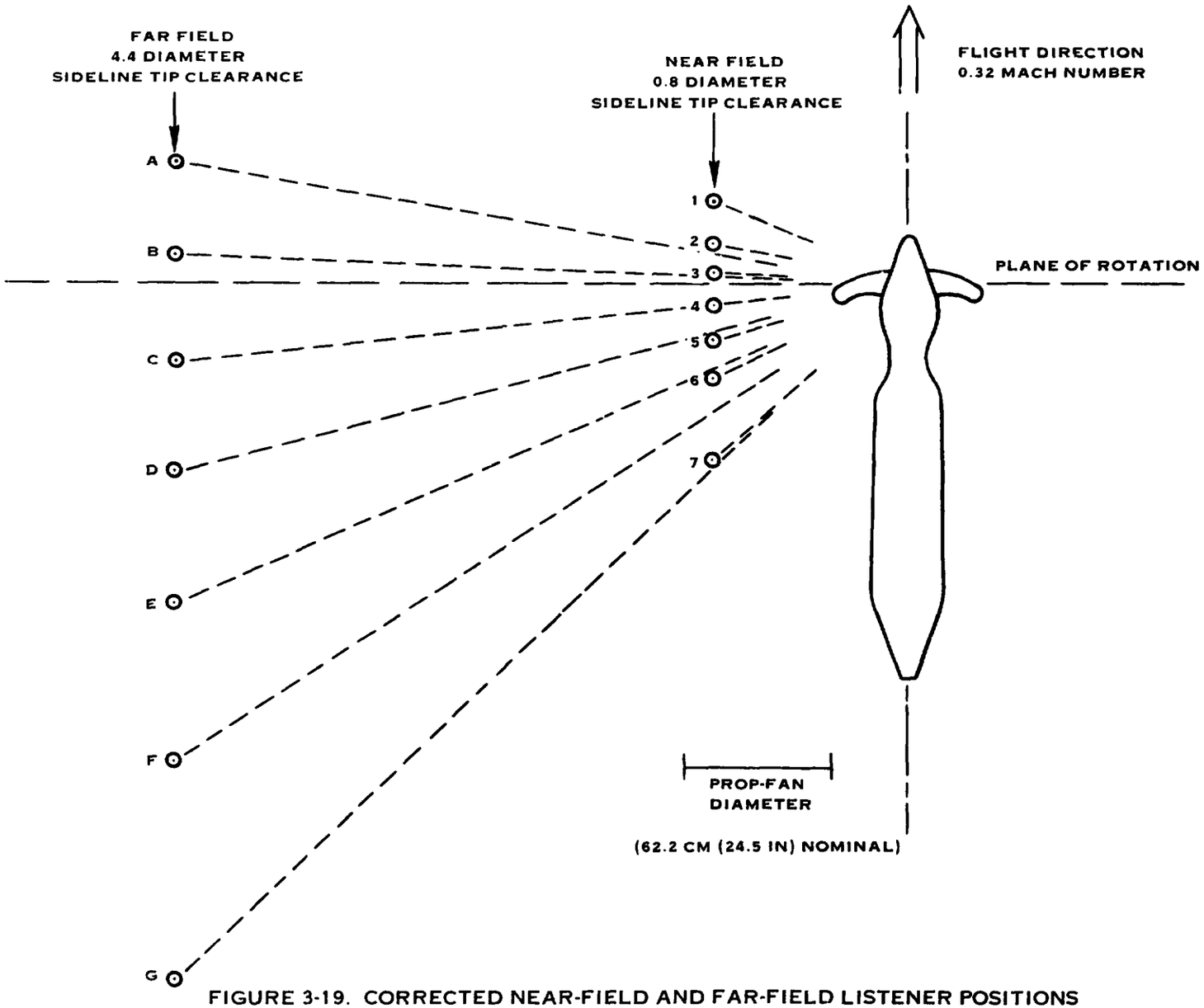

FIGURE 3-19. CORRECTED NEAR-FIELD AND FAR-FIELD LISTENER POSITIONS

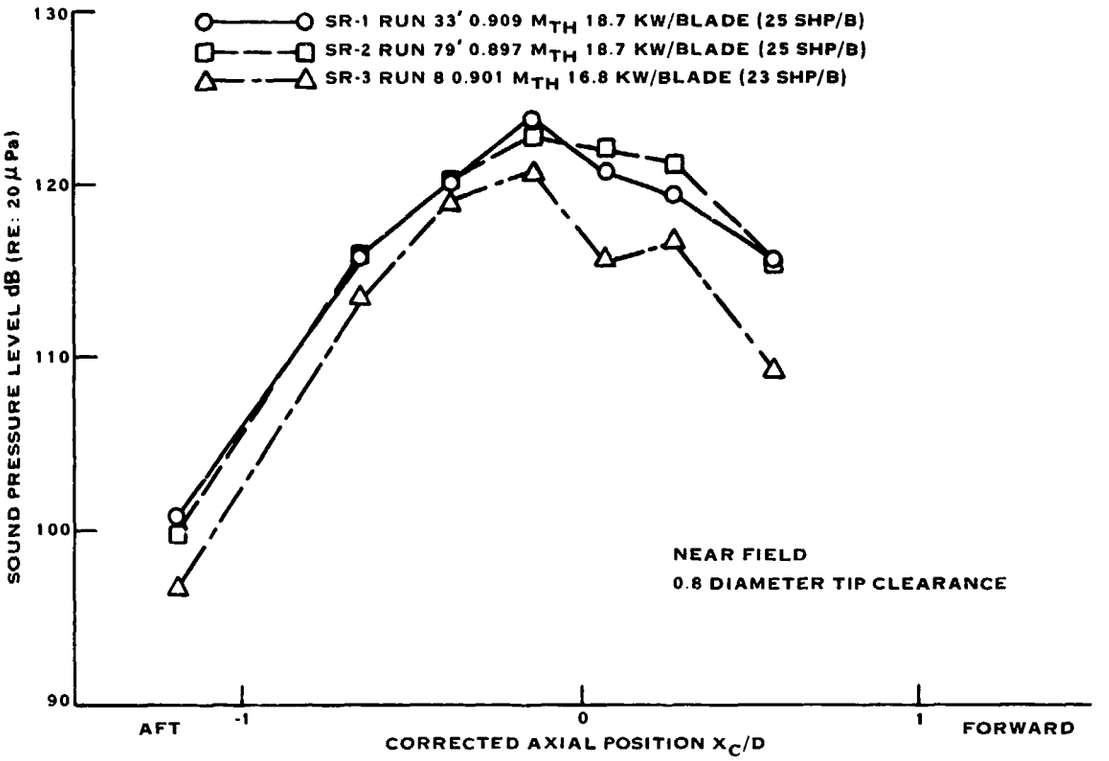

FIGURE 3-20A. 8P HARMONIC SIDELINE DIRECTIVITY TWO BLADES

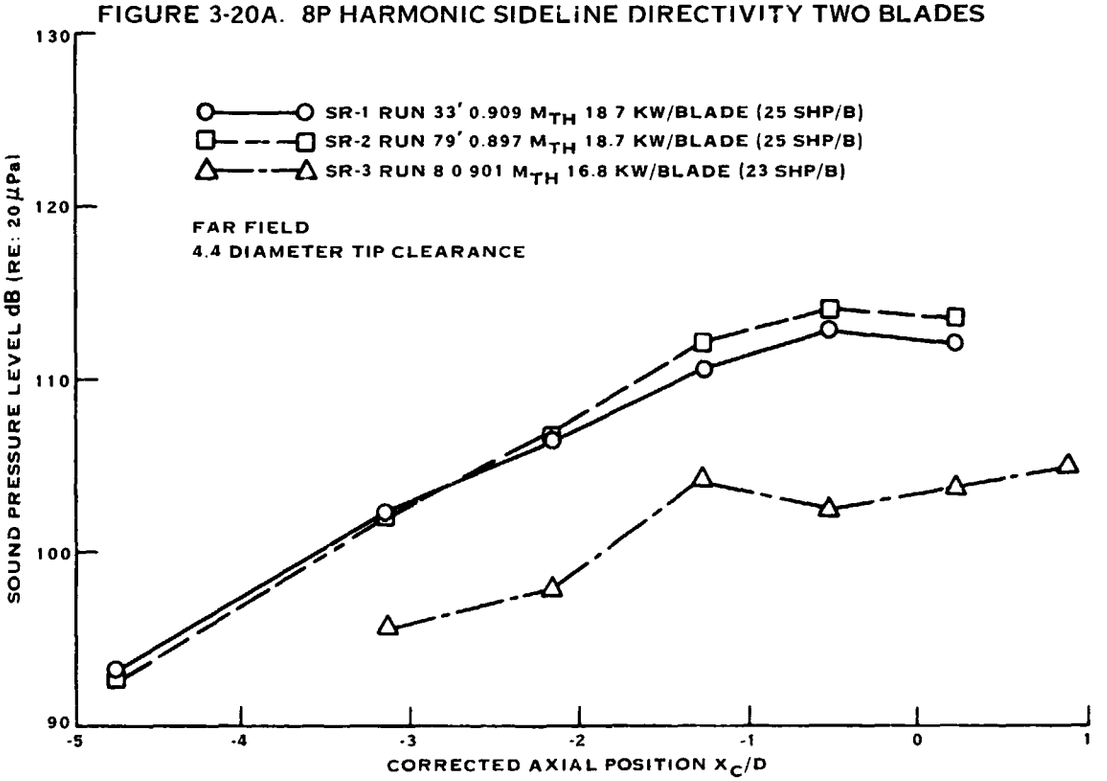

FIGURE 3-20B. 8P HARMONIC SIDELINE DIRECTIVITY TWO BLADES

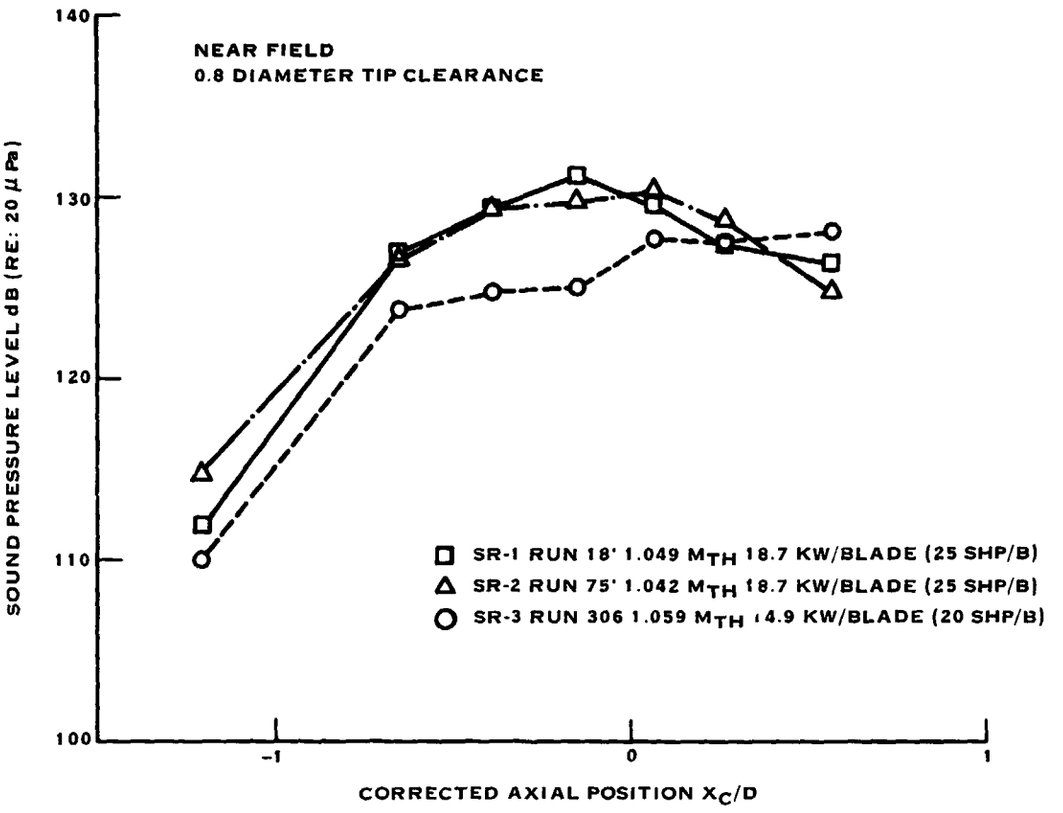

FIGURE 3-21A. 8P HARMONIC SIDELINE DIRECTIVITY - TWO BLADES

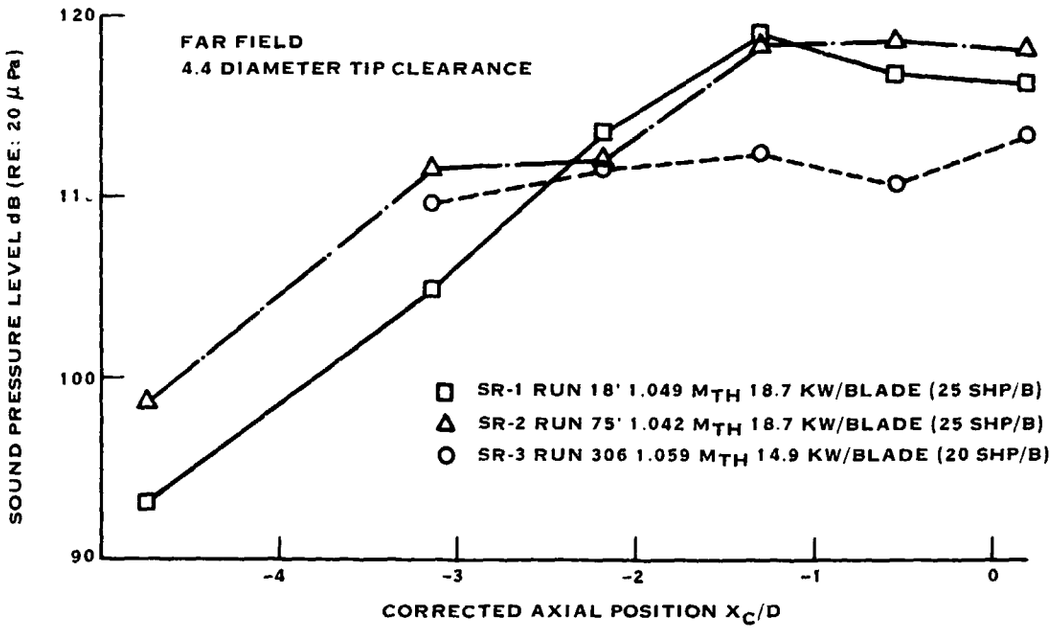

FIGURE 3-21B. 8P HARMONIC SIDELINE DIRECTIVITY - TWO BLADES

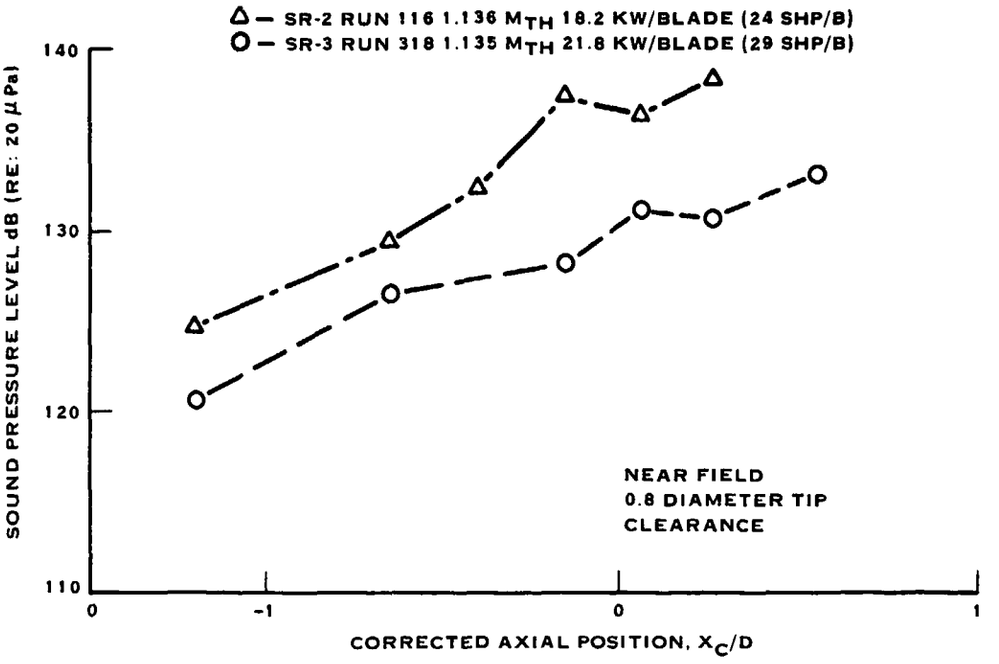

FIGURE 3-22A. 8P HARMONIC SIDELINE DIRECTIVITY - TWO BLADES

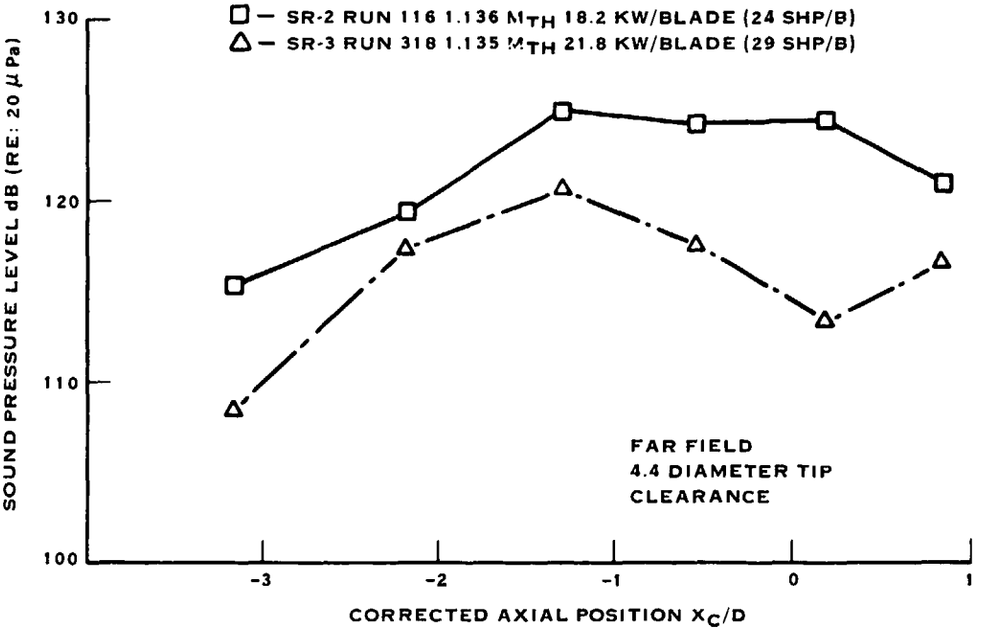

FIGURE 3-22B. 8P HARMONIC SIDELINE DIRECTIVITY - TWO BLADES

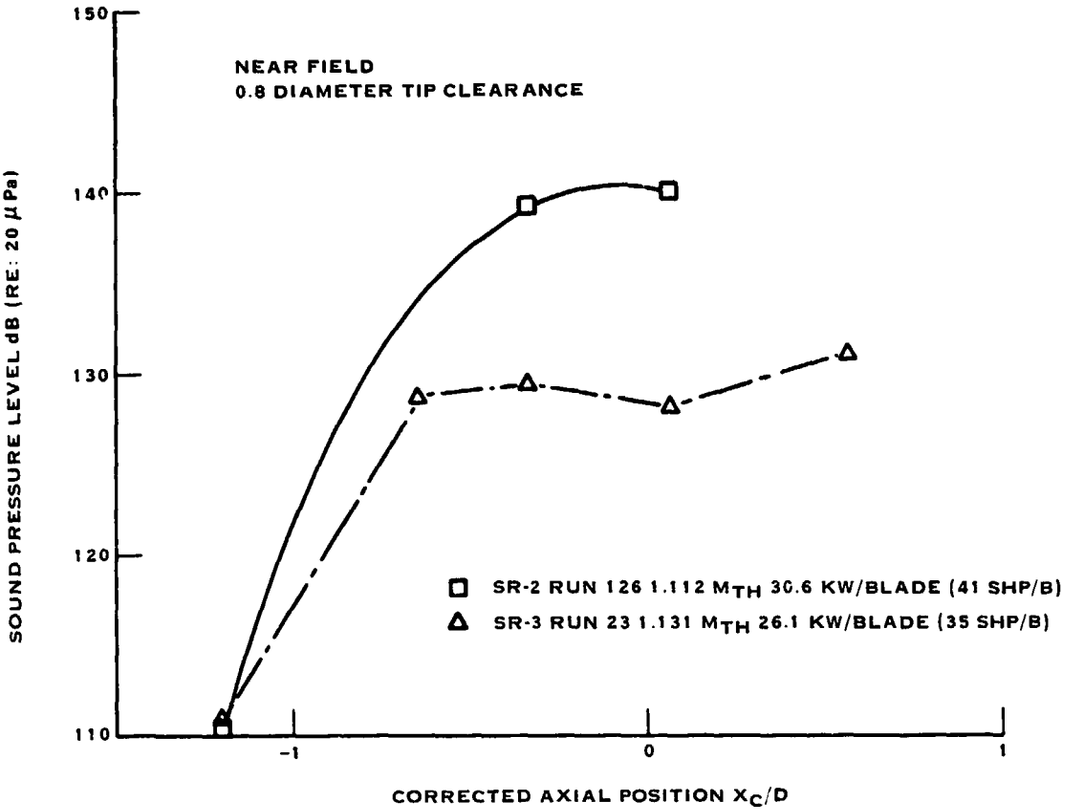

FIGURE 3-23A. 8P HARMONIC SIDELINE DIRECTIVITY - TWO BLADES

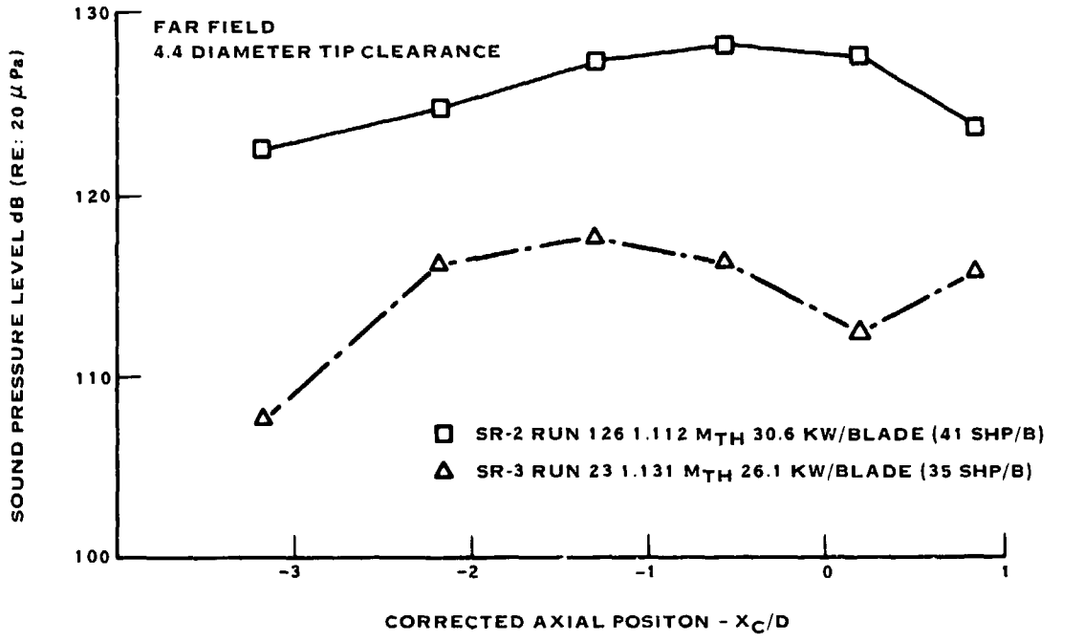

FIGURE 3-23B. 8P HARMONIC SIDELINE DIRECTIVITY - TWO BLADES

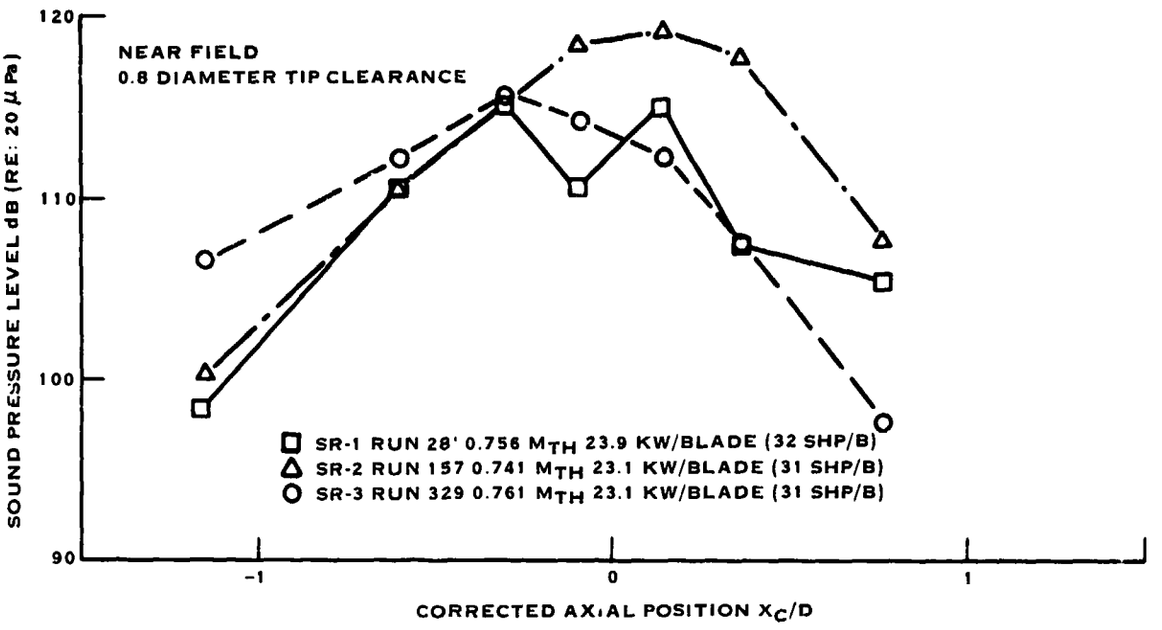

FIGURE 3-24A. 8P HARMONIC SIDELINE DIRECTIVITY - TWO BLADES

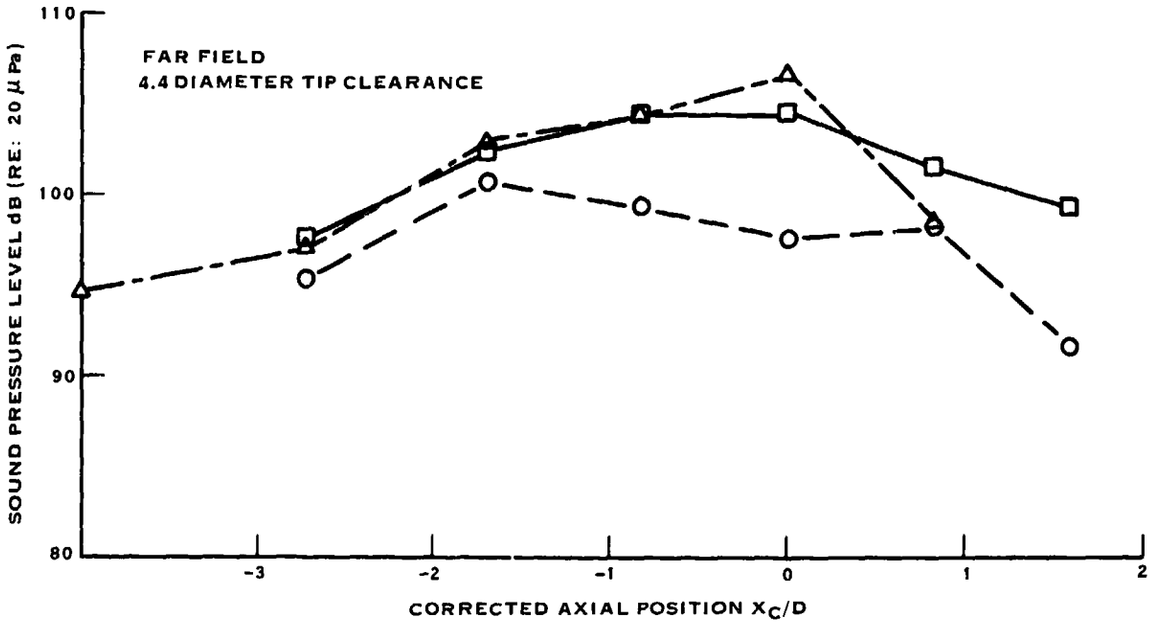

FIGURE 3-24B. 8P HARMONIC SIDELINE DIRECTIVITY - TWO BLADES

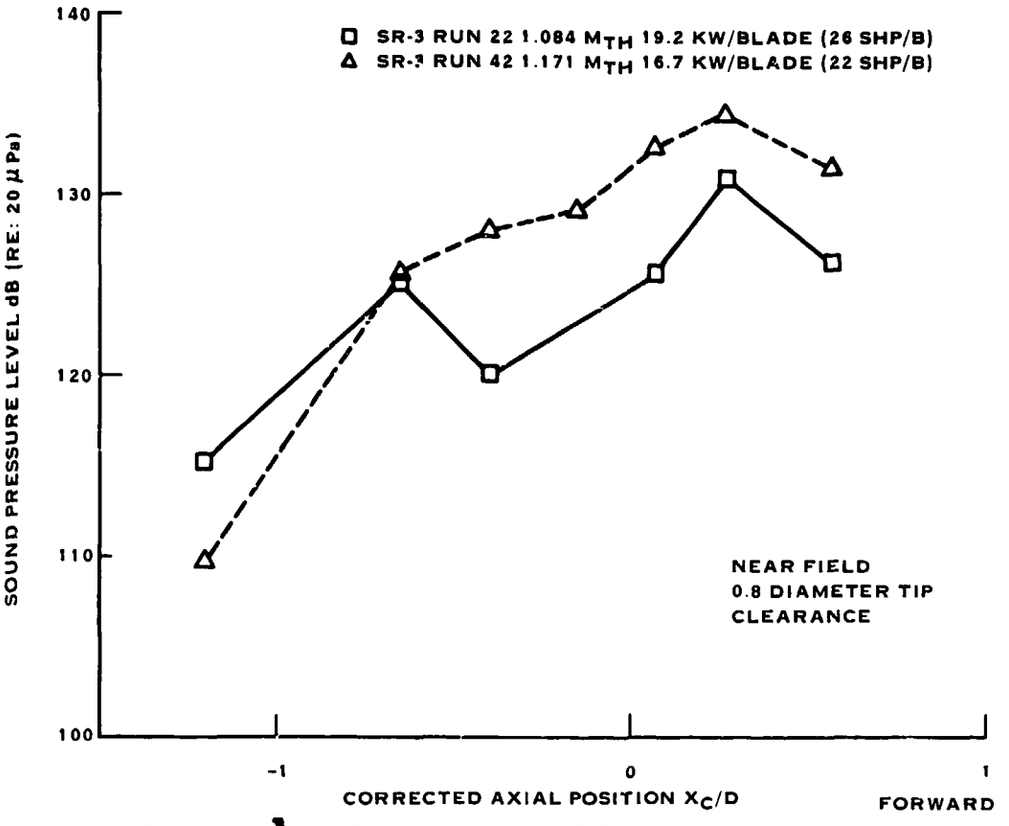

FIGURE 3-25A. 8P HARMONIC SIDELINE DIRECTIVITY - TWO BLADES

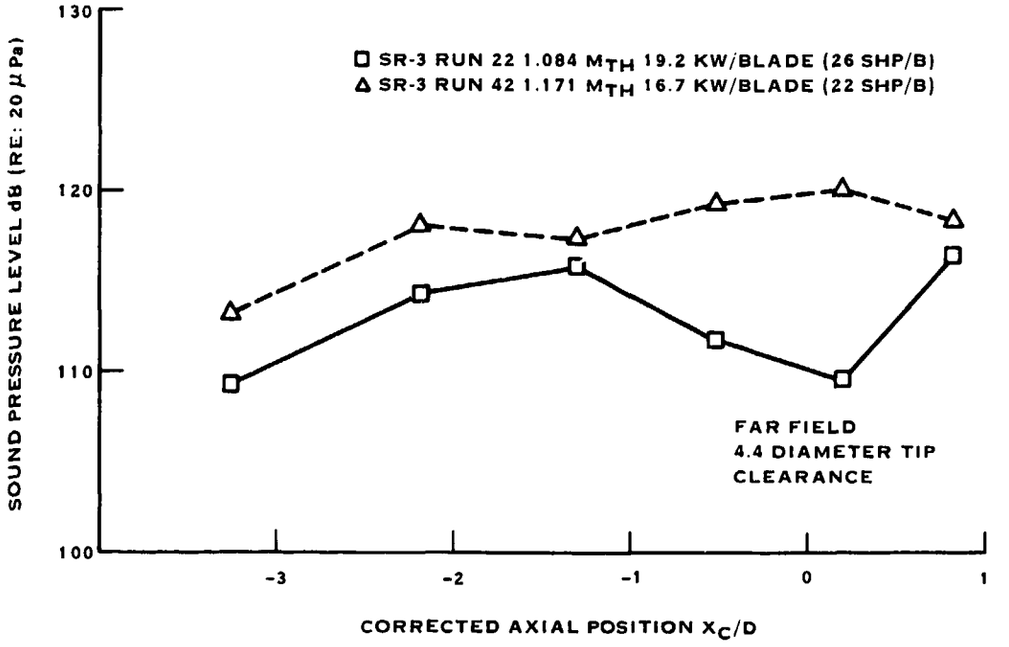

FIGURE 3-25B. 8P HARMONIC SIDELINE DIRECTIVITY - TWO BLADES

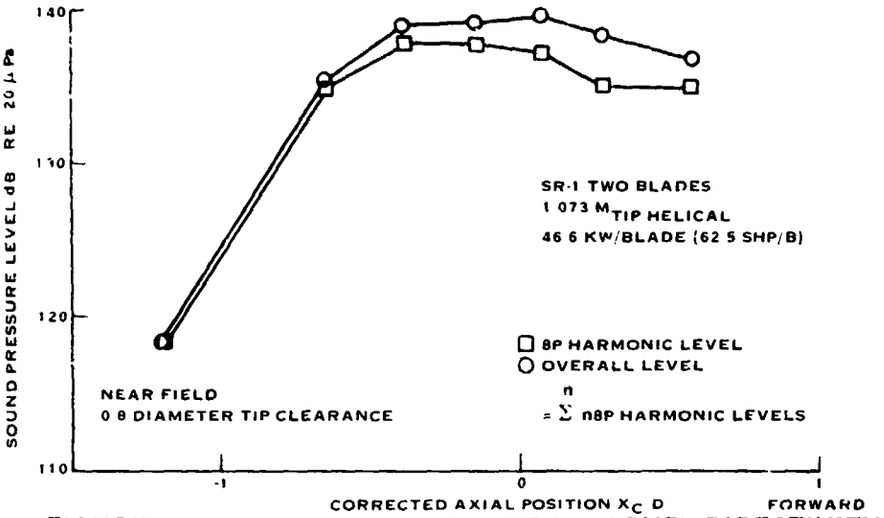

FIGURE 3-26. 8P HARMONIC VS. OVERALL LEVEL DIRECTIVITY

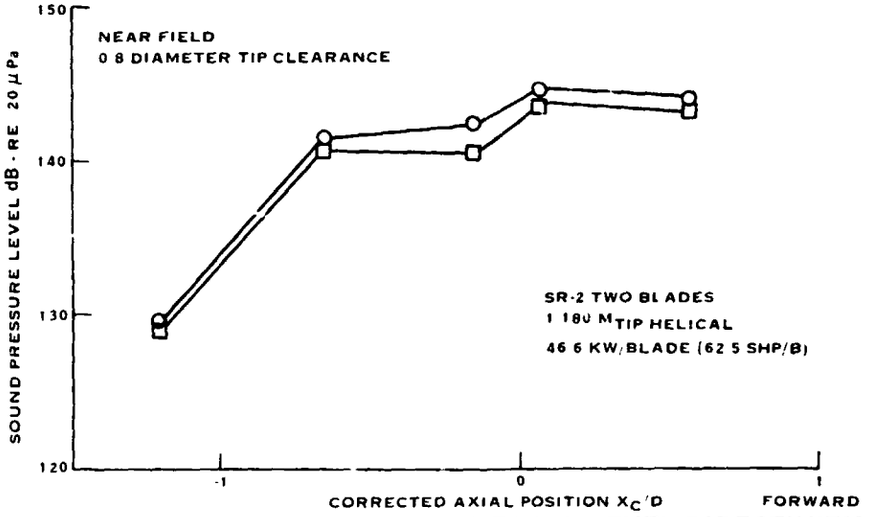

FIGURE 3-27. 8P HARMONIC VS. OVERALL LEVEL DIRECTIVITY

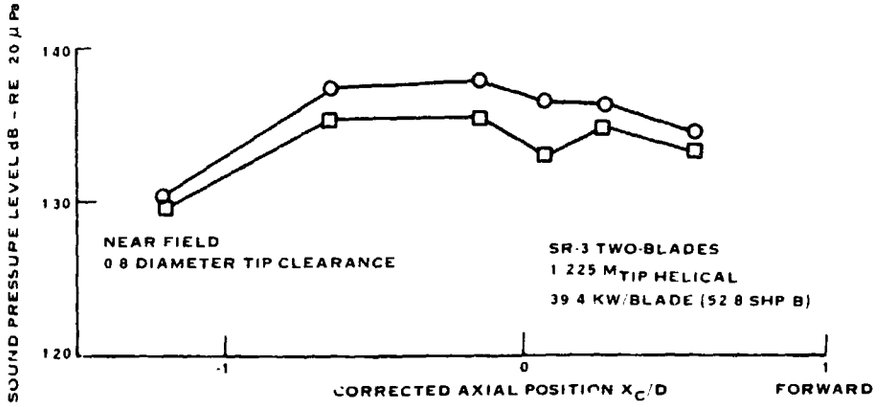

FIGURE 3-28. 8P HARMONIC VS. OVERALL LEVEL DIRECTIVITY

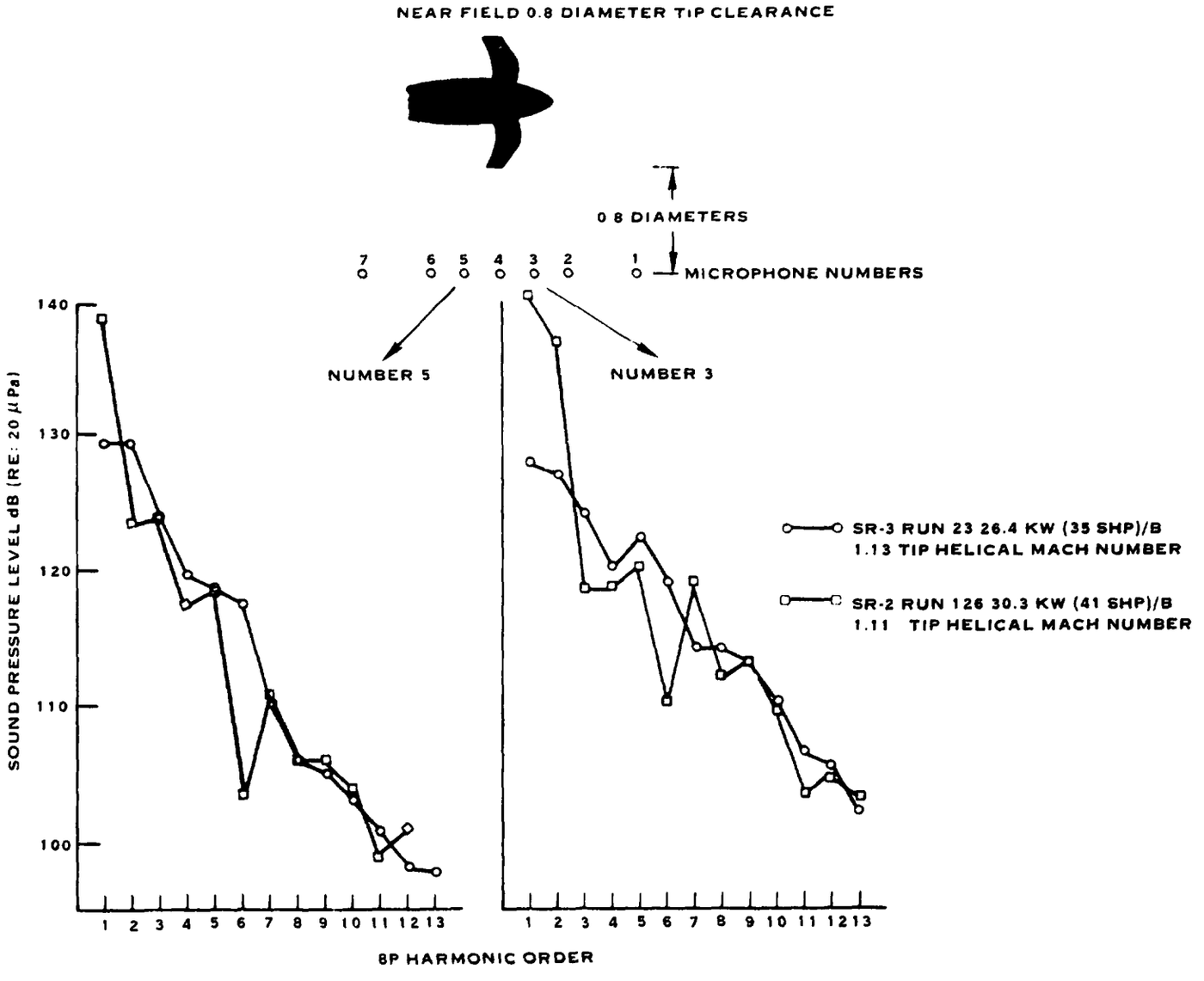

FIGURE 3-29. COMPARISON OF SR-3 AND SR-2 SPECTRA AT HIGH TIP SPEED IN NEAR FIELD

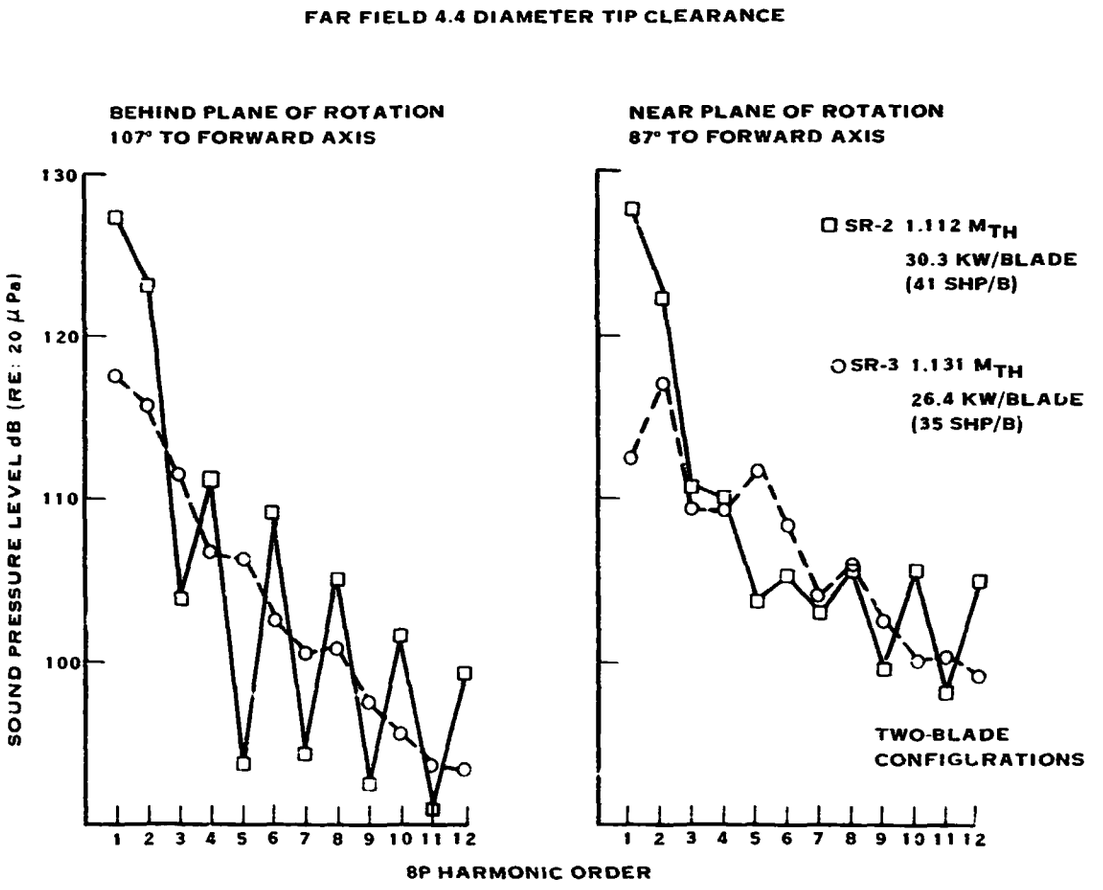

FIGURE 3-30. COMPARISON OF SR-3 AND SR-2 SPECTRA AT HIGH TIP SPEED IN FAR FIELD

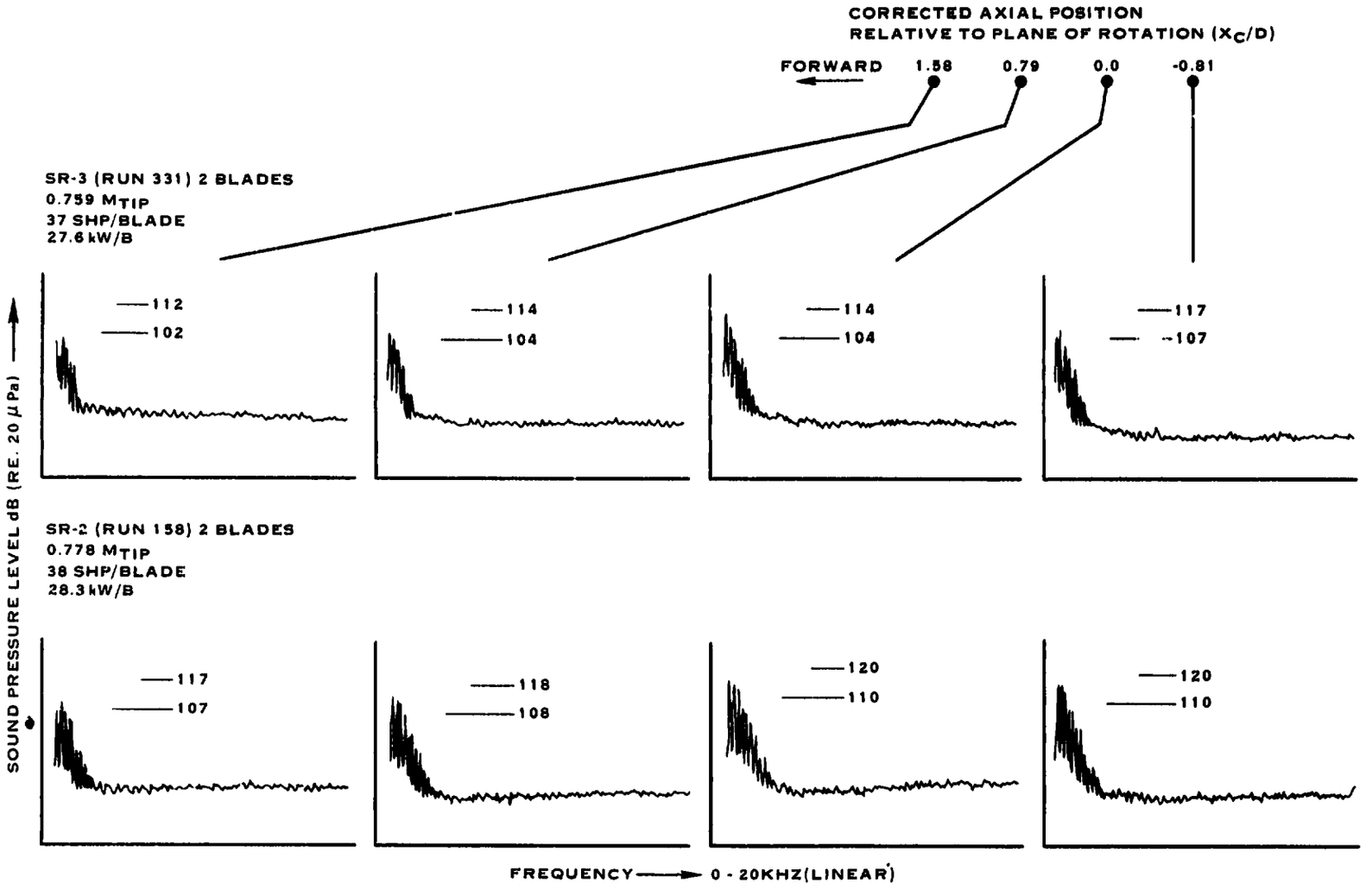

FIGURE 3-31. COMPARISON OF SR-3 AND SR-2 SPECTRA IN FAR FIELD

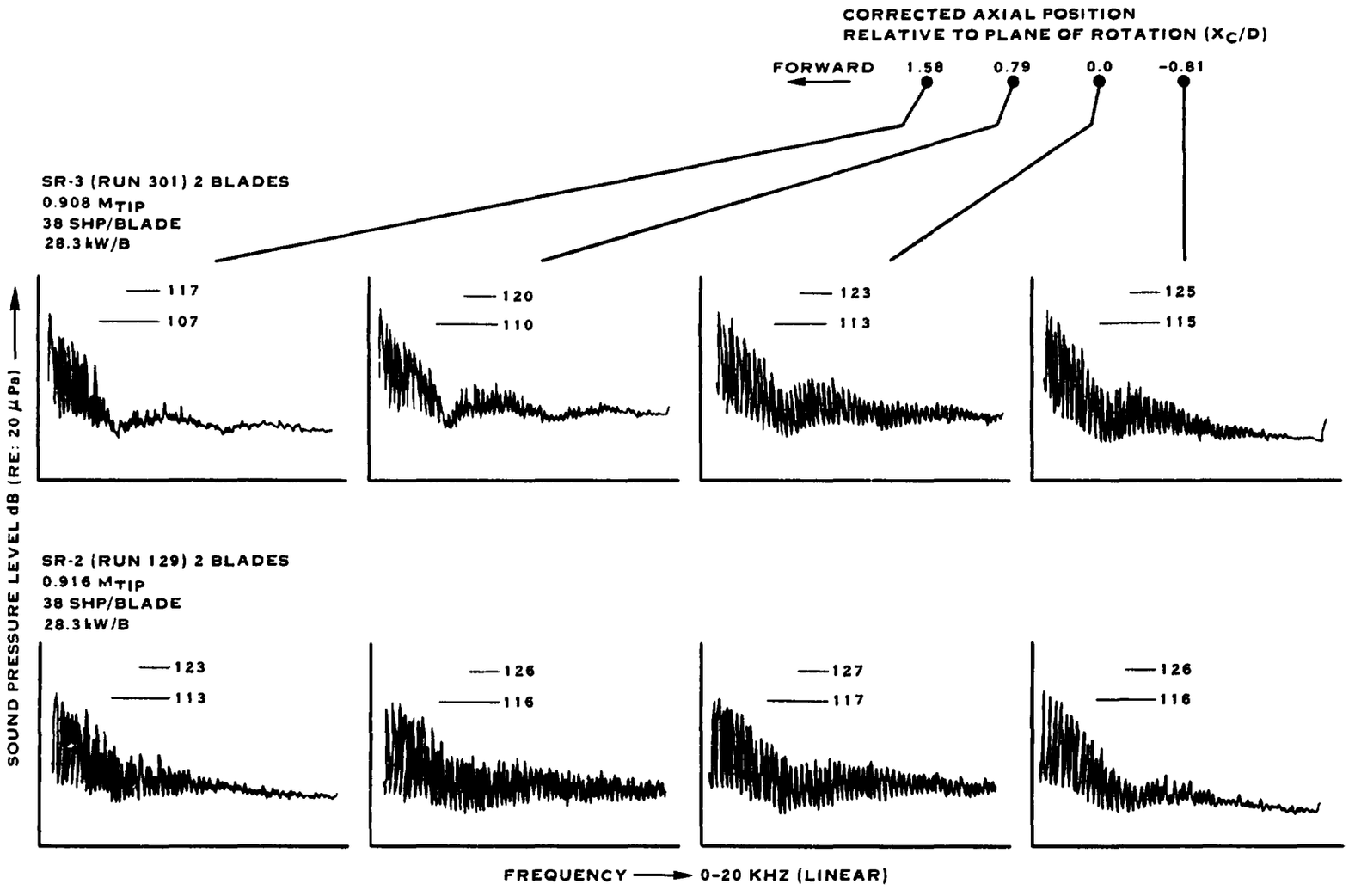

FIGURE 3-32. COMPARISON OF SR-3 AND SR-2 SPECTRA IN FAR FIELD

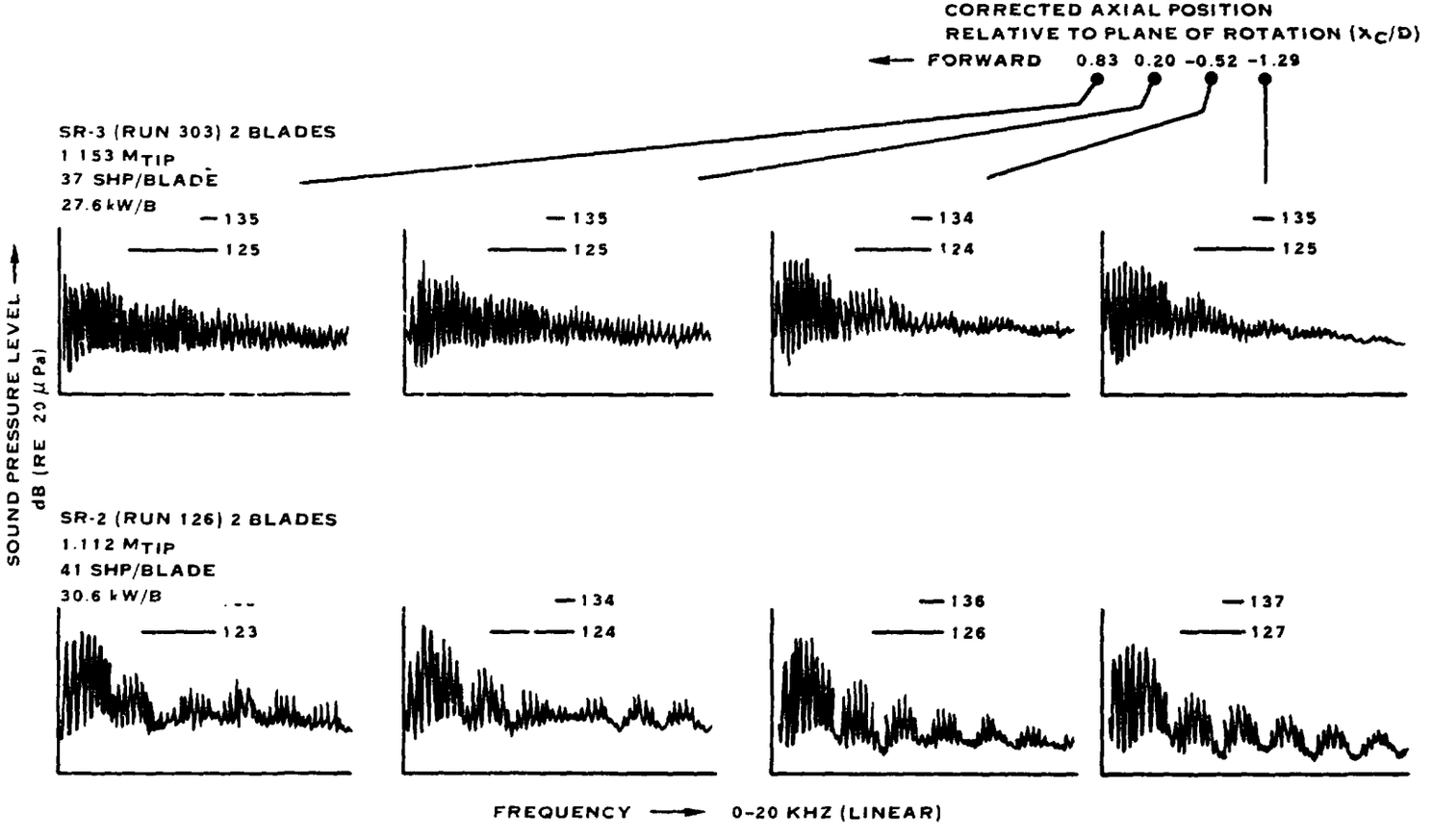

FIGURE 3-33. COMPARISON OF SR-3 AND SR-2 SPECTRA IN FAR FIELD

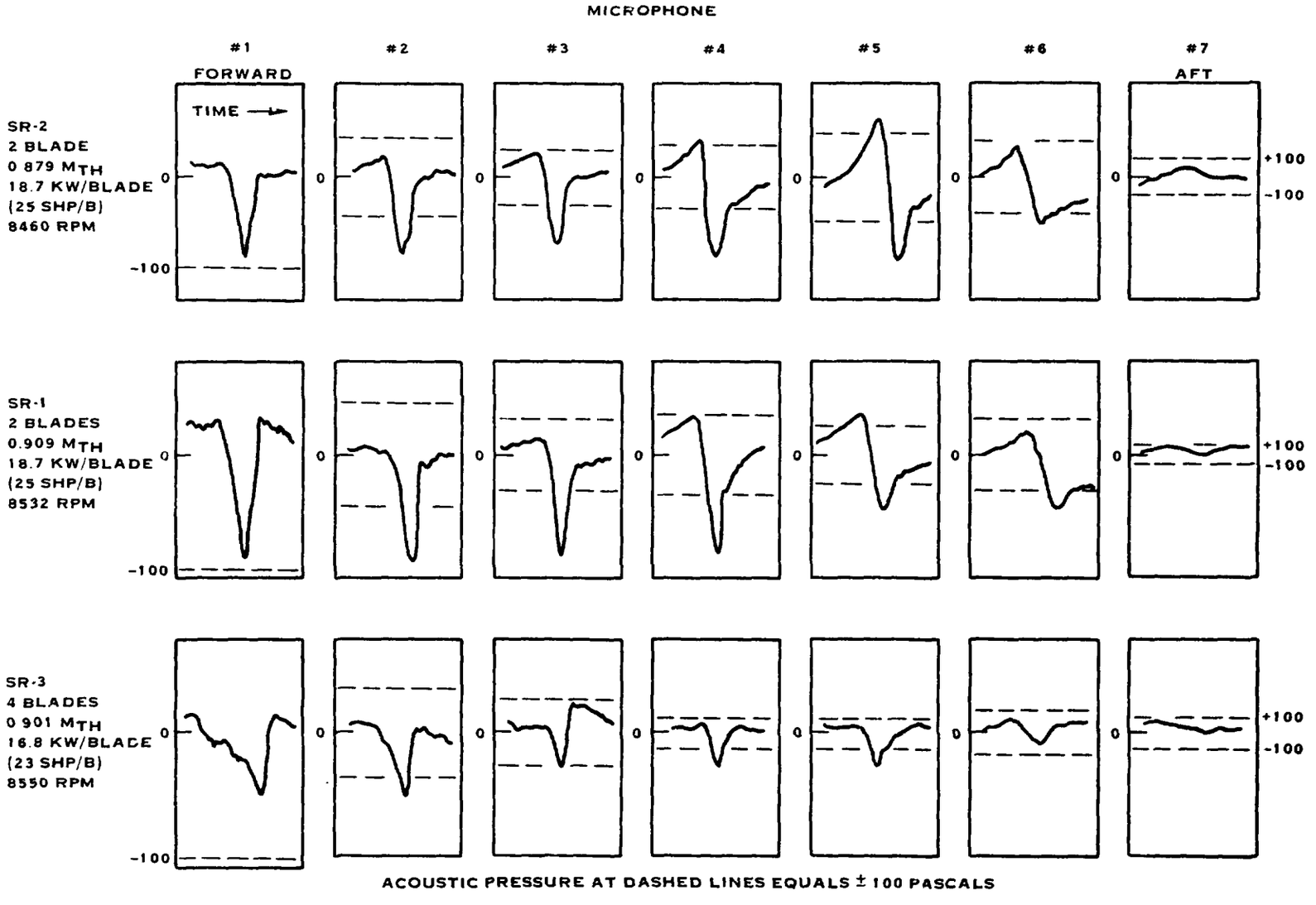

FIGURE 3-34. NEAR FIELD ACOUSTIC WAVEFORMS (0.8D TIP CLEARANCE)

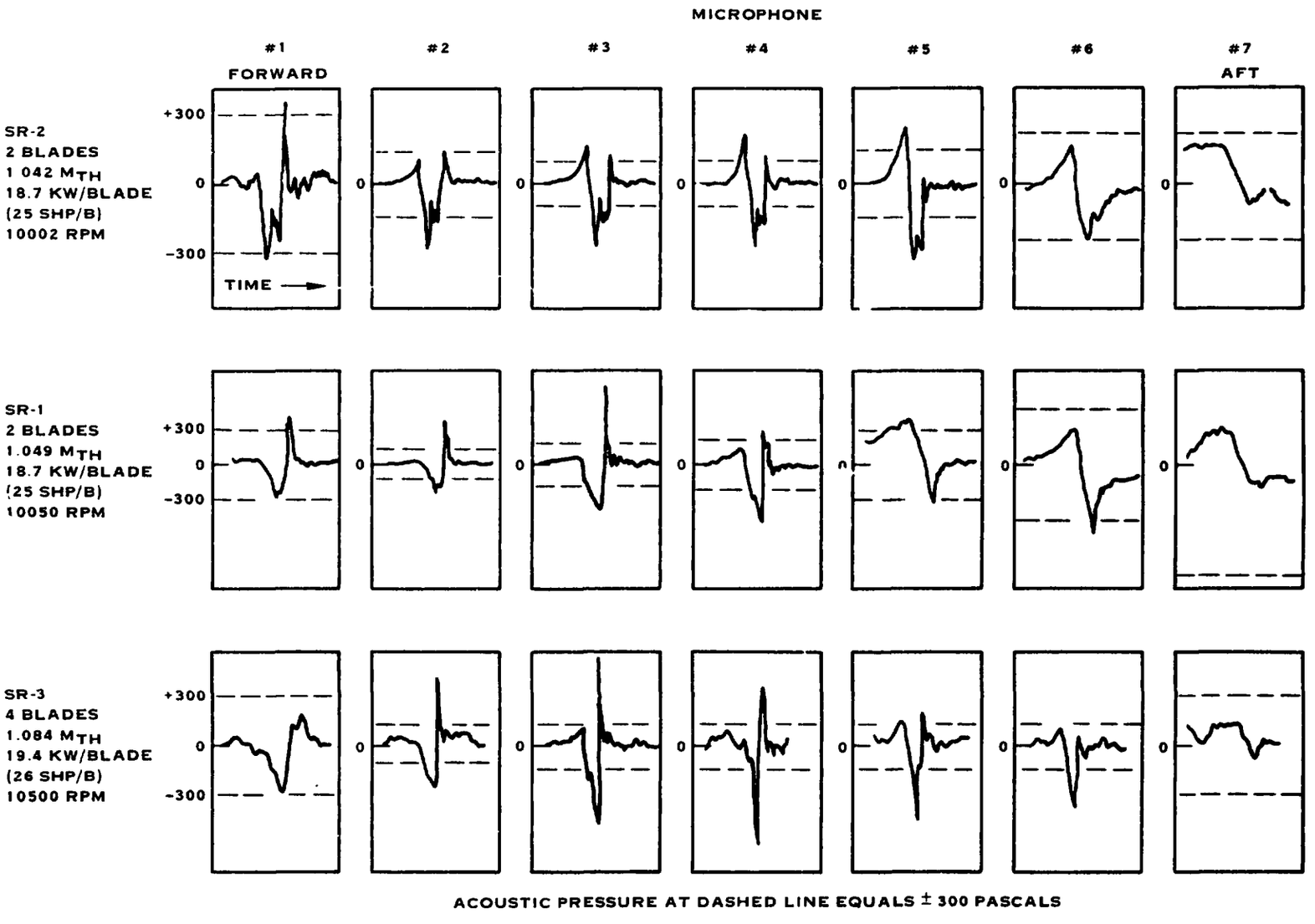

FIGURE 3-35. NEAR FIELD ACOUSTIC WAVEFORMS (0.8D TIP CLEARANCE)

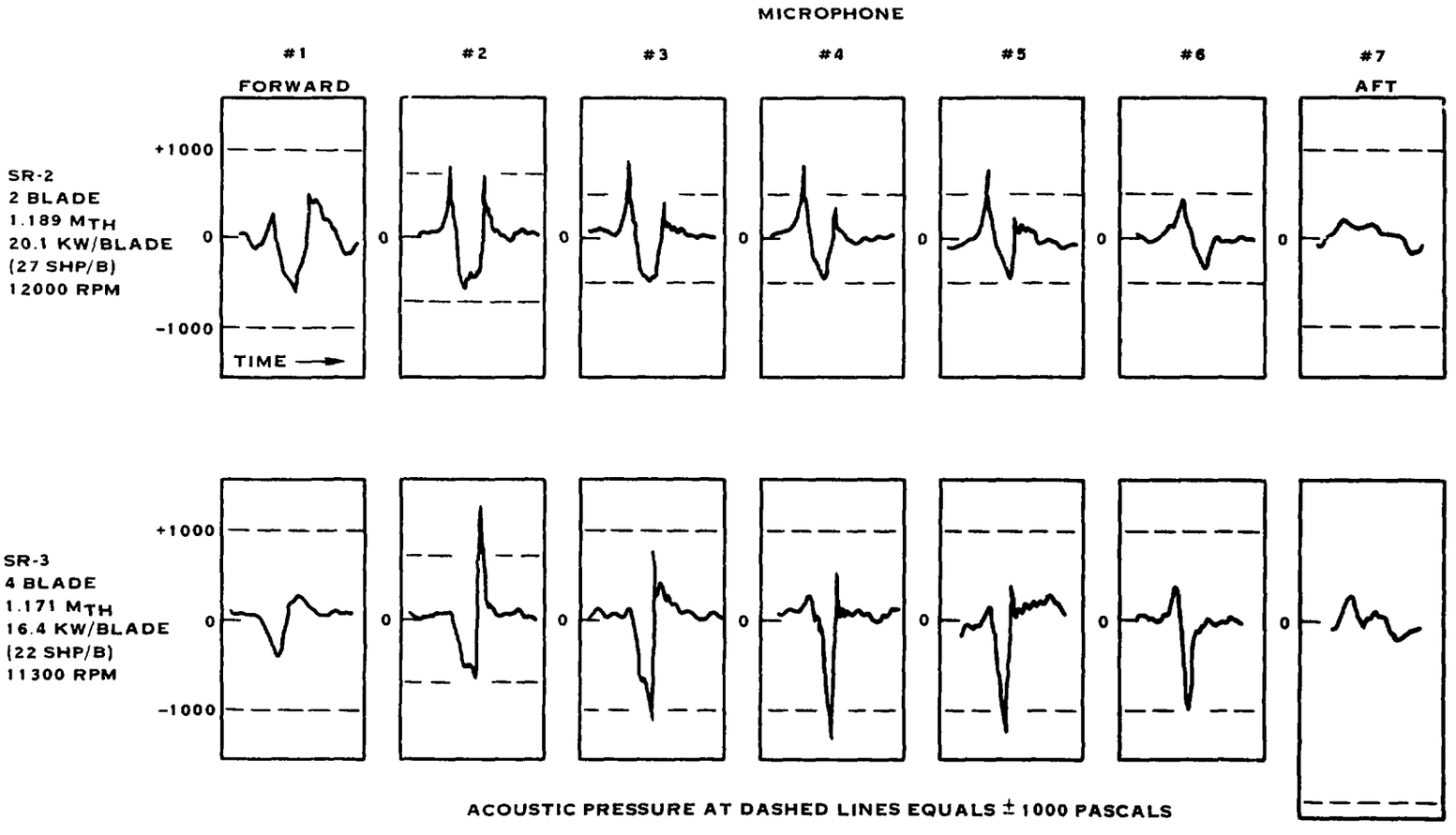

FIGURE 3-36. NEAR FIELD ACOUSTIC WAVEFORMS (0.8D TIP CLEARANCE)

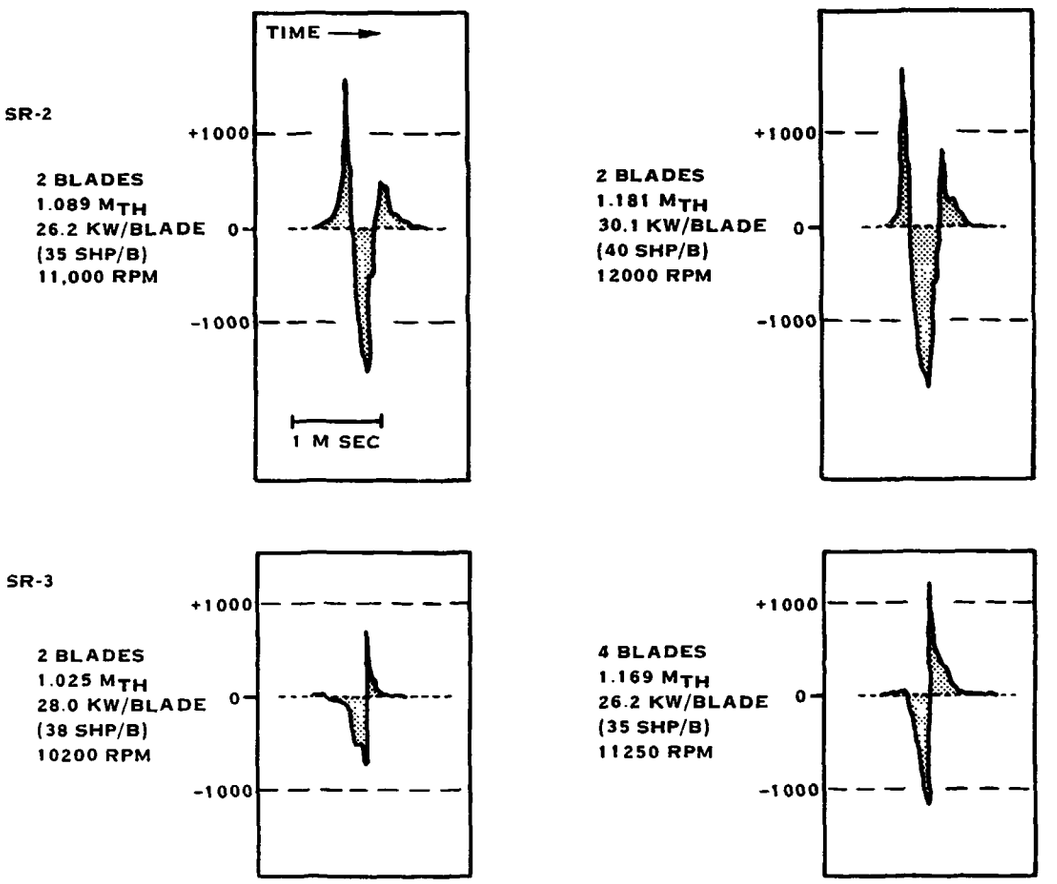

FIGURE 3-37. NEAR FIELD ACOUSTIC WAVEFORMS (0.8 DIAMETER TIP CLEARANCE)

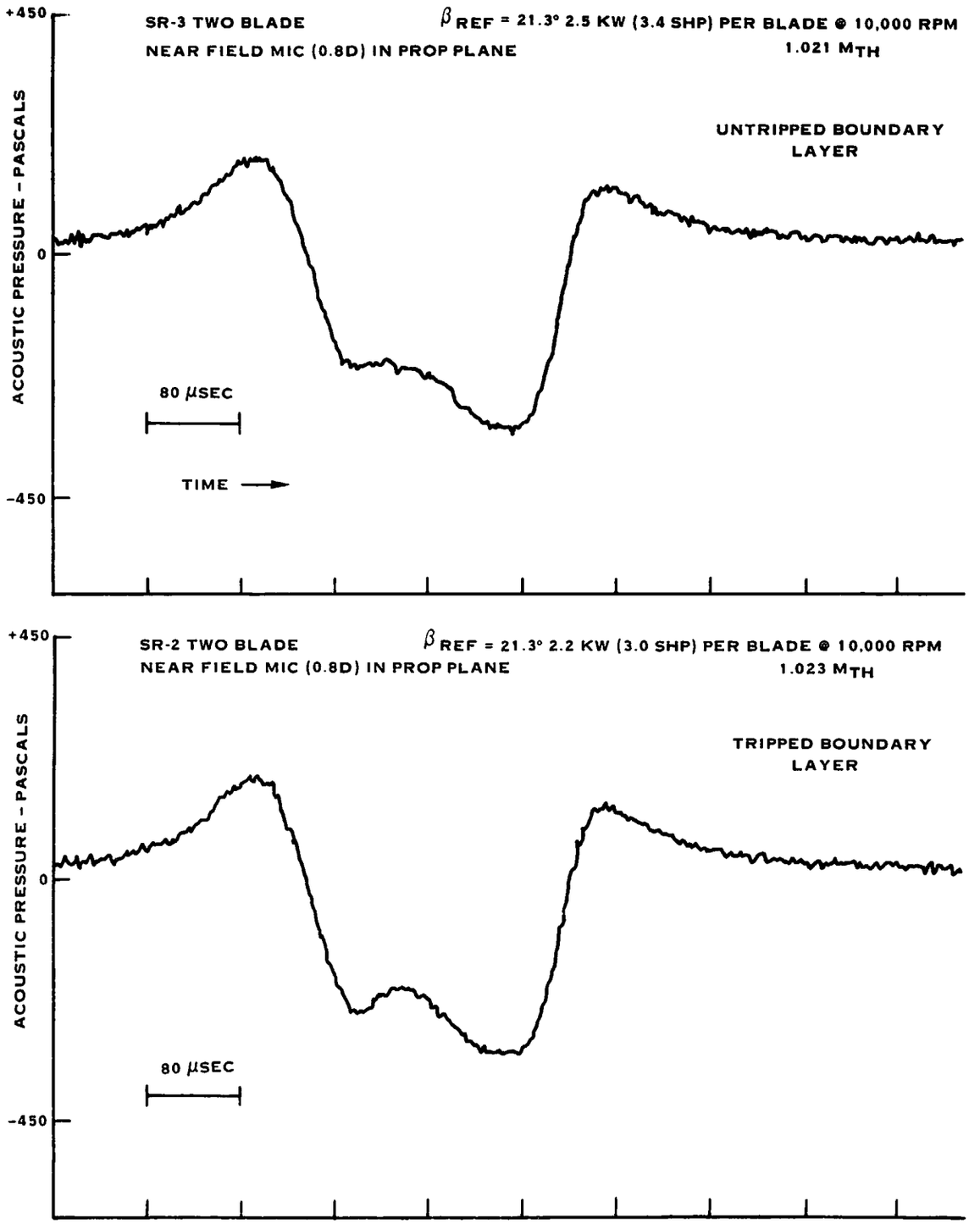

FIGURE 3-38. COMPARISON OF ACOUSTIC WAVEFORMS WITH UNTRIPPED AND TRIPPED BOUNDARY LAYER

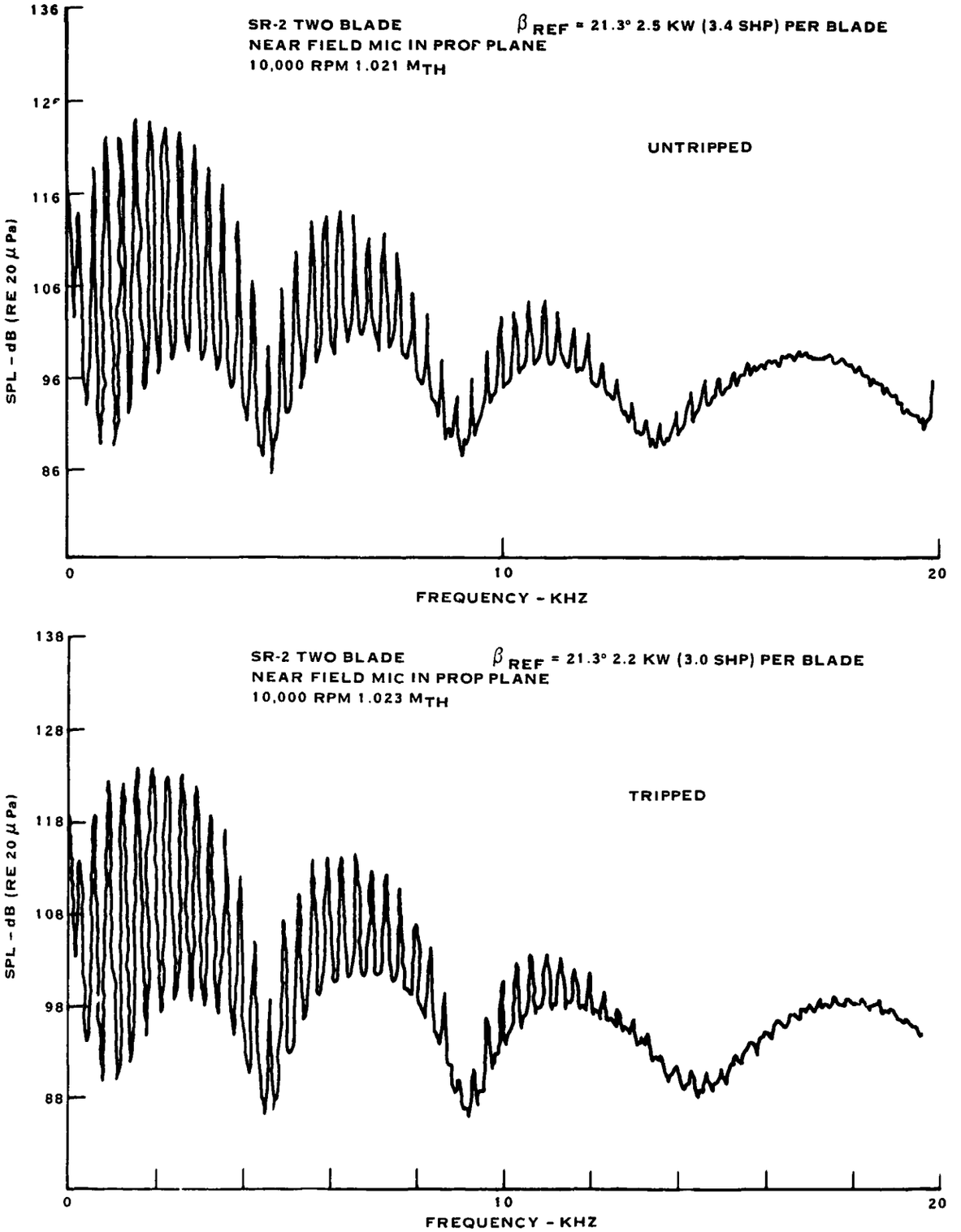

FIGURE 3-39. COMPARISON OF ACOUSTIC SPECTRA WITH UNTRIPPED AND TRIPPED BOUNDARY LAYER

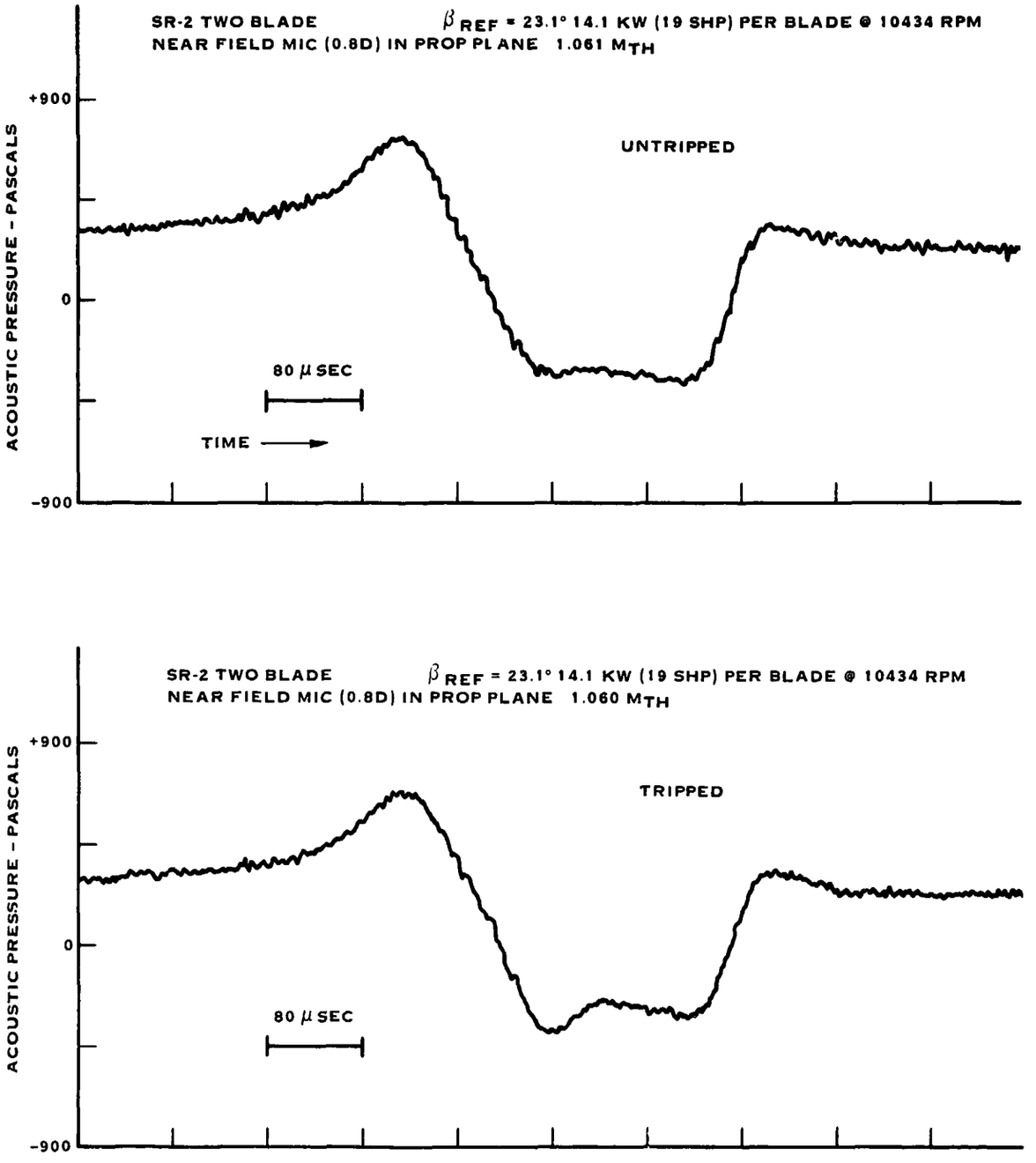

FIGURE 3-40. COMPARISON OF ACOUSTIC WAVEFORMS WITH UNTRIPPED AND TRIPPED BOUNDARY LAYER

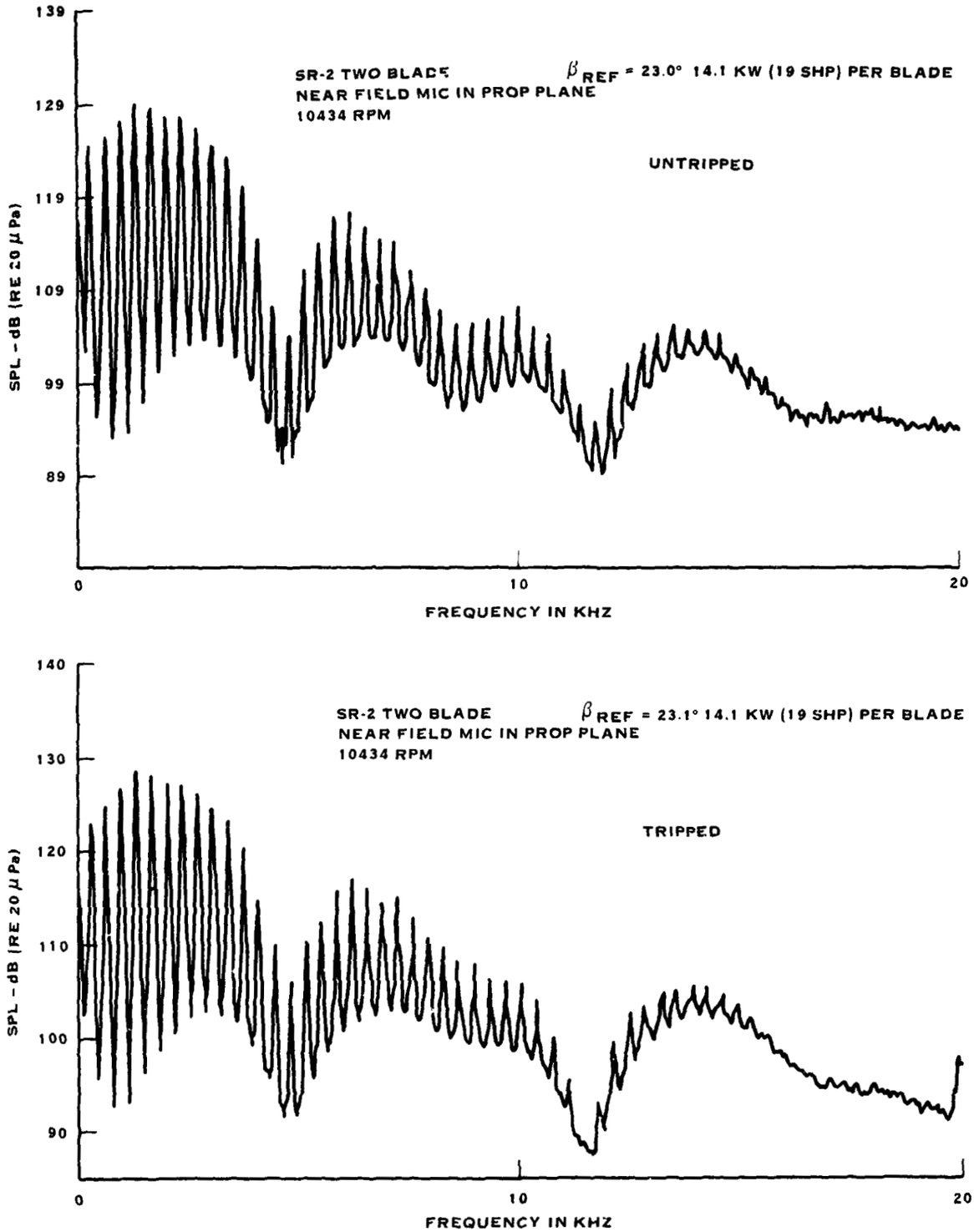

FIGURE 3-41. COMPARISON OF ACOUSTIC SPECTRA WITH UNTRIPPED AND TRIPPED BOUNDARY LAYER

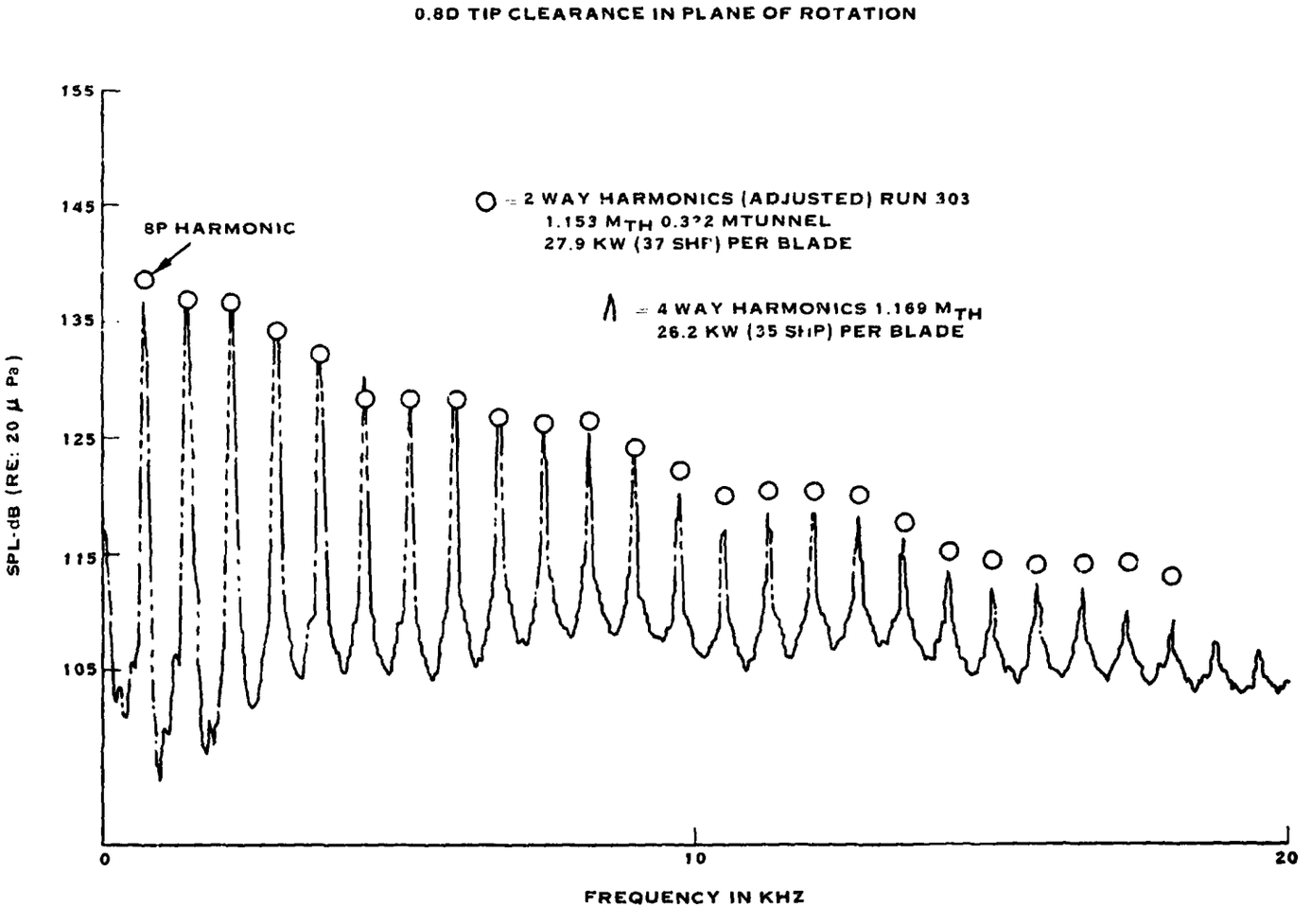

FIG. 3-42 TWO WAY VS. FOUR WAY SUPERPOSITION FOR SR-3

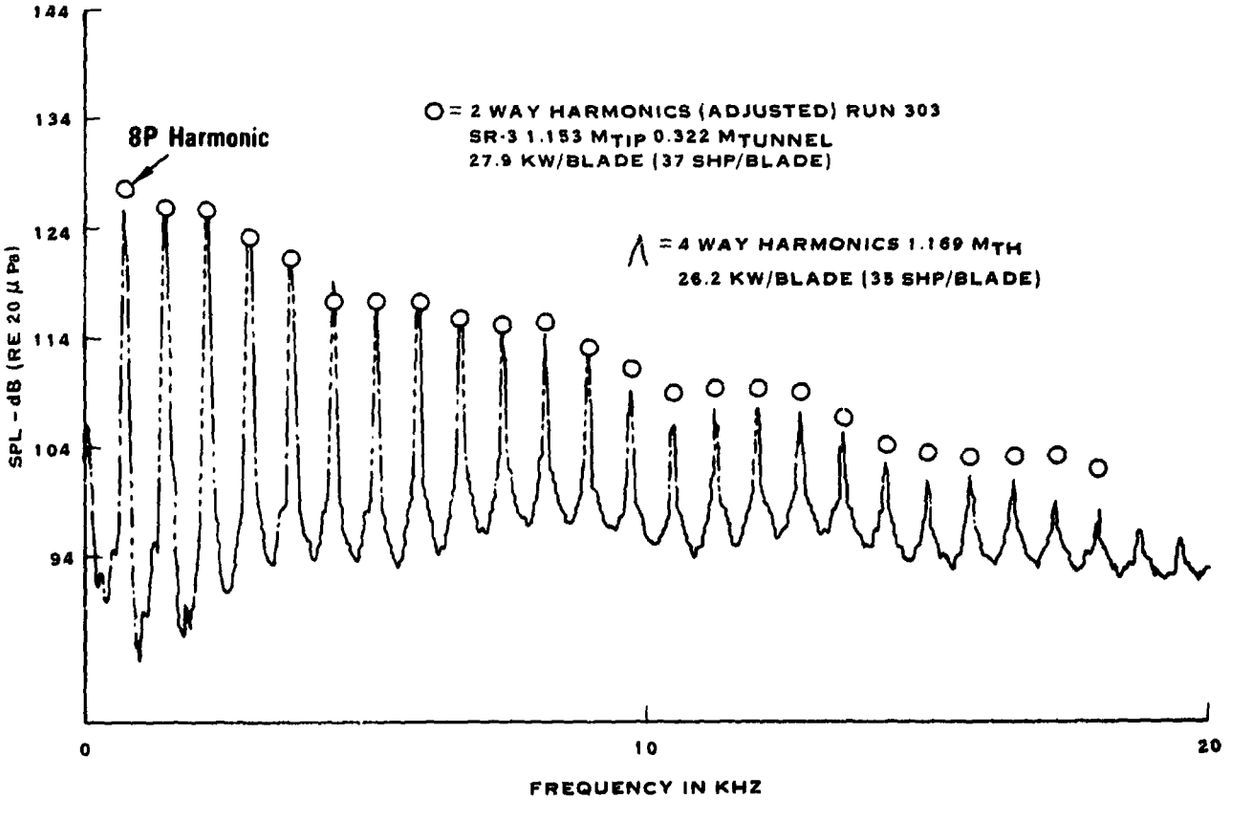

FIGURE 3-43. TWO WAY VS. FOUR WAY SUPERPOSITION FOR SR-3 (FAR FIELD AT 4.4D TIP CLEARANCE AFT OF PLANE OF ROTATION)

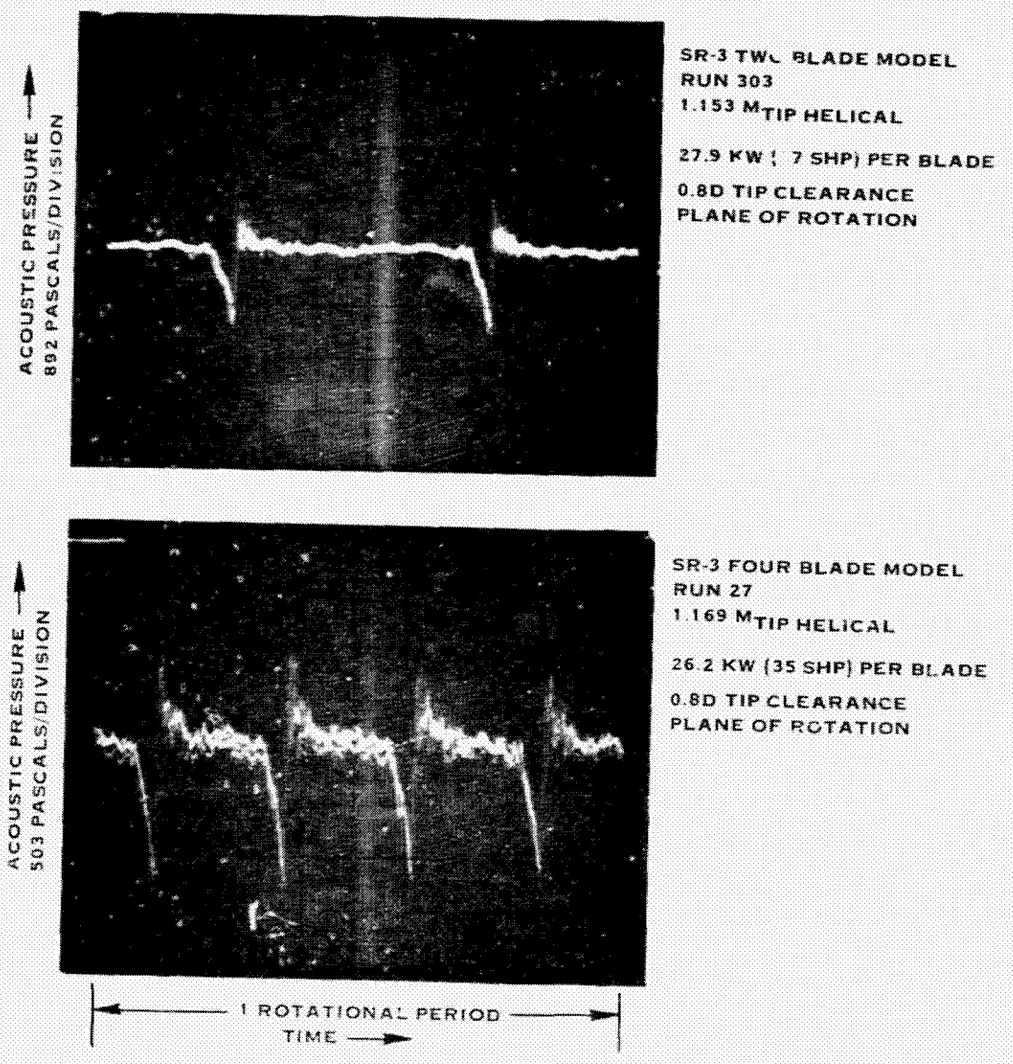

FIGURE 3-44. TWO BLADE AND FOUR BLADE SR-3 ACOUSTIC PRESSURE PULSE WAVEFORMS

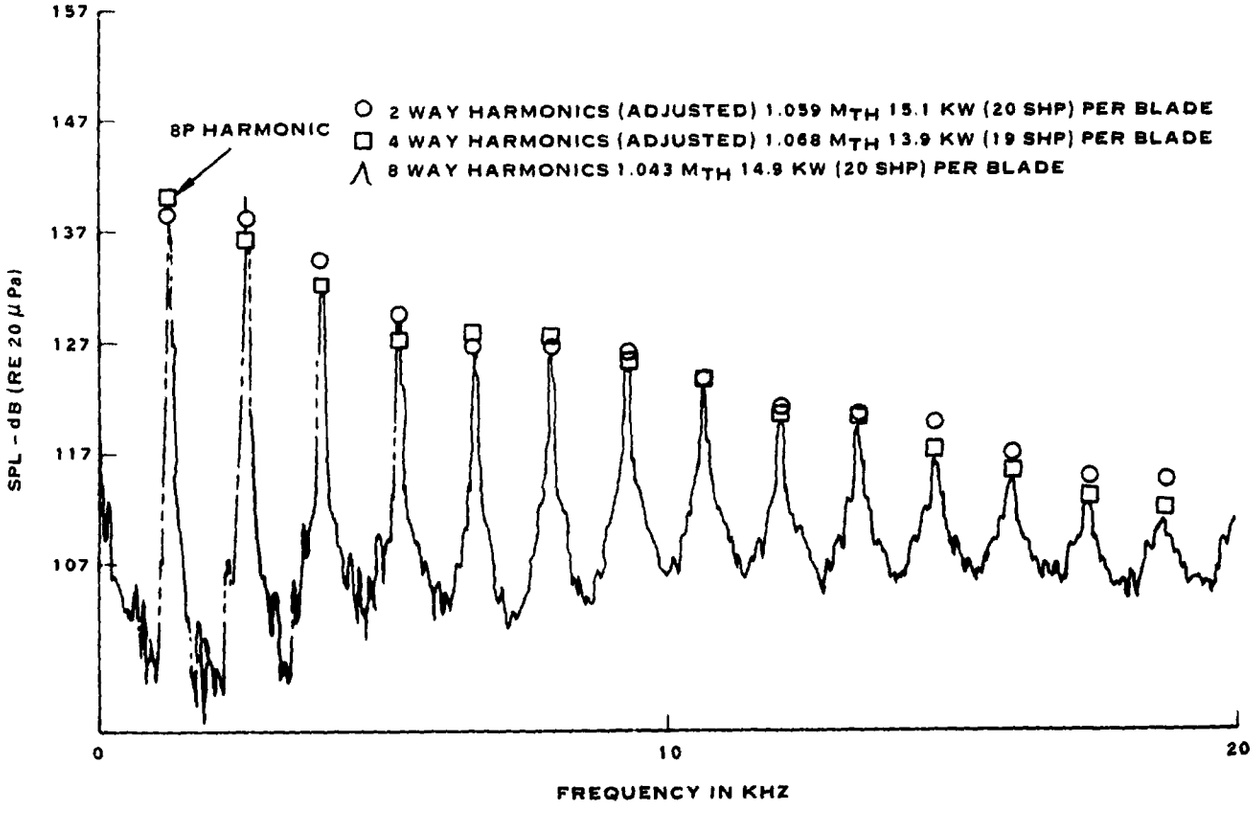

FIGURE 3-45. TWO WAY, FOUR WAY, AND EIGHT WAY SUPERPOSITION FOR SR-3 (0.8D TIP CLEARANCE IN PLANE OF ROTATION)

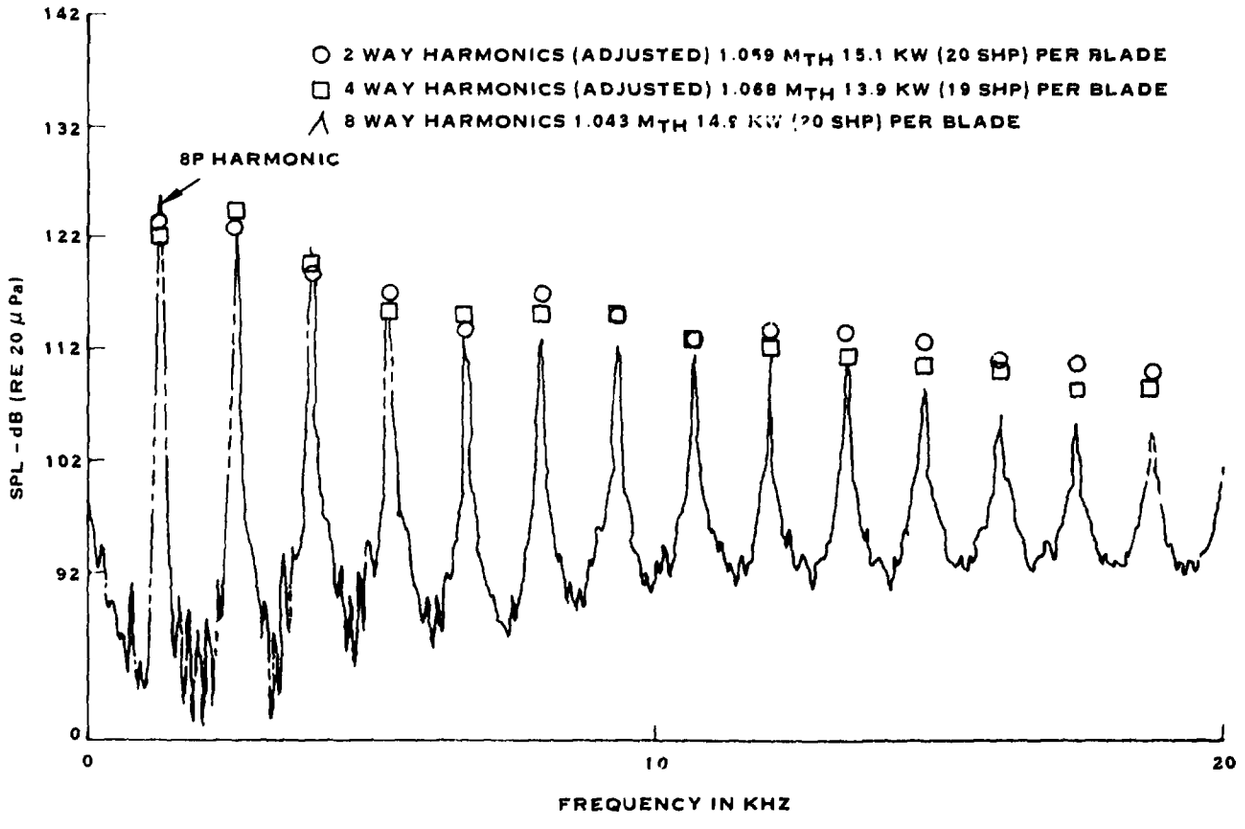

FIGURE 3-46. TWO WAY, FOUR WAY AND EIGHT WAY SUPERPOSITION FOR SR-3 (FAR FIELD AT 4.4D TIP CLEARANCE IN PLANE OF ROTATION)

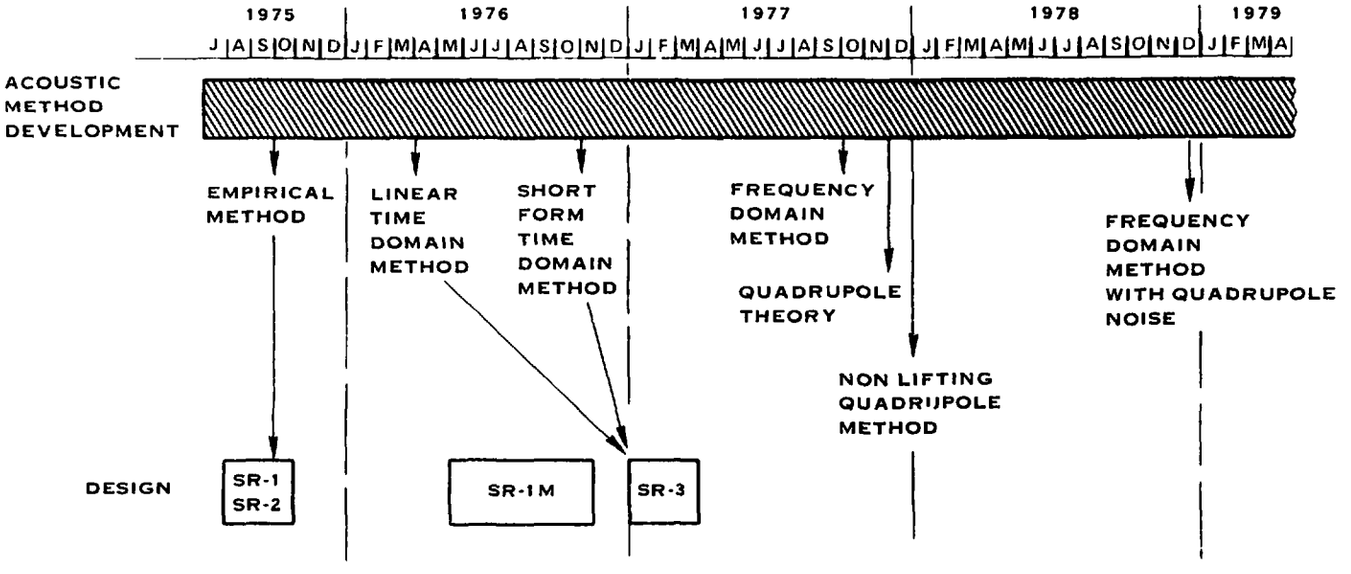

FIGURE 3-47. EVOLUTION OF PROP-FAN NOISE PREDICTION METHODOLOGY

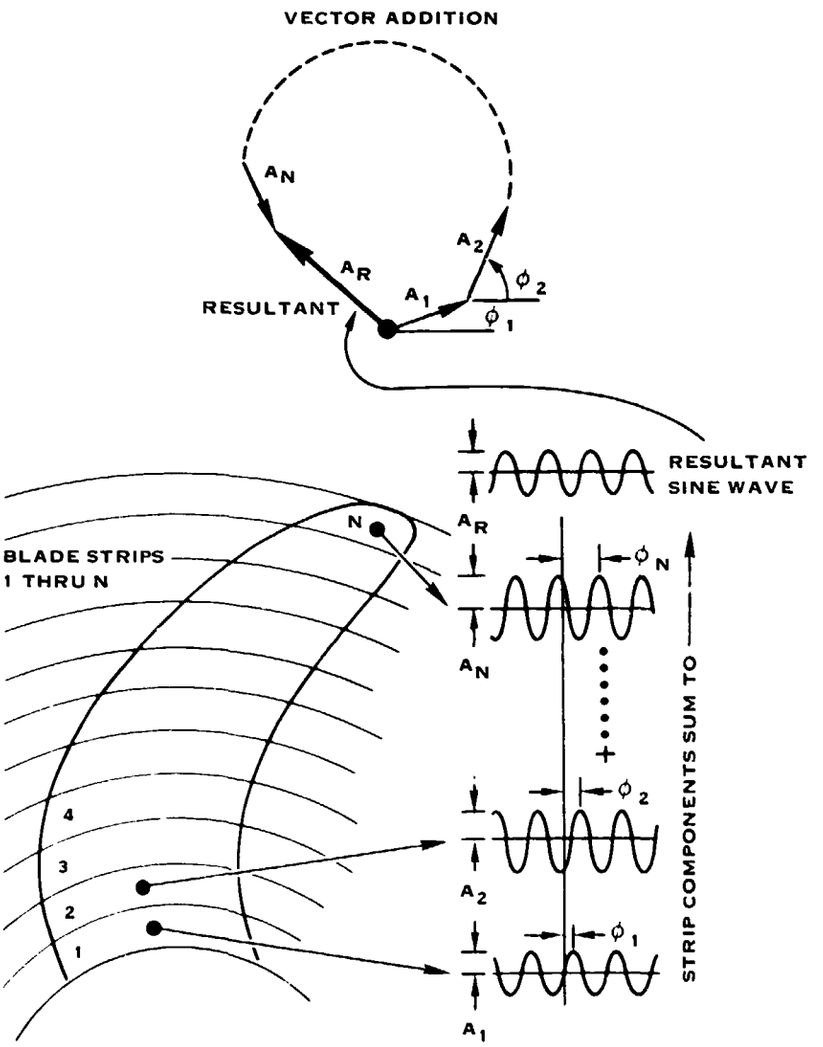

FIGURE 3-48. ACOUSTIC STRIP ANALYSIS CONCEPT

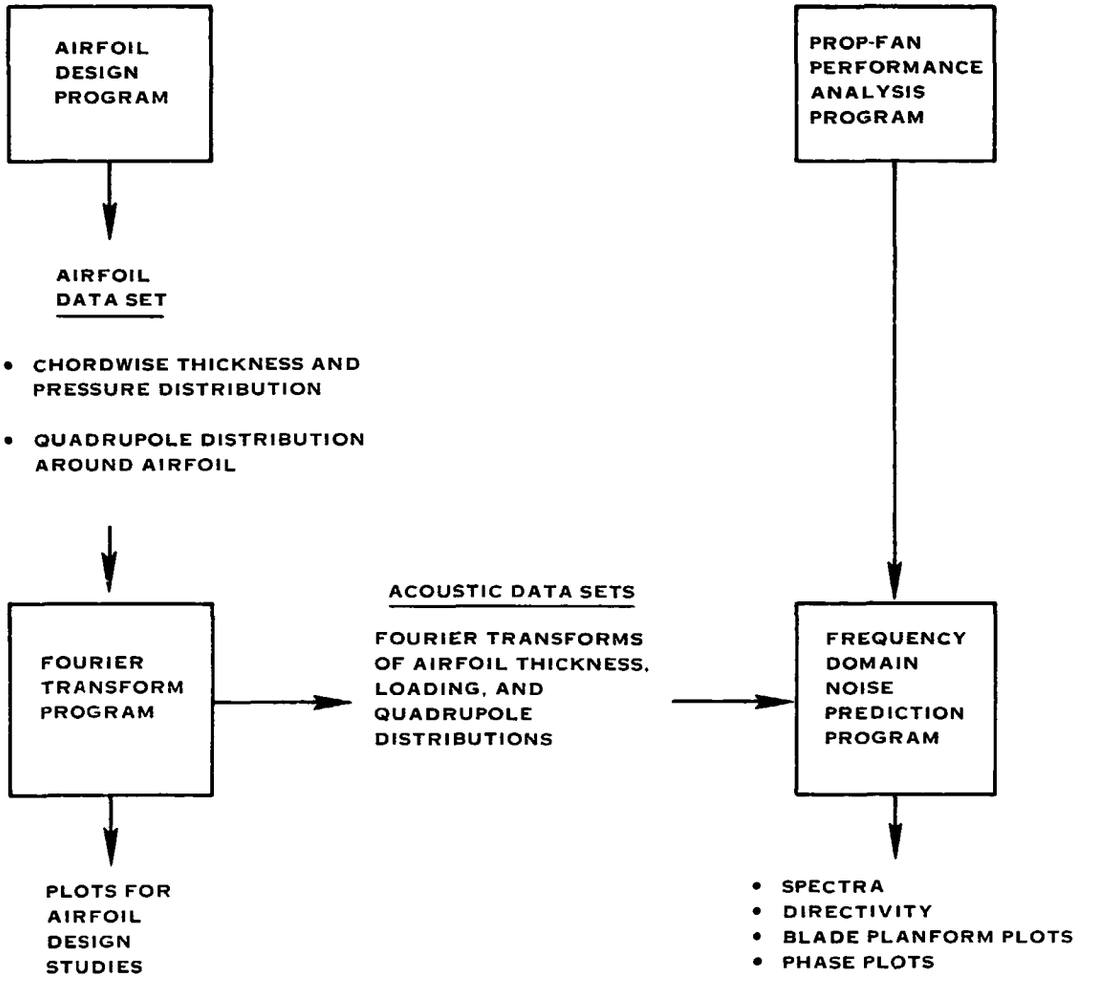

FIGURE 3-49. FREQUENCY DOMAIN NOISE PREDICTION METHOD

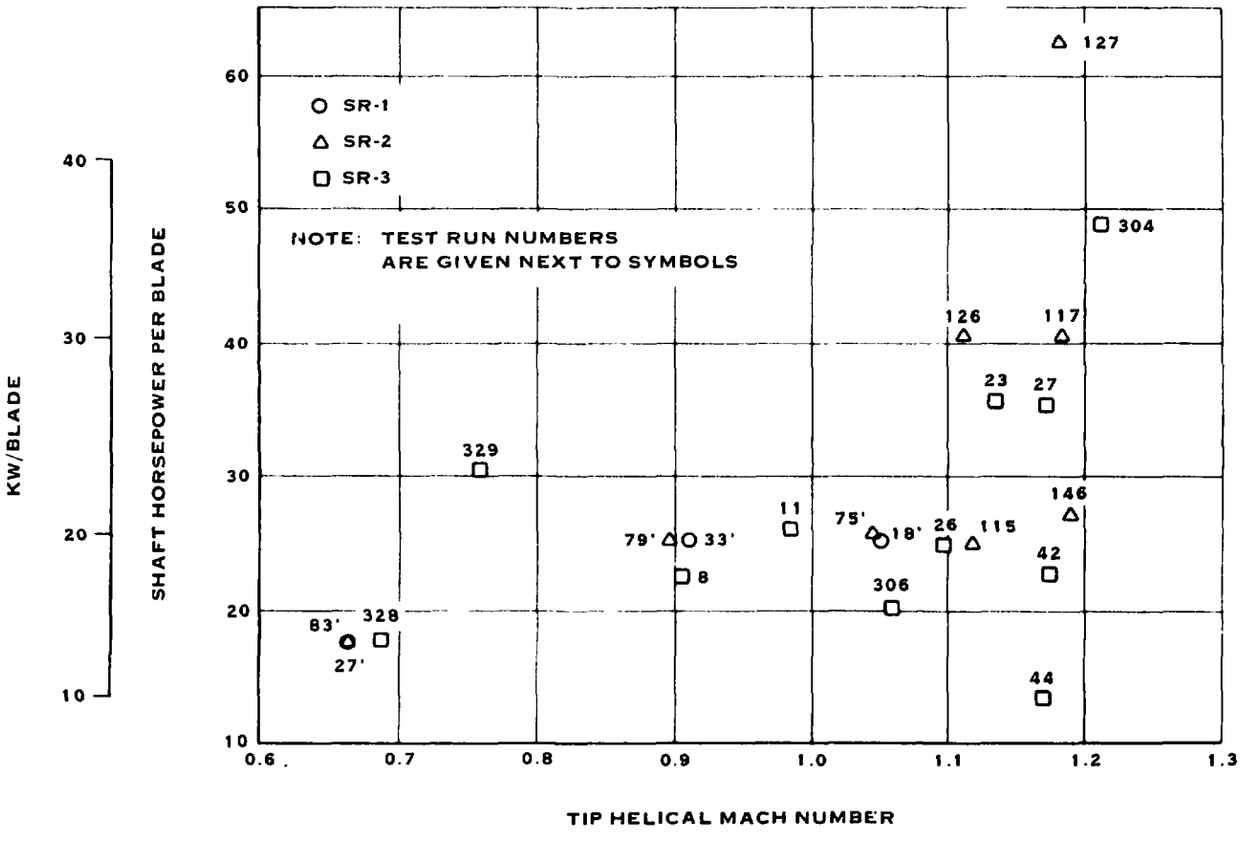

FIGURE 3-50. TEST CONDITIONS SELECTED FOR ANALYSIS

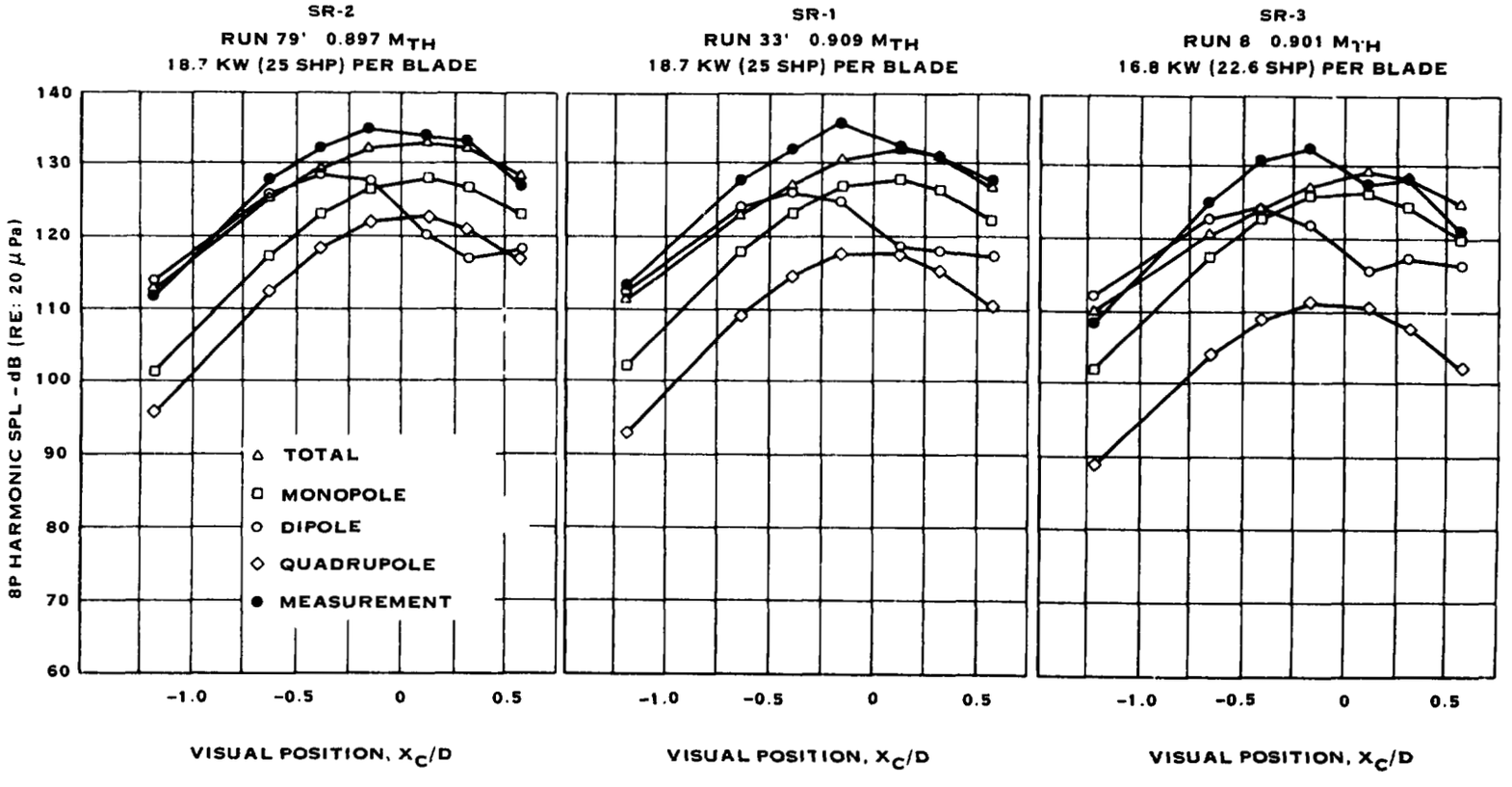

D = NOMINAL PROP-FAN DIAMETER 62.2 CM (24.5 IN.)

FIGURE 3-51. COMPARISON OF SR-2, SR-1, AND SR-3 DIRECTIVITY WITH THEORY

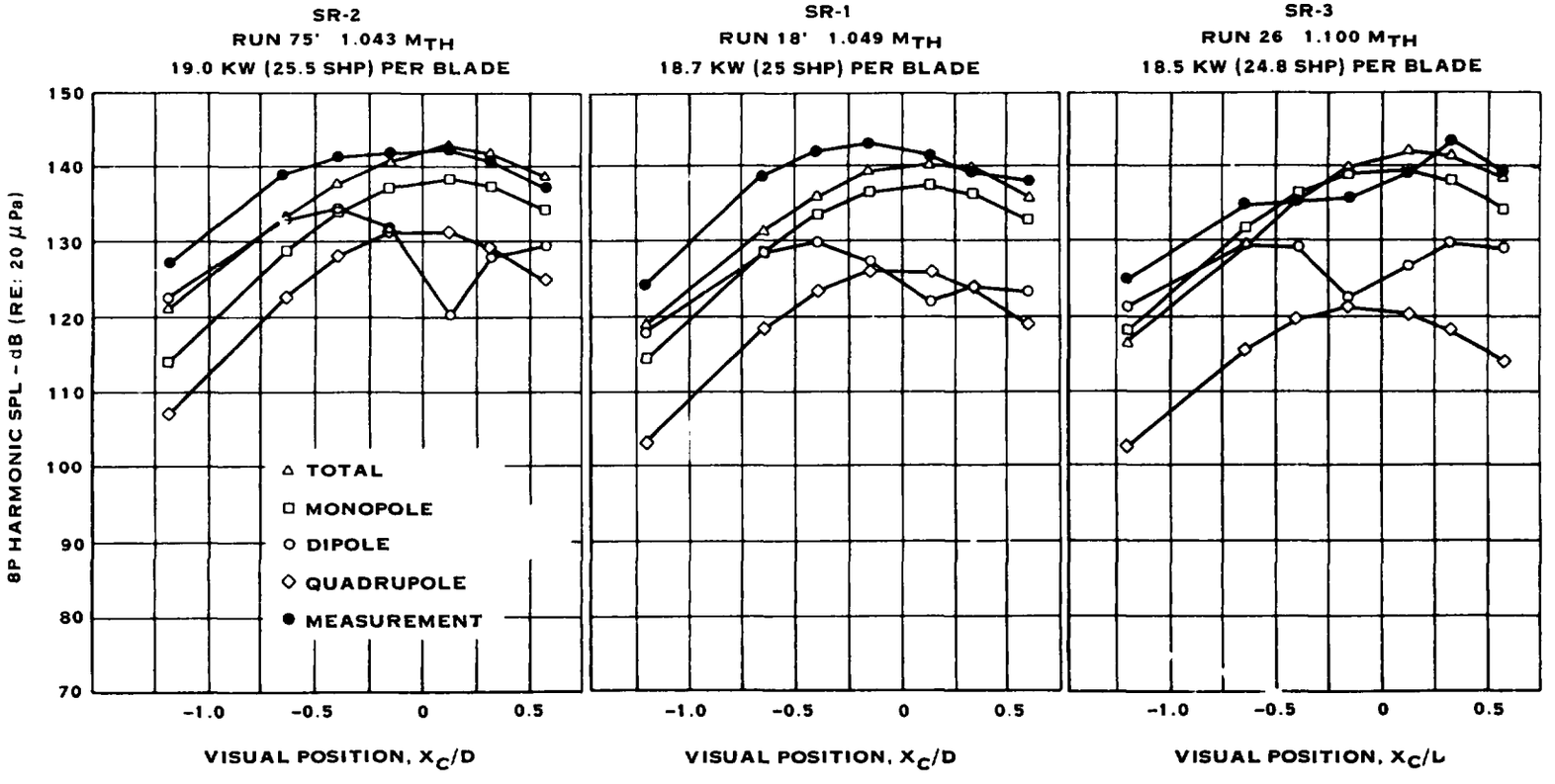

D = NOMINAL PROP-FAN DIAMETER 62.2 CM (24.5 IN.)

FIGURE 3-52. COMPARISON OF SR-2, SR-1 AND SR-3 DIRECTIVITIES WITH THEORY

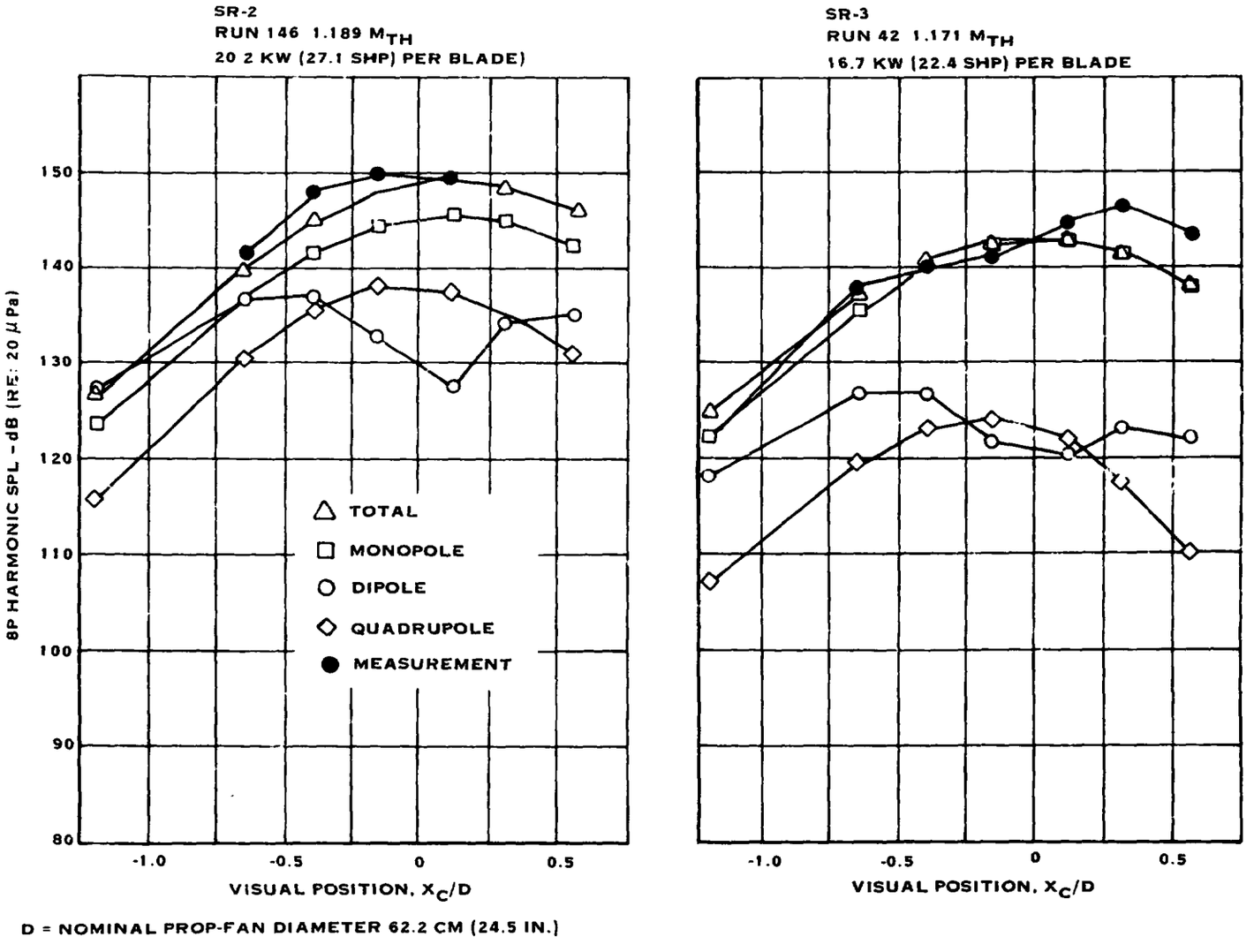

D = NOMINAL PROP-FAN DIAMETER 62.2 CM (24.5 IN.)

FIGURE 3-53. COMPARISON OF SR-2 AND SR-3 DIRECTIVITIES WITH THEORY

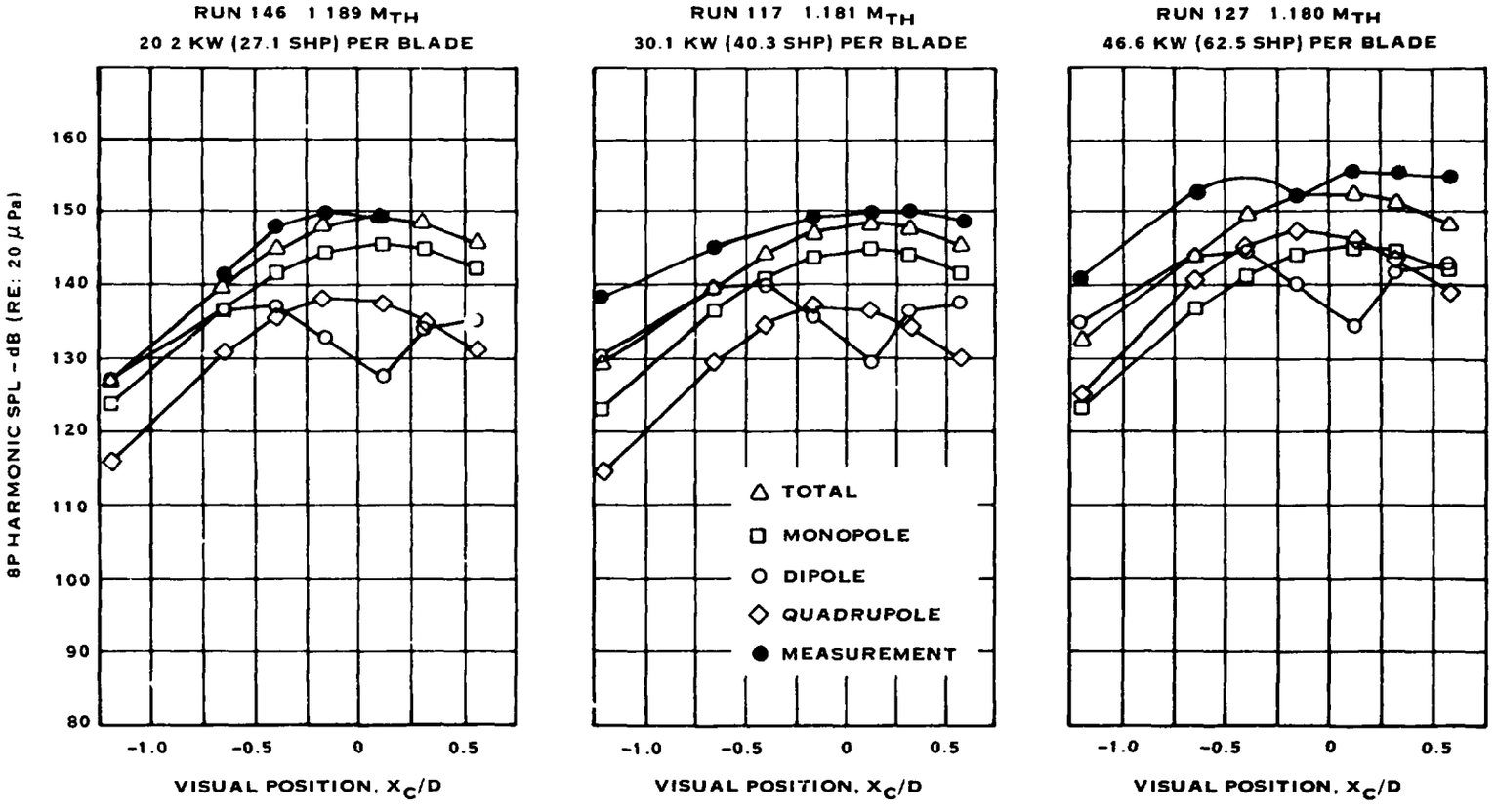

FIGURE 3-54. COMPARISON OF SR-2 DIRECTIVITIES WITH THEORY

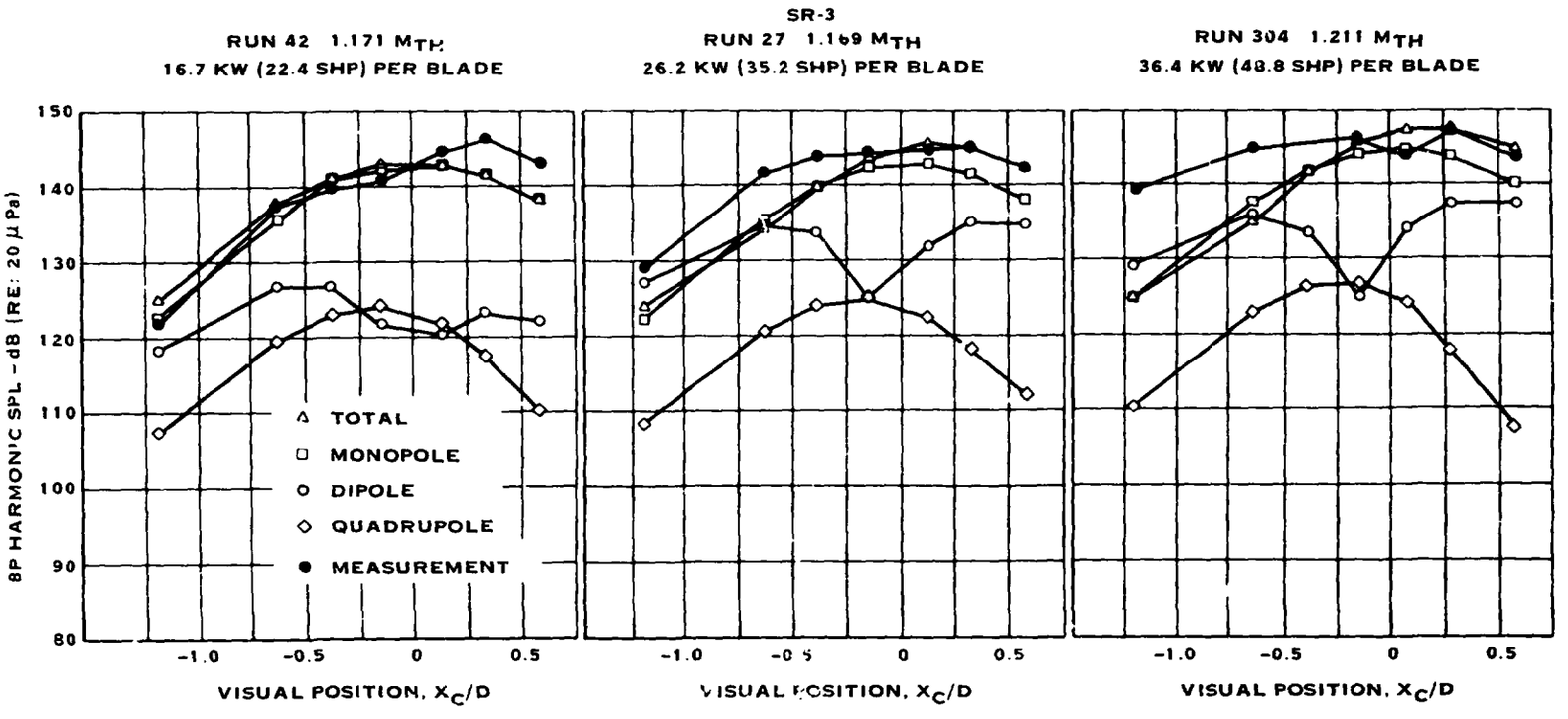

D = NOMINAL PROP-FAN DIAMETER 62.2 CM (24.5 IN.)

FIGURE 3-55. COMPARISON OF SR-3 DIRECTIVITIES WITH THEORY

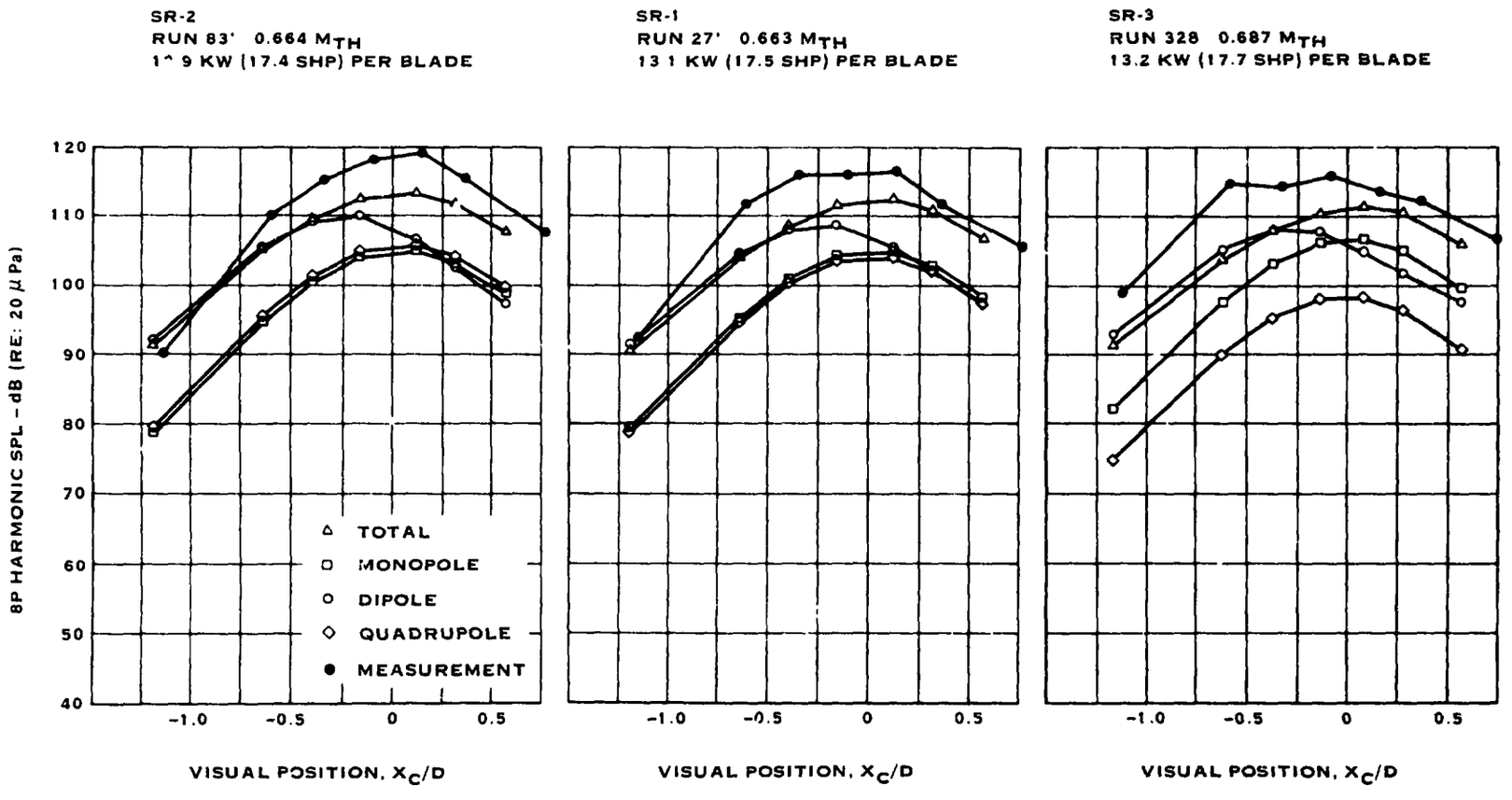

D = NOMINAL PROP-FAN DIAMETER 62.2 CM (24.5 IN.)

FIGURE 3-56. COMPARISON OF SR-2, SR-1 AND SR-3 DIRECTIVITIES WITH THEORY

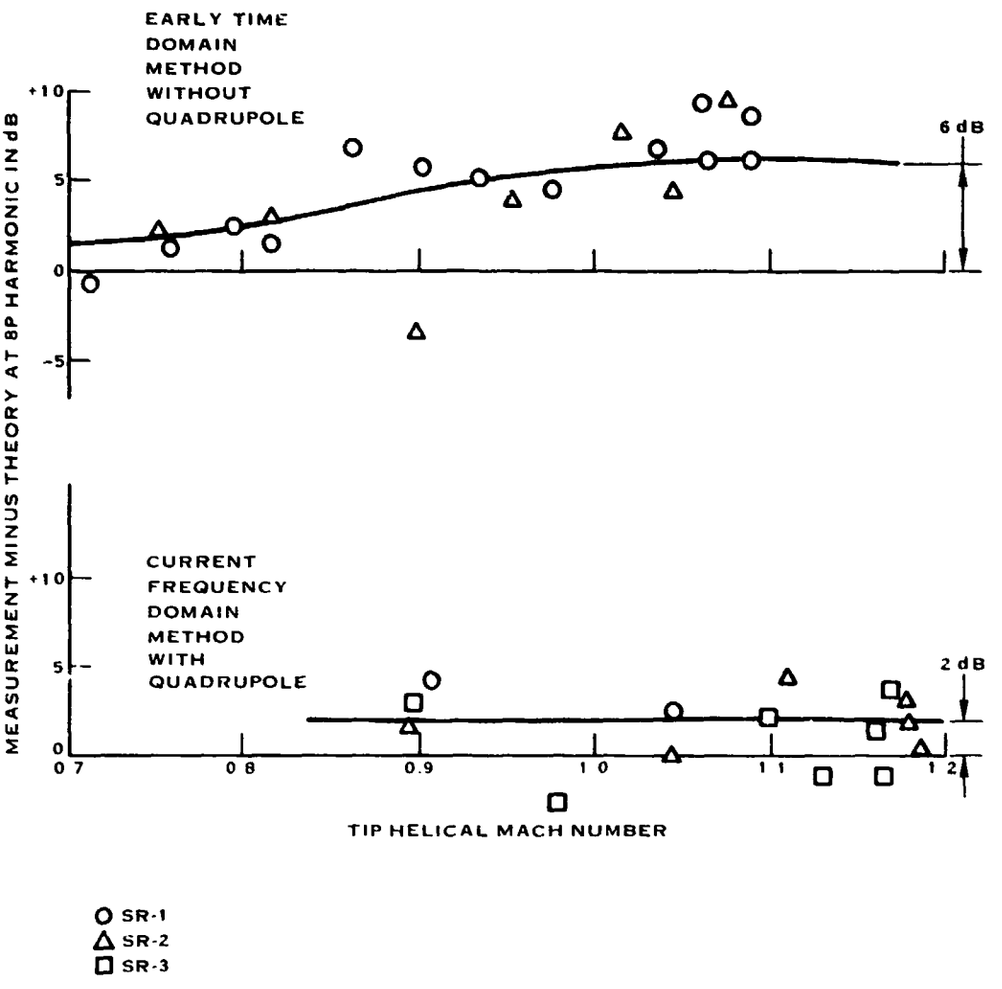

FIGURE 3-57. COMPARISON OF TEST AND THEORY

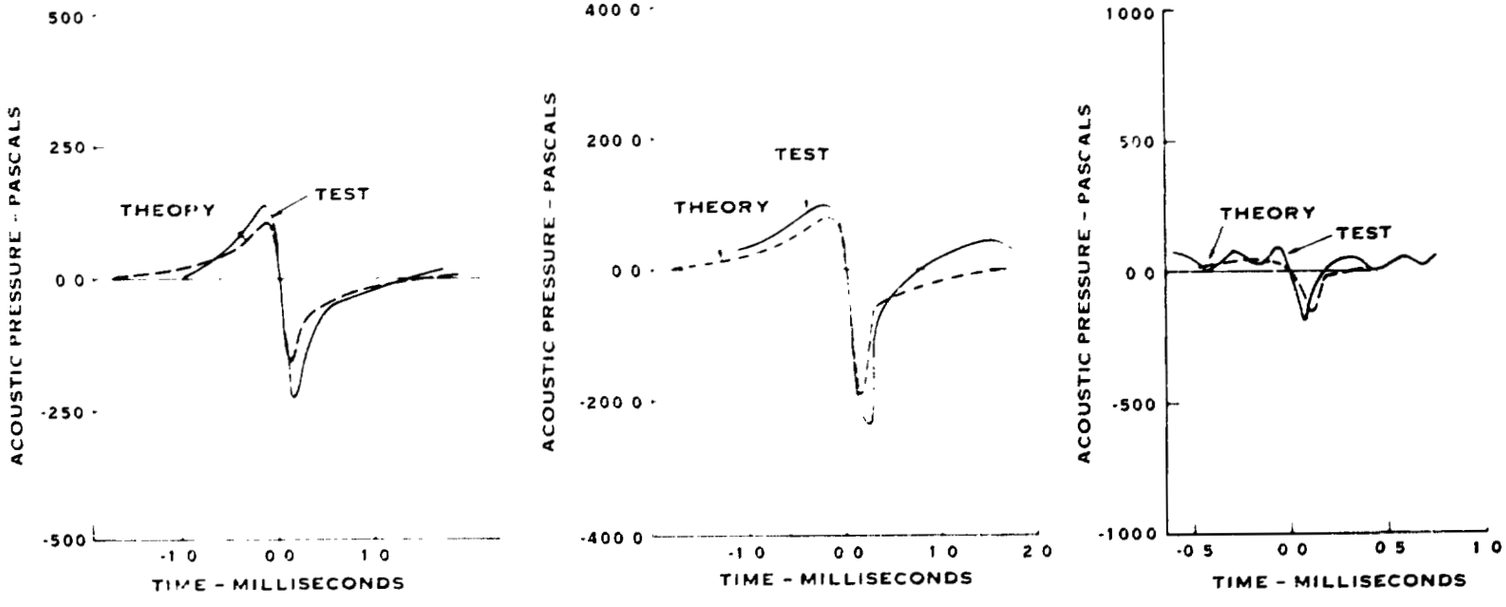

SR-2, RUN 79', 8460 RPM
18 7 KW/BLADE,
M_X = 0 322, M_{TH} = 0.897
WAVEFORM FOR MIC 4

SR-1, RUN 33', 8532 RPM
18 7 KW/BLADE,
M_X = 0 323, M_{TH} = 0 909,
WAVEFORM FOR MIC 4

SR-3, RUN 8, 8550 RPM
16 8 KW/BLADE
M_X = 0 321, M_{TH} = 0 901
WAVEFORM FOR MIC 4

FIGURE 3-58 COMPARISON OF SR-2, SR-1 AND SR-3 WAVEFORMS

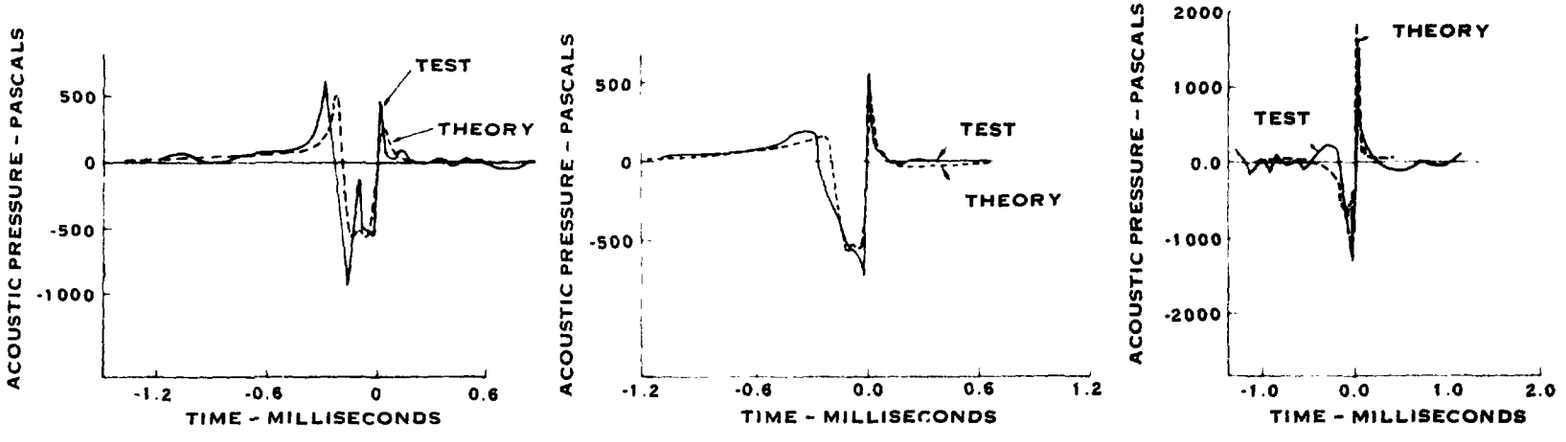

SR-2, RUN 75', 10002 RPM,
19.0 KW/BLADE
$M_X = 0.321$, $M_{TH} = 1.043$
WAVEFORM FOR MIC 3

SR-1, RUN 18', 10050 RPM,
18.7 KW/BLADE,
$M_X = 0.321$, $M_{TH} = 1.049$
WAVEFORM FOR MIC 4

SR-3, RUN 26, 10,550 RPM
18.5 KW/BLADE
$M_X = 0.320$, $M_{TH} = 1.100$
WAVEFORM FOR MIC 3

FIGURE 3-59. COMPARISON OF SR-2, SR-1 AND SR-3 WAVEFORMS

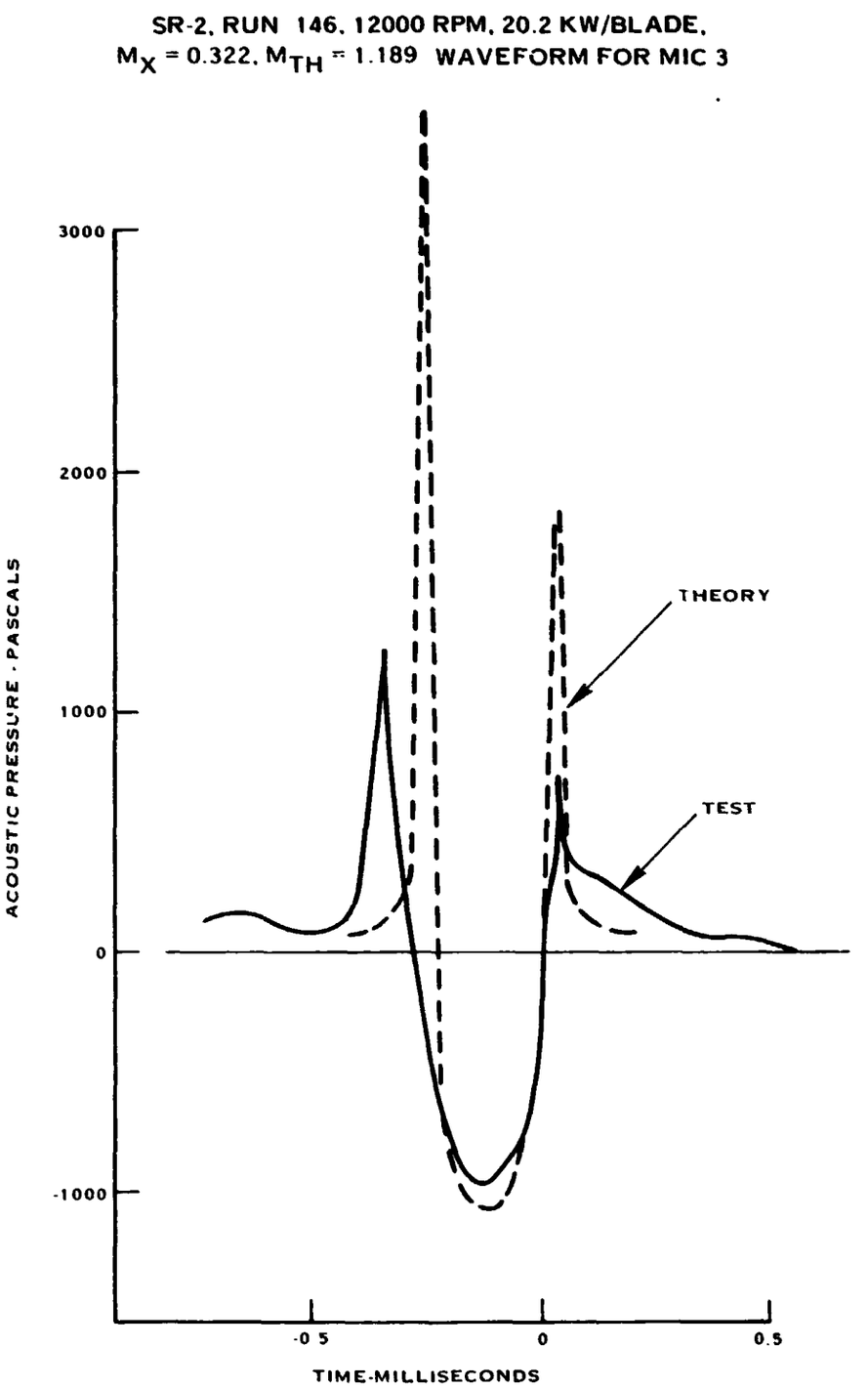

FIGURE 3-60. SR-2 WAVEFORM PREDICTION AND MEASUREMENT

SR-3, RUN 42, 11300 RPM, 16.7 KW/BLADE,
WAVEFORM FOR MIC 3 M_X = .322, M_{TH} = 1.171

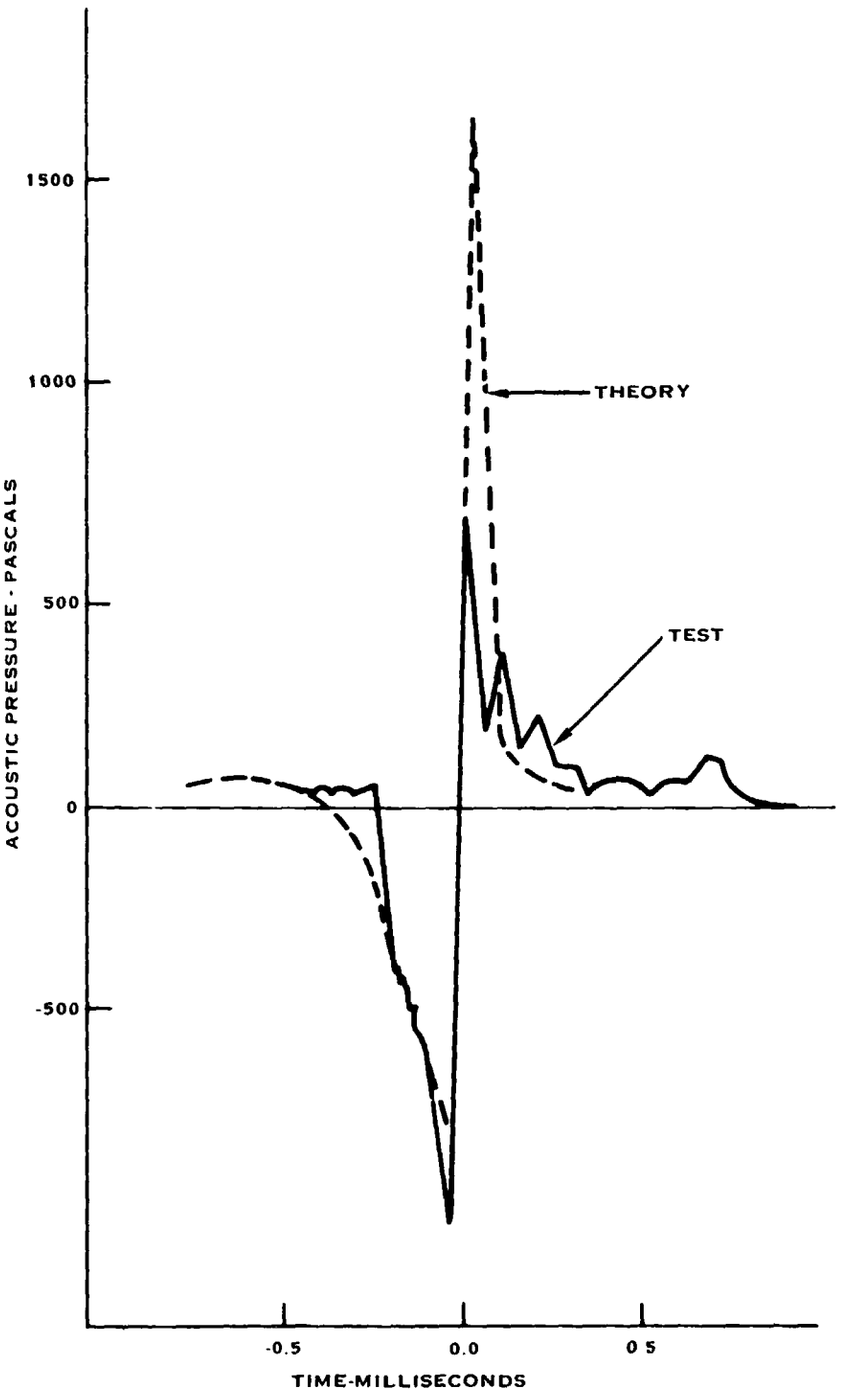

FIGURE 3-61. SR-3 WAVEFORM PREDICTION AND MEASUREMENT

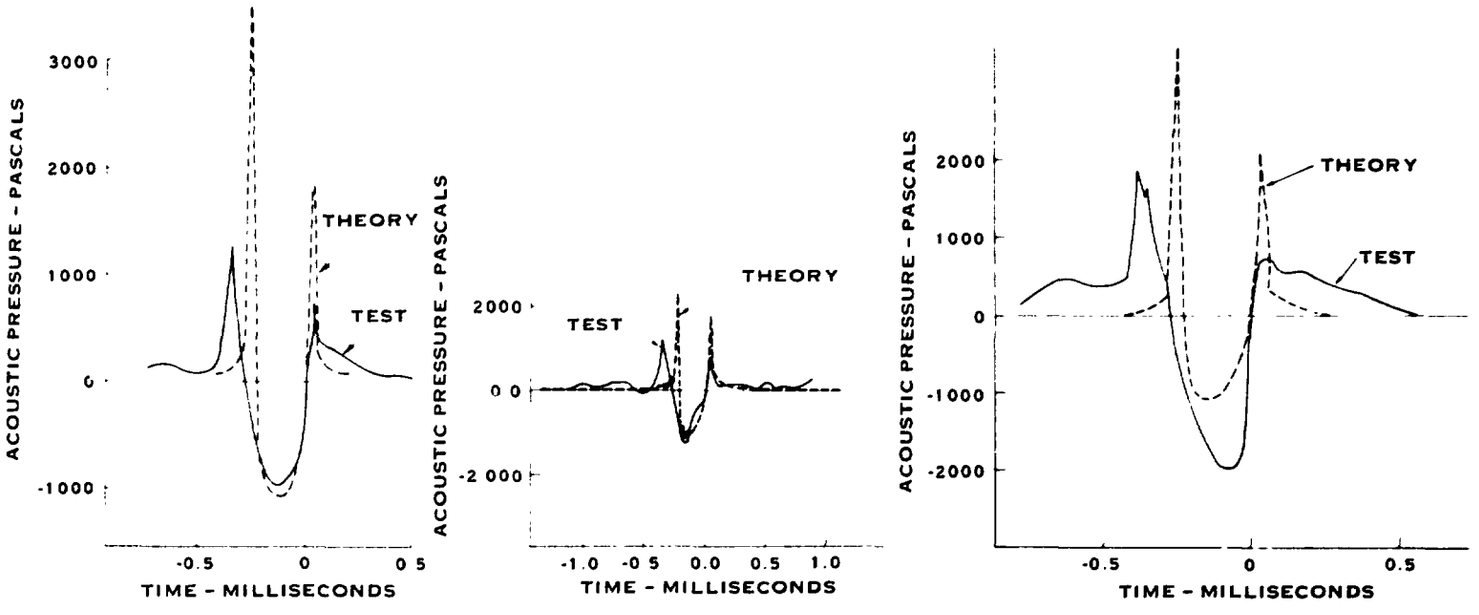

FIGURE 3-62. SR-2 WAVEFORM COMPARISONS

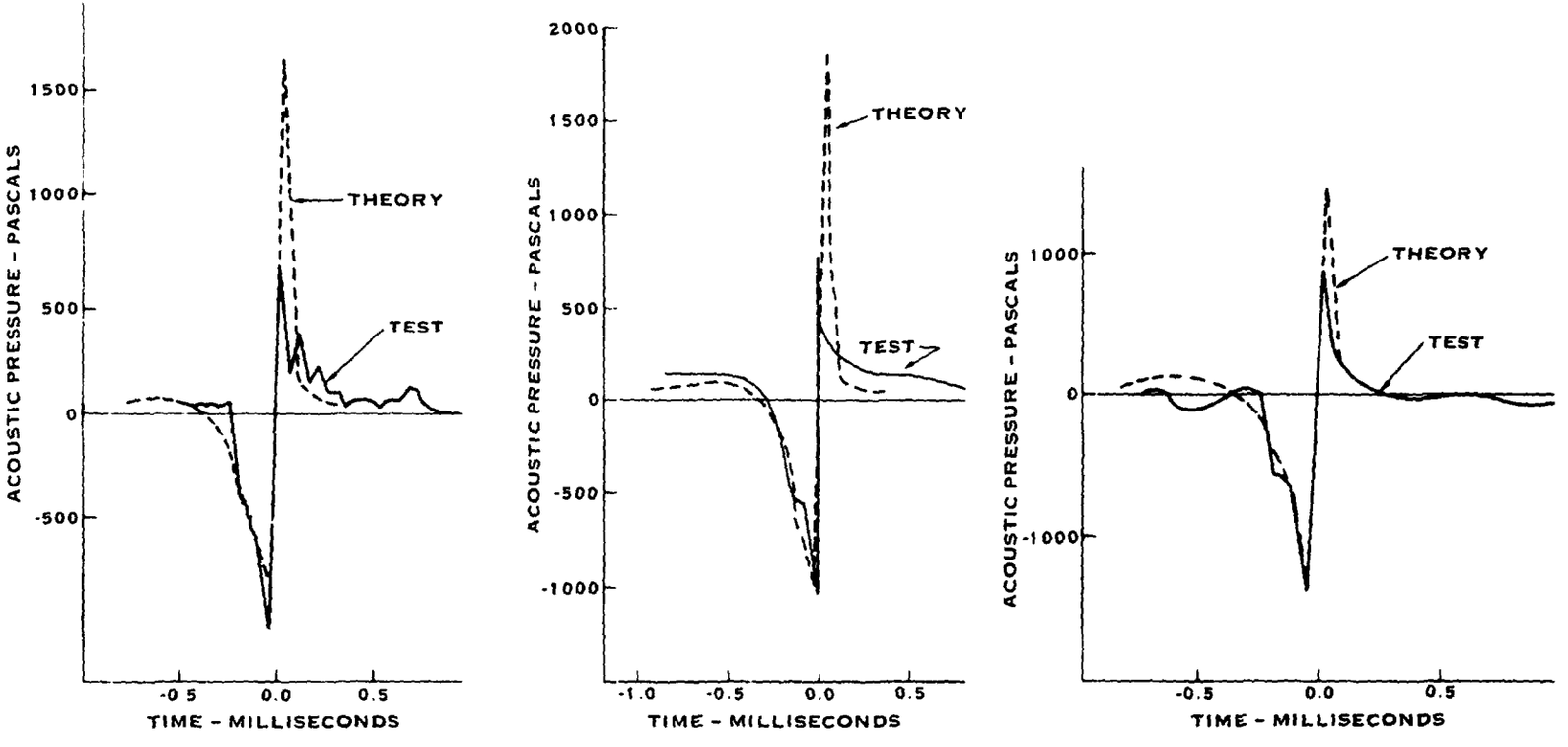

SR-3, RUN 42, 11300 RPM
16.7 KW/BLADE
$M_X = 0.322$, $M_{TH} = 1.171$
WAVEFORM FOR MIC 3

SR-3, RUN 27, 11250 RPM
26.2 KW/BLADE
$M_X = 0.322$, $M_{TH} = 1.169$
WAVEFORM FOR MIC 3

SR-3, RUN 304, 11800 RPM
36.4 KW/BLADE,
$M_X = 0.323$, $M_{TH} = 1.211$
WAVEFORM FOR MIC 3

FIGURE 3-63. SR-3 WAVEFORM COMPARISONS

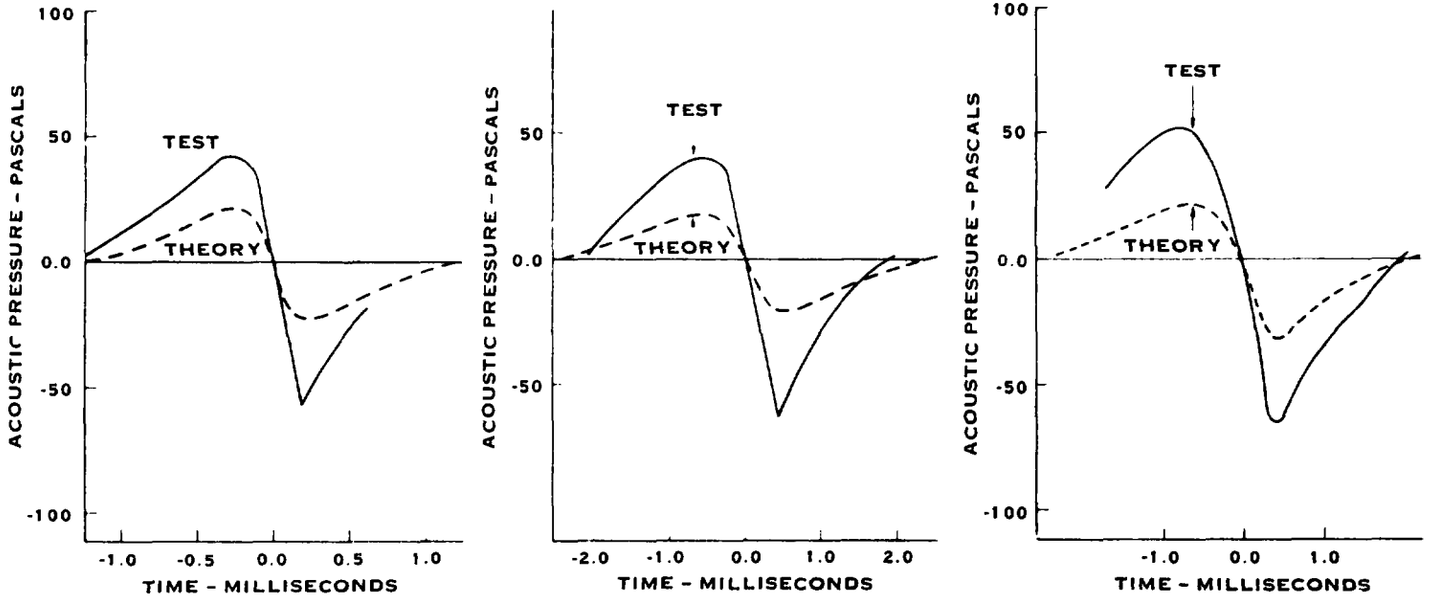

FIGURE 3-64. LOW SPEED WAVEFORM COMPARISONS

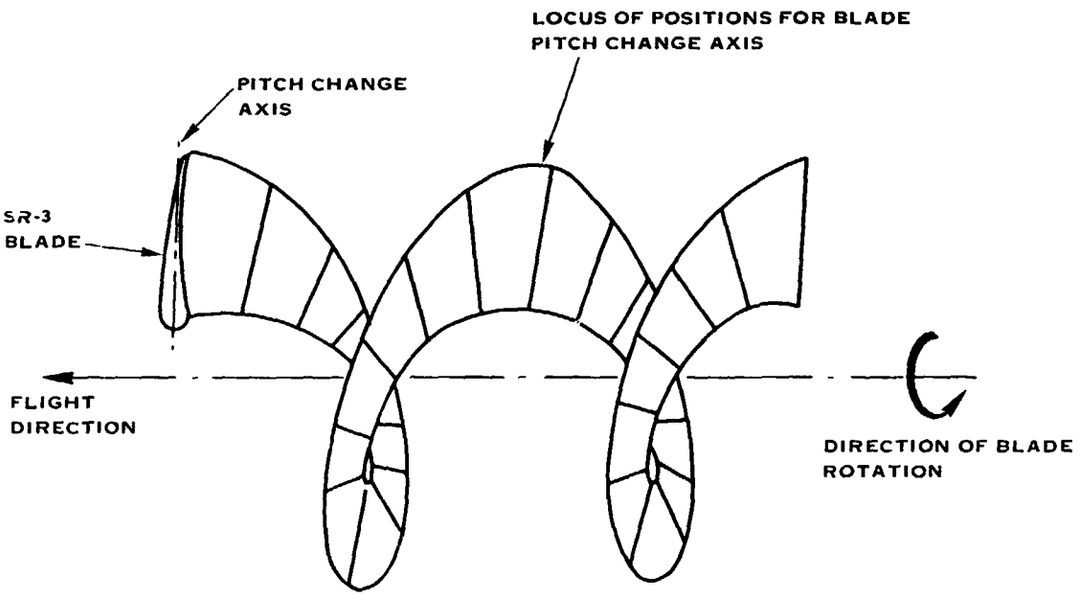

FIGURE 3-65. BLADE HELICOIDAL SURFACE

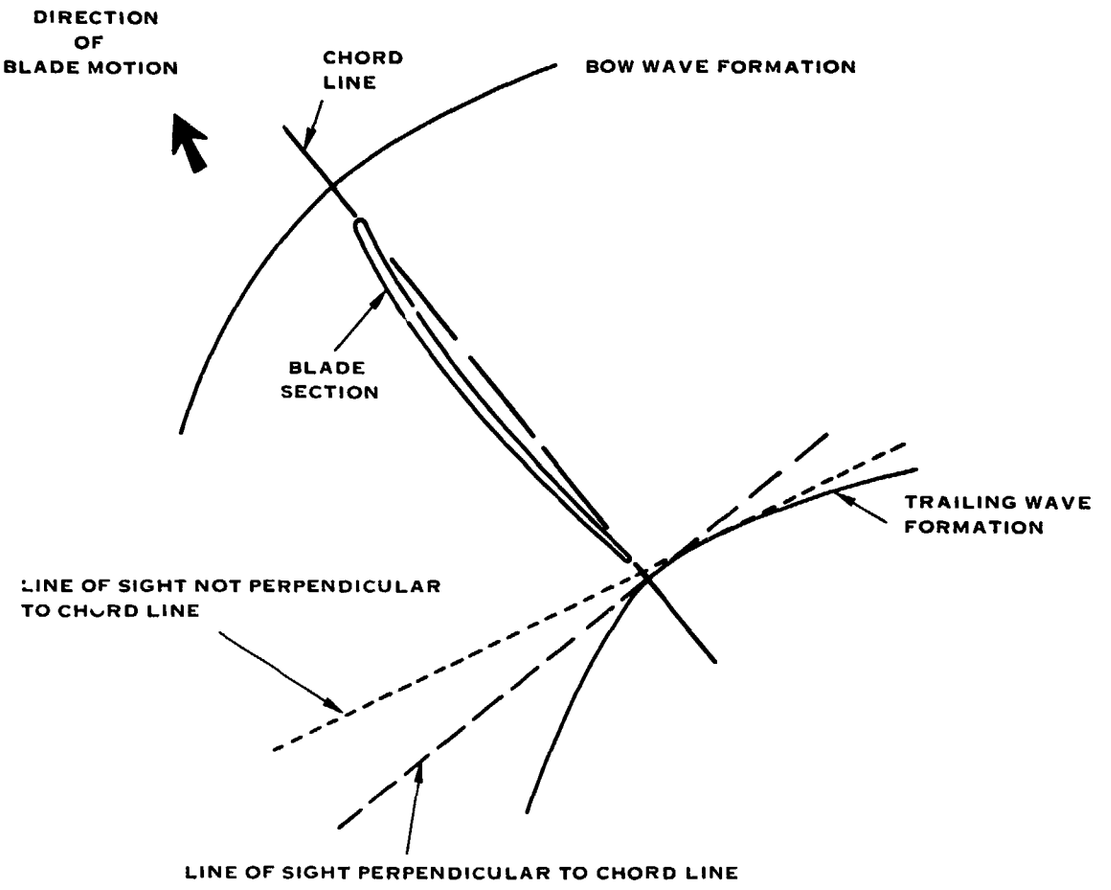

FIGURE 3-66. LINE OF SIGHT ORIENTATION RELATIVE TO BLADE CHORD

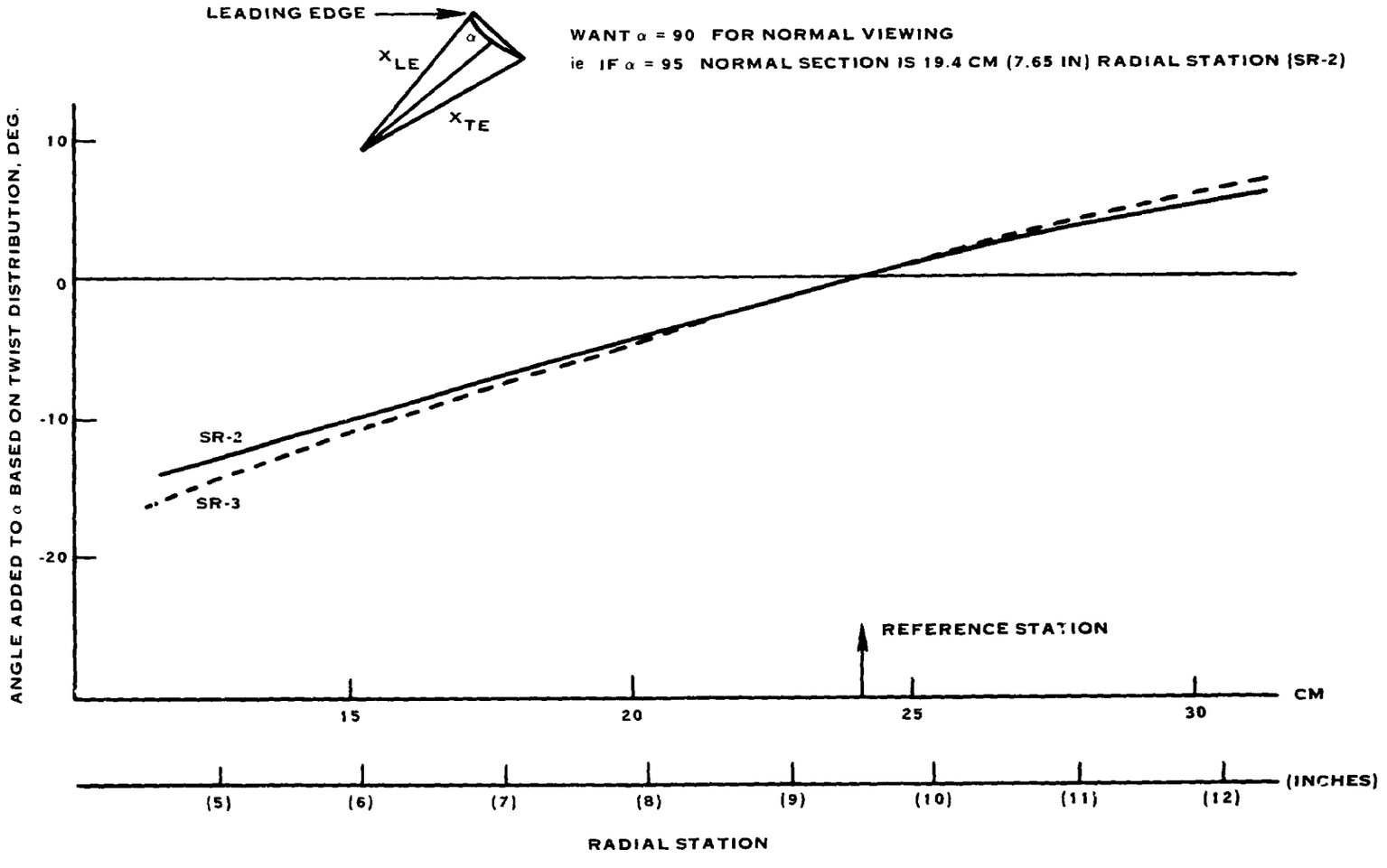

FIGURE 3-67 SR-2 AND SR-3 BLADE TWIST DISTRIBUTION RELATIVE TO REFERENCE STATION

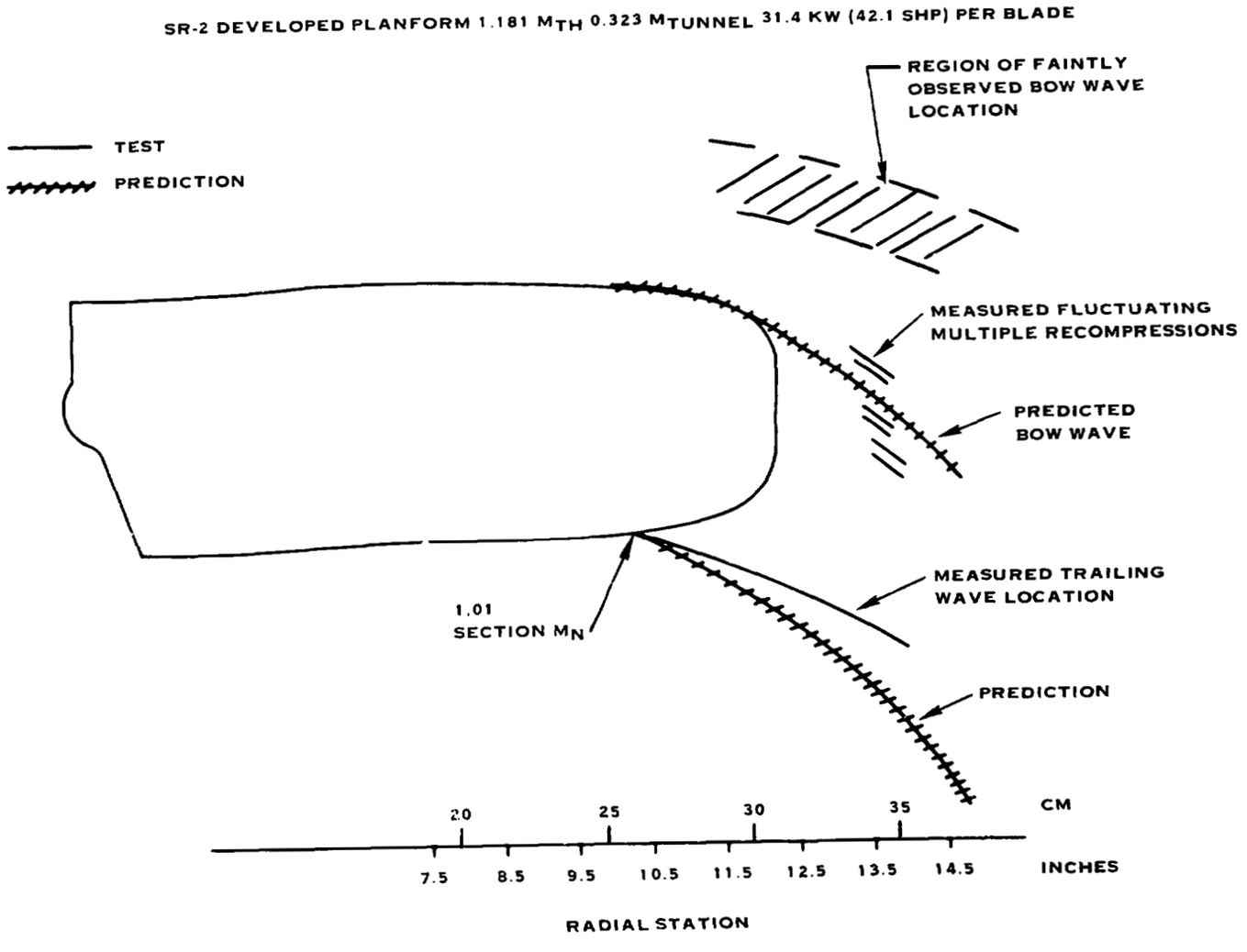

FIGURE 3-68. SHADOWGRAPH MEASUREMENTS OF SR-2 WAVE FORMATIONS

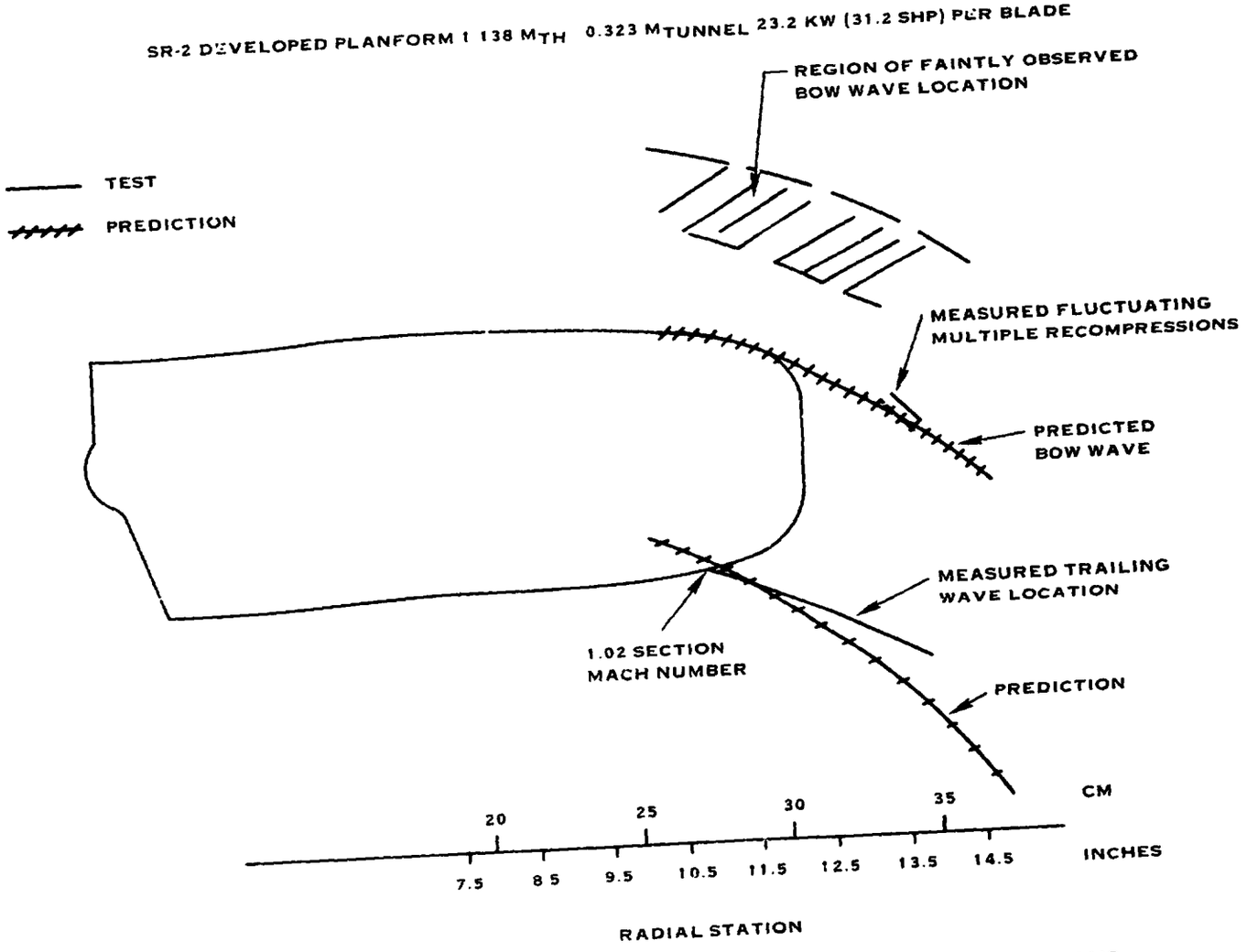

FIGURE 3-69. SHADOWGRAPH MEASUREMENTS OF SR-2 WAVE FORMATIONS

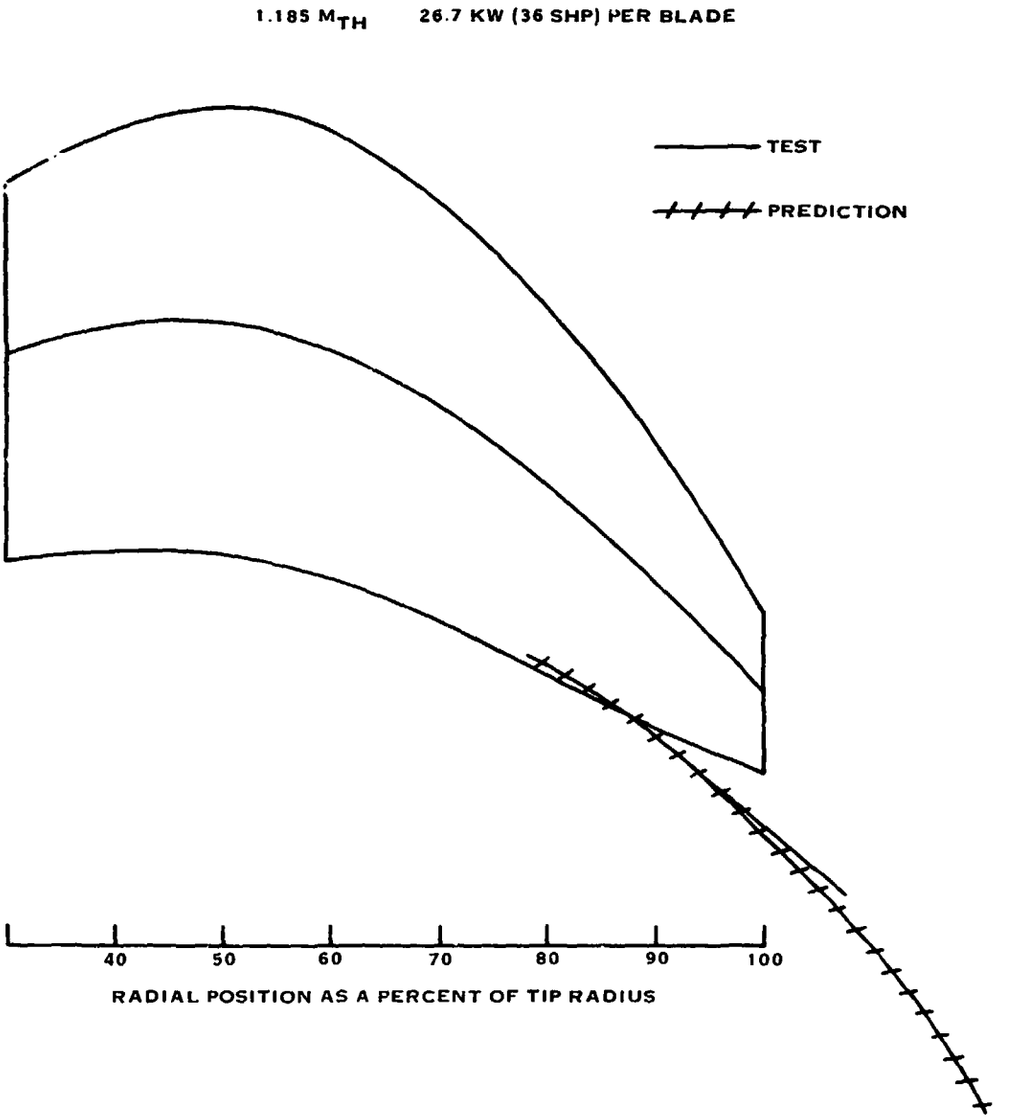

FIGURE 3-70. SHADOWGRAPH MEASUREMENTS OF SR-3 WAVEFORMS VS. THEORETICAL PREDICTIONS

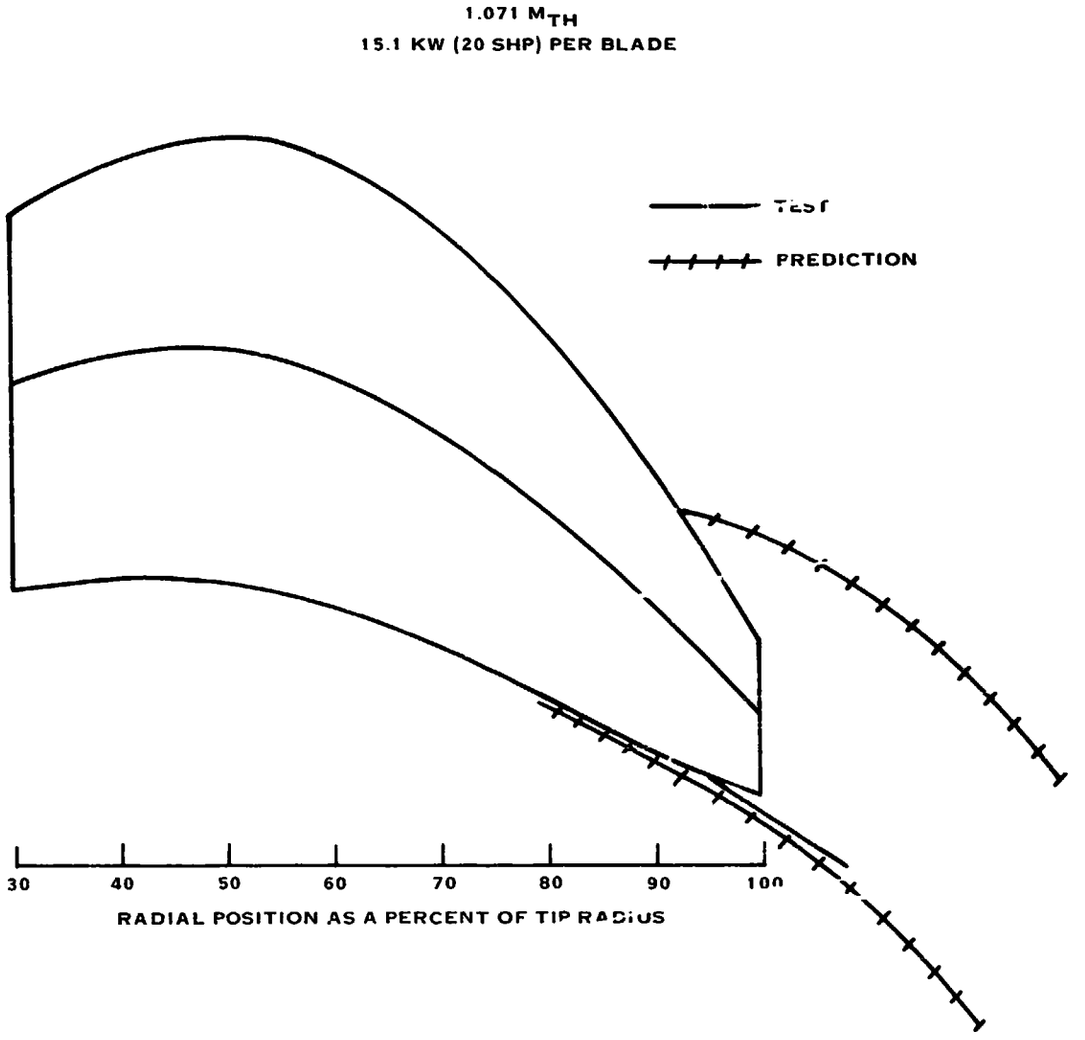

FIGURE 3-71. SHADOWGRAPH MEASUREMENTS OF SR-3 WAVE FORMATIONS VS. THEORETICAL PREDICTIONS

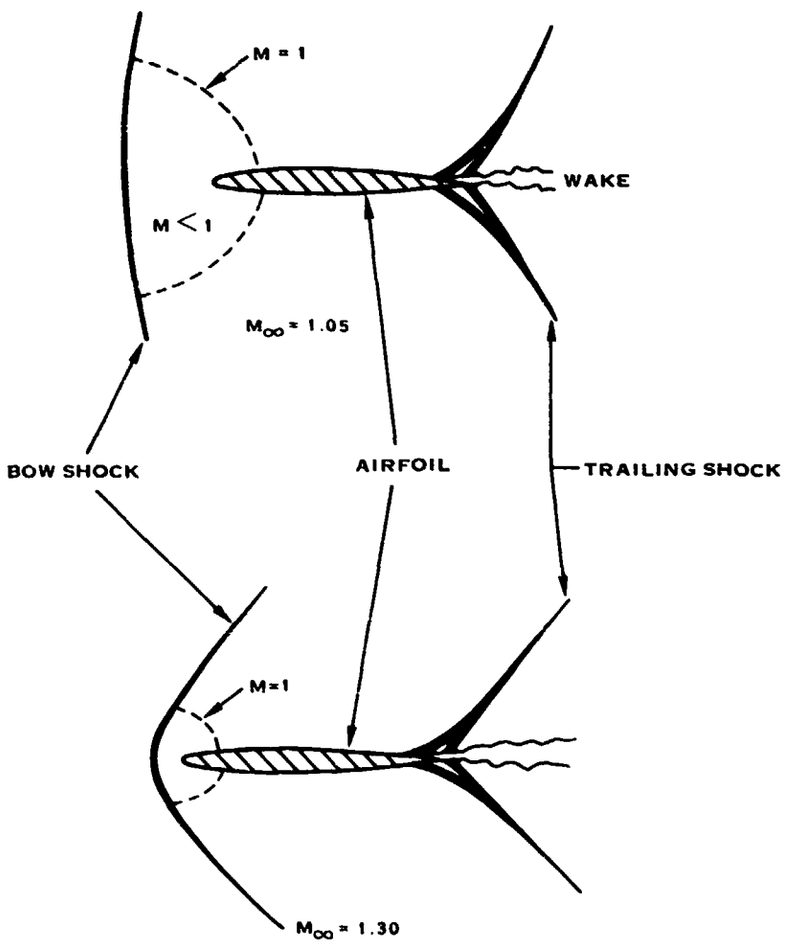

FIGURE 3-72. BOW SHOCK DETACHMENT FOR 2-D AIRFOILS AT LOW SUPERSONIC MACH NUMBERS. SKETCHES ADAPTED FROM SHAPIRO (REF 3-7) FIGURE 22-5.

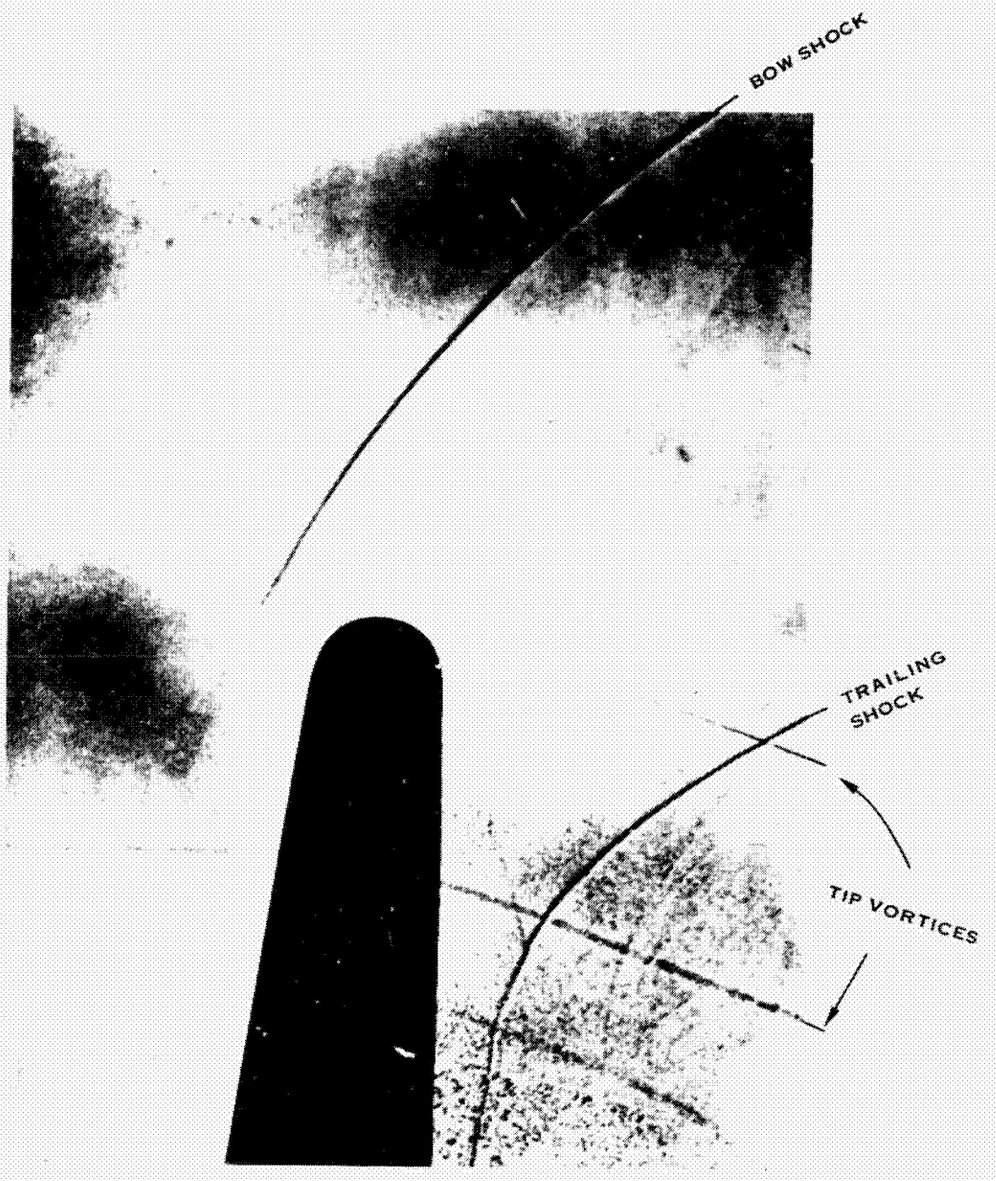

FIGURE 3-73. SHADOWGRAPH BY HILTON (REF. 3-12) FOR A CONVENTIONAL PROPELLER OVERSPED TO $M_T = 1.21$. BOW SHOCK STANDS OFF FROM LEADING EDGE, CONTRARY TO PREDICTIONS FROM LINEAR THEORY

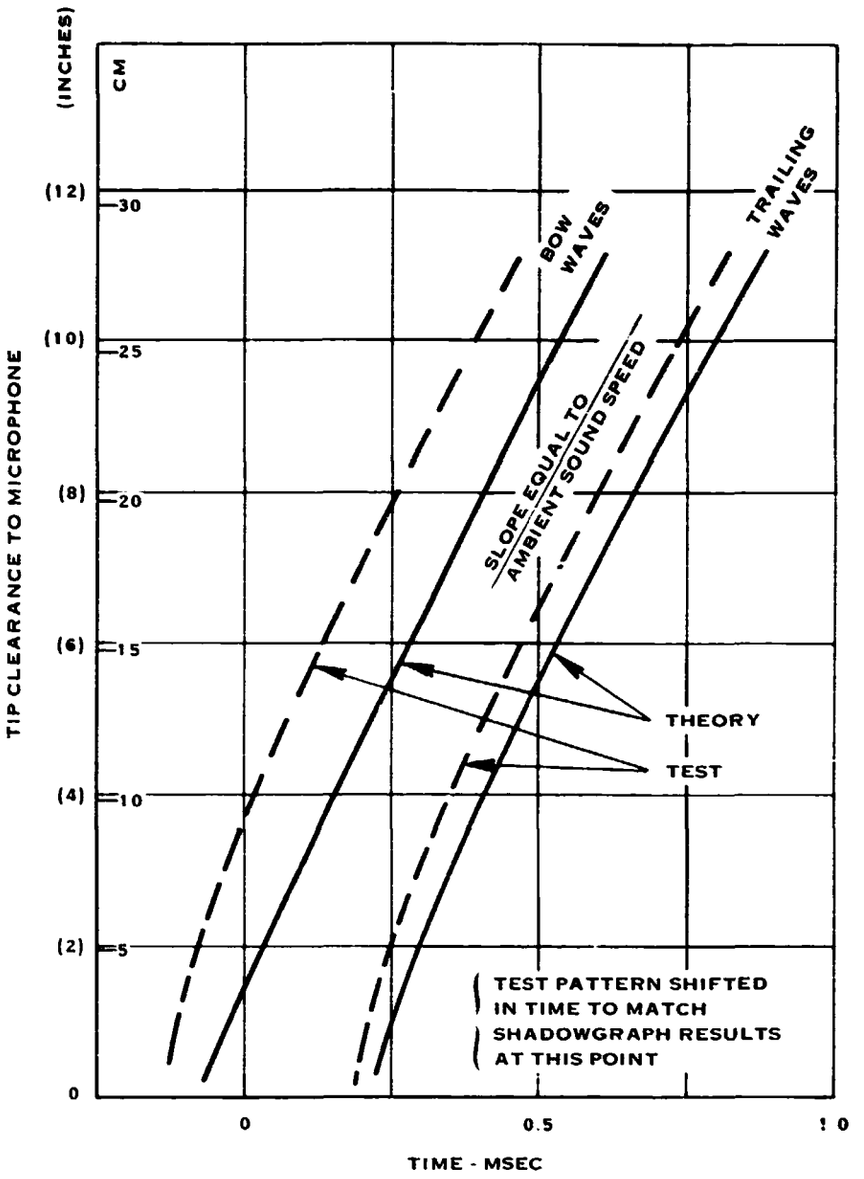

FIGURE 3-74. COMPARISONS OF MEASURED WAVE ARRIVAL TIMES WITH PREDICTIONS OF LINEAR THEORY

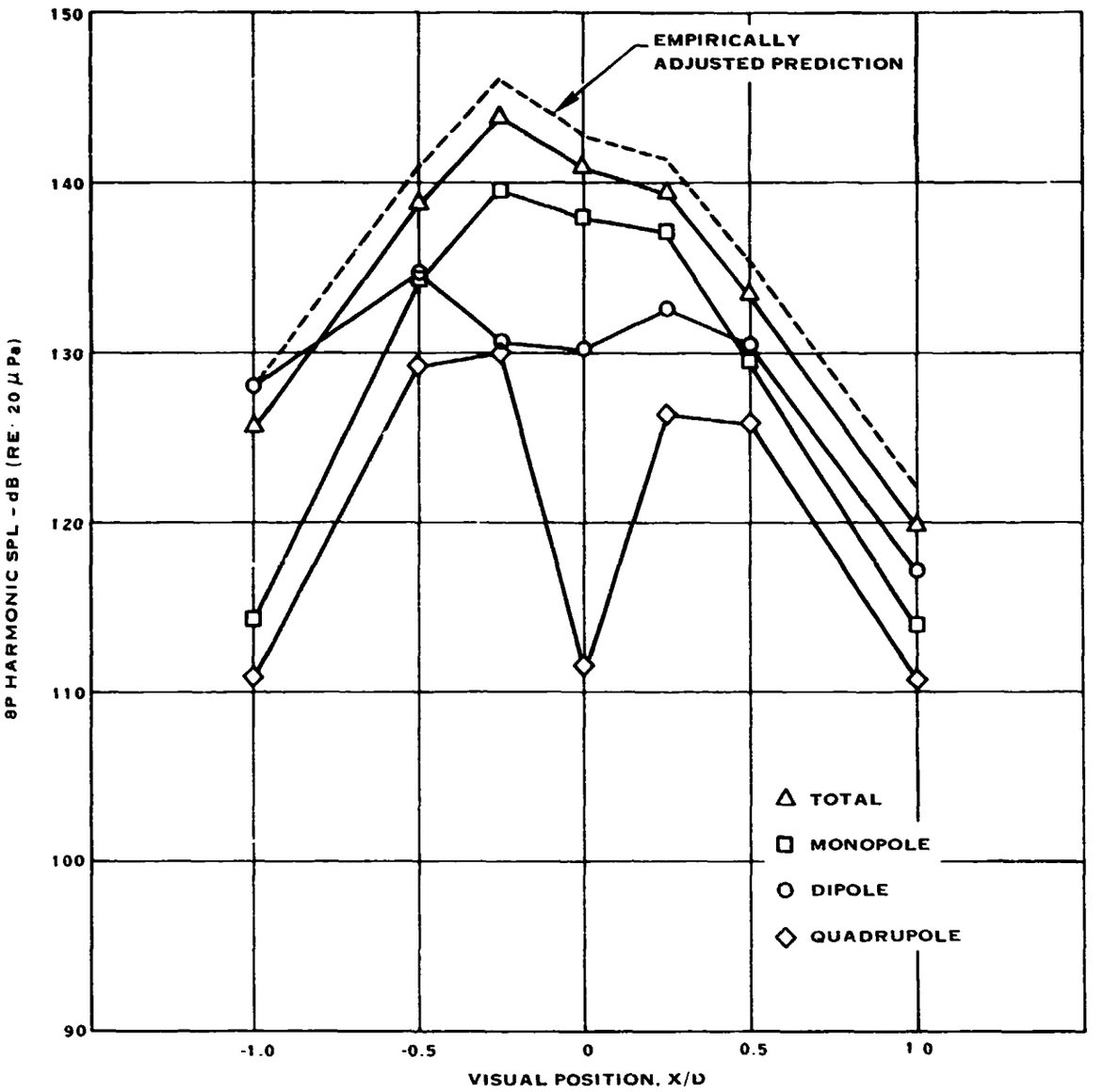

FIGURE 3-75. SR-3 DIRECTIVITY IN FULL SCALE AT CRUISE 0.8 DIAMETER TIP CLEARANCE

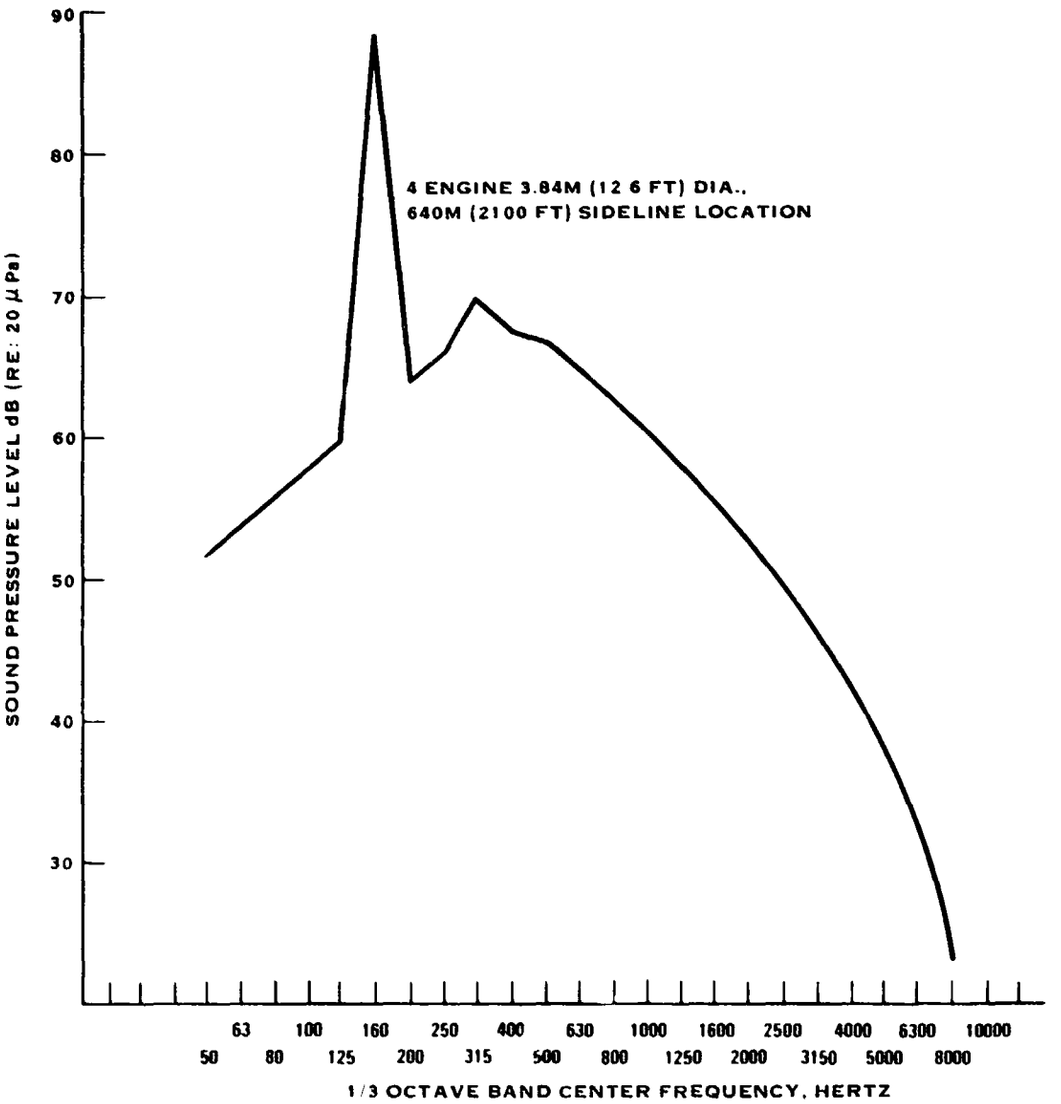

FIGURE 3-76. FULL SCALE SR-3 PROP FAN SPECTRUM AT TAKEOFF

CONCLUSIONS

The following conclusions have been reached as a result of the program summarized in this report:

1. The blade sweep of SR-3 is quite beneficial for reducing noise in both the near field and far field. However, the blade sweep of the SR-1 design is not sufficient to reduce noise at supersonic tip speeds and it is of minor benefit at subsonic tip speeds.

2. The blade sweep noise reduction benefits appear greatest at the high loading conditions typical of prop-fan operation. Smaller benefits occur at the lighter loadings more typical of conventional propellers. It appears that greater sweep would provide even greater noise reduction.

3. The current prop-fan noise prediction methodology is significantly better than the earlier methodology which did not include the quadrupole noise source. Peak sideline noise predictions in the near field are underpredicted by about 2 dB. Aft of the plane of rotation larger underpredictions occur at the higher loading conditions. This is believed due to a discrepancy in spanwise loading distribution used as an input to the noise calculation.

4. Measured and predicted acoustic pressure pulses show good general agreement over the complete range of the test program indicating that the methodology includes all of the basic sources necessary for accurate predictions. However, the length of the pressure pulse is underpredicted indicating that nonlinear flow effects may be required in further refinements to the calculation procedure. This lack of agreement in pressure duration can cause a lack of agreement between measurement and prediction at higher frequencies in the prop-fan noise spectrum.

5. Shadowgraphs showed the presence of trailing waves in the SR-2 and SR-3 and evidence of recompressions due to interactions with the blade turbulent boundary layer near the leading edge of the SR-2 blade. However, the bow waves predicted by the noise methodology and seen in the measured acoustic pressure pulses were not found in the shadowgraphs. The location of the trailing edge of the SR-3 ahead of the predicted and measured trailing wave indicates that the trailing edge of the SR-3 did not have sufficient sweep to minimize the effects of the trailing wave. The leading edge of the SR-3 does appear to be swept behind the bow wave as intended in this design.

6. Hot wire anemometry measurements of the blade wakes demonstrated their feasibility for defining the wake defects of model prop-fan blades operating at supersonic tip speeds. The shape of these wake defects is an indication of airfoil performance at various spanwise locations on the blades.

7. The peak sideline blade passage frequency noise of the SR-3 at cruise conditions of 244 m/s (800 ft/sec) tip speed, 302 kW/m^2 (37.5 SHP/D^2), 10 667 m (35 000 ft) altitude and 0.8 D tip clearance was estimated to be 146 dB on the basis of the prop-fan noise prediction methodology as adjusted by findings in the correlation of measurements and predictions of this report. The major reason for the high level of noise predicted is the lack of sufficient blade sweep in the SR-3 design.

8. Far field noise was estimated at 640 m (2100 ft) to the side of a 102 060 kg (225 000 lb) four engine aircraft with 3.84 m (12.6 ft) diameter 8 blade prop-fans at takeoff conditions of 244 M/s (800 ft/sec) tip speed, 564 kW/M^2 (70 SHP/D^2) loading, 25°C (77 F), 70% relative humidity and 0.2 Mach number forward speed. This estimate was based on scaling blade passage frequency harmonic levels from the model test data and adding the broadband noise predicted for full scale propellers. A level of 91.5 EPNdB was estimated for this condition. This is consistent with earlier predictions which showed the level of prop-fan transports to be lower than current noise certification requirements.

REFERENCES

2-1 Black, D. M.; Menthe, R. W.; and Wainauski, H. S.; Aerodynamic Design and Performance Testing of an Advanced 30° Swept, Eight Bladed Propeller at Mach Numbers from 0.2 to 0.85. NASA CR-3047, 1978.

2-2 Jeracki, R. J.; et al: Wind Tunnel Performance of Four Energy Efficient Propellers Designed for Mach 0.8 Cruise, NASA TM 79124, 1979.

2-3 Metzger, F. B.; Rohrbach, C.: Aeroacoustic Design of the Prop-Fan. AIAA 79-0610, 1979

2-4 Paterson, R. W.; Vogt, P. G.; and Foley, W. M.: Design and Development of the United Aircraft Research Laboratories Acoustic Research Tunnel. J. Aircraft, Volume 10, No. 7, 1973, pp. 427-433.

2-5 Holman, J. P.: Experimental Methods for Engineers, McGraw- Hill, New York, 1966.

2-6 Braslow, A. L.; et al: Simplified Method for Determination of Critical Height of Distributed Roughness Particles for Boundary Layer Transition at Mach Numbers from 0 to 5, NACA TN 4363, 1958.

3-1 Schlinker, R. H. and Amiet, R. K.: Experimental Assessment of Theory for Refraction of Sound by a Shear Layer; NASA CR-145359; 1978.

3-2 Federal Aviation Regulations, Part 36: Noise Standards, Aircraft Type and Airworthiness Certification. Change 8, Effective April 3, 1978.

3-3 Hanson, D. B.: The Influence of Propeller Design Parameters on Far Field Harmonic Noise in Forward Flight, AIAA Paper 79-0609, March 1979.

3-4 Hawkings, D. L.; and Lowson, M. V.: Theory of Open Supersonic Rotor Noise, J. Sound and Vibration, Vol. 36, No. 1, 1974.

3-5 Farassat, F.: Theory of Noise Generation from Moving Helicopter Blades with an Application to Helicopter Rotors, NASA TR-R-451, 1975.

3-6 Hanson, D. B.: Near Field Noise of High Tip Speed Propellers in Forward Flight, AIAA Paper 76-565, 1976.

3-7 Shapiro, A. H.: Compressible Fluid Flow; Ronald Press, New York, 1953.

REFERENCES (Continued)

3-8 Bennett, J. C.: High-Response Measurements of Prop-Fan Flow Fields, Presented at Dynamic Flow Conference 1978, Baltimore, MD. September 1978, also published as UTRC Report 78-65.

3-9 Ffowcs Williams, J. E.; and Hawkings, D. L.: Sound Generated by Turbulence and Surfaces in Arbitrary Motion, Phil. Trans. Roy. Soc. London Series A, Vol. 264, 1969.

3-10 Gutin, L. J.: On the Sound Field of a Rotating Propeller, Physi Ralisehi Jetschrift det Sowjetunio.., Vol. 9, No. 1, 1936. Presented as ARC Paper 3115 or NACA Tech. Memo 1195.

3-11 Hanson, D. B.; and Fink, M. R.: The Importance of Quadrupole Sources in Prediction of Transonic Tip Speed Propeller Noise, Journal of Sound and Vibration, Volume 62, January 1979.

3-12 Hilton, W. F.: The Photography of Airscrew Sound Waves, Proc. Roy. Soc. A., Vol. 169, 1938.

3-13 Ffowcs Williams, J. E.: On the Role of Quadrupole Source Terms Generated by Moving Bodies, AIAA Paper 79-0576, 1979.

APPENDIX A
PREDICTED AND MEASURED 8P DIRECTIVITIES AND ACOUSTIC PRESSURE PULSES

This appendix presents the measured and predicted 8P directivities and acoustic pressure pulses for 22 selected test conditions. Table AI lists the conditions selected including the figure number in the appendix, number of blades on the rotor, power absorbed per blade, RPM, tunnel through flow Mach number, and tip helical Mach number. For each condition selected, two figures are presented. The first shows the near field 8P harmonic directivity measured at 0.8 D sideline tip clearance, compared with predicted total 8P harmonic noise as well as the monopole, dipole and quadrupole that are summed to obtain total noise. The second figure for each condition shows the acoustic pressure pulse predicted and measured at the 8P harmonic measured peak sideline location. Several test conditions include comparisons of predicted and measured pulses at other 0.8 D sideline near field locations. The predicted pulses include the monopole and dipole contributions and have been generated with the frequency response of the measurement system included in the calculation. The measured and predicted pulses are overlayed with an arbitrary reference point, generally a zero pressure crossing. This was necessary since the Azimuthal position of the test model rotor was known with an uncertainty of ±5 degrees. This uncertainty was not present in calculations.

Table A-I. Operating Conditions For Test Points Used in Directivity Corrections

Figure Number	Run	Number of Blades	Power Loading kW/Blade	Power Loading SHP/Blade	RPM	Tunnel Mach Number	Tip Helical Mach Number
SR-1							
A-1	18'	2	18.7	25	10 050	0.321	1.049
A-2	27'	2	13.1	17.5	6 410	0.199	0.663
A-3	33'	2	18.7	25	8 532	0.323	0.909
SR-2							
A-4	75'	2	19.0	25.5	10 002	0.321	1.043
A-5	79'	2	18.7	25	8 460	0.322	0.897
A-6	83'	2	12.9	17.4	6 420	0.203	0.664
A-7	115	2	18.5	24.8	11 300	0.321	1.118
A-8	117	2	30.1	40.3	12 000	0.321	1.181
A-9	126	2	30.3	40.7	11 250	0.321	1.112
A-10	127	2	46.6	62.5	12 000	0.323	1.180
A-11	146	2	20.2	27.1	12 000	0.322	1.189
SR-3							
A-12	8	4	16.8	22.6	8 550	0.321	0.901
A-13	11	4	19.3	25.9	9 300	0.322	0.982
A-14	23	4	26.4	35.4	11 000	0.323	1.131
A-15	26	4	18.5	24.8	10 550	0.320	1.100
A-16	27	4	26.2	35.2	11 250	0.322	1.169
A-17	42	4	16.7	22.4	11 300	0.322	1.171
A-18	44	4	9.9	13.2	11 200	0.320	1.165
A-19	304	2	36.4	48.8	11 800	0.323	1.211
A-20	306	2	15.1	20.2	10 200	0.323	1.059
A-21	328	2	13.2	17.7	6 700	0.203	0.687
A-22	329	2	22.8	30.5	7 500	0.203	0.761

SR1, RUN 18', 10050 RPM, 18.7 KW/BLADE,
DIRECTIVITY AT 0.8D TIP CLEARANCE $M_X = 0.3210$, $M_{TH} = 1.049$

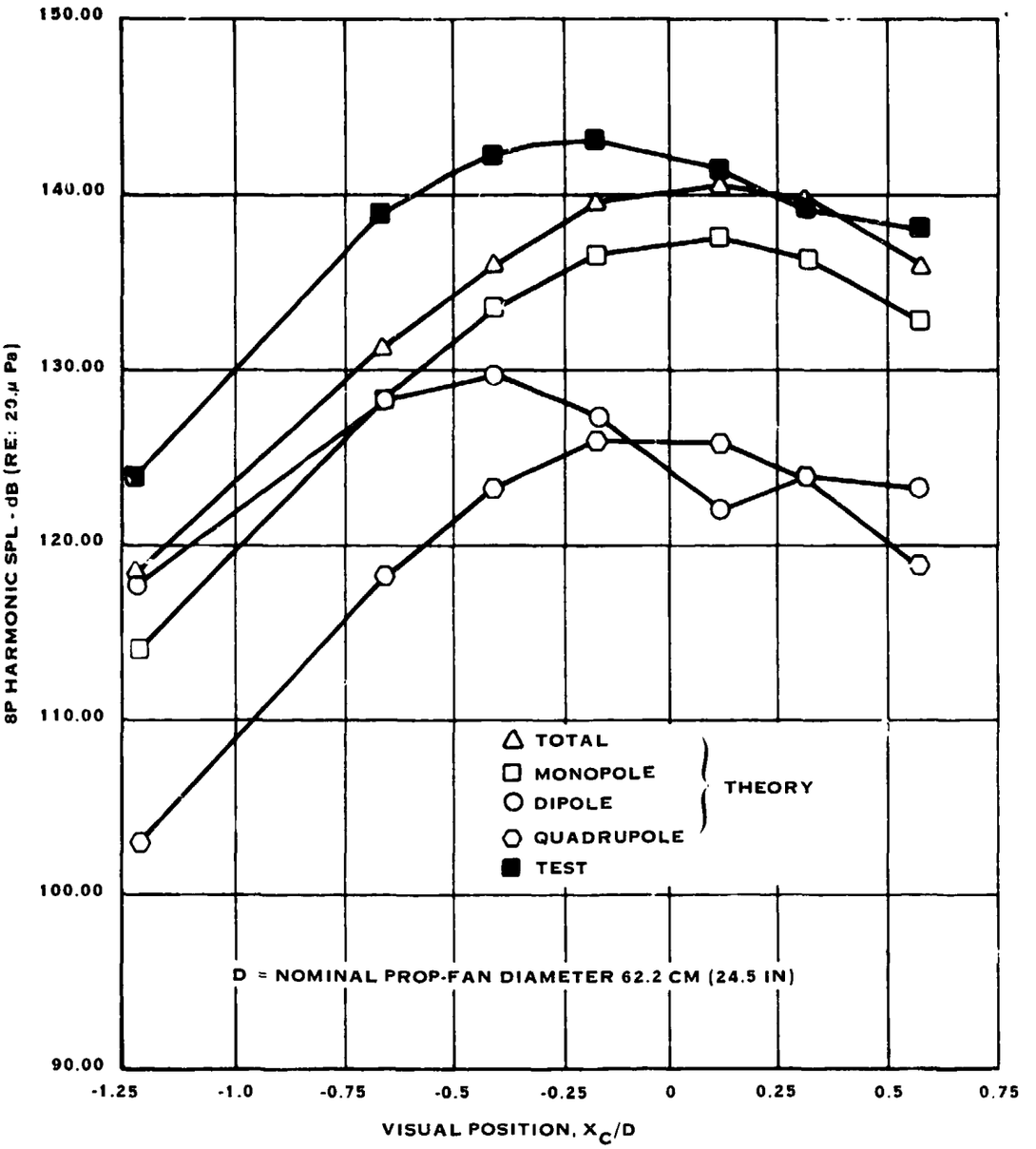

FIGURE A-1A

SR-1, RUN 18', 10050 RPM, 18.7 KW/BLADE,
$M_X = 0.321$, $M_{TH} = 1.049$ WAVEFORM FOR MIC 4

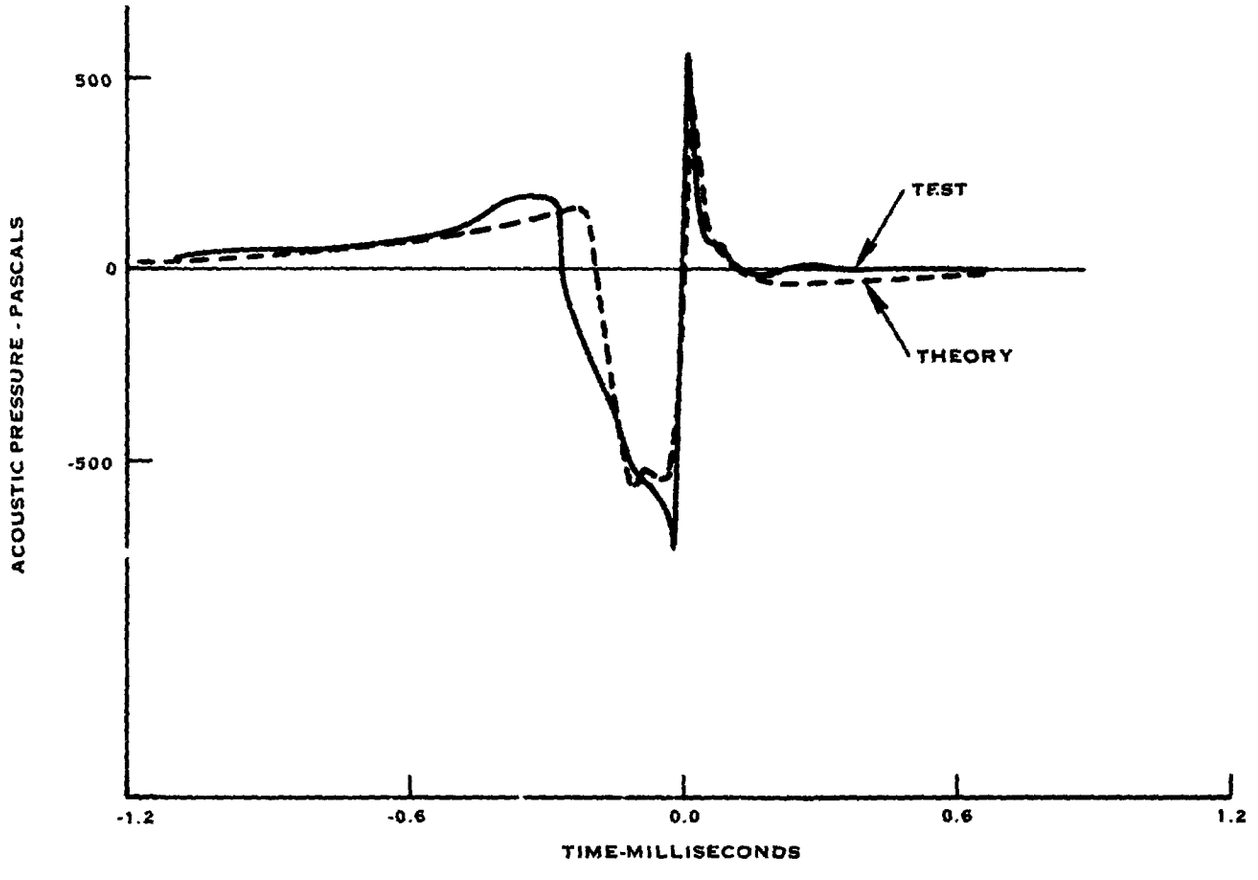

FIGURE A-1B

SR1, RUN 27', 6410 RPM, 13.1 KW/BLADE,
$M_X = 0.199$ $M_{TH} = 0.663$ DIRECTIVITY AT 0.8D TIP CLEARANCE

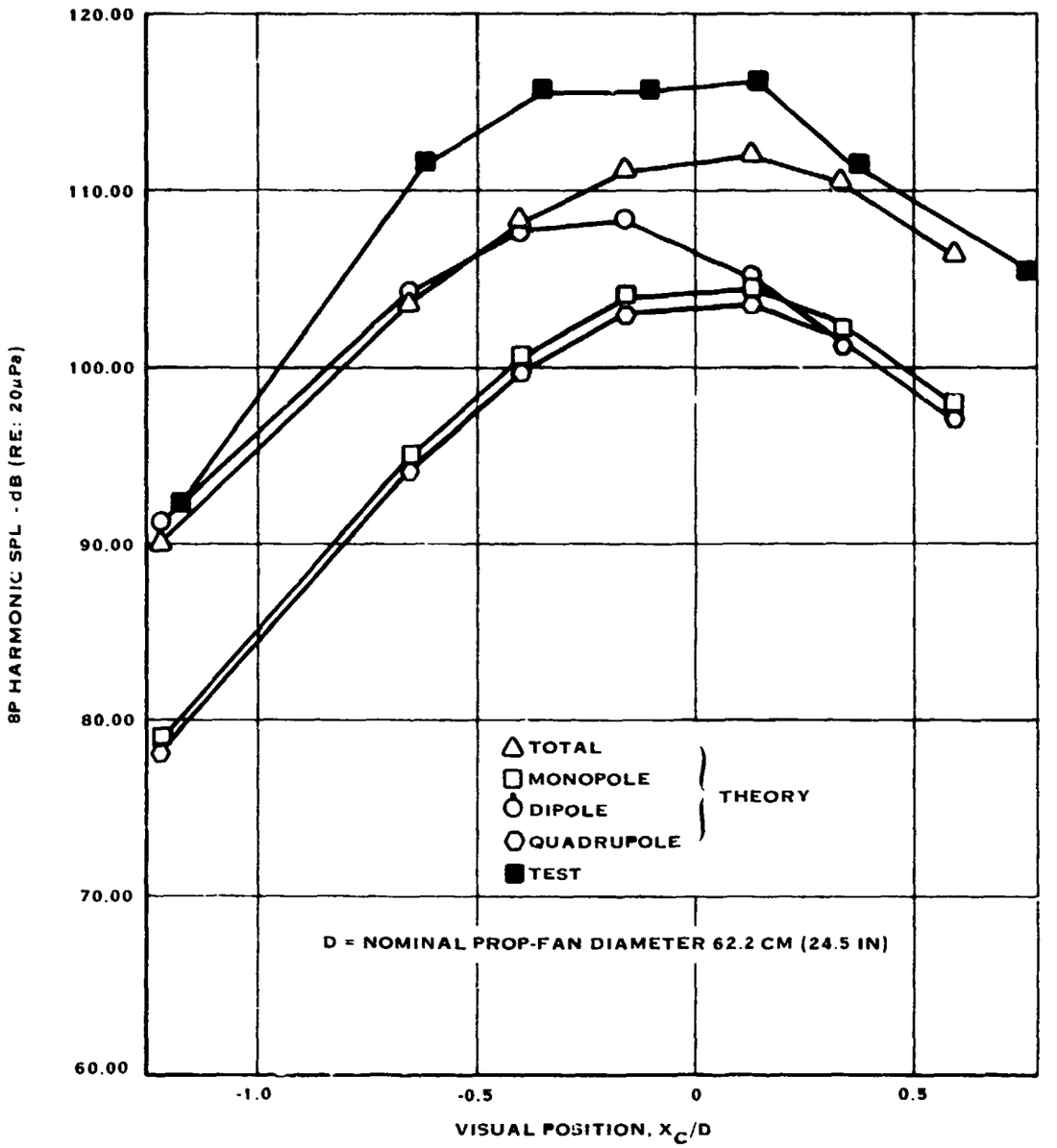

FIGURE A-2A

SR1, RUN 27', 6410 RPM, 13.1 KW/BLADE,
M_X = 0.199 M_{TH} = 0.663 WAVEFORM FOR MIC 3

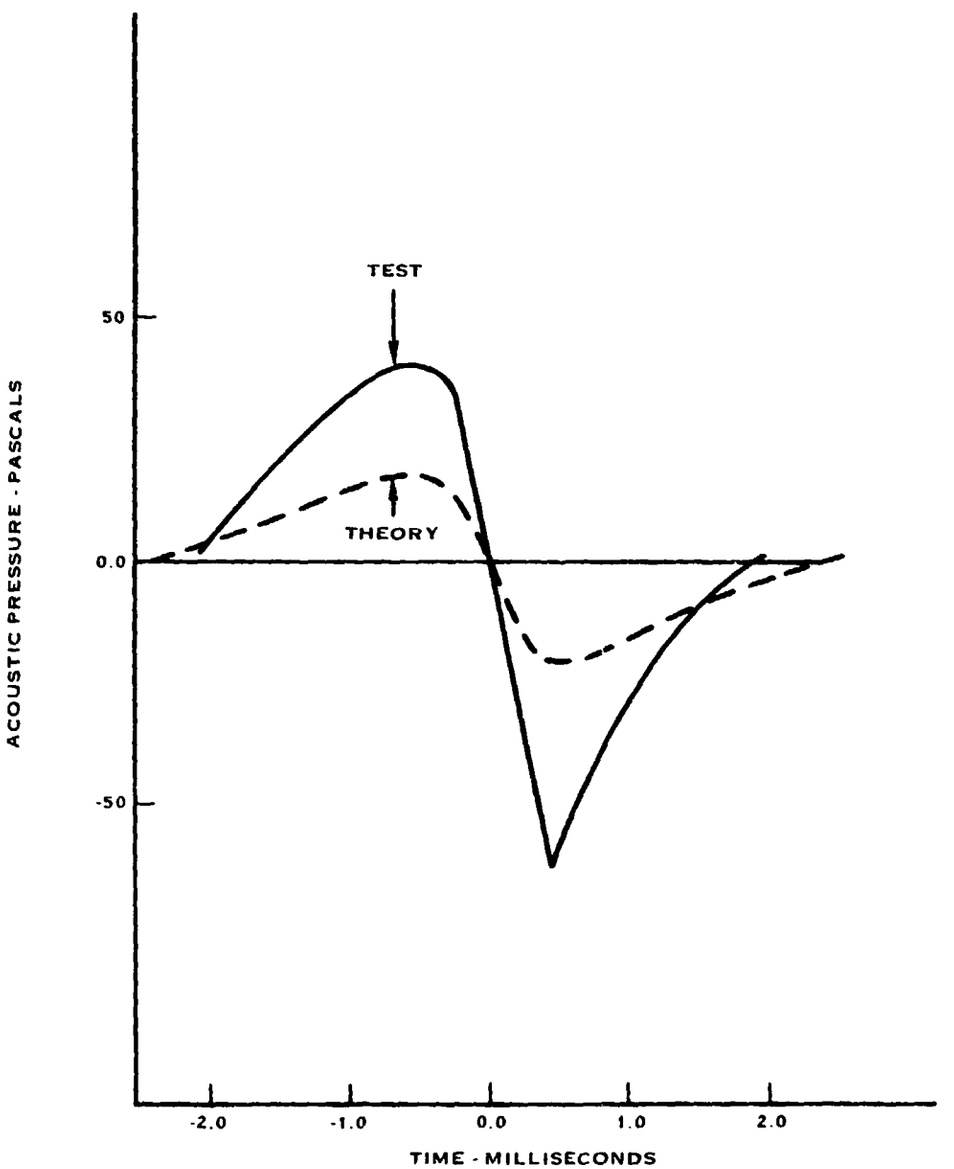

FIGURE A-2B

SR1, RUN 33', 8532 RPM, 18.7 KW/BLADE,
$M_X = 0.323$ $M_{TH} = 0.909$ DIRECTIVITY AT 0.8D TIP CLEARANCE

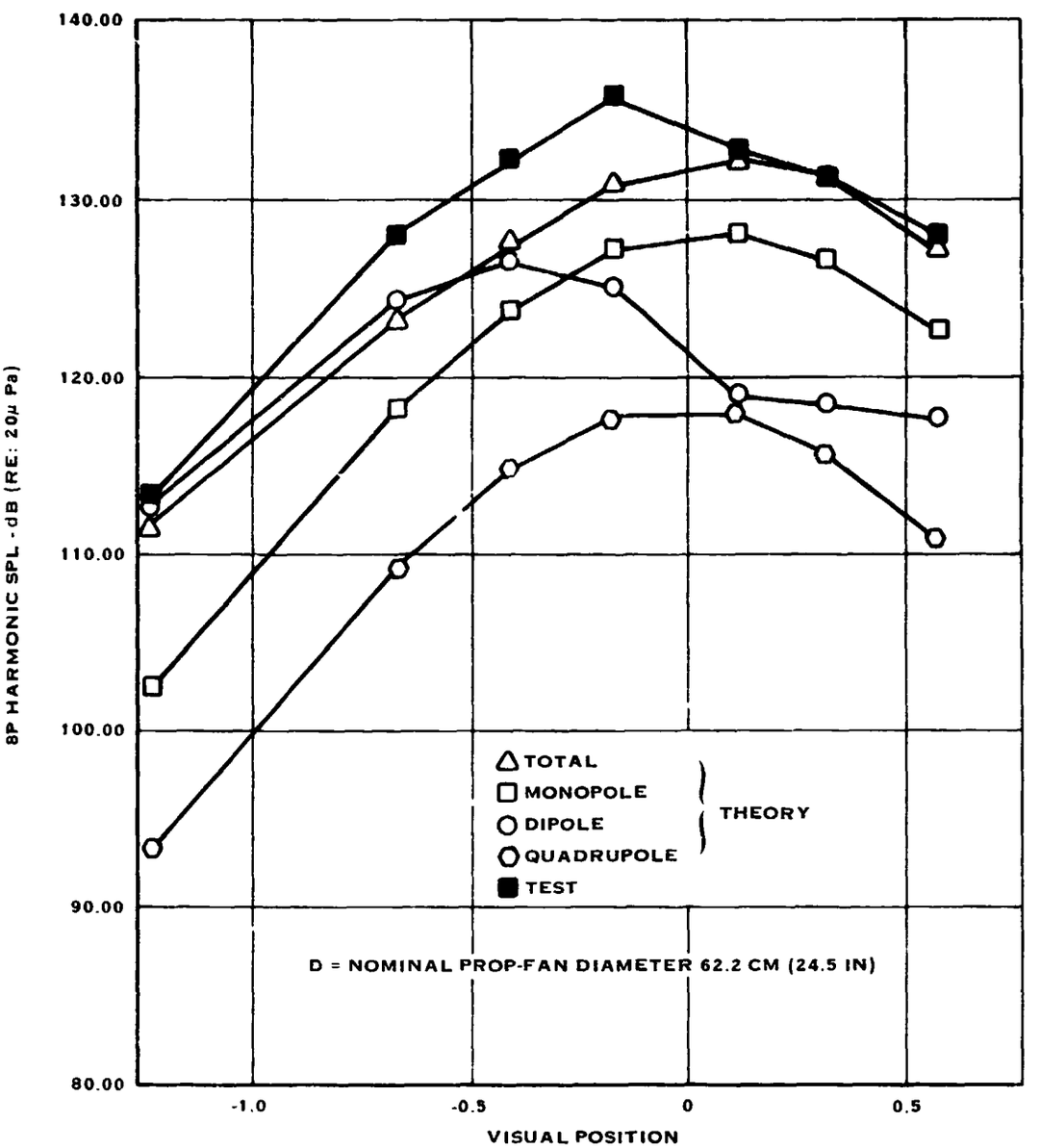

FIGURE A-3A

SR1, RUN 33', 18.7 KW/BLADE,
$M_X = 0.323$, $M_{TH} = 0.909$ WAVEFORM FOR MIC 4

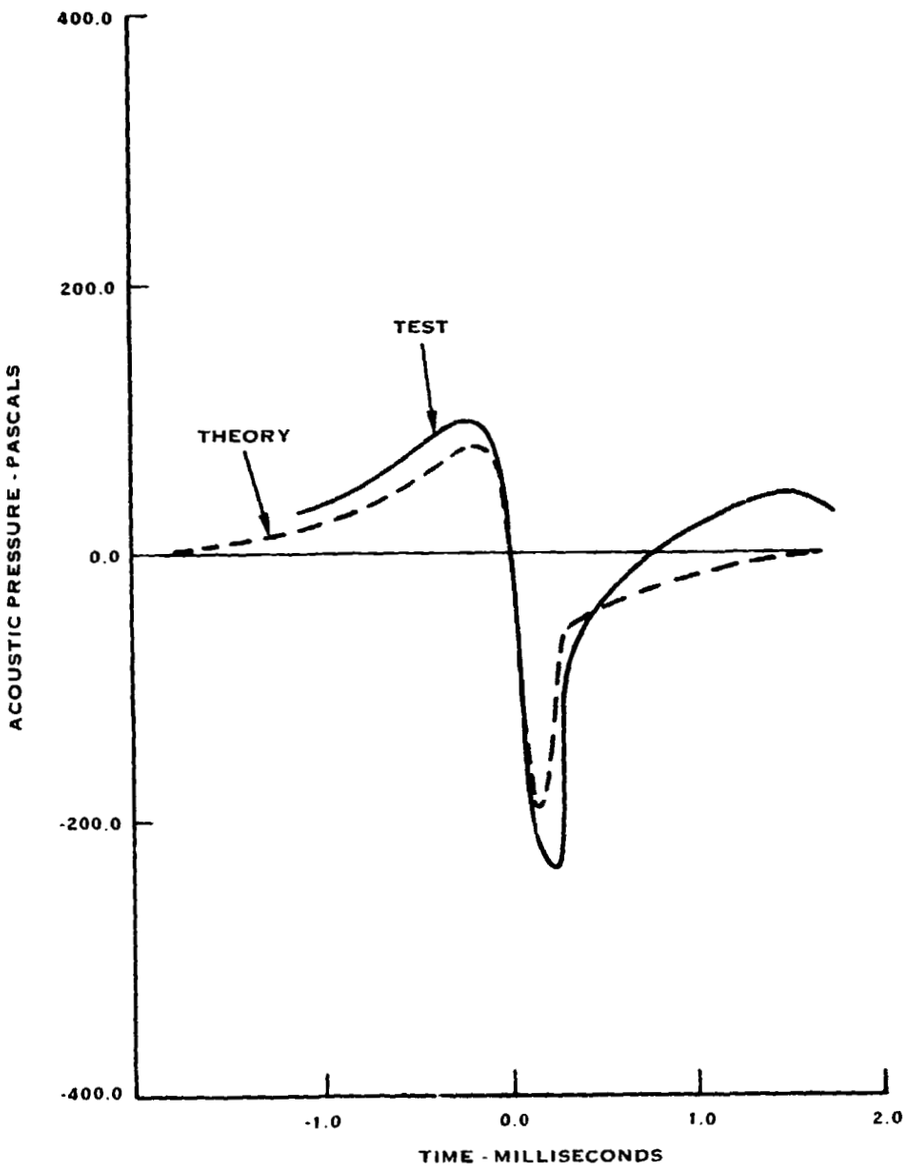

FIGURE A-3B

SR2, RUN 75', 10002 RPM, 19.0 KW/BLADE,
M_X = 0.321, M_{TH} = 1.043 DIRECTIVITY AT 0.8D TIP CLEARANCE

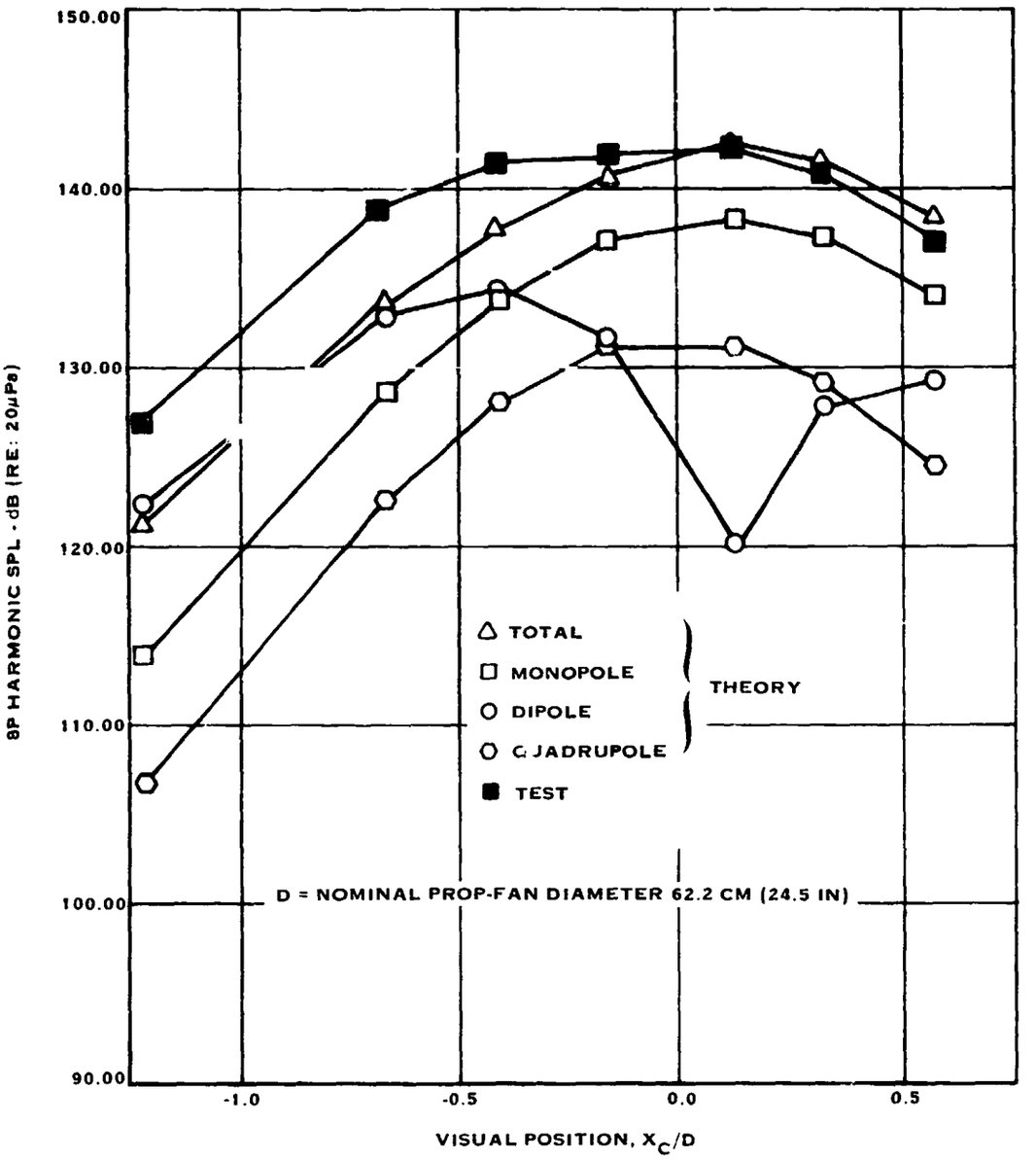

FIGURE A 4A

SR-2, RUN 75', 10002 RPM, 19.0 KW/BLADE,
M_X = 0.321, M_{TH} = 1.043 WAVEFORM FOR MIC 3

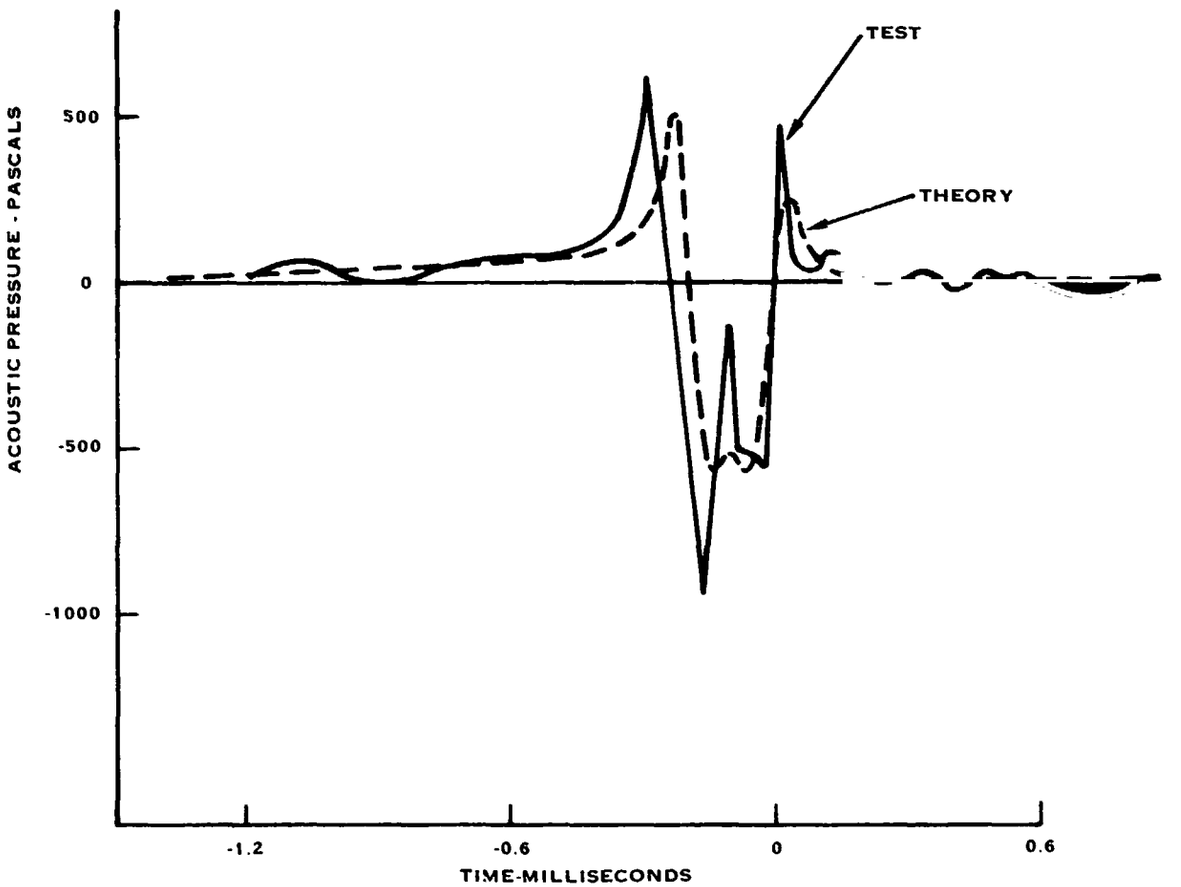

FIGURE A-4B

SR2, RUN 79', 8460 RPM, 18.7 KW/BLADE,
$M_X = 0.3220$, $M_{TH} = 0.897$ DIRECTIVITY AT 0.8D TIP CLEARANCE

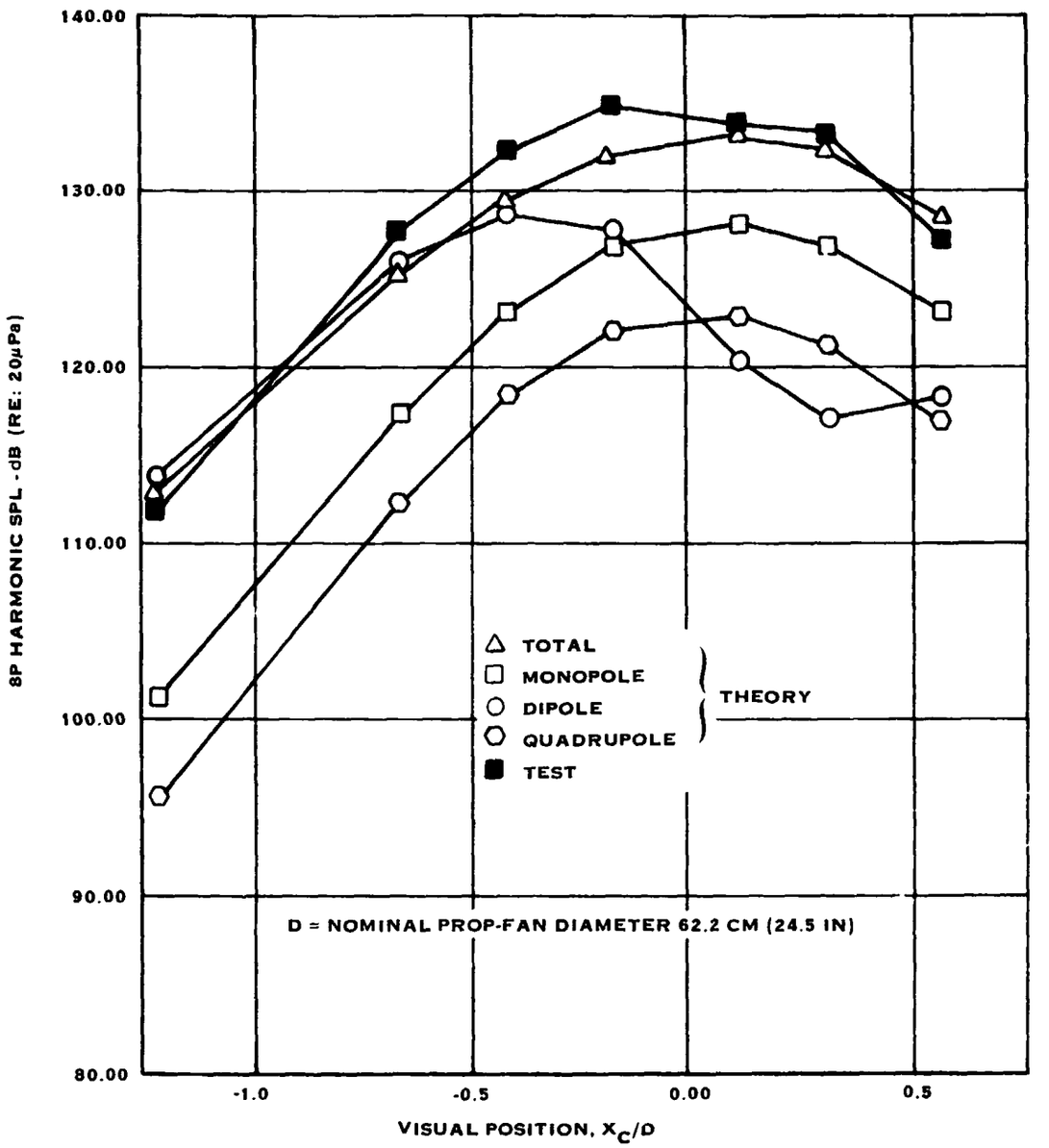

FIGURE A-5A

SR2, RUN 79', WAVEFORM FOR MIC 4, 18.7 KW/BLADE,
$M_X = 0.322$, $M_{TH} = 0.897$

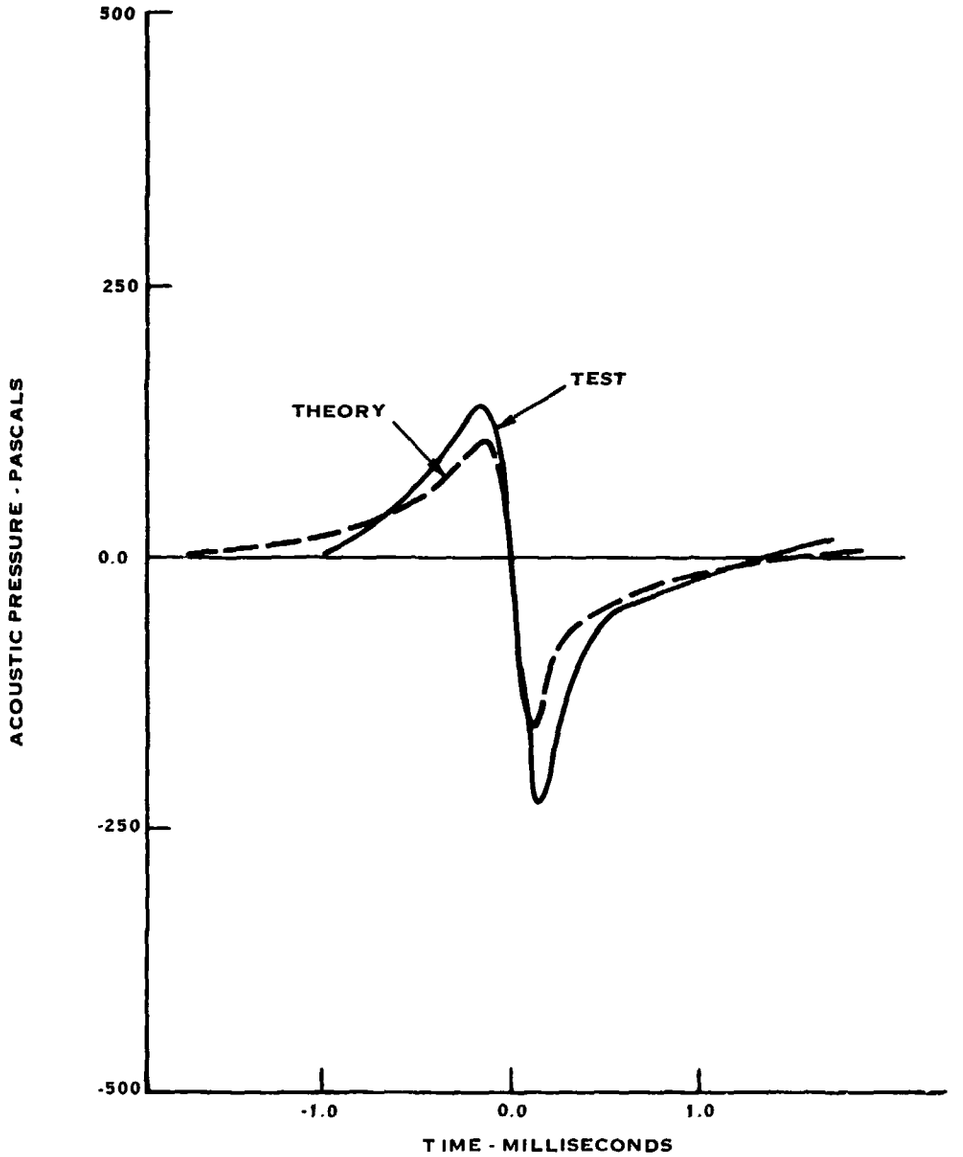

FIGURE A-5B

SR2, RUN 83, 6420 RPM, 12.9 KW/BLADE,
$M_X = 0.203$, $M_{TH} = 0.664$ DIRECTIVITY AT 0.8D TIP CLEARANCE

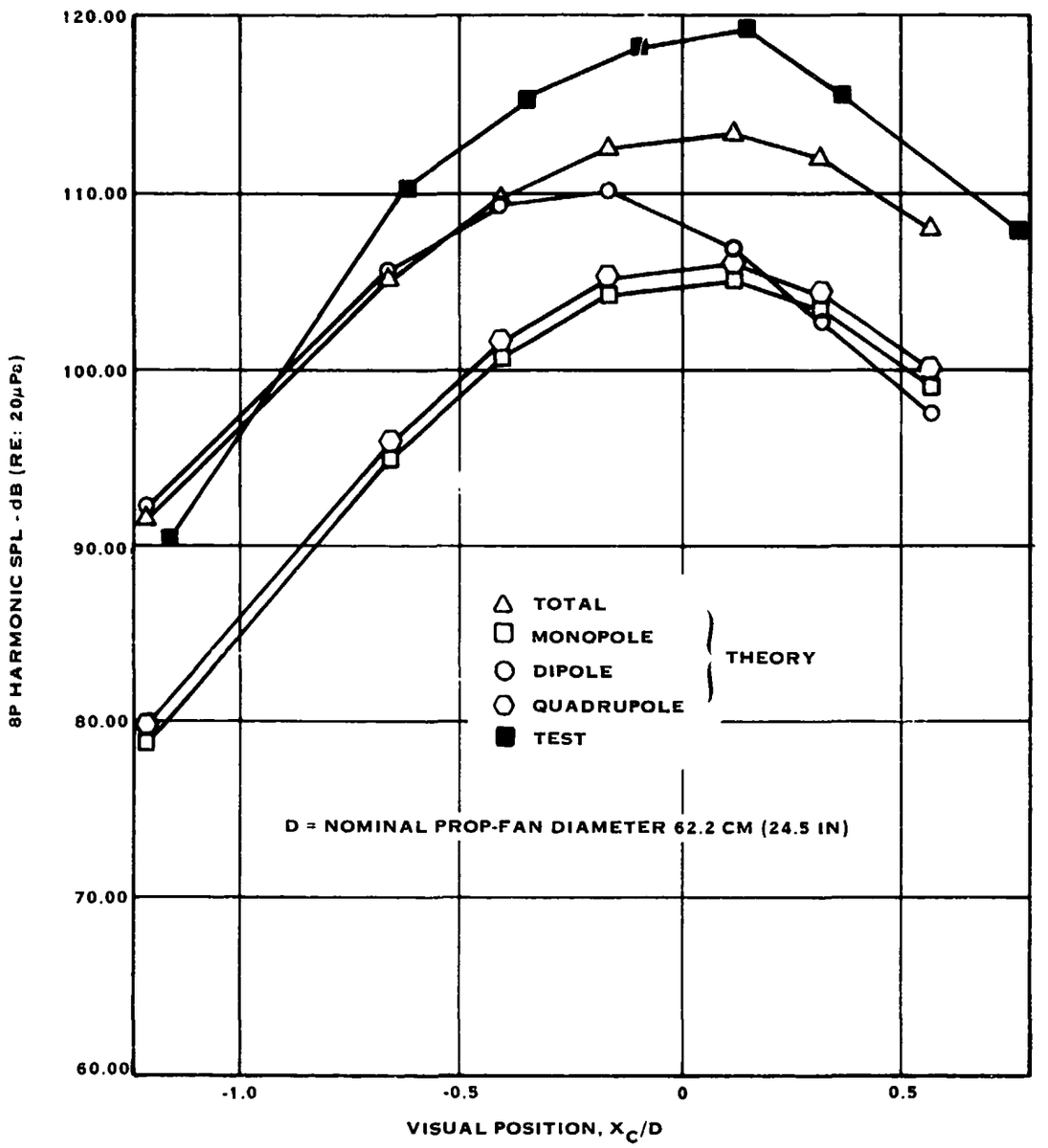

FIGURE A-6A

SR2, RUN 83', WAVEFORM FOR MIC 3, 12.9 KW/BLADE,

$M_X = 0.203$, $M_{TH} = 0.664$

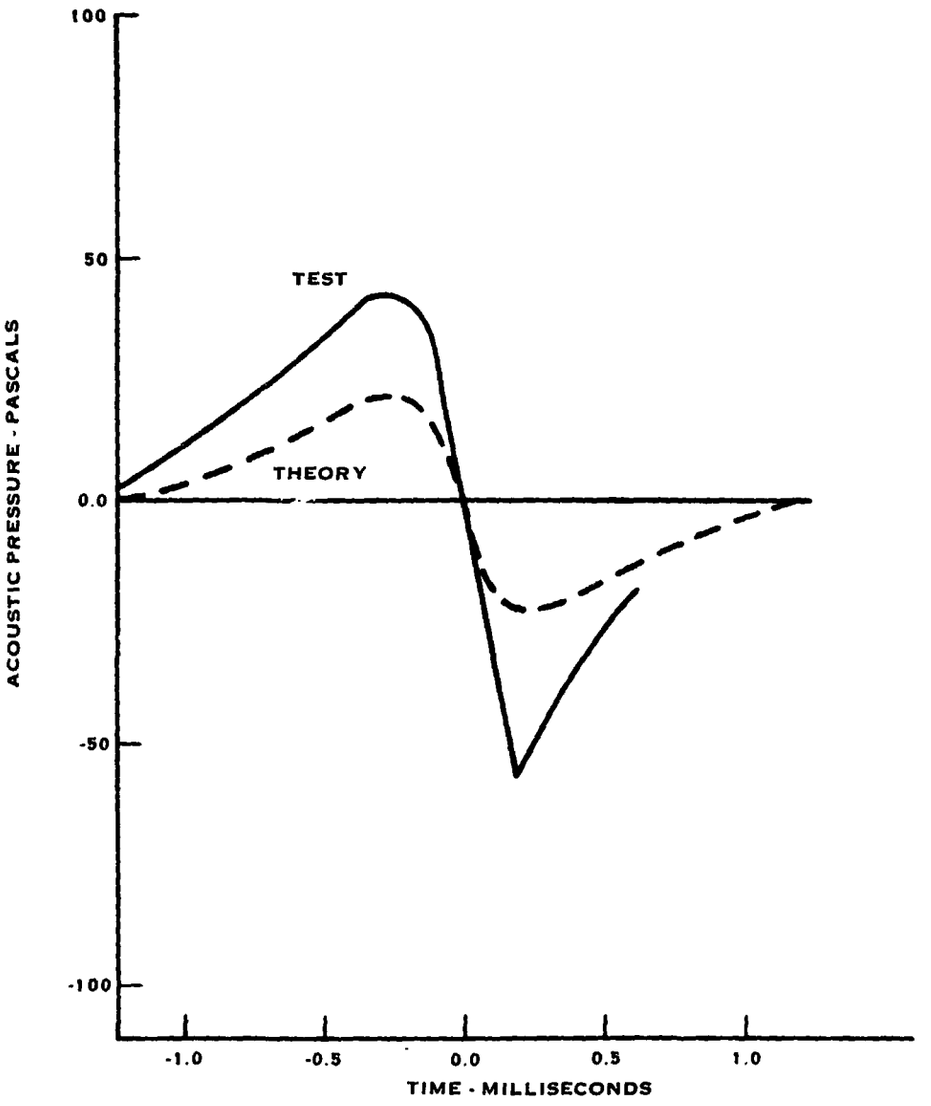

FIGURE A-6B

SR2, RUN 115, 11300 RPM, 18.5 KW/BLADE,
M_X = 0.3210, M_{TH} = 1.118 DIRECTIVITY AT 0.8D TIP CLEARANCE

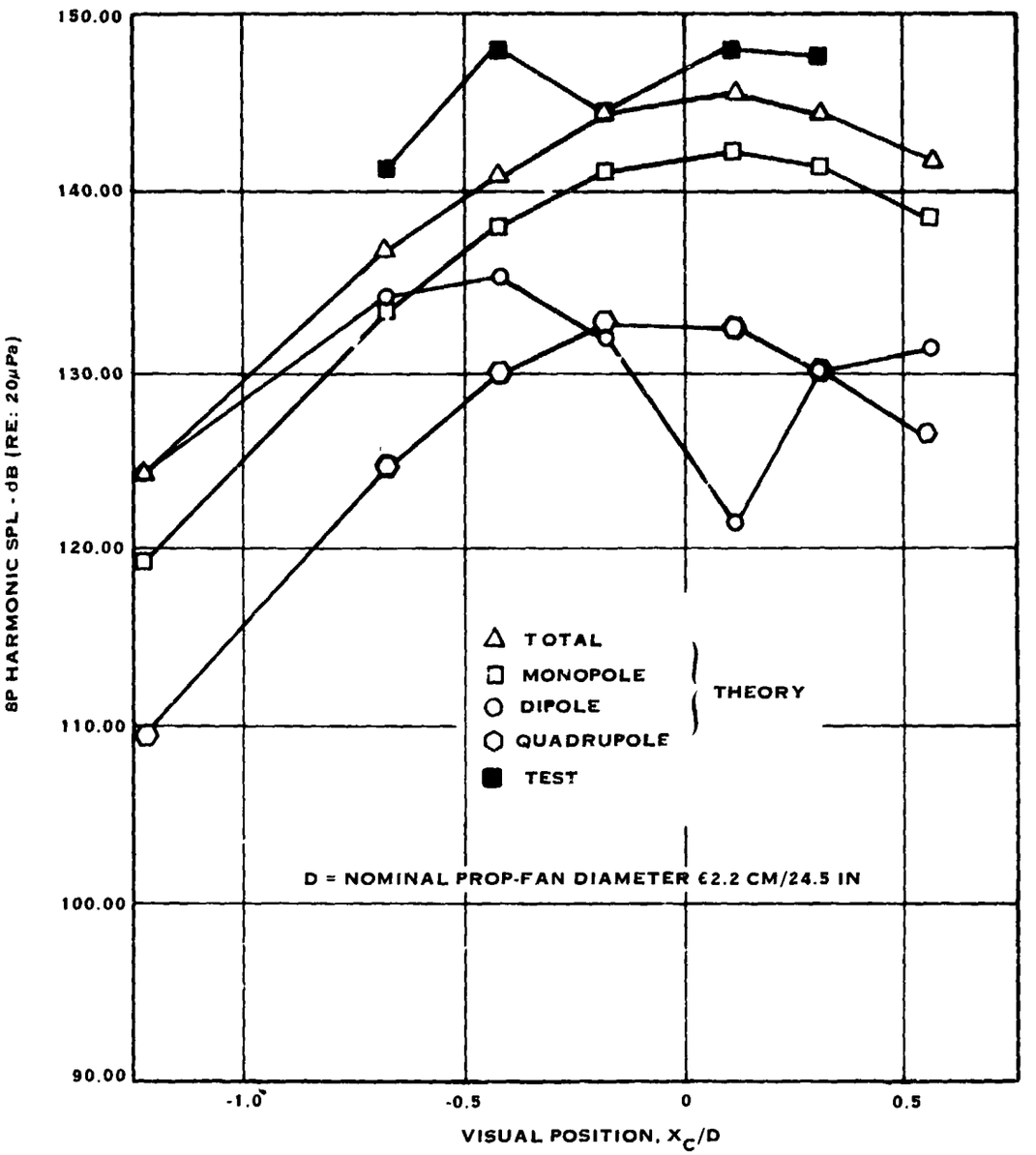

FIGURE A-7A

SR2, RUN 115, WAVEFORM FOR MIC 3 18.5 KW/BLADE,
$M_X = 0.321$, $M_{TH} = 1.118$

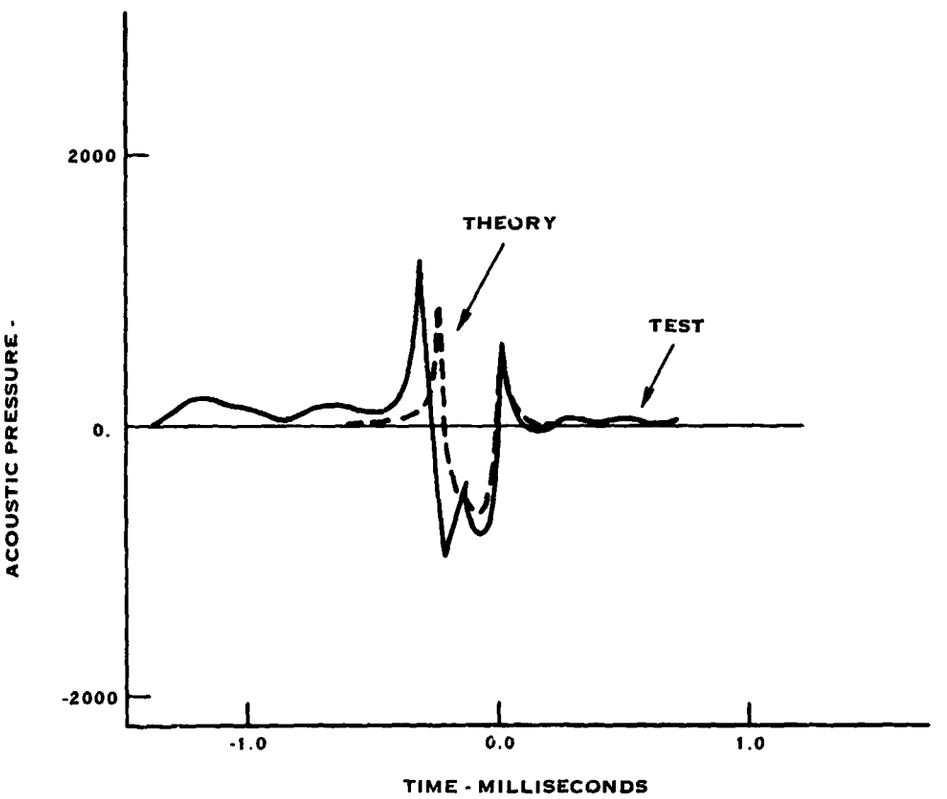

FIGURE A-7B

SR2, RUN 117, 12000 RPM, 30.1 KW/BLADE,
M_X= 0.3210, M_{TH}= 1.181 DIRECTIVITY AT 0.8 TIP CLEARANCE

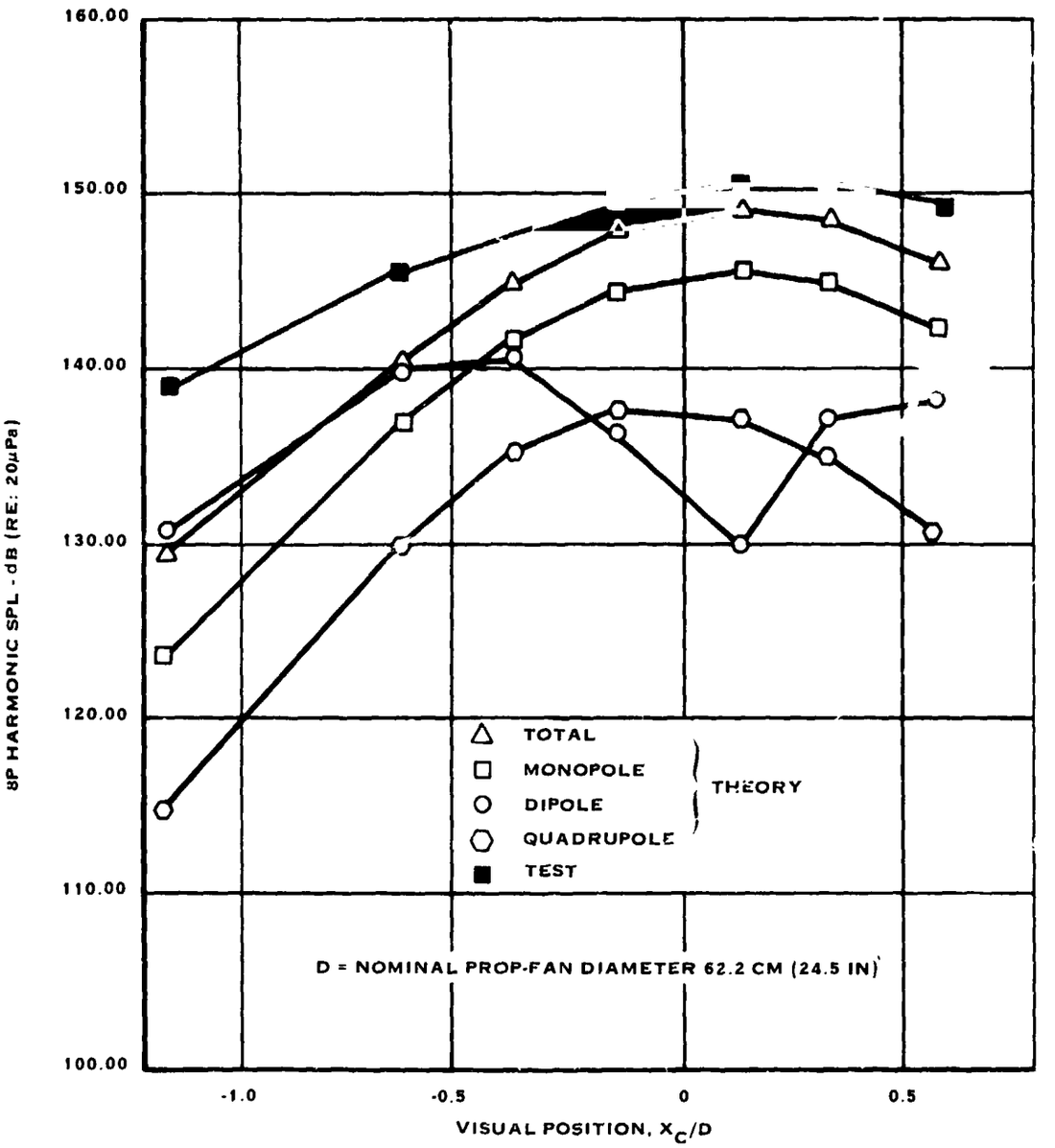

FIGURE A-8A

SR2, RUN 117, 12,000 RPM, 30.1 kW/BLADE
M_X 0.321, M_{TIP} 1.181, WAVEFORM FOR MIC 2

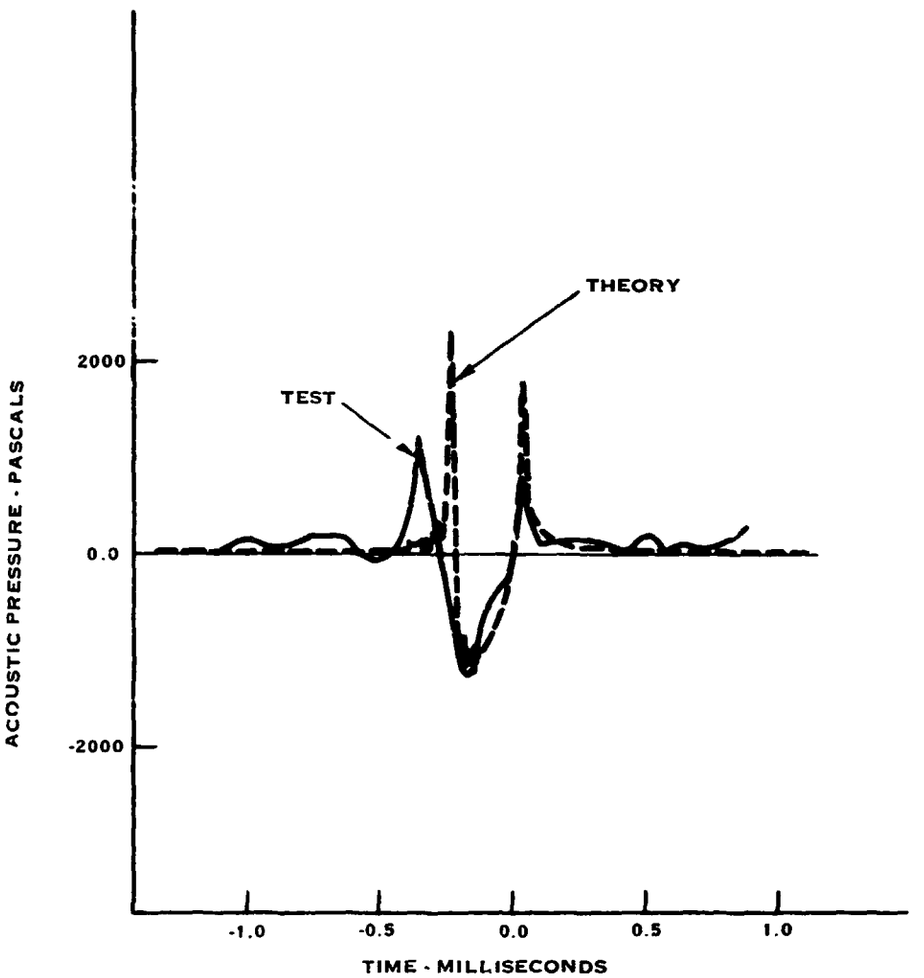

FIGURE A-8B

SR2, RUN 126, 11250 RPM, 30.3 KW/BLADE,
M_X = 0.321, M_{TH} = 1.112 DIRECTIVITY AT 0.8D TIP CLEARANCE

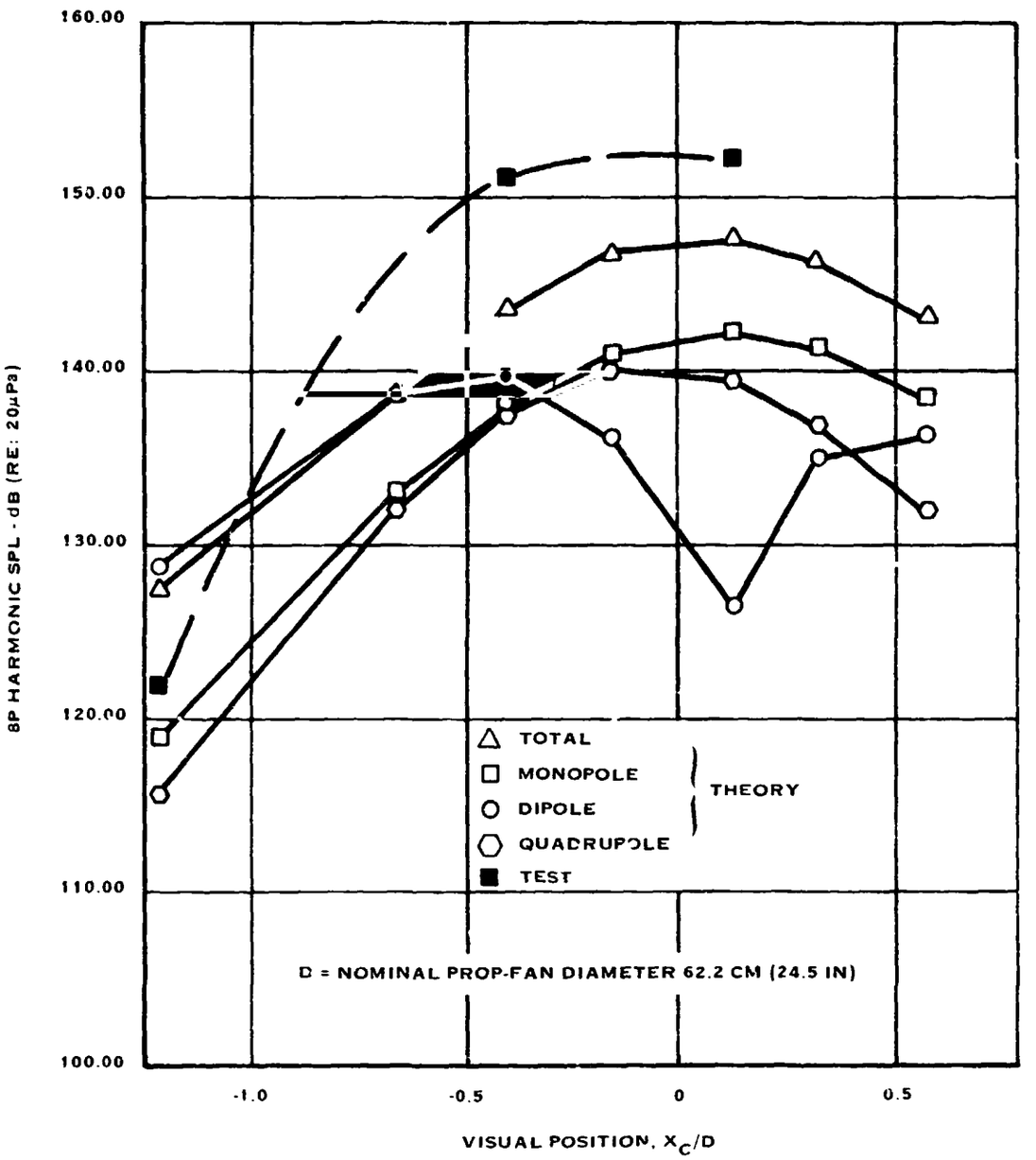

FIGURE A-9A

SR2, RUN 126, WAVEFORM FOR MIC 3 30.3 KW/BLADE,
$M_X = 0.321$, $M_{TH} = 1.112$

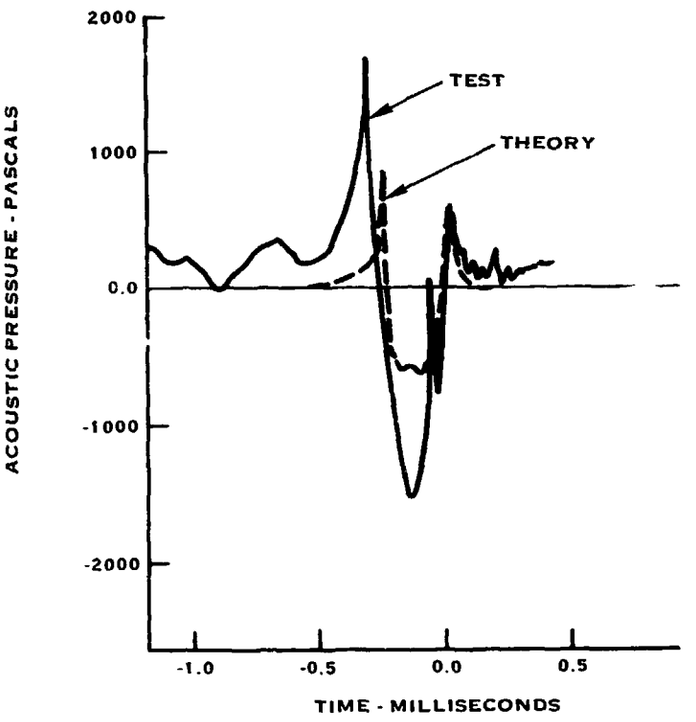

FIGURE A-9B

SR2, RUN 127, 12000 RPM, 46.6 KW/BLADE,
$M_X = 0.323$, $M_{TH} = 1.180$ DIRECTIVITY AT 0.8D TIP CLEARANCE

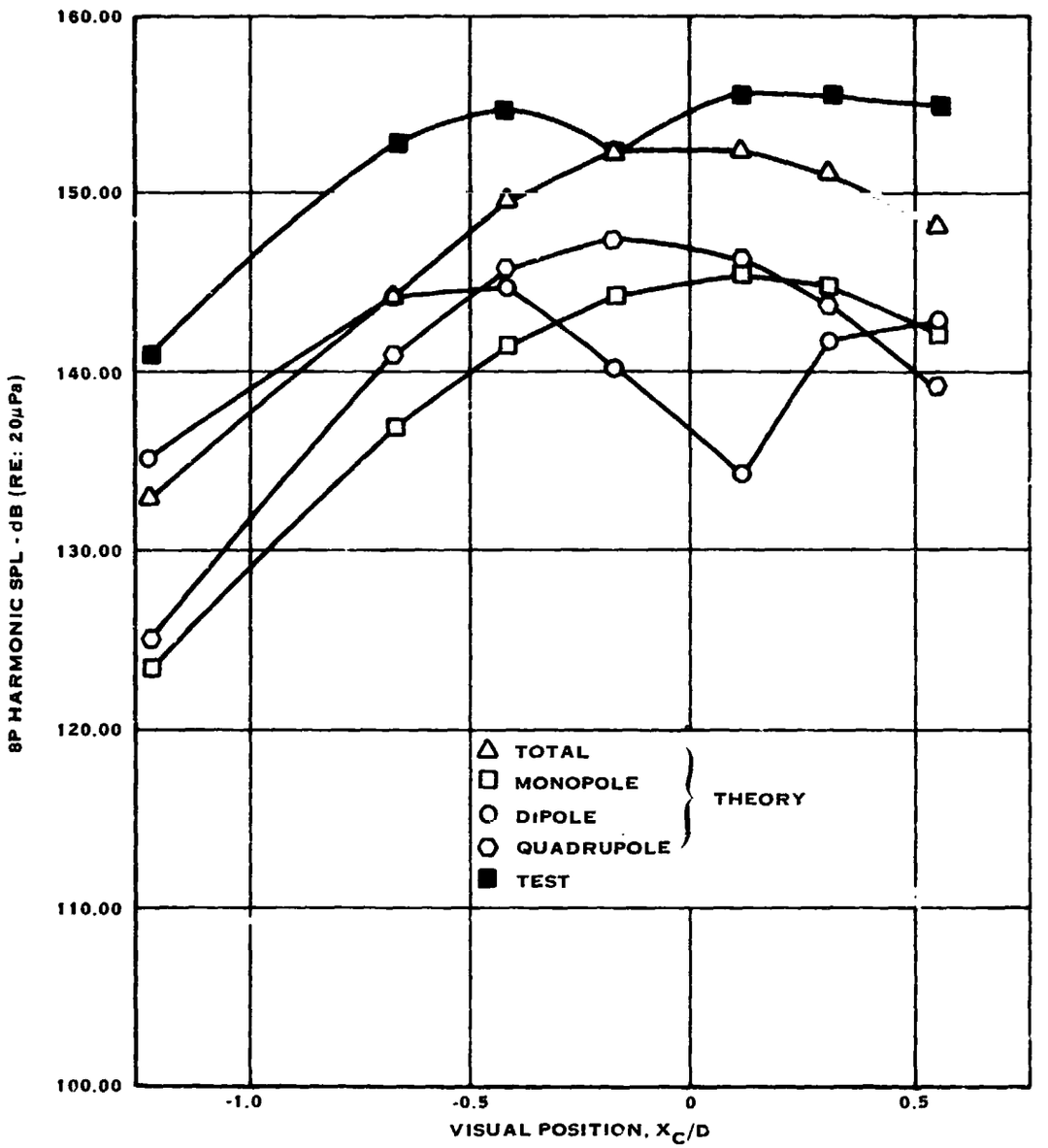

FIGURE A-10A

SR2, RUN 127, 12000 RPM, 46.6 KW/BLADE,
$M_X = 0.323$, $M_{TH} = 1.180$ WAVEFORM FOR MIC 3

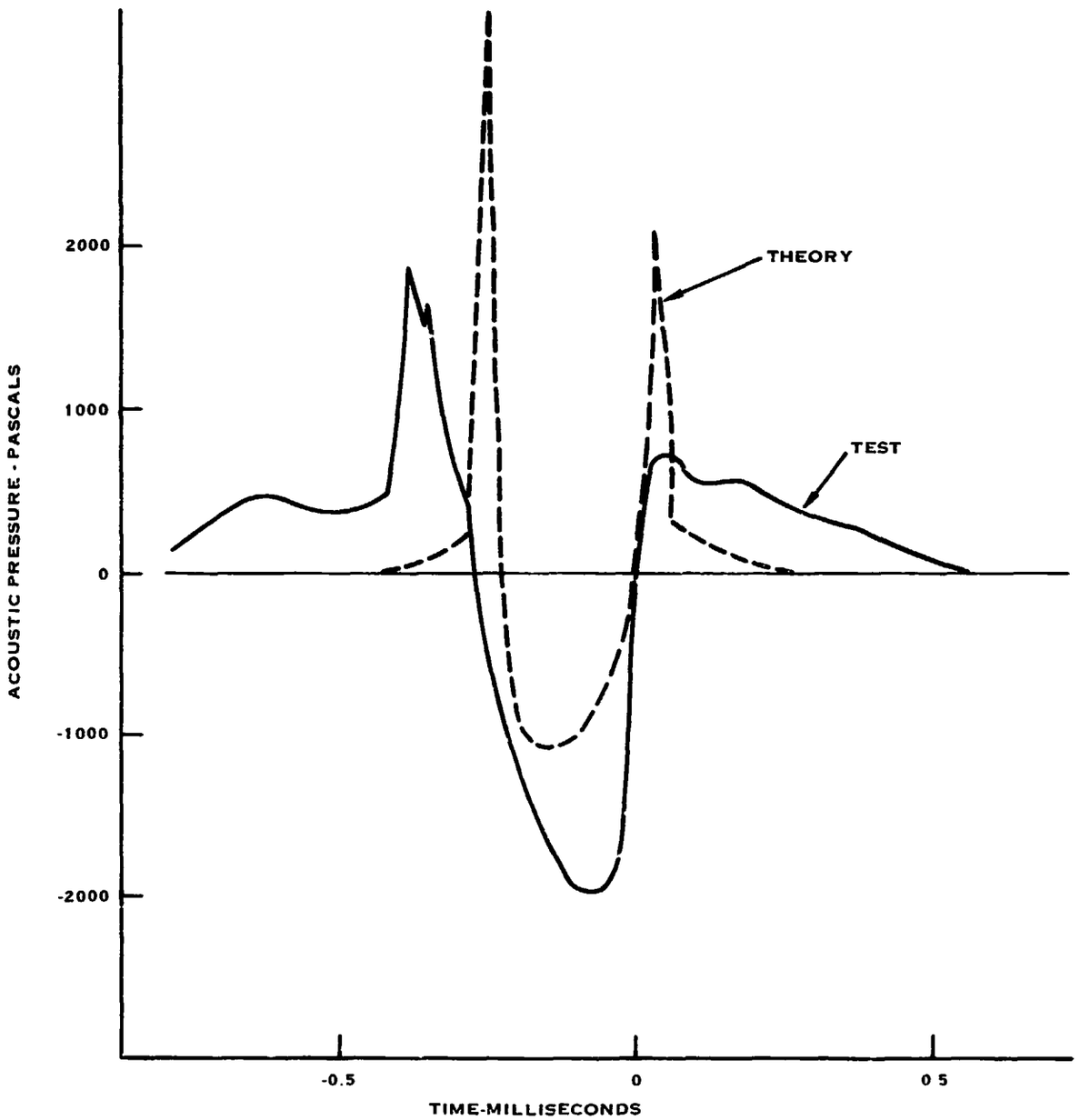

FIGURE A-10B

SR2, RUN 146, 12000 RPM, 20.2 KW/BLADE,
$M_X = 0.322$ $M_{TH} = 1.189$ DIRECTIVITY AT 0.8D TIP CLEARANCE

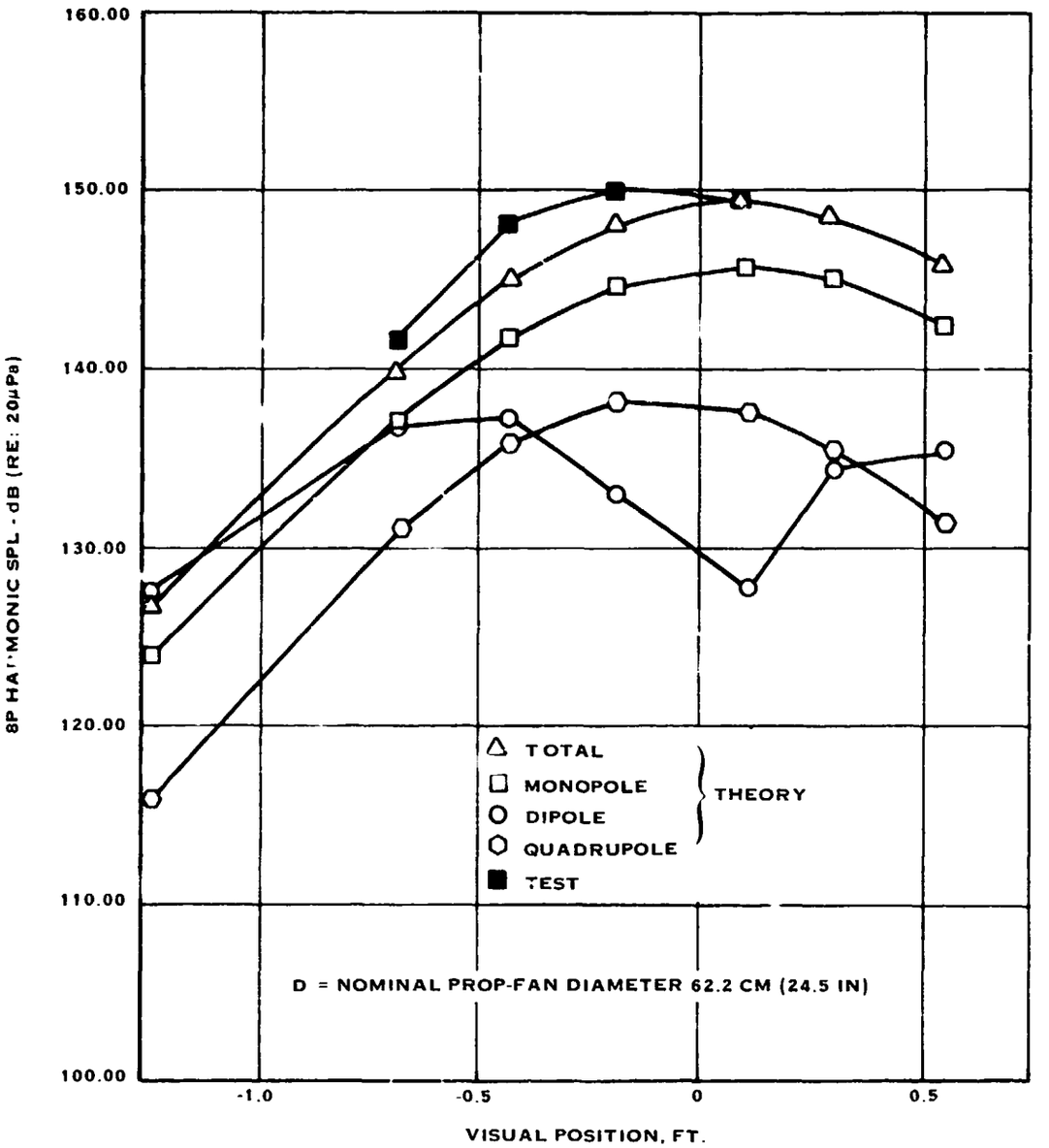

FIGURE A-11A

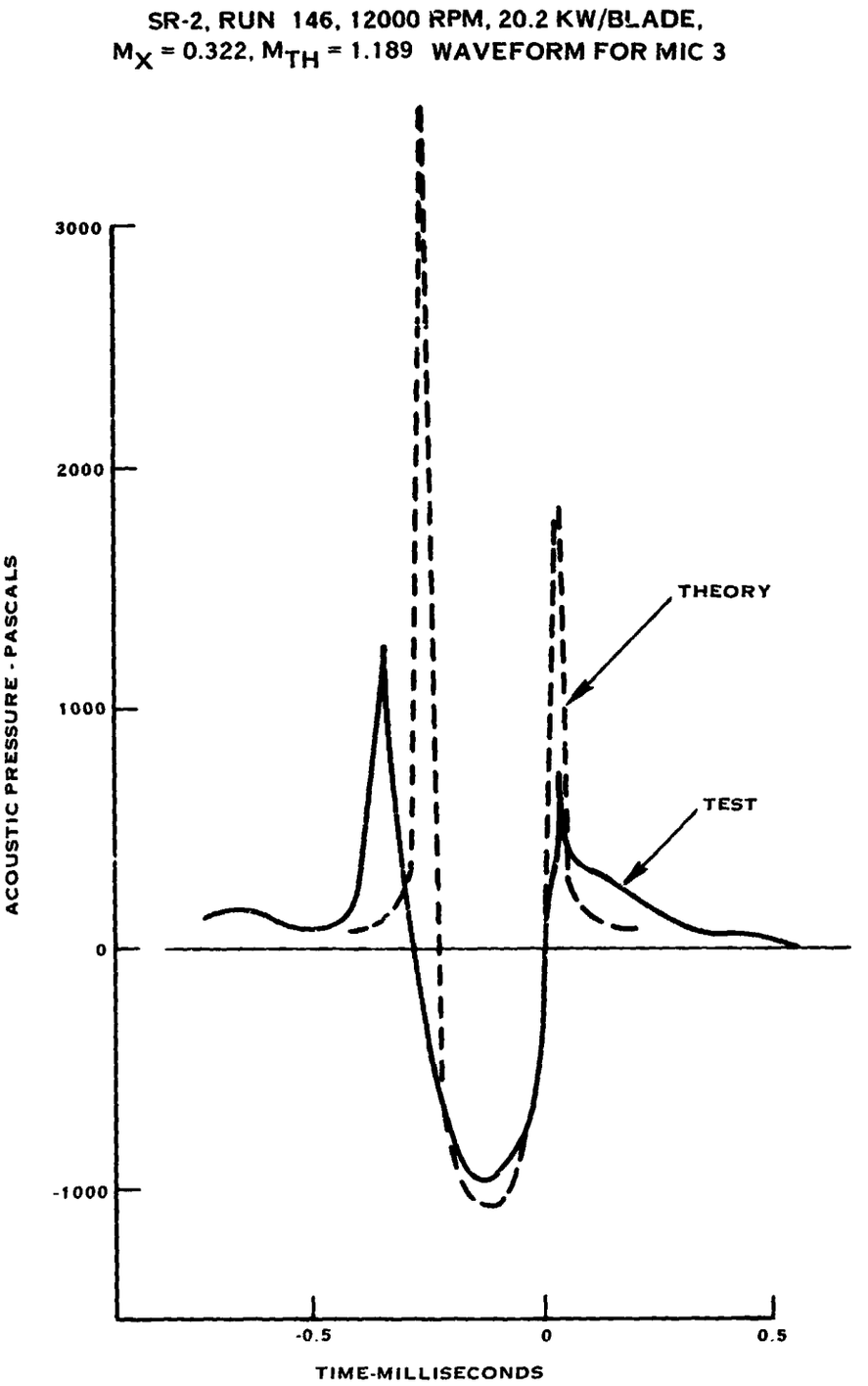
SR-2, RUN 146, 12000 RPM, 20.2 KW/BLADE,
M_X = 0.322, M_{TH} = 1.189 WAVEFORM FOR MIC 3
3000
2000
1000
0
-1000
ACOUSTIC PRESSURE - PASCALS
THEORY
TEST
-0.5
0
0.5
TIME-MILLISECONDS

FIGURE A-11B

SR3, RUN 8, 8550 RPM, 16.8 KW/BLADE
$M_X = 0.321$ $M_{TH} = 0.901$ DIRECTIVITY AT 0.8D TIP CLEARANCE

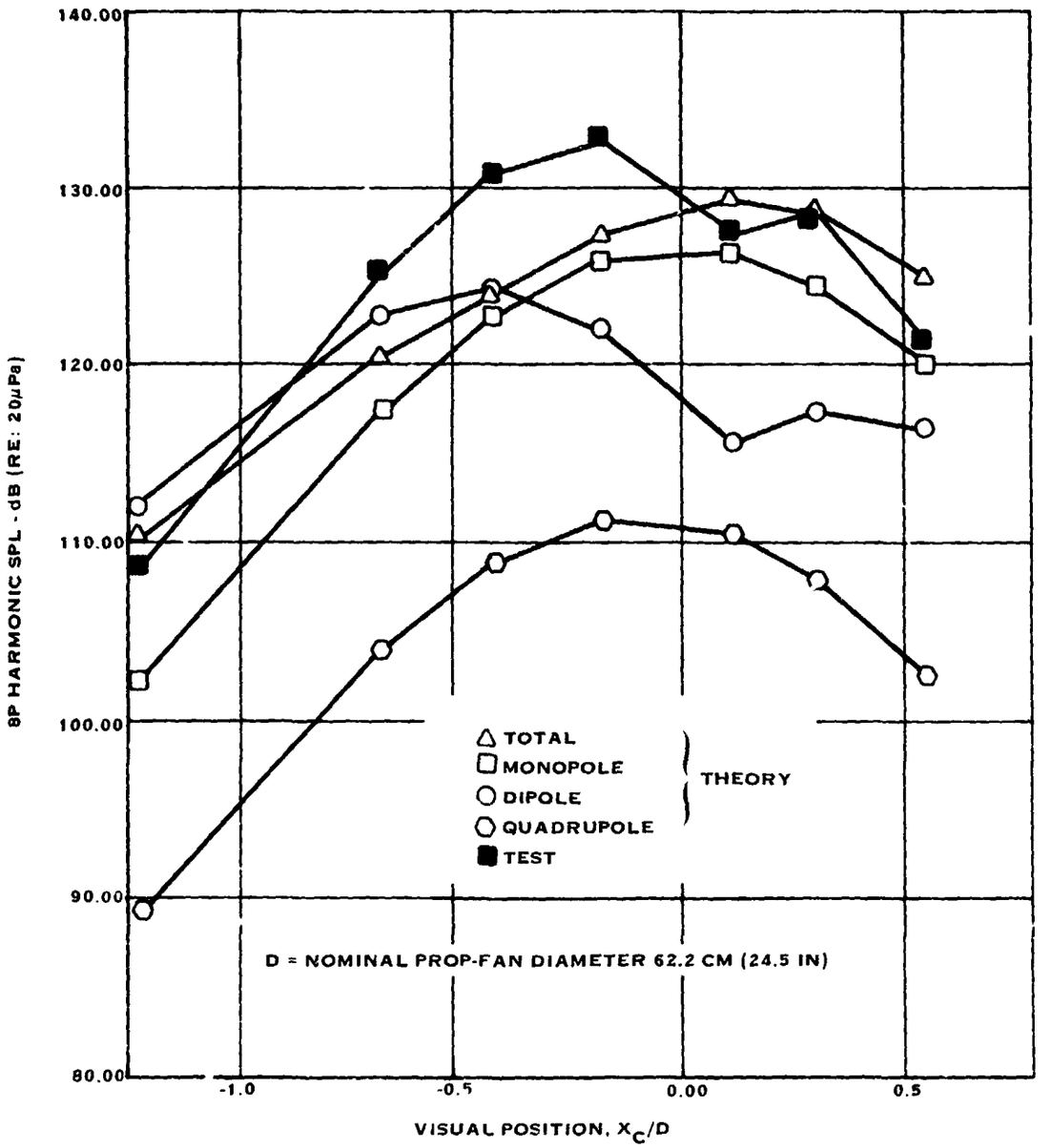

FIGURE A-12A

SR3, RUN 8, WAVEFORM FOR MIC 4 16.8 KW/BLADE
$M_X = 0.321$ $M_{TH} = 0.901$

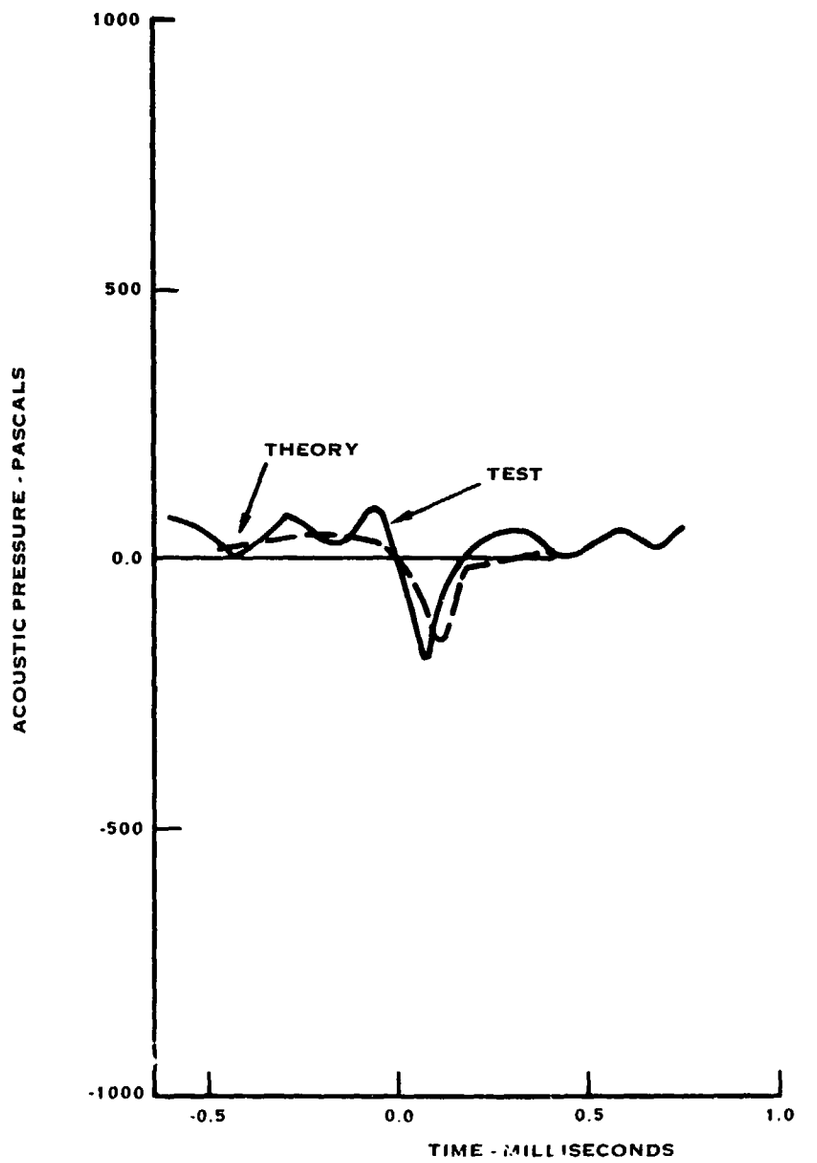

FIGURE A-12B

SR3, RUN 11, 9300 RPM, 19.3 KW/BLADE,
$M_X = 0.322$ $M_{TH} = 0.982$ DIRECTIVITY AT 0.8D TIP CLEARANCE

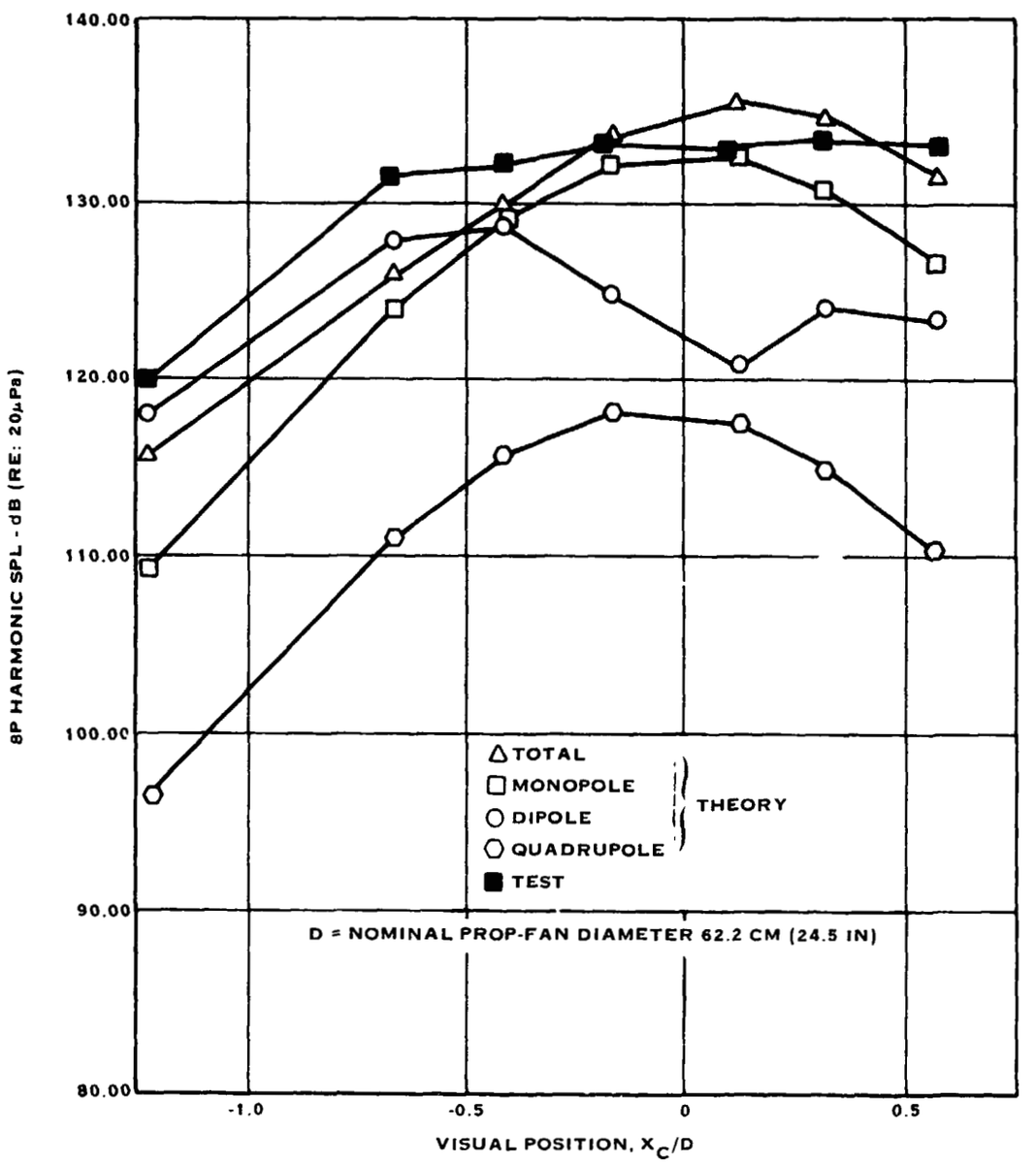

FIGURE A-13A

SR-3 RUN 11, 9300 RPM, 19.3 KW/BLADE,
M_X = 0.322, M_{TH} = 0.982 WAVEFORM FOR MIC 2

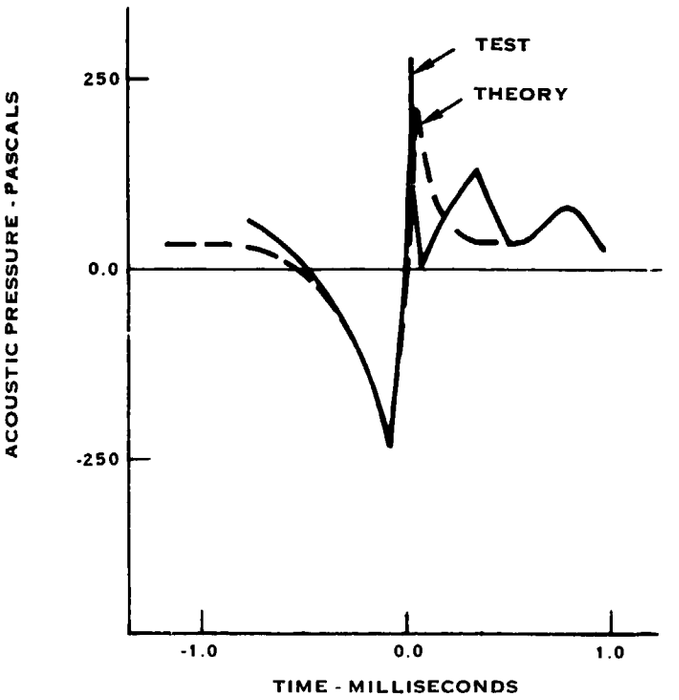

FIGURE A-13B

SR3, RUN 23, 11000 RPM, 26.4 KW/BLADE,
$M_X = 0.323$ $M_{TH} = 1.131$ DIRECTIVITY AT 0.8D TIP CLEARANCE

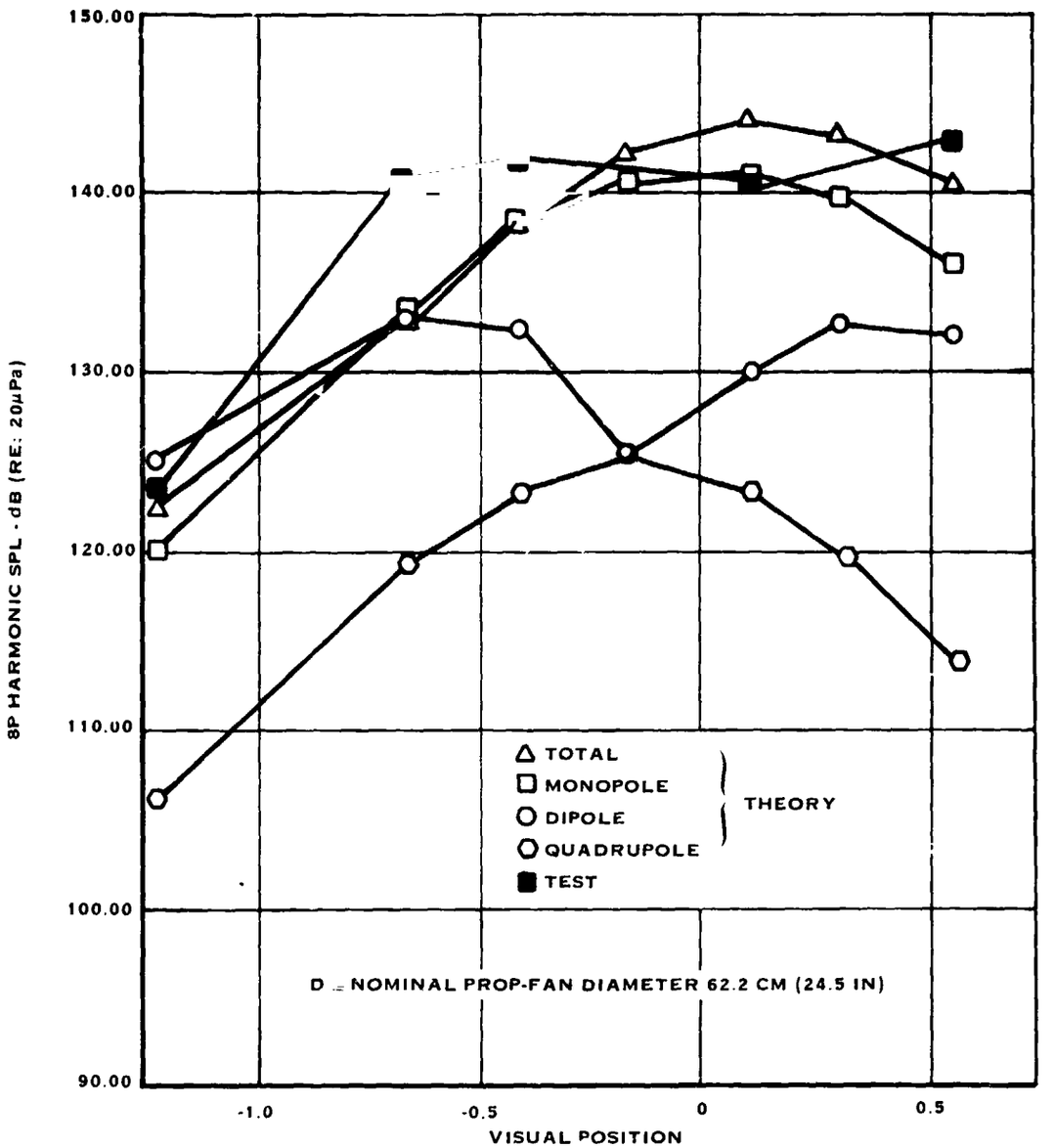

FIGURE A-14A

SR3, RUN 23, WAVEFORM FOR MIC 3, 26.4 KW/BLADE,

$M_X = 0.323$, $M_{TH} = 1.131$

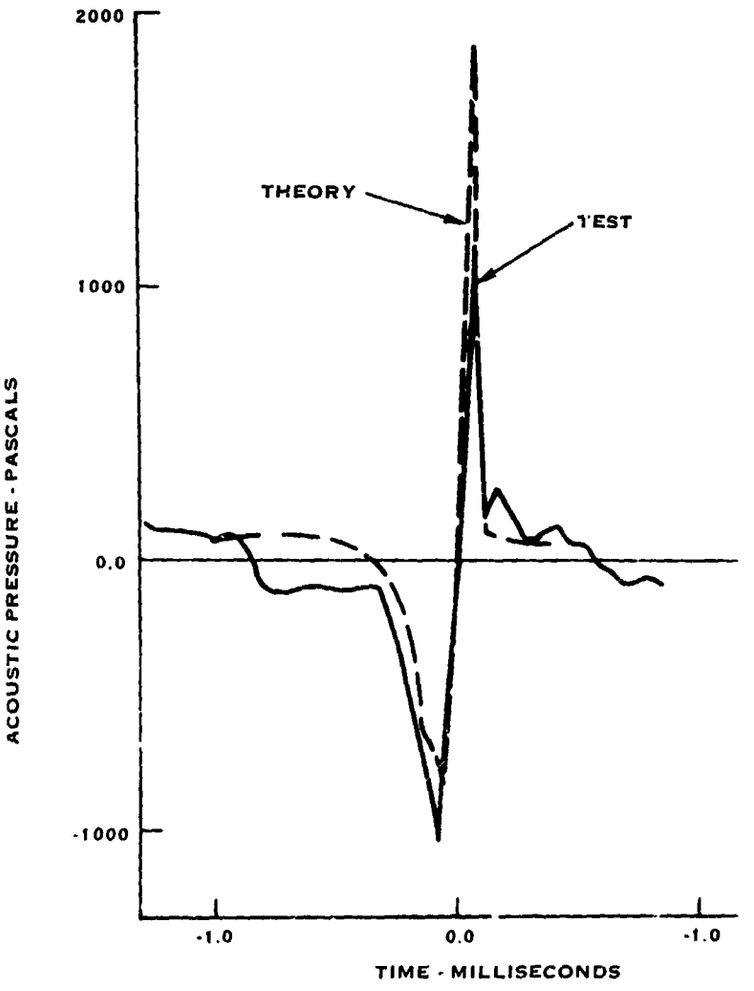

FIGURE A-14B

SR3, RUN 26, 10550 RPM, 18.5 KW/BLADE,
$M_X = 0.320$, $M_{TH} = 1.100$ DIRECTIVITY AT 0.8D TIP CLEARANCE

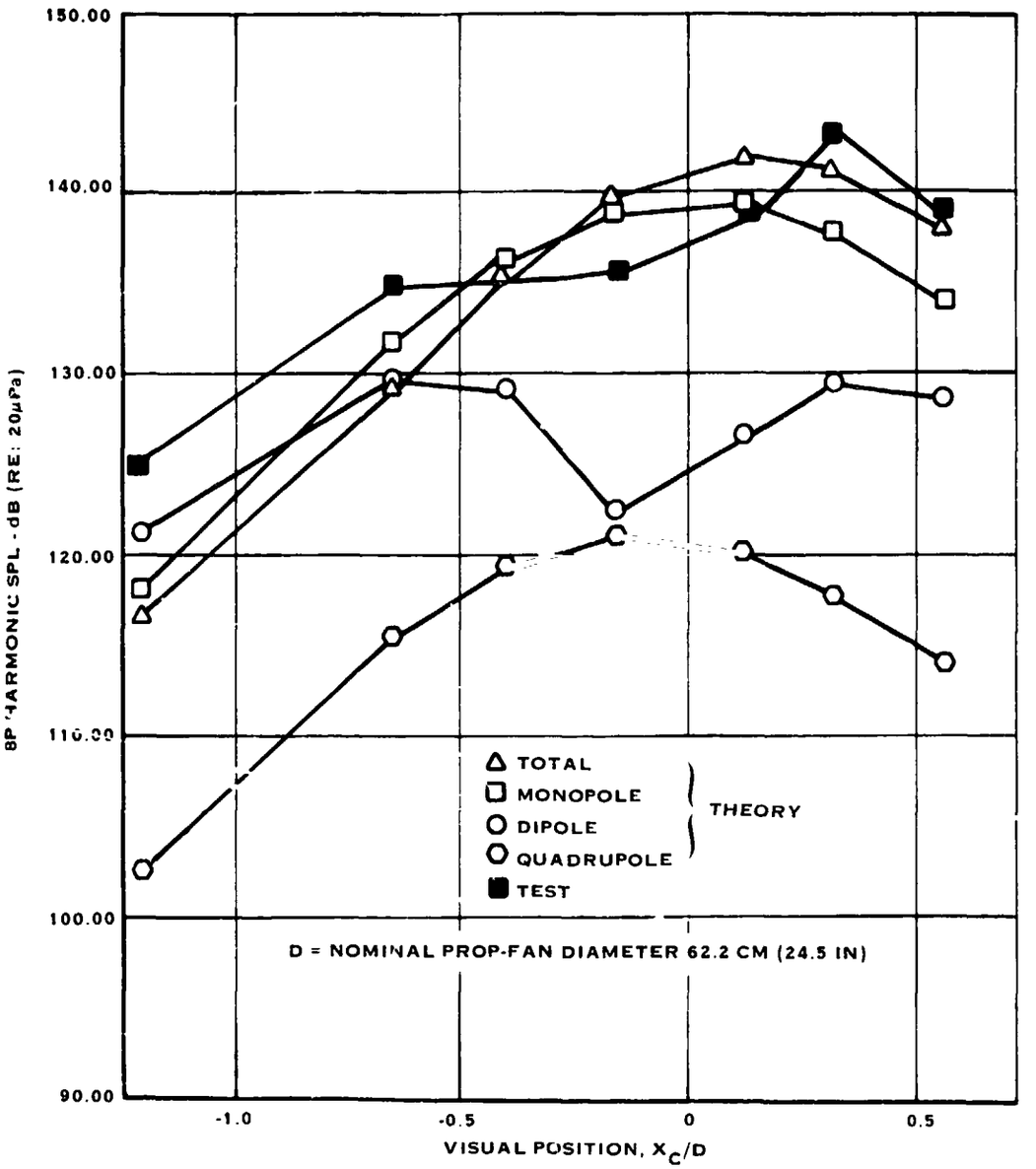

FIGURE A-15A

SR3, RUN 26, WAVEFORM FOR MIC 3 18.5 KW/BLADE,
$M_X = 0.320$, $M_{TH} = 1.100$

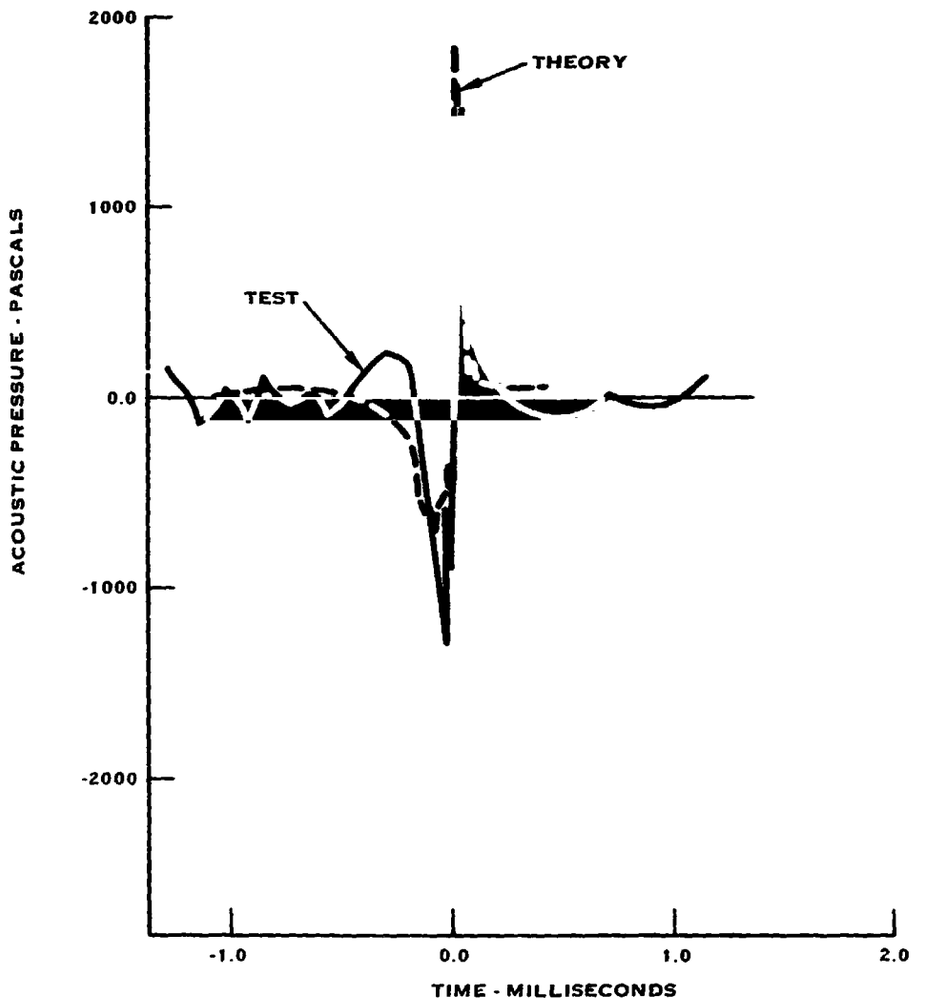

FiGURE A-15B

C-3

SR3, RUN 27, 11250 RPM, 26.2 KW/BLADE,
M_X = 0.322, M_{TH} = 1.169 DIRECTIVITY AT 0.8D TIP CLEARANCE

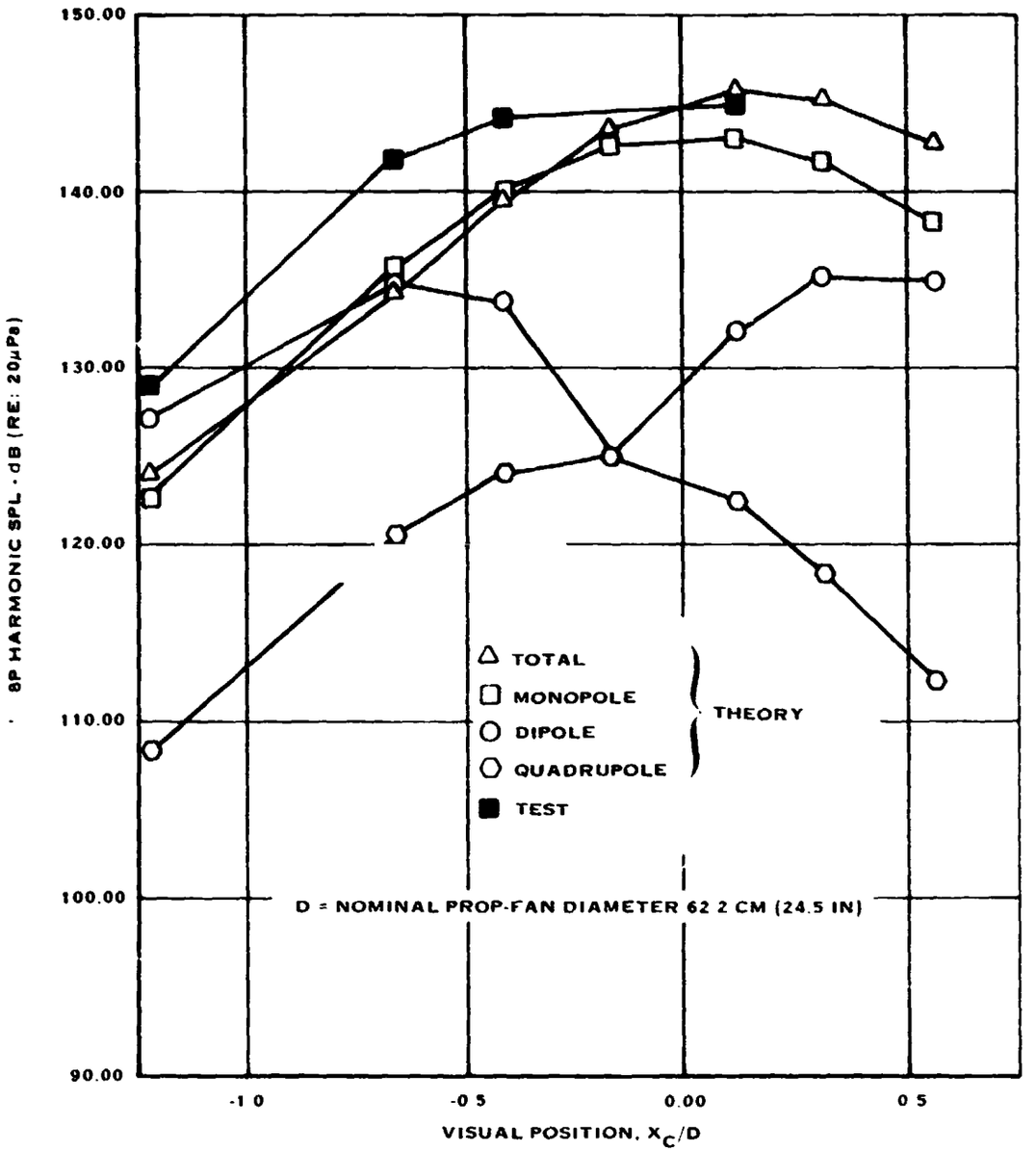

FIGURE A-16A

SR3, RUN 27, WAVEFORM FOR MIC 3 26.2 KW/BLADE,
$M_X = 0.322$, $M_{TH} = 1.169$

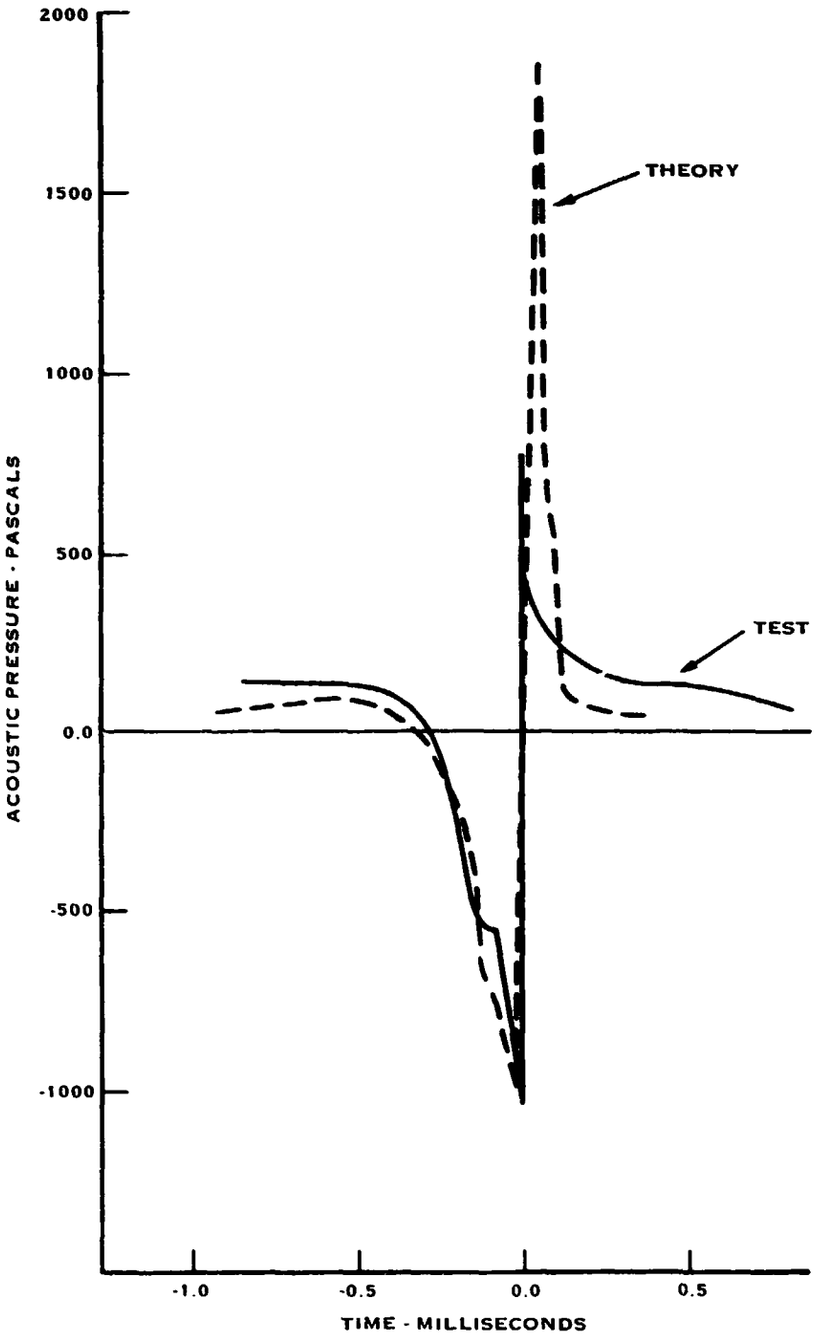

FIGURE A-16B

SR3, RUN 42, 11300 RPM, 16.7 KW/BLADE,

$M_X = 0.322$, $M_{TH} = 1.171$ DIRECTIVITY AT 0.8D TIP CLEARANCE

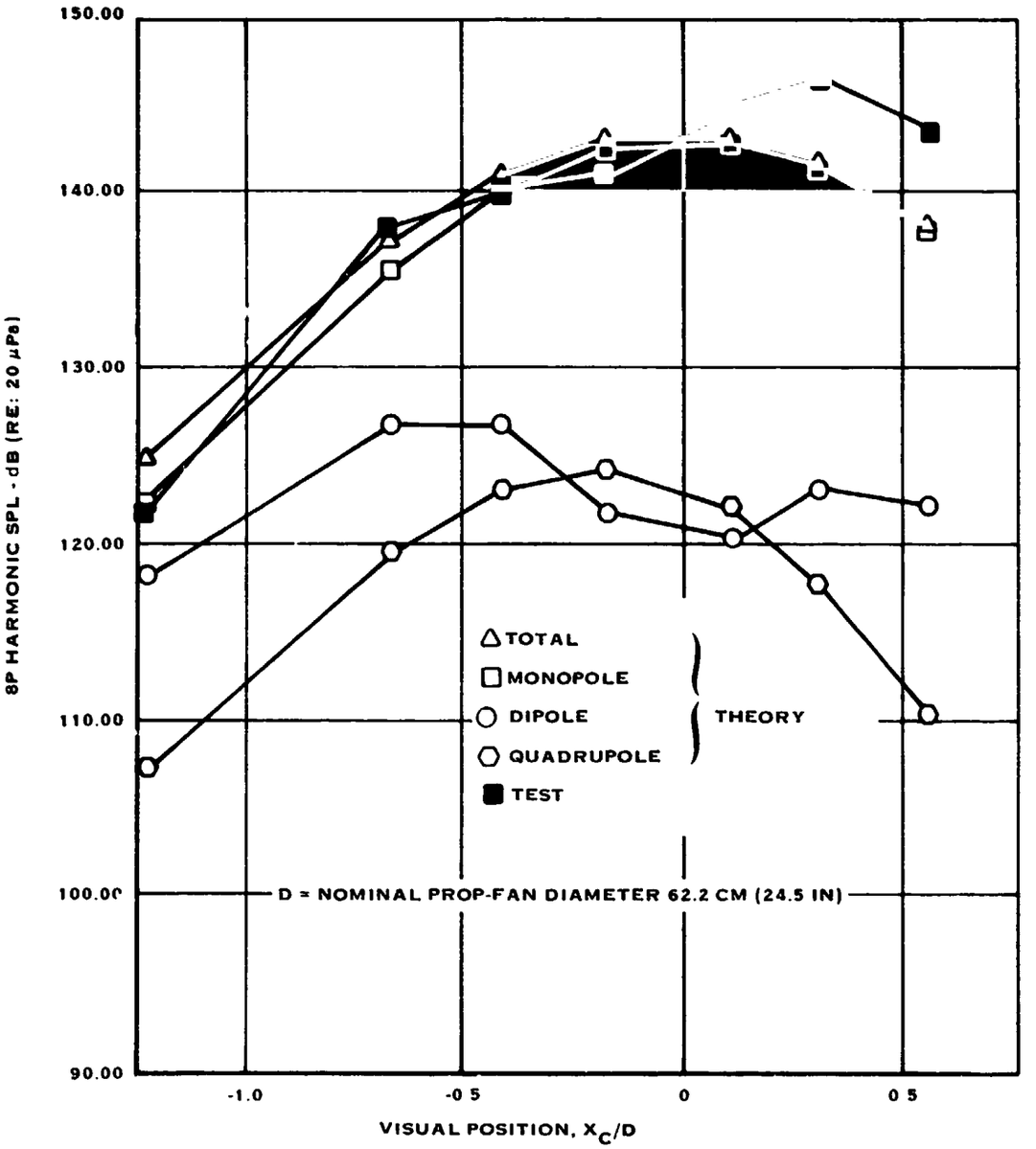

FIGURE A-17A

SR-3, RUN 42, 11300 RPM, 16.7 KW/BLADE,
WAVEFORM FOR MIC 3, M_X = .322, M_{TH} = 1.171

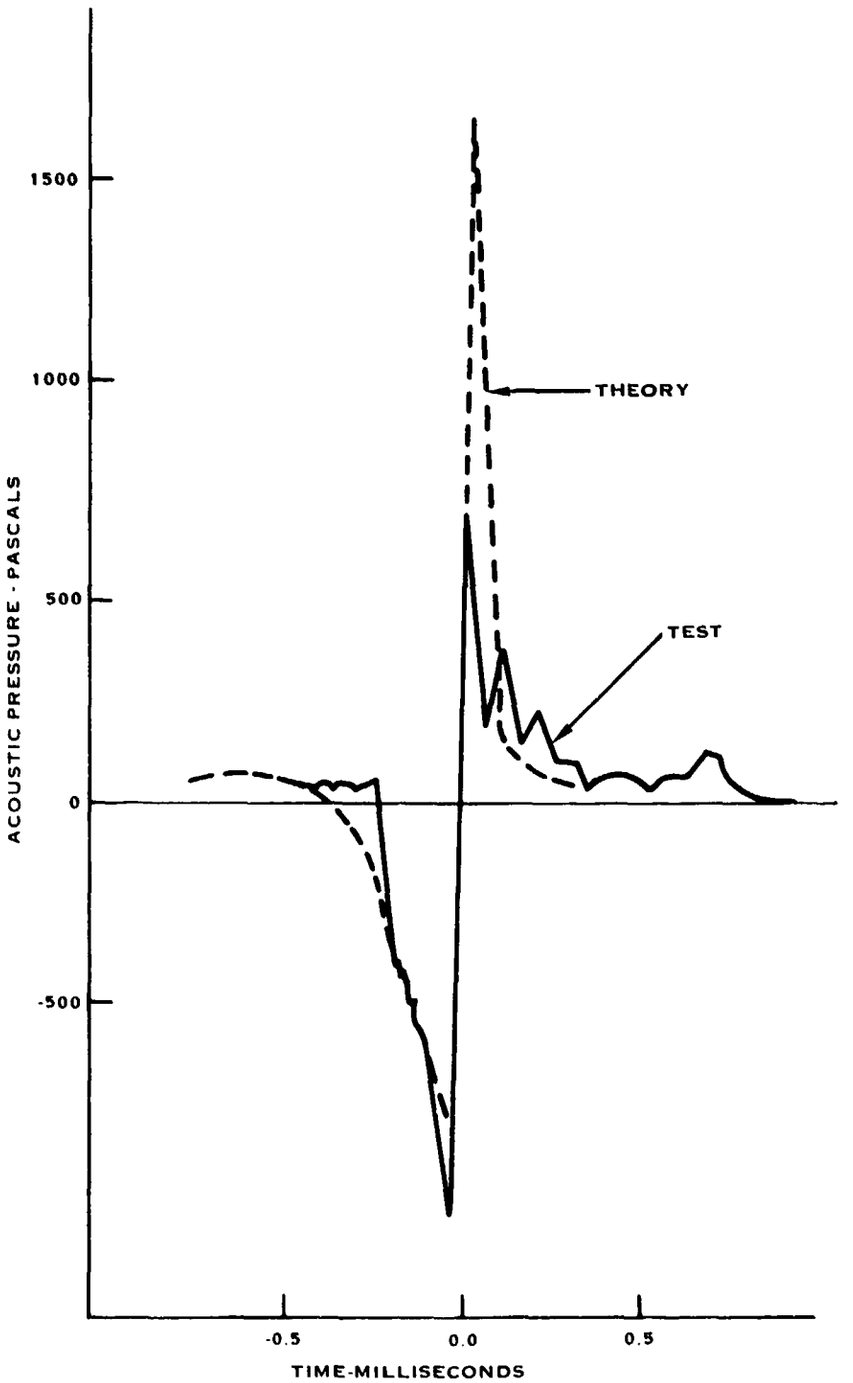

FIGURE A-17B

SR3, RUN 44, 11200 RPM, 9.9 KW/BLADE,
$M_X = 0.3200$, $M_{TH} = 1.165$ DIRECTIVITY AT 0.8D TIP CLEARANCE

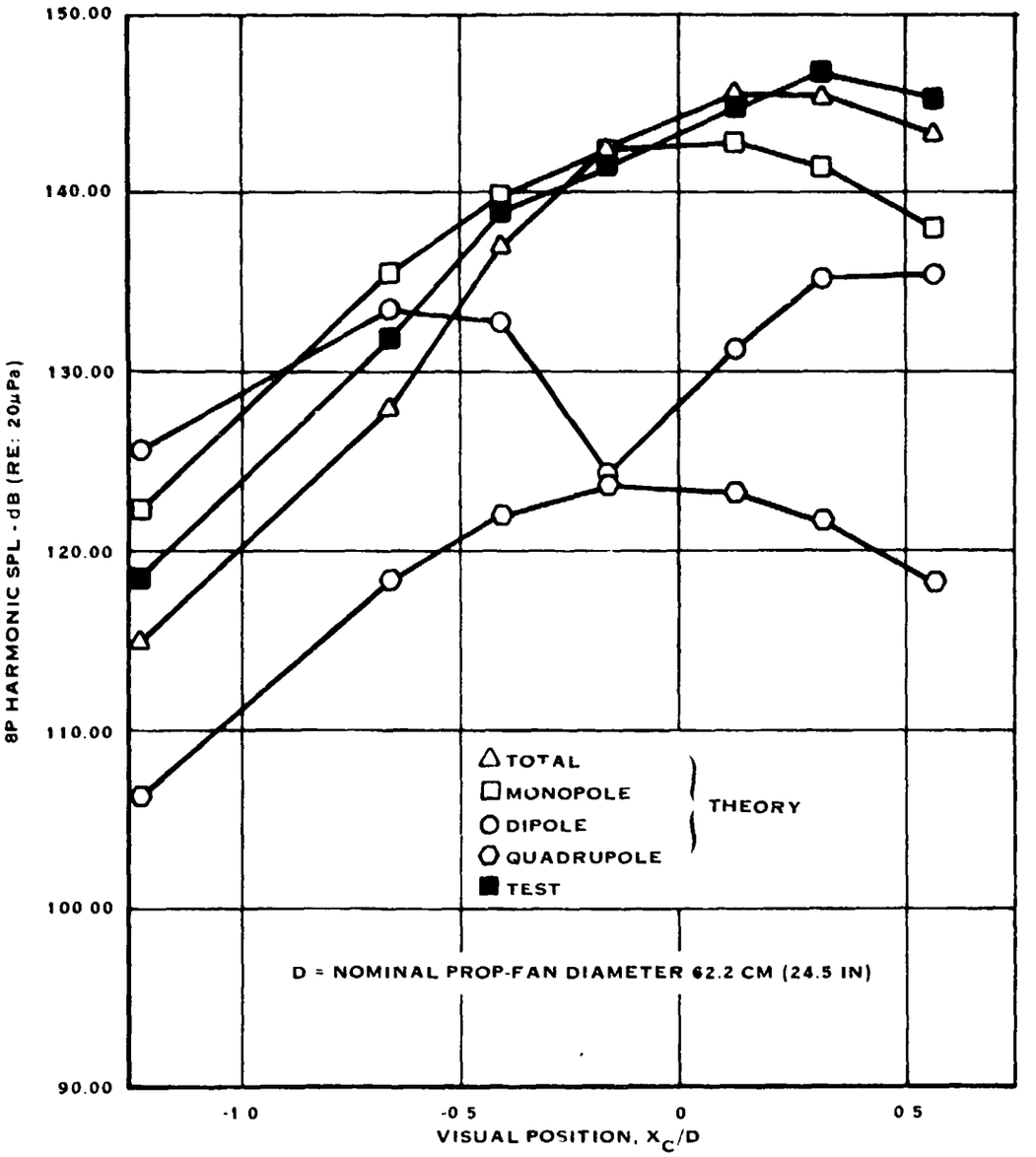

FIGURE A-18A

SR3, RUN 44, WAVEFORM FOR MIC 2 9.9 KW/BLADE,
$M_X = 0.320$, $M_{TH} = 1.165$

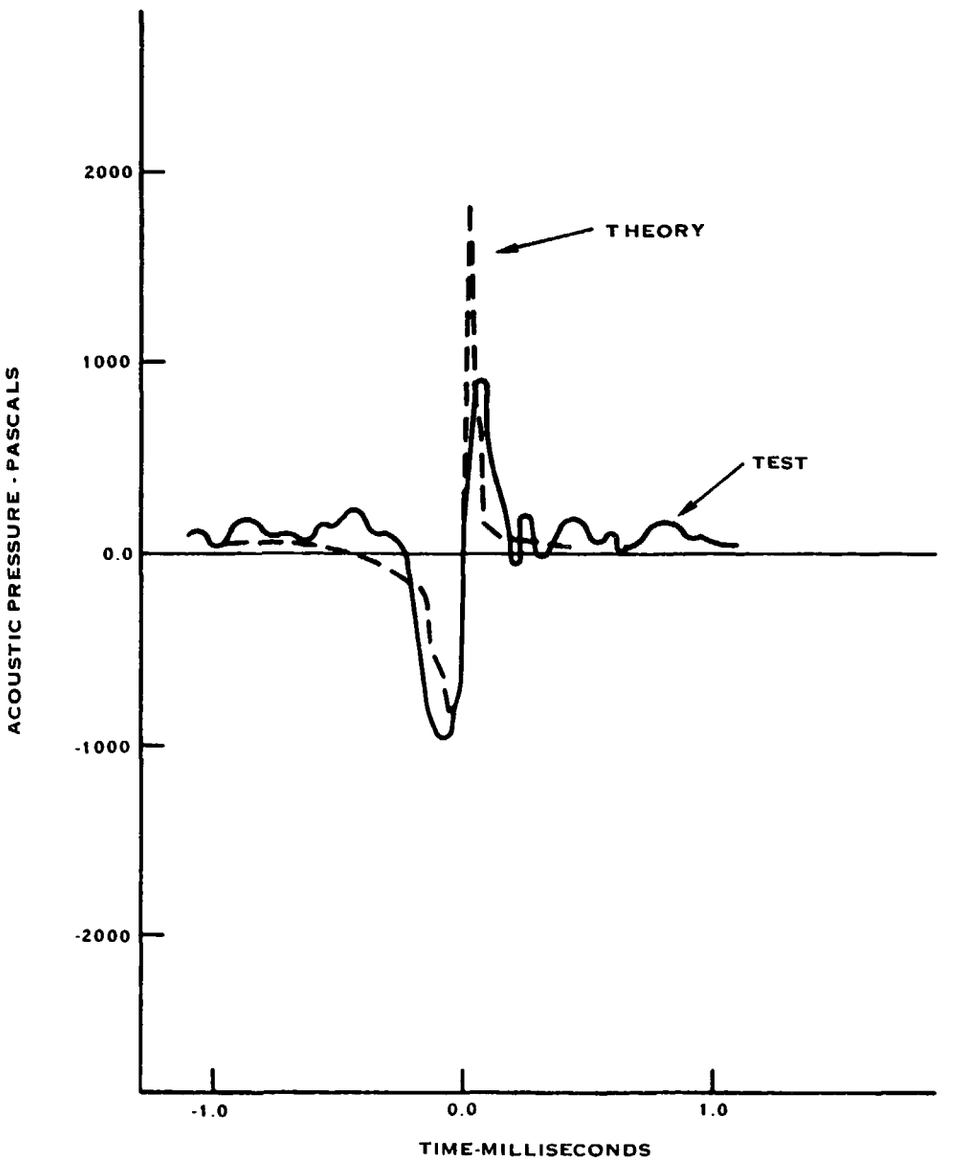

FIGURE A-18B

SR3, RUN 304, 11800 RPM, 36.4 KW/BLADE,
$M_X = 0.323$, $M_{TH} = 1.211$ DIRECTIVITY AT 0.8D TIP CLEARANCE .

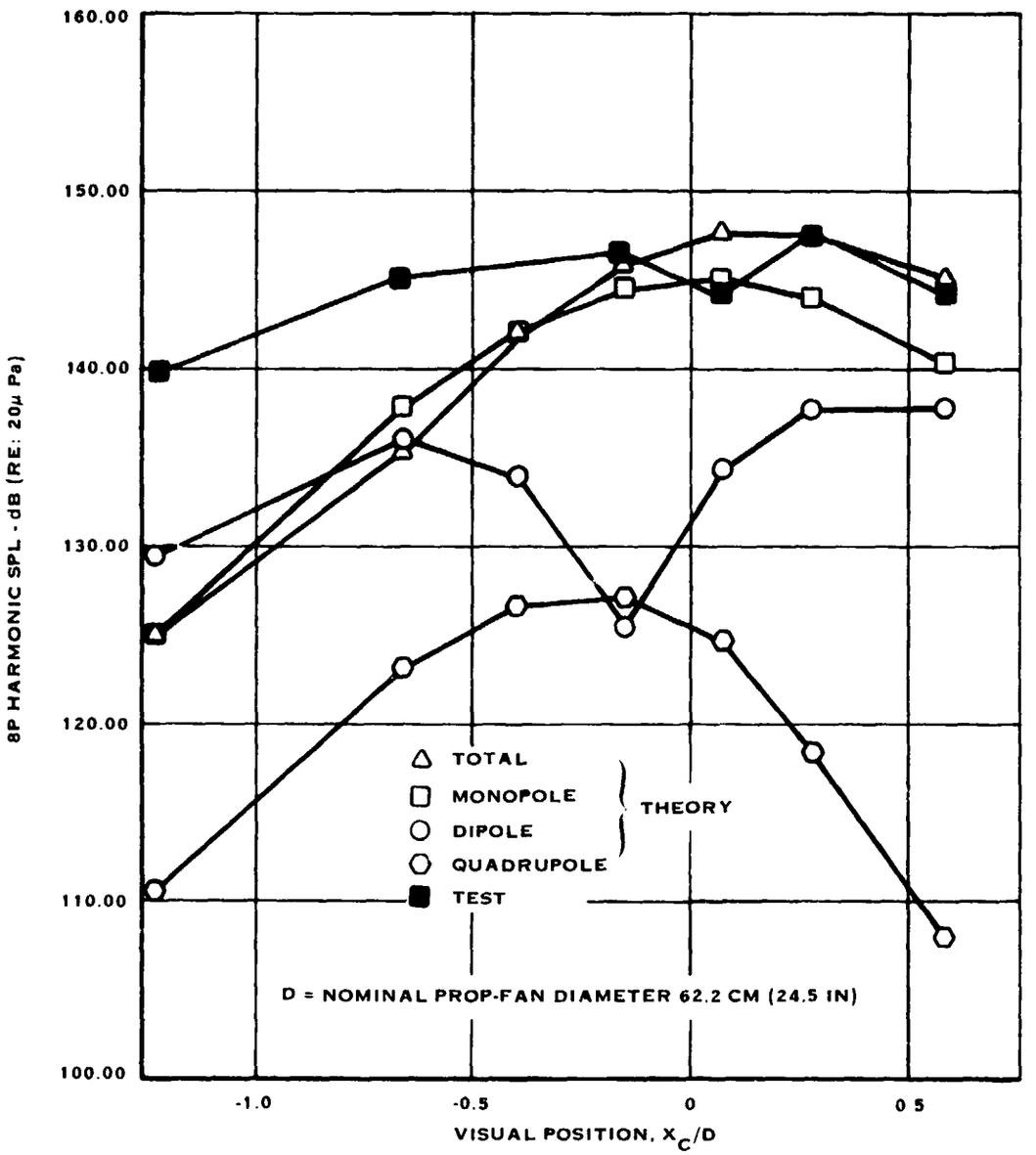

FIGURE A-19A

SR-3, RUN 304, 11800 RPM, 36.4 KW/BLADE,
$M_X = 0.323$, $M_{TH} = 1.211$ WAVEFORM FOR MIC 3

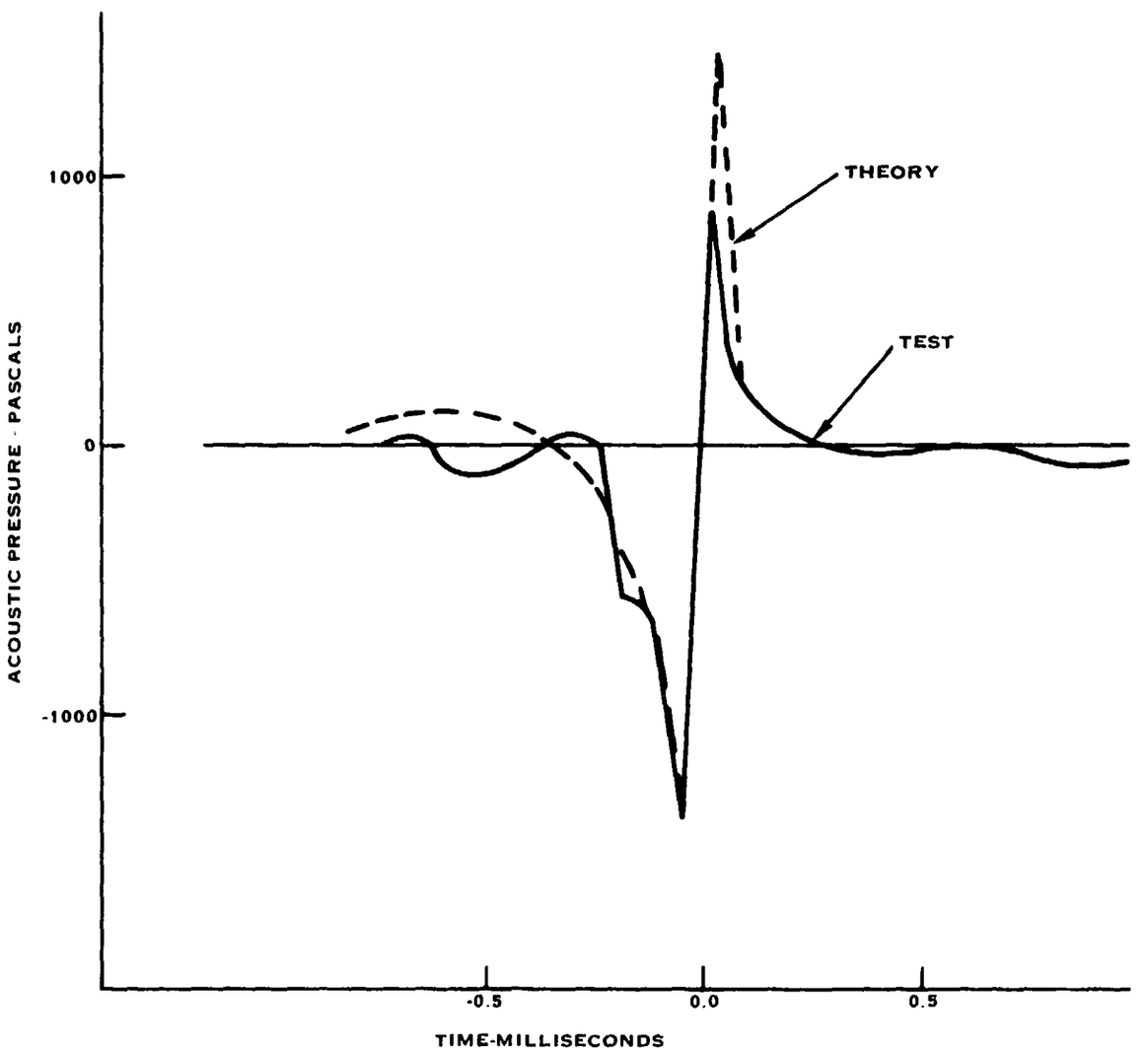

FIGURE A-19B

SR3, RUN 306, 10200 RPM; 15.1 kW/BLADE,
M_X = 0.323, M_{TH} =1.059 DIRECTIVITY AT 0.8D TIP CLEARANCE

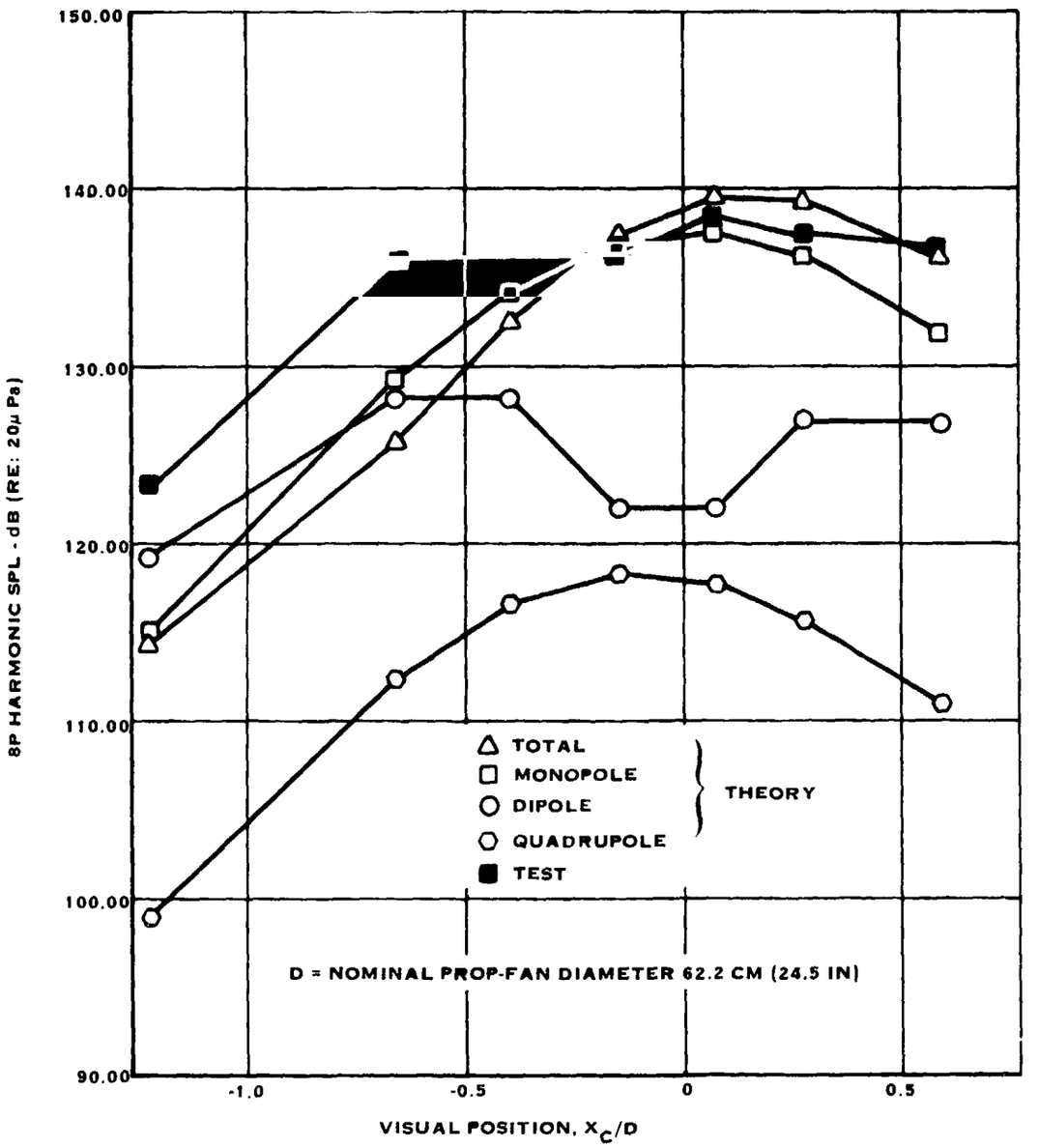

FIGURE A-20A

SR3, RUN 306, WAVEFORM FOR MIC 3, 15.1kW/BLADE

$M_X = 0.323$, $M_{TH} = 1.059$

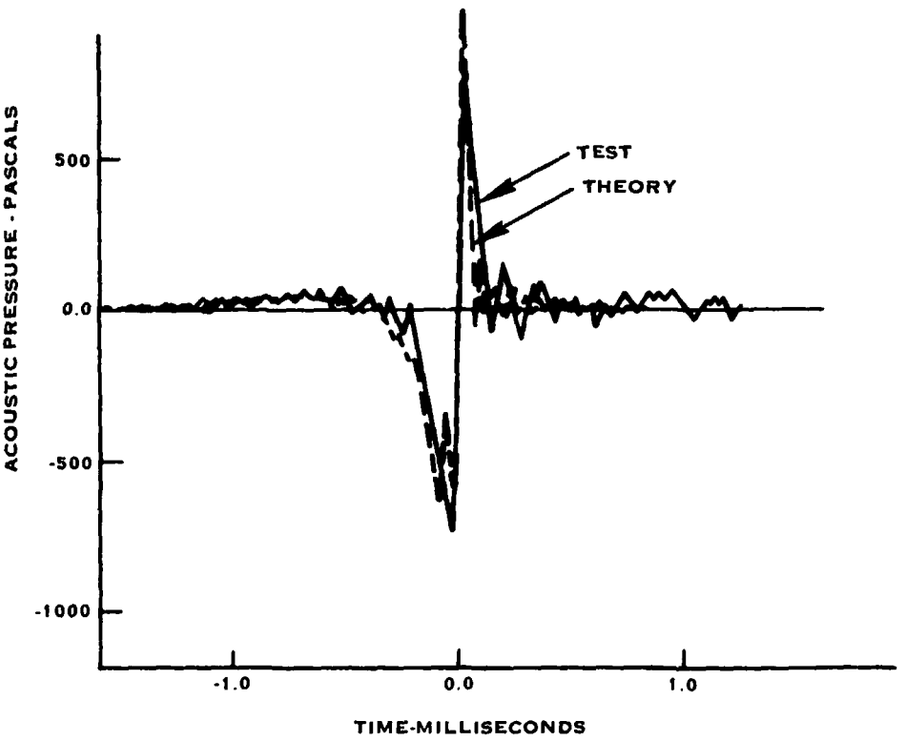

FIGURE A-20B

SR3, RUN 328, 6700 RPM, 13.2 KW/BLADE,
M_X=0.203 M_{TH}=0.687 DIRECTIVITY AT 0.8D TIP CLEARANCE

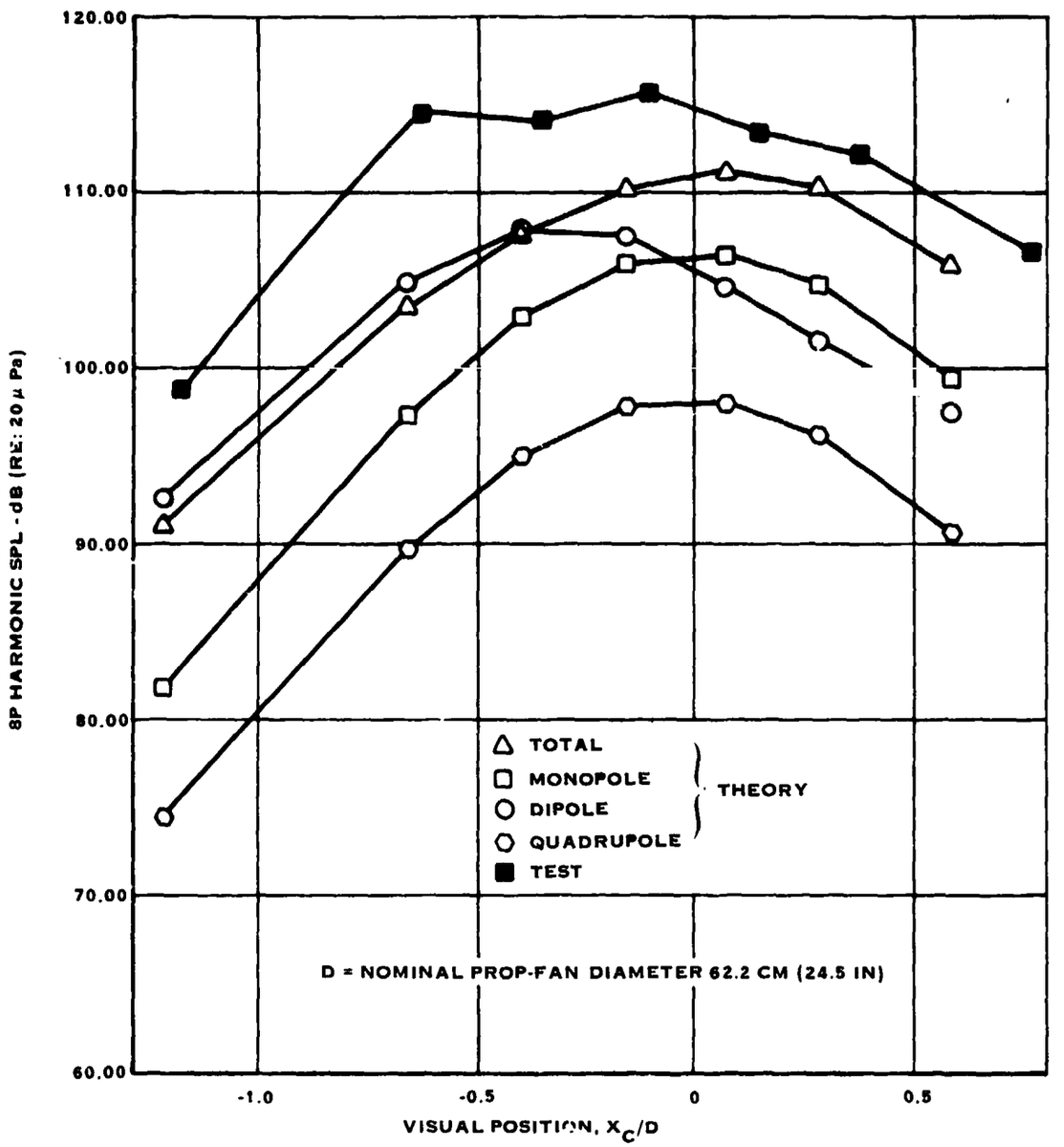

FIGURE A-21A

SR3, RUN 328, WAVEFORM FOR MIC 4 13.2 KW/BLADE,
$M_X = 0.203$, $M_{TH} = 0.687$

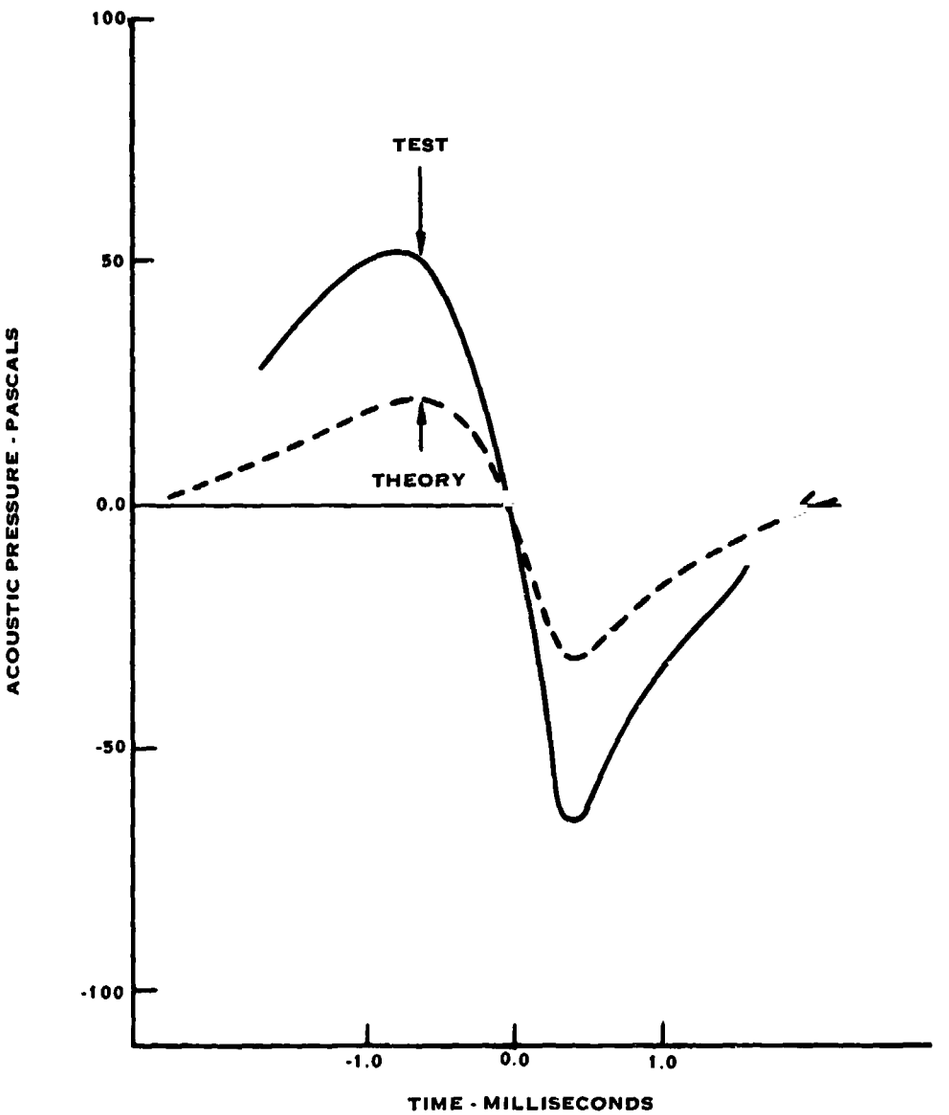

FIGURE A-21B

SR3, RUN 329, 7500 RPM, 22.8 KW/BLADE

$M_X = 0.203$ $M_{TH} = 0.761$ DIRECTIVITY AT 0.8D TIP CLEARANCE

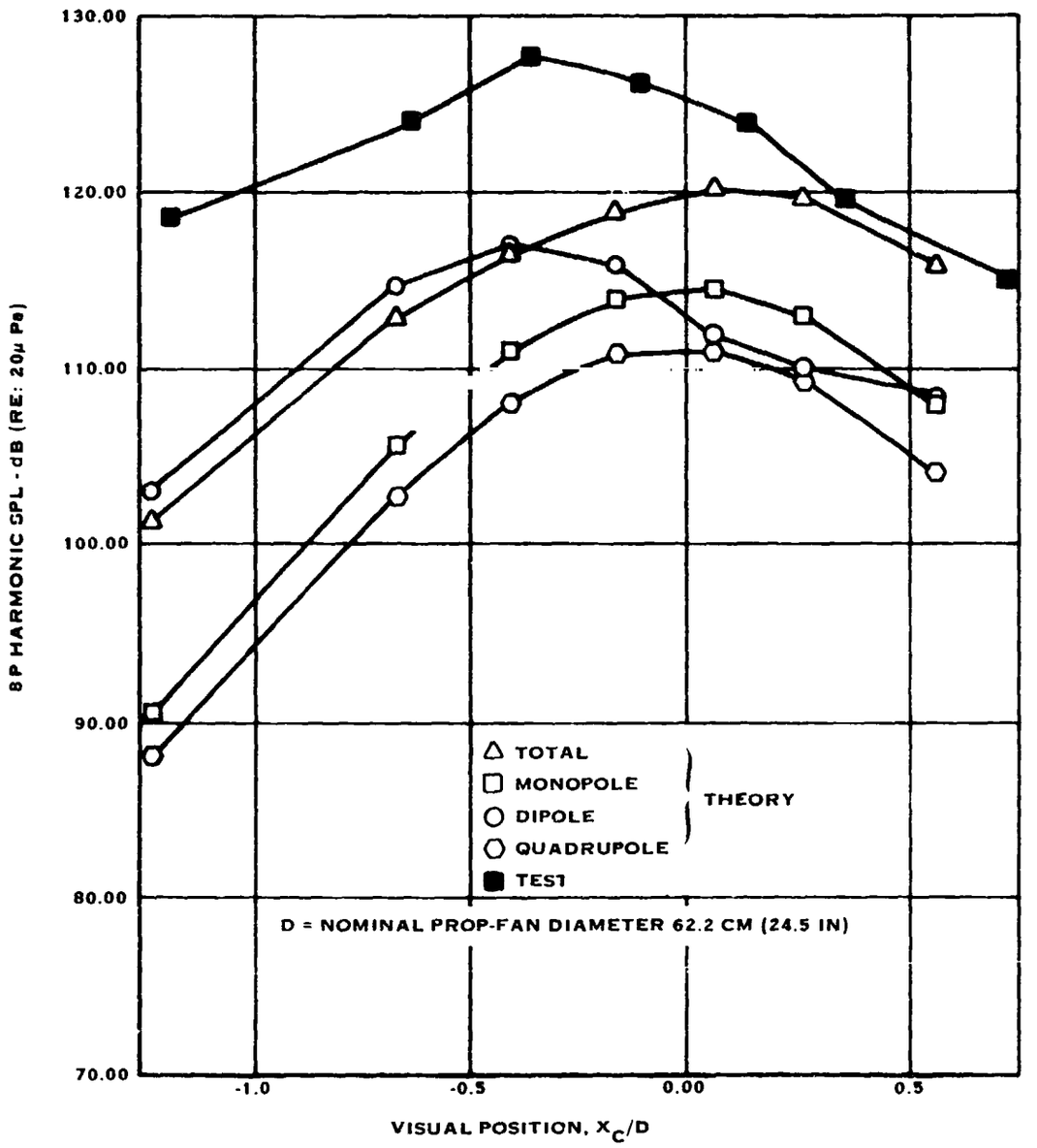

FIGURE A-22 A

SR3, RUN 329, WAVEFORM FOR MIC 5, 22.8 KW/BLADE,
$M_X = 0.203$, $M_{TH} = 0.761$

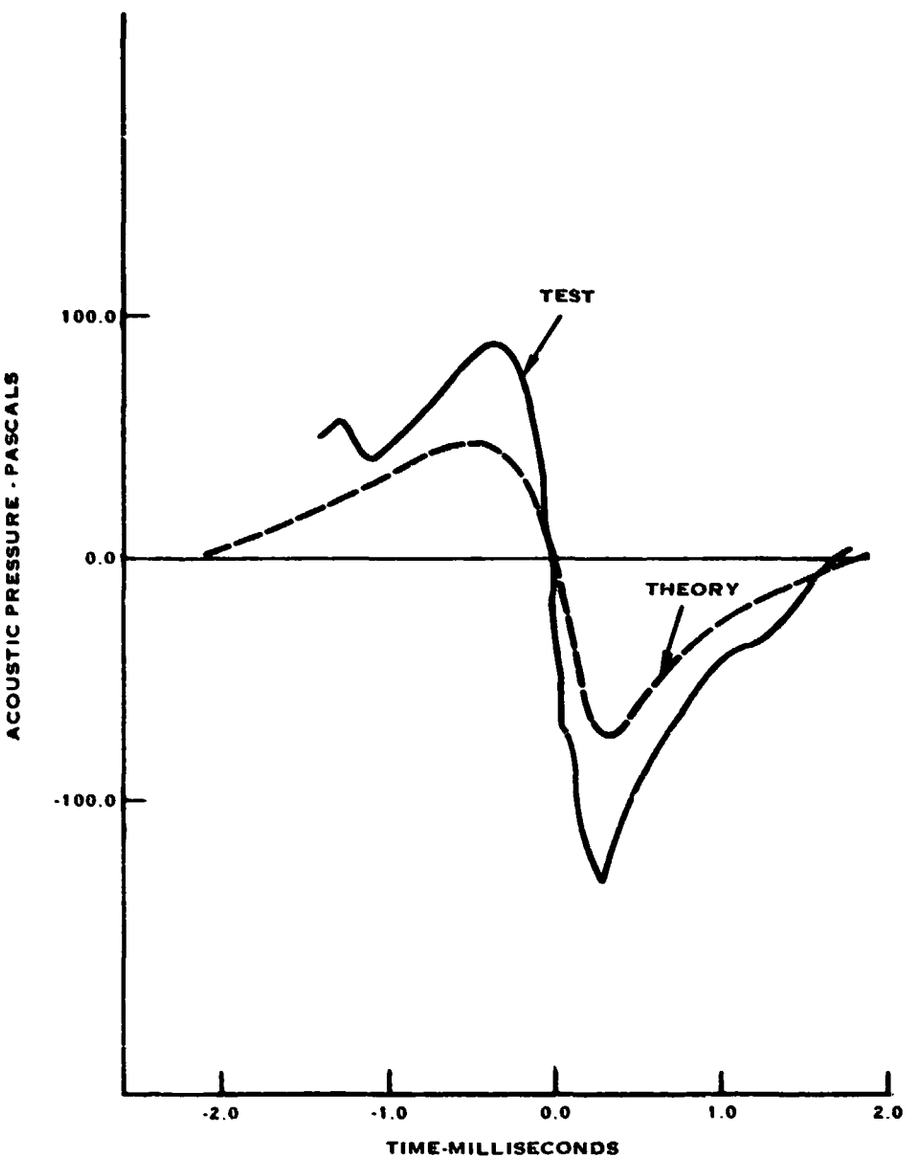

FIGURE A-22B

APPENDIX B
SHADOWGRAPHS USED FOR BOW AND TRAILING WAVE ANALYSIS

In this appendix samples of the shadowgraphs used in the analysis of the locations of bow and trailing waves are presented. For ease in interpreting the shadowgraphs, Figure B-1 is presented which shows the location of the camera relative to the blades while the planform shadowgraphs of Figures B-2 through B-9 were taken for SR-2 and SR-3. Two operating conditions for each model were photographed in planform view as shown in Figures B-2 through B-9. Due to the test set-up geometry, shadowgraphs of the SR-2 blade in three aximuth positions were required to define the locations of the wave formations for each operating condition. Shadowgraphs of only one azimuth position were needed for the SR-3 cases. Figure B-10 shows an edge view of the SR-3 to demonstrate the three-dimensional character of the bow and trailing waves. The blur to the right of shadow is the unfocused image of the blade itself. Figure B-11 is a sketch of the Figure B-10 edge view provided to assist the reader. Figure B-12 is an artists concept of the three-dimensional surface described by the blade trailing wave. The line of maximum second order density gradient pointed out in Figure B-12 is the line seen at the blade trailing edge in Figures B-2 through B-9. In addition to the wave formations, blade tip vortices are visible in the shadowgraphs.

Figure B-13 is a series of shadowgraphs for the SR-3 blade operating at high tip speed, with the blade in different azimuth positions. In this figure, movement of the line indicating the location of the trailing wave illustrates the three-dimensional character of the wave. A similar series of SR-3 model shadowgraphs in edge view is shown in Figure B-14. A faint line which may be the bow wave is seen in the second and third shadowgraphs in the series. In the first of the series a tip vortex and viscous trailing wake are visible near the tip of the blade at the right of the shadowgraph.

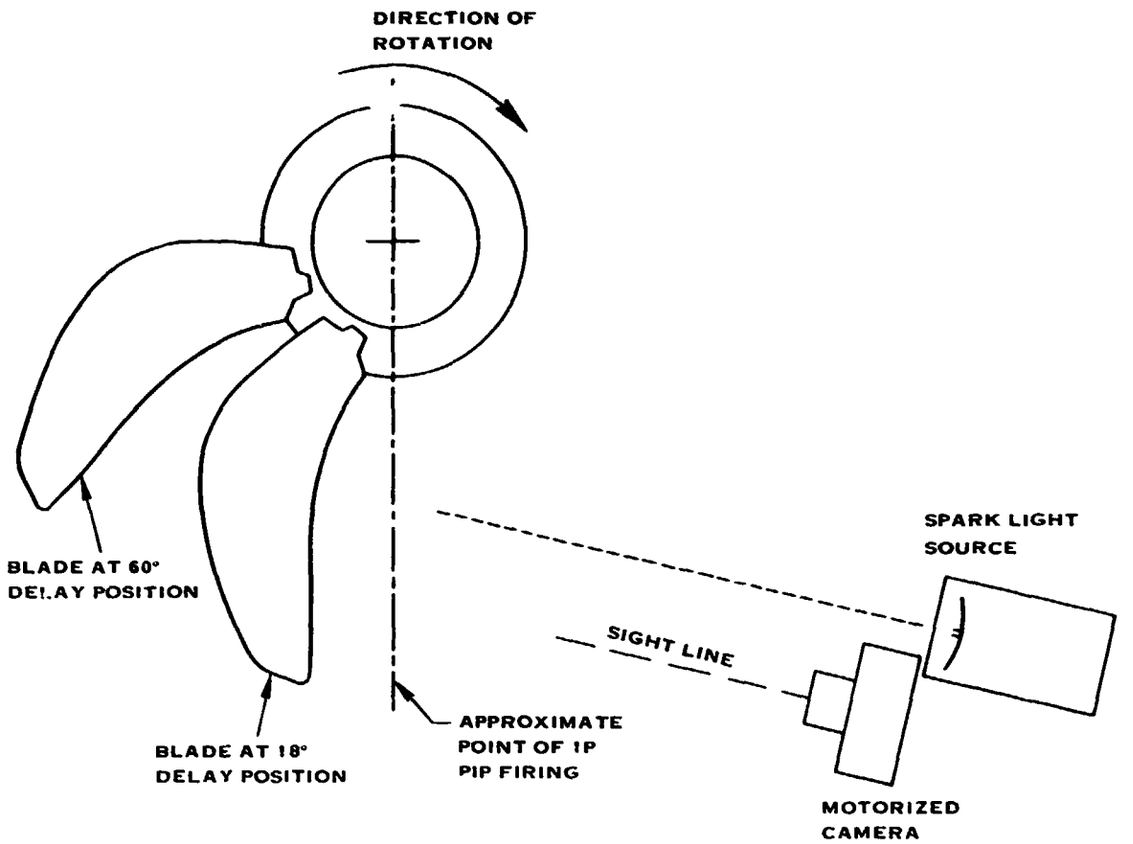

FIGURE B-1. VIEW OF SHADOWGRAPH SET-UP (LOOKING DOWNSTREAM)

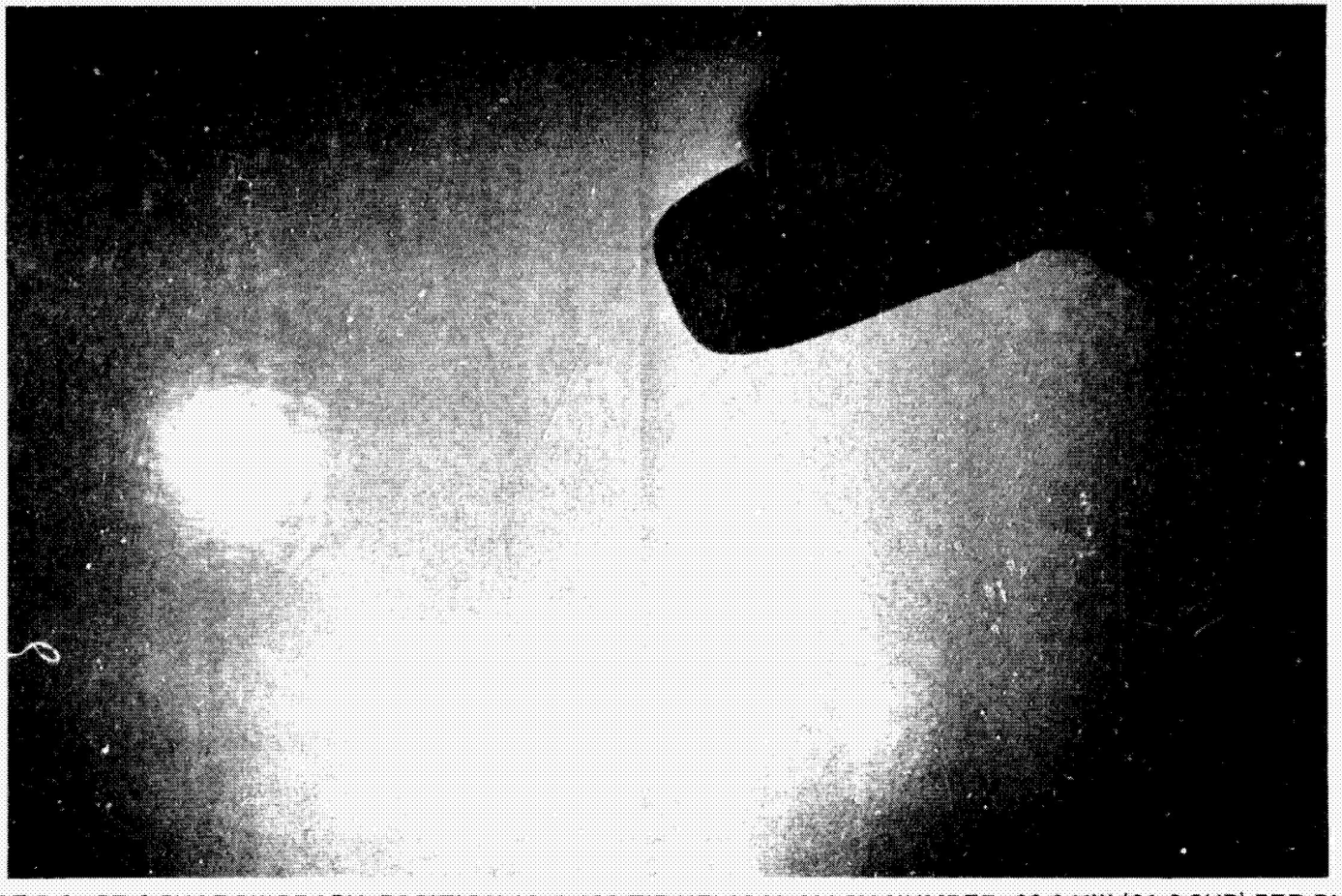

FIGURE B-2. SR-2 SHADOWGRAPH POSITION 12, 1.138 TIP HELICAL MACH NUMBER, 23.2 KW (31.2 SHP) PER BLADE

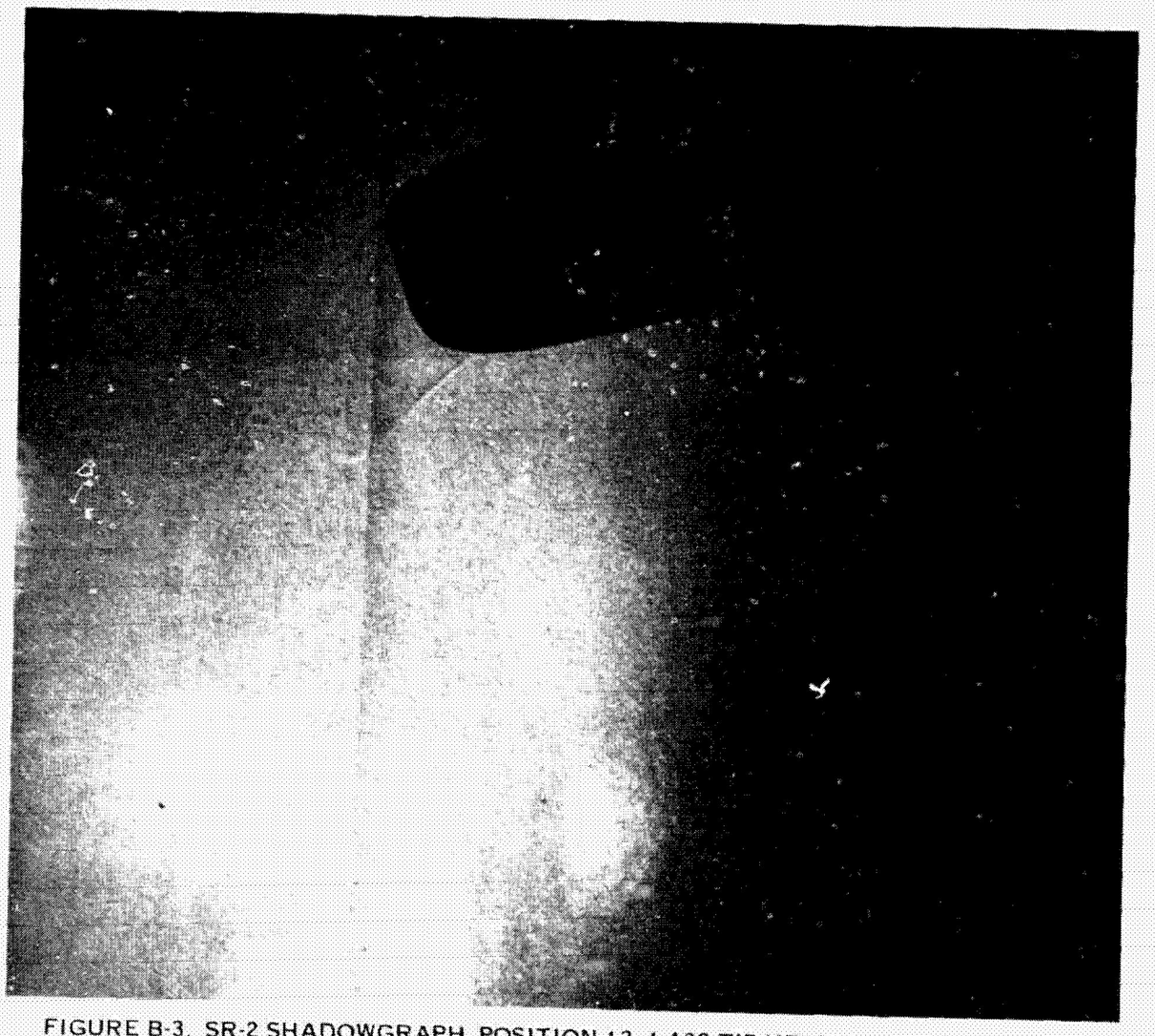

FIGURE B-3. SR-2 SHADOWGRAPH, POSITION 13, 1.138 TIP HELICAL MACH NUMBER, 23.2 KW (31.2 SHP) PER BLADE

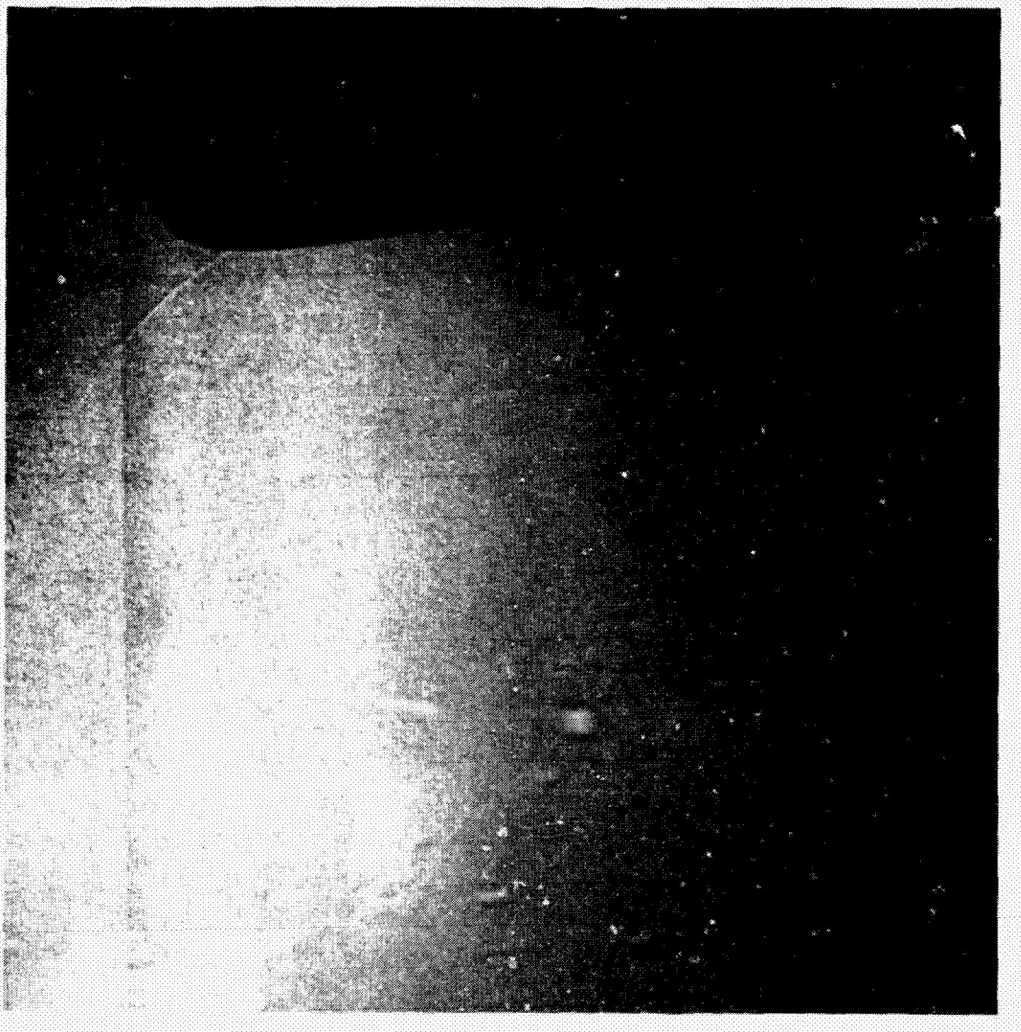

FIGURE B-4. SR-2 SHADOWGRAPH, POSITION 14, 1.138 TIP HELICAL MACH NUMBER, 23.2 KW (31.2 SHP) PER BLADE

FIGURE B-5. SR-2 SHADOWGRAPH, POSITION 12, 1.181 TIP HELICAL MACH NUMBER, 31.4 KW (42.1 SHP) PER BLADE

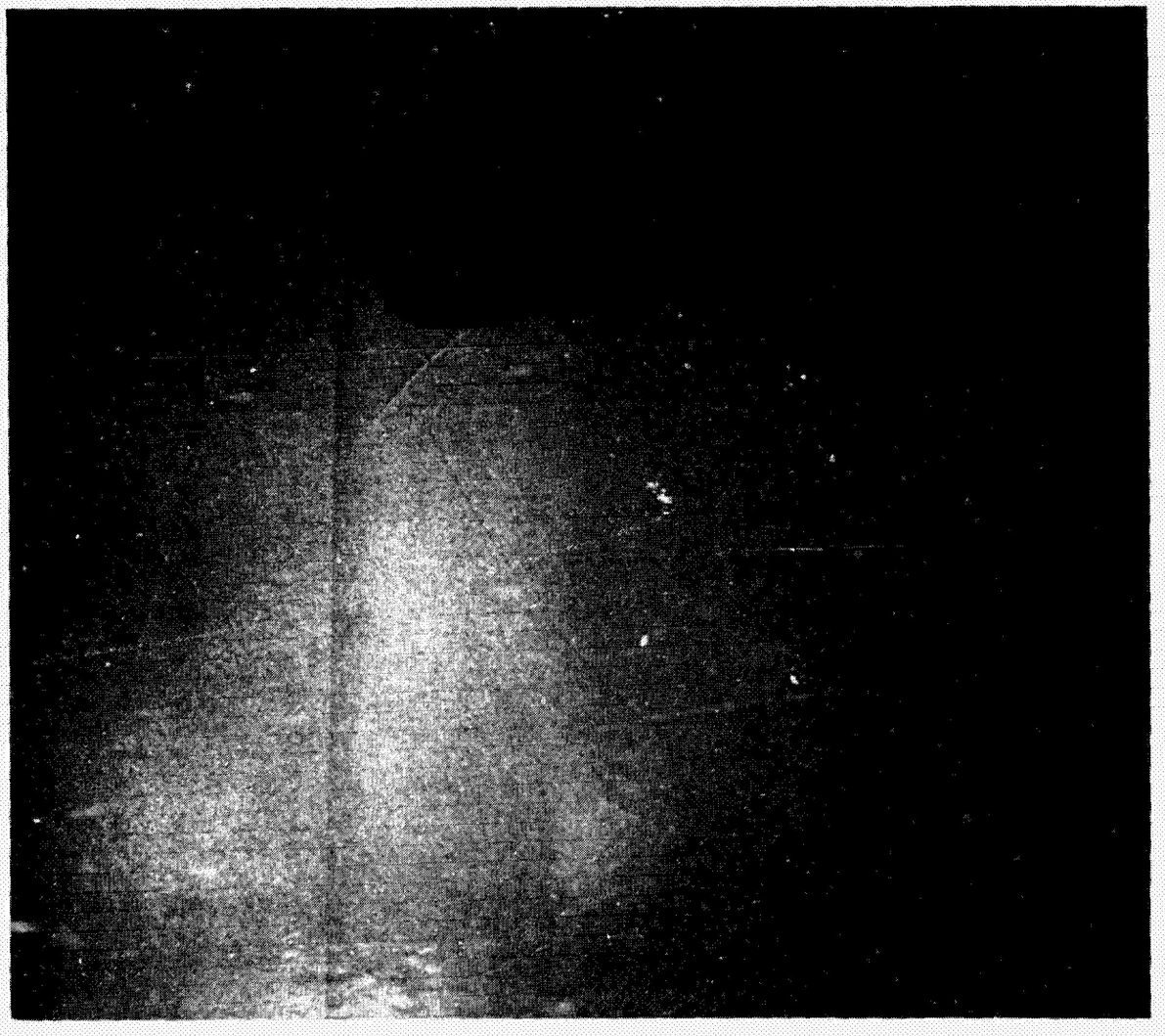

FIGURE B-6. SR-2 SHADOWGRAPH POSITION 13, 1.181 TIP HELICAL MACH NUMBER, 31.4 KW (41.2 SHP) PER BLADE

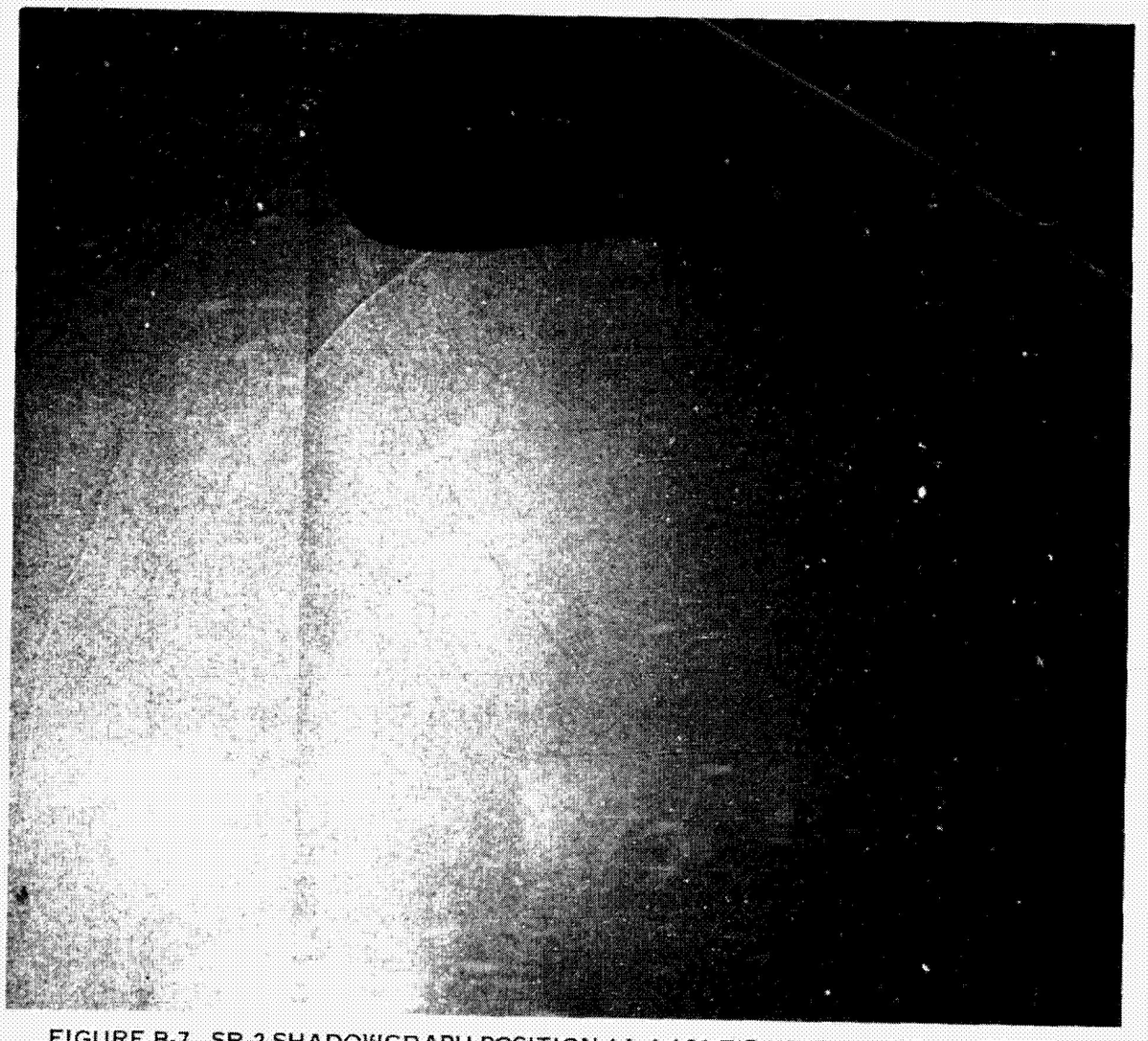

FIGURE B-7. SR-2 SHADOWGRAPH POSITION 14, 1.181 TIP HELICAL MACH NUMBER, 31.4 KW (42.1 SHP) PER BLADE

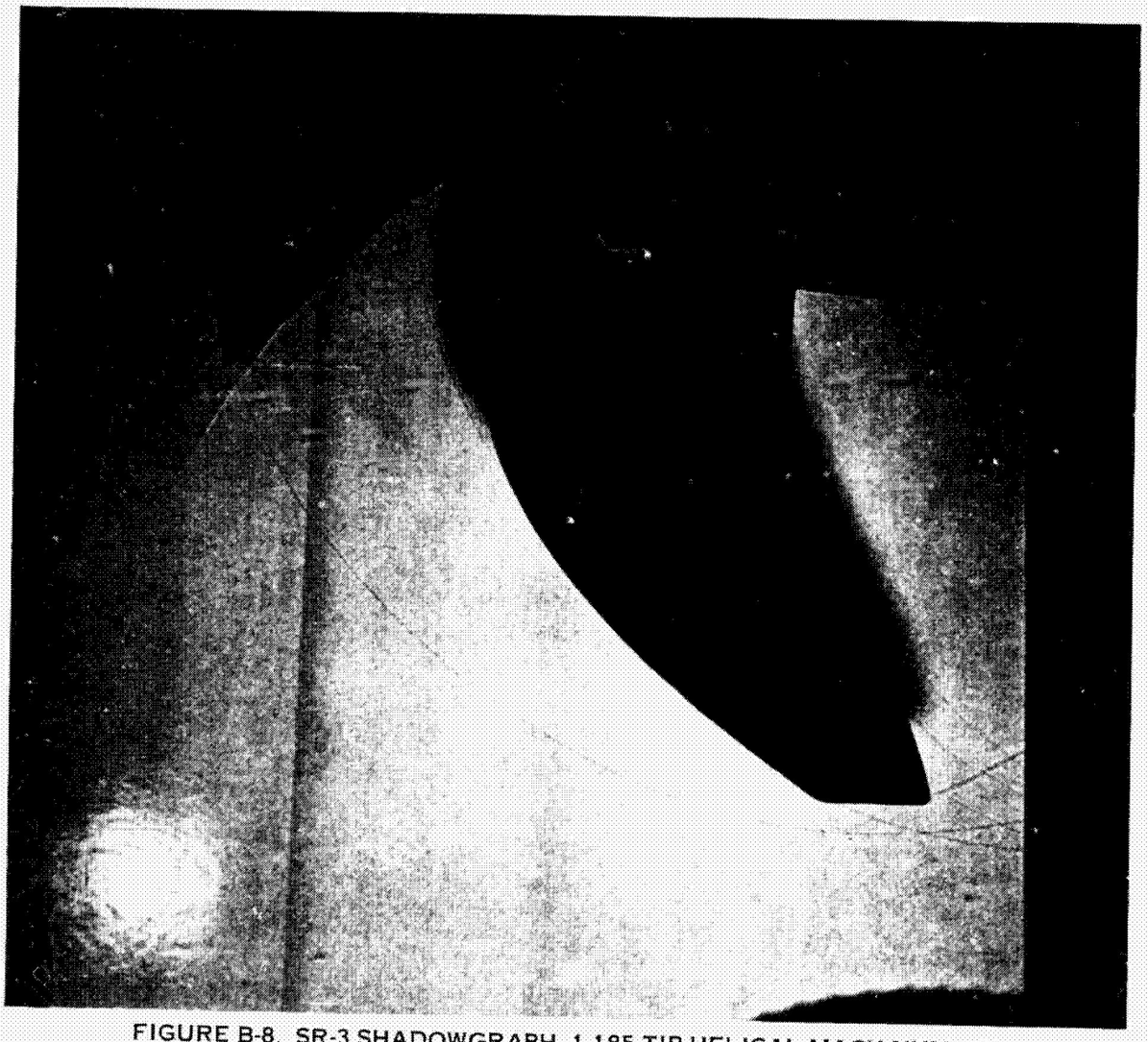

FIGURE B-8. SR-3 SHADOWGRAPH, 1.185 TIP HELICAL MACH NUMBER, 26.7 KW (36 SHP) PER BLADE

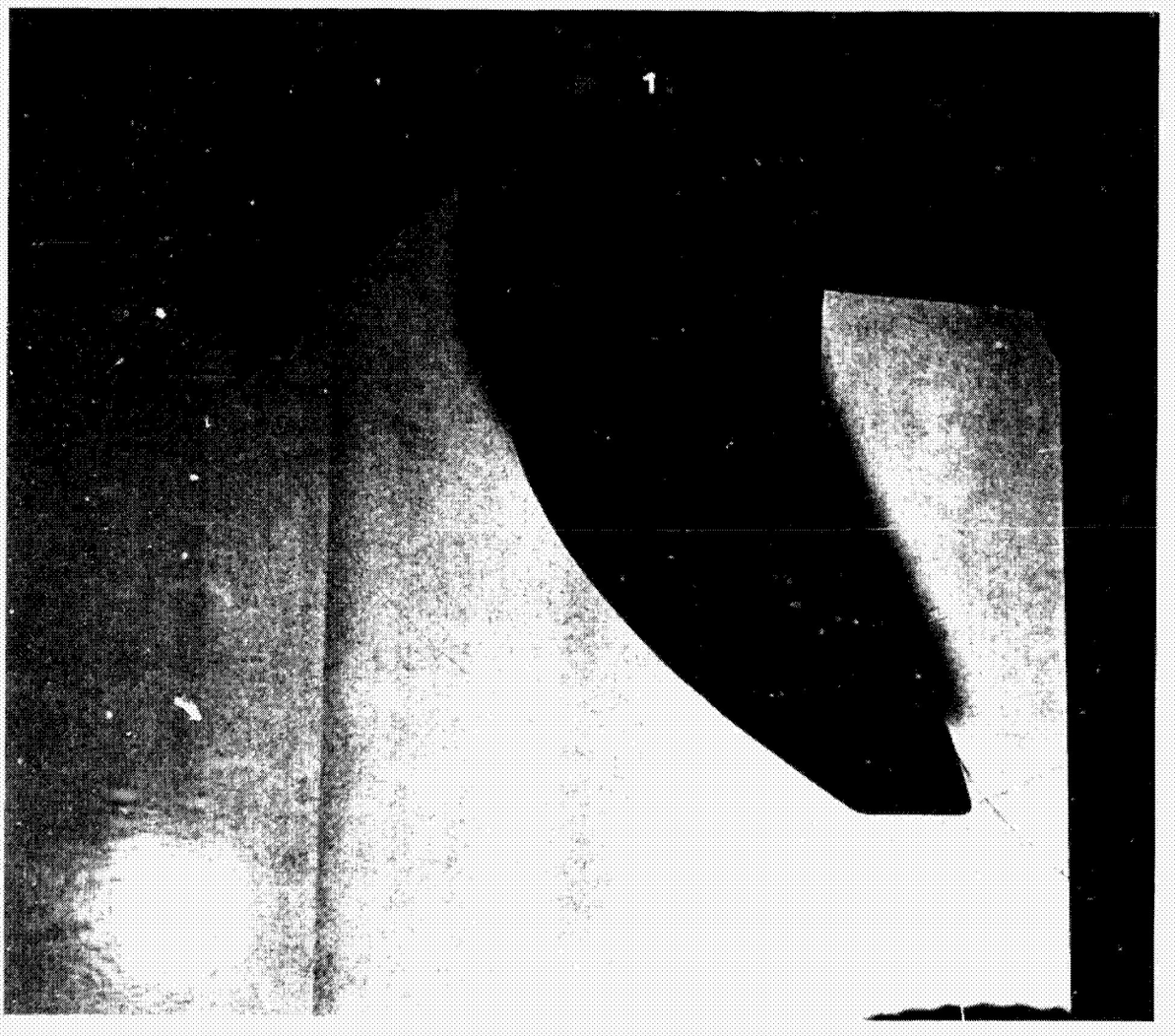

FIGURE B-9. SR-3 SHADOWGRAPH, 1.071 TIP HELICAL MACH NUMBER, 15.1 KW (20 SHP) PER BLADE

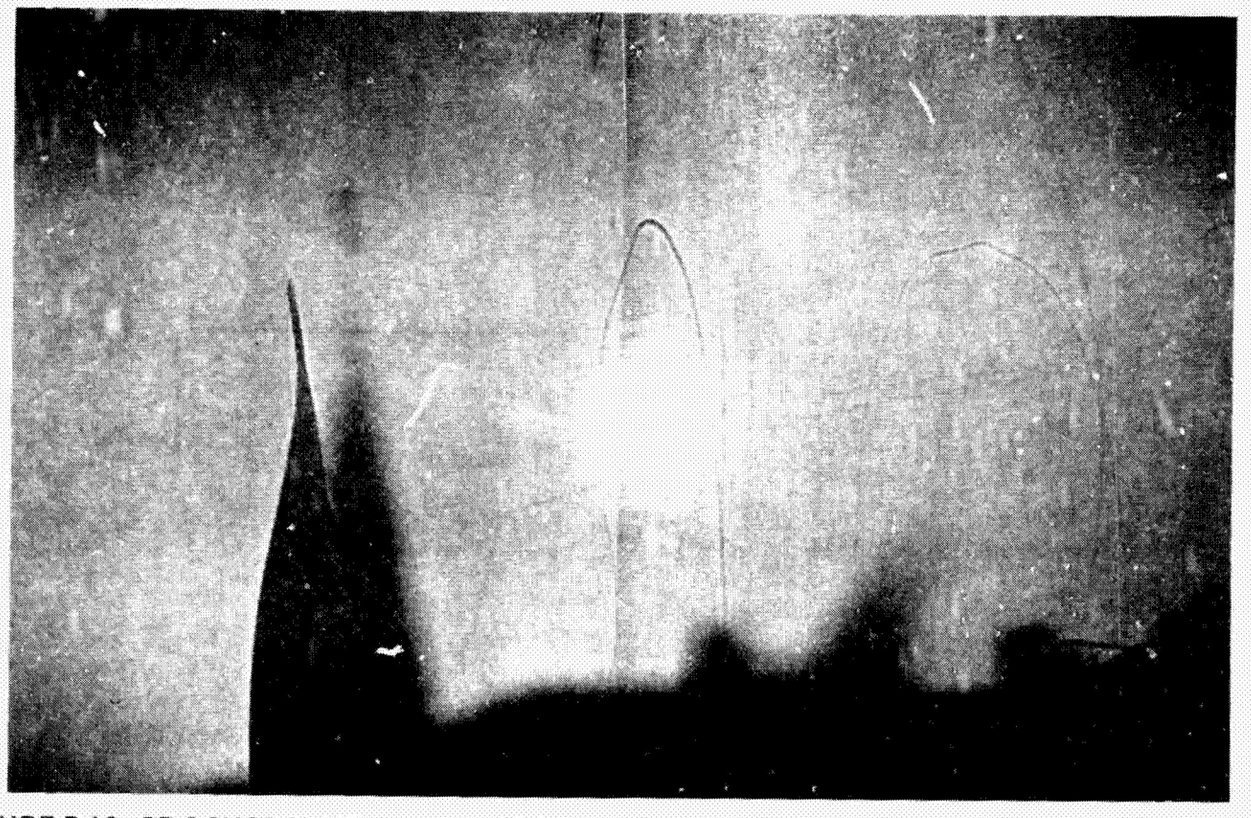

FIGURE B-10. SR-3 SHADOWGRAPH, 1.174 TIP HELICAL MACH NUMBER, 24.0 KW (32.2 SHP) PER BLADE

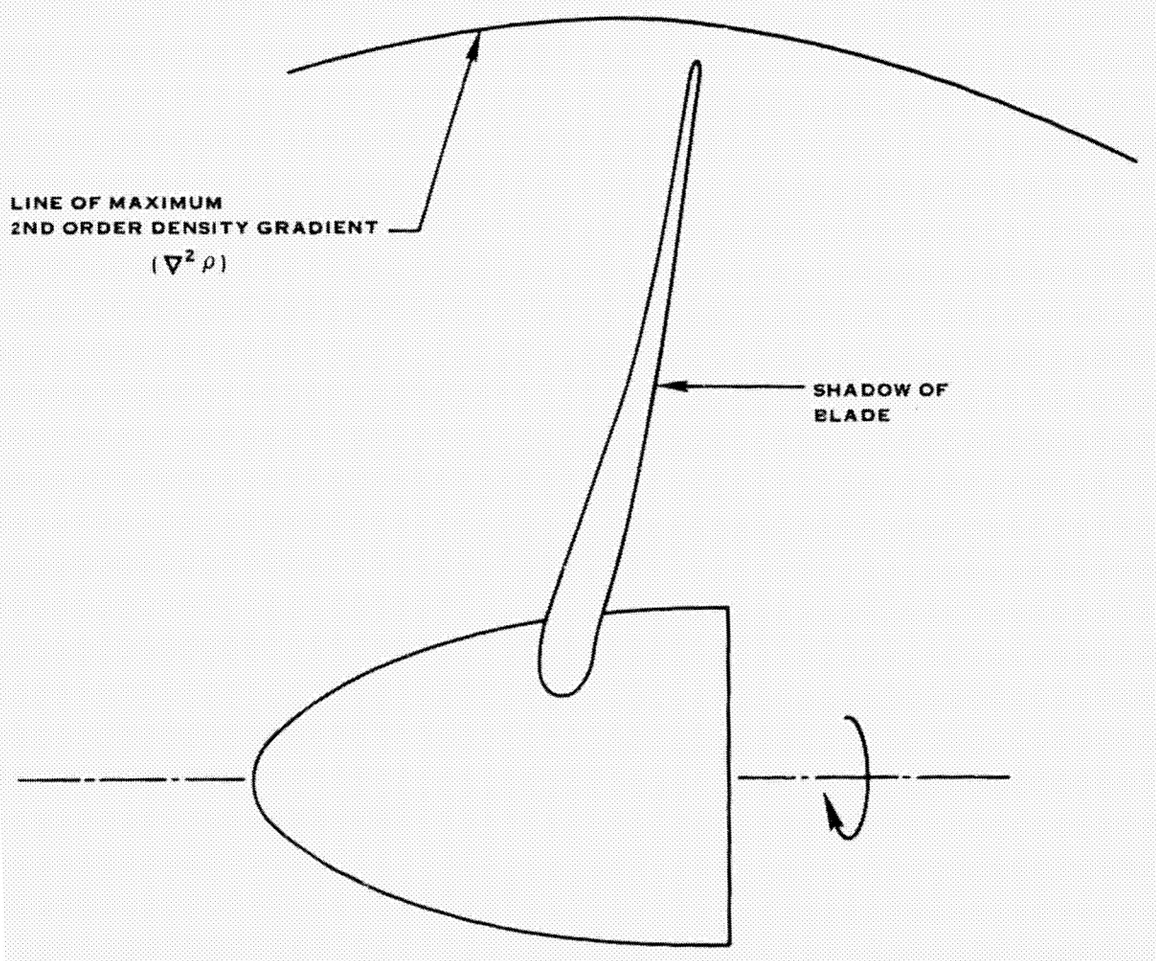

FIGURE B-11. SHADOWGRAPH EDGE VIEW

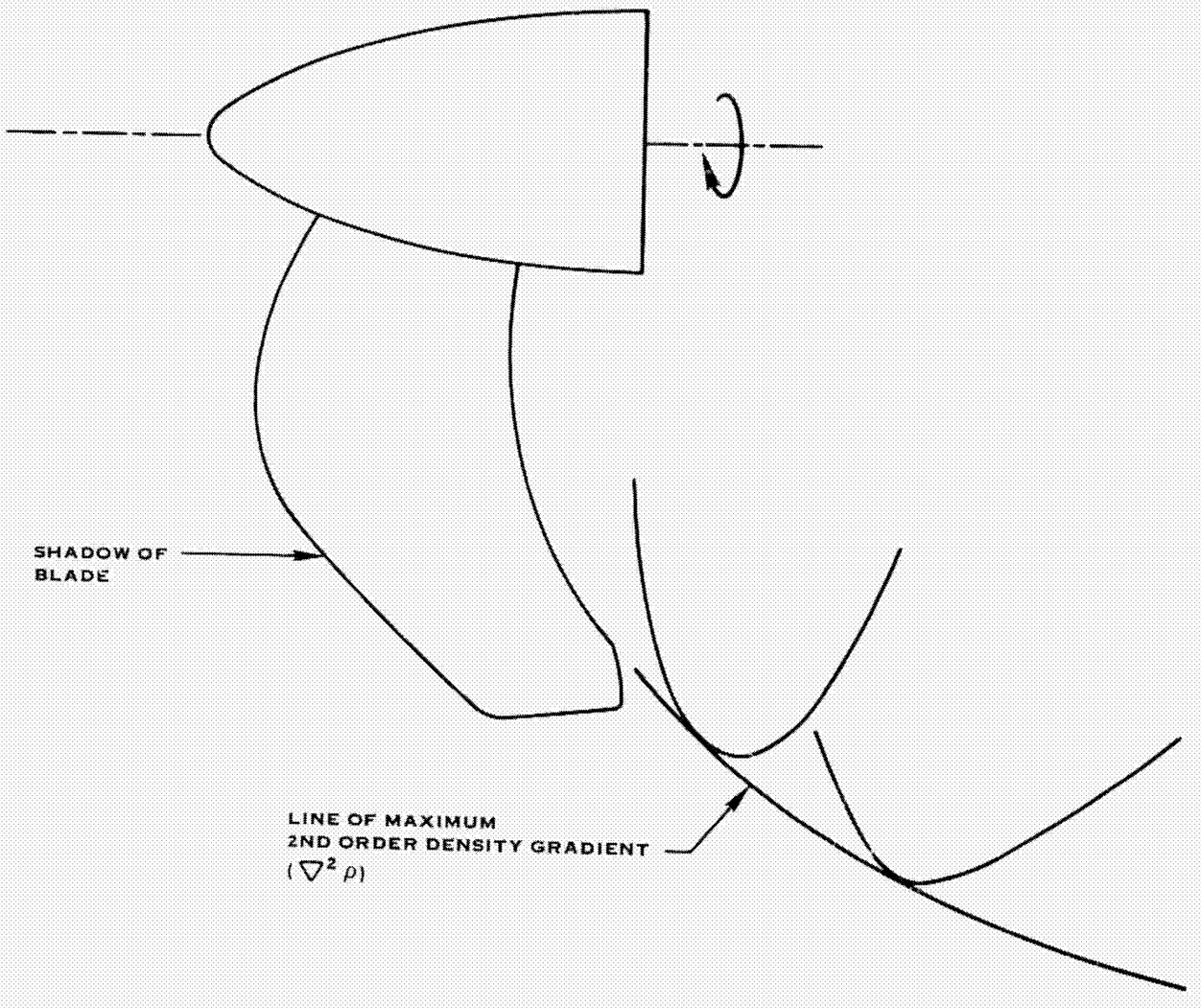

FIGURE B-12 SHADOWGRAPH PLANFORM VIEW

FIGURE B-13. SR-3 SHADOWGRAPH SERIES 1.185 TIP HELICAL MACH NUMBER 26.7 KW (36 SHP) PER BLADE

FIGURE B-14. SR-3 SHADOWGRAPH SERIES 1.174 TIP HELICAL MACH NUMBER 24.0 KW (32.2 SHP) PER BLADE